

---

Electronic Thesis and Dissertation Repository

---

12-14-2022 10:00 AM

## The Origin and Evolution of Impact Crater Lakes: A Case Study of the Ries Impact Structure, Germany

Matthew J. O. Svensson, *The University of Western Ontario*

Supervisor: Osinski, Gordon R., *The University of Western Ontario*

Co-Supervisor: Longstaffe, Fred J., *The University of Western Ontario*

A thesis submitted in partial fulfillment of the requirements for the Doctor of Philosophy degree in Geology

© Matthew J. O. Svensson 2022

Follow this and additional works at: <https://ir.lib.uwo.ca/etd>



Part of the [Geology Commons](#)

---

### Recommended Citation

Svensson, Matthew J. O., "The Origin and Evolution of Impact Crater Lakes: A Case Study of the Ries Impact Structure, Germany" (2022). *Electronic Thesis and Dissertation Repository*. 9079.  
<https://ir.lib.uwo.ca/etd/9079>

This Dissertation/Thesis is brought to you for free and open access by Scholarship@Western. It has been accepted for inclusion in Electronic Thesis and Dissertation Repository by an authorized administrator of Scholarship@Western. For more information, please contact [wlsadmin@uwo.ca](mailto:wlsadmin@uwo.ca).

## Abstract

Impact events are known to generate hydrothermal systems, which can subsequently vent into an overlying crater lake and potentially create ideal conditions for some microbial life-forms. Thus, early post-impact sedimentary deposits would be excellent targets for Mars sample return, and as such, the robust characterization of such deposits on Earth is critical. In this thesis, we establish an improved understanding of how the Ries crater lake formed, and how an active impact-generated hydrothermal system influenced its early evolution. The ~14.8 Ma Ries impact structure hosts the majority of its paleolake deposits within the structure's central basin with some deposits situated at higher stratigraphic positions beyond the central basin's edge. This research highlights and reconciles differences between the basal sedimentary deposits within the central basin sampled by the Nördlingen drill core, and those beyond the edge of the central basin sampled by the Wörnitzostheim drill core. We suggest that the Wörnitzostheim sedimentary deposits likely represent the transition from a back stepping alluvial fan to a playa lake system. The basal conglomerates representing the Wörnitzostheim alluvial fan host 100–130 °C mineral deposits localized to void and fracture spaces. Illite, kaolinite and particularly smectitic clay minerals were major constituents throughout the alluvial fan to playa lake transition, and their  $\delta^{18}\text{O}$  and  $\delta^2\text{H}$  indicate formation from weakly alkaline, local meteoric water at ~20 °C. The basal sedimentary deposits of the Nördlingen drill core likely represent a water-laden debris flow, as opposed to previous interpretations suggesting subaerial deposition from an ejecta plume. These deposits lack accretionary lapilli and were affected by pervasive alteration; they host 100–200 °C, void-filling mineralization in their basal conglomerate and gravelstone sections. This re-interpretation implies that ejecta plume fallback deposits are not always well-preserved and that they may not always be ideal marker beds, and points to concomitant fluvio-lacustrine deposition and hydrothermal activity. Overall, the results of this thesis have shown evidence of spatially diverse lacustrine processes during early sedimentary deposition and contributes the first mineralogical evidence of hydrothermal alteration at temperatures of ~100 °C or greater in early post-impact sedimentary deposits in an impact structure on Earth.

## Keywords

Impact cratering, sedimentary petrology, isotope geochemistry, sequence stratigraphy, paleolimnology, clay mineralogy, planetary geology, Mars analogues.

## Summary for Lay Audience

Meteorite impact events are well known for their destructive force, imparting massive amounts of energy into the surface of rocky bodies throughout the solar system. If an impact event is big enough, the energy from the impact can potentially create pools of molten rock, which can retain their heat for thousands of years as they gradually cool. On Earth, and potentially on ancient Mars, craters made by meteorite impacts can also infill with lake systems. In cases where water begins to fill an impact crater that still has hot masses of rock the heat causes that water to circulate through the cracks and fractures in the impact structure, potentially creating ideal conditions for early forms of life. The interaction between an impact crater lake and hot rocks created by the impact are potentially recorded in the rock record as the lake deposits accumulate over time. This thesis investigates the interface between rocks made by impact crater lakes and the previously molten rocks created by the impact event itself to better understand the environmental conditions in the early crater lake environment. The Ries impact structure in southern Germany, being one of the best preserved and well-studied impact structures on Earth, makes an excellent candidate for this case study. The rocks representing the earliest parts of the Ries crater lake were characterized, and their sedimentary structures and mineralogy indicated that they likely represented debris flows and the formation of alluvial fans. Additionally, the minerals in the fractures and voids of these rocks indicated that slightly alkaline, high temperature 100–130 °C fluids were present, which cooled to ~20 °C. High temperature minerals were more abundant in central regions of the crater lake environment than they were towards the edge of the lake system. Not only is this crater lake environment spatially diverse, but the processes that formed it were also shown to complicate the preservation of plumes of dust launched into the air by the impact event, making them less useful as markers for timing than previously thought.

## Co-Authorship Statement

**Chapter 2:** The data for this chapter was collected and processed by Matthew Svensson with the aid of technical staff: Marc Beauchamp, Liane Loiselle, Alex Rupert and Kim Law. Data for this chapter was partially collected for contributions to research regarding In Situ X-Ray Diffraction (ISXRD) for the exploration of Mars led by Dr. Roberta Flemming. This chapter was guided mainly by Dr. Gordon Osinski. A manuscript version of the chapter was written by Matthew Svensson with edits from Dr. Gordon Osinski, Dr. Fred Longstaffe, and Dr. Tim Goudge. Although largely complete, this work has not yet been published.

**Chapter 3:** The data for this chapter was collected and processed by Matthew Svensson with the aid of technical staff: Marc Beachamp, Grace Yao and Kim law. This chapter was guided primarily by Dr. Fred Longstaffe. This work is largely reliant on the foundation set by Chapter 2. Comments and editing were provided by Dr. Gordon Osinski and Dr. Fred Longstaffe. Additional data collection is anticipated prior to the publication of this chapter.

**Chapter 4:** The data for this chapter was collected and processed by Matthew Svensson with the aid of technical staff: Liane Loiselle, Peter Christoffersen and Josh Laughton. This chapter was guided primarily by Dr. Gordon Osinski. Comments and edits for this chapter were provided by Dr. Gordon Osinski and Dr. Fred Longstaffe. Additional data collection is anticipated prior to the publication of this chapter.

## Acknowledgments

I am deeply grateful for the guidance, mentorship and support of my supervisors Dr. Gordon Osinski and Dr. Fred Longstaffe. I would like to thank Oz for the freedom and exploration afforded to me during my time in his research group. All the unforgettable field courses, the trips to the Ries, the uniquely fascinating analogue missions, the discussions and fun at conferences, and the wonderful people I have met over the last few years are because you answered the email of a curious undergraduate student in spring of 2016. I would like to thank Fred for his light-hearted, supportive mentorship, and patience as I navigated my academic growth in the world of science. The steps I take in my career will always be taken with the example you set as a mentor, scientist, and leader in mind. Thank you to the members of my Ph.D. committee: Dr. Robert Linen and Dr. Tim Goudge. Thank you to Bob for keeping me on my toes during my comprehensive exam in a far more significant manner than I had anticipated. Thank you to Tim for your thoughtful input and guidance throughout the final years of my degree. Thanks as well to Dr. Livio Tornabene for your time and tutelage as I took my first steps into world of spectroscopy.

Thank you to the examiners: Dr. Roberta Flemming, Dr. Phil McCausland, Dr. Gernot Arp and Dr. Peter Ashmore. Thank you for your time and attention as you participated in my defense, and provided edits, comments and suggestions on my thesis. Thank you as well to the chair of my defense, Dr. Carole Creuzenet for your attentive moderation.

Thank you to the technical staff who have made the completion of this degree at all possible: Kim Law, Grace Yau, Li Huang, Jacob Walker, Marc Beauchamp, Liane Loiselle, Josh Laughton, Peter Christoffersen, Laura Jenkins, and Alex Rupert. I would like to especially thank Kim Law whose guidance and patience fostered my technical understanding and ability in the lab throughout my entire degree. I would also like to thank my friends and colleagues in the lab group, whom I will look up to for the rest of my career as you made the long hours in the lab possible and inspired me to better myself every day: Zach Morse, Patrick Hill, Matt Cross, Sarah Simpson, Christy Caudill, Haley Sapers and Cassandra Marion.

Thank you to Alexis Pascual, Mohammed Chamma and Stephen Amey for making the High-Altitude Balloon Initiative the uniquely memorable and fun experience that it was. Thank you for your unwavering comradery, your revitalizing senses of humor, and friendship as we navigated the great many challenges of managing and running the initiative for two years. Special thanks to field team 2, who kept field team 1 from self-destructing.

Thank you to the many friends who have come and gone during my time in grad school. Thank you for the laughs, the lunches, the teams, the support and community on our rollercoaster rides through grad school. Thank you for making goodbyes difficult and thank you for saying hello and welcome later on.

Thank you to my family who have been unwavering in their support as I inexplicably decided to study rocks for a living. Throughout my trials and growth, you have always been present and supportive, and I will in turn always be there for you. Thank you to my grandmother who was always a gentle and joyful presence in my life. You are dearly missed every day.

This work was made possible by funding contributions of the Province of Ontario through the Ontario Graduate Scholarship (OGS) (ms), the Natural Sciences and Engineering Research Council of Canada (NSERC) Postgraduate Scholarships Doctoral Program (ms), the NSERC Discovery Grants Program (fjl), the Canada Research Chairs Program (fjl), and the technical support of the Laboratory for Stable Isotope Science (LSIS) and the Earth and planetary Materials Analysis (EPMA) Laboratory teams. Thank you to the team at ZERIN, particularly Poes Gisela, Dr. Stefan Holzl and Karen Heck for their valuable support in field work and sample acquisition.

## Land Acknowledgement

I acknowledge that Western University is located on the traditional lands of the Anishinaabek, Haudenosaunee, Lūnaapéewak and Attawandaron peoples, on lands connected with the London Township and Sombra Treaties of 1796 and the Dish with One Spoon Covenant Wampum. This land continues to be home to diverse Indigenous peoples (e.g. First Nations, Métis and Inuit) whom we recognize and thank as contemporary stewards of the land.

# Table of Contents

Abstract .....	ii
Summary for Lay Audience .....	iv
Co-Authorship Statement (where applicable).....	v
Acknowledgments.....	vi
Table of Contents .....	ix
List of Tables .....	xiii
List of Figures .....	xiv
List of Appendices (where applicable) .....	xvii
1 Introduction and Literature Review .....	1
1.1 Introduction.....	1
1.2 Geological Setting of the Ries Impact Structure.....	2
1.3 The Impact Cratering Process .....	4
1.4 Impact Generated Hydrothermal Systems .....	7
1.5 Terrestrial Impact Crater Lakes .....	10
1.5.1 Ries Impact Structure, Germany .....	11
1.5.2 Bosumtwi Impact Structure, Ghana .....	14
1.5.3 Lonar Lake Impact Structure, India .....	16
1.5.4 Boltysh Impact Structure, Ukraine.....	18
1.5.5 The Haughton Impact Structure, Canada.....	20
1.5.6 Summary .....	22
1.6 Clay Minerals.....	26
1.7 Thesis Outline .....	28
1.7.1 Chapter 2: A mineralogical and textural investigation of the impact melt-bearing breccia to post-impact sedimentary transition in the Wörnitzostheim drill core, Ries impact structure, Germany .....	28

1.7.2	Chapter 3: Tracing the fluid evolution of early post-impact fluvio-lacustrine systems beyond the central basin of the Ries impact structure, Germany .....	29
1.7.3	Chapter 4: Revisiting the origin of the Ries graded suevite: implications for plume fallback preservation and early post-impact sedimentary deposition. ....	29
1.7.4	Chapter 5: Discussion and Conclusions.....	30
1.8	References .....	30
2	A mineralogical and textural investigation of the impact melt-bearing to post-impact sedimentary transition in the Wörnitzostheim drill core, Ries impact structure, Germany .....	1
2.1	Introduction.....	50
2.2	Background .....	51
2.3	Samples and Analytical Techniques .....	55
2.4	Results: Drill core, mineral chemistry and petrographic descriptions .....	59
2.4.1	<i>Impact melt-bearing breccias</i> (>32 – 20.1 m; units 15 and 14).....	62
2.4.2	Conglomerates (20.1–13.1 m; units 13, 12 and 11).....	68
2.4.3	Sandstones and sandstone conglomerate (13.1 – 10.7 m; units 10, 9 and 8) .....	77
2.4.4	<i>Marlstones</i> (10.7–2.0 m; units 7, 6, 5, 4, and 3) .....	79
2.4.5	Mudstones (3.0 – 0 m; units 2 and 1).....	84
2.5	DISCUSSION.....	85
2.5.1	Comparison with previous work.....	85
2.5.2	Post-impact sedimentation and environmental record.....	89
2.5.3	Hydrothermal activity during early post-impact sedimentation .....	96
2.6	Conclusions.....	98
2.7	References.....	100
3	Tracing the fluid evolution of early post-impact fluvio-lacustrine systems beyond the central basin of the Ries impact structure, Germany .....	50

3.1	Introduction.....	107
3.2	Geological Setting.....	109
3.3	Methodology.....	115
3.4	Results.....	121
3.4.1	Clay Mineral Chemistry.....	121
3.4.2	Clay Mineralogy (X-ray Diffraction).....	125
3.4.3	$\delta^2\text{H}$ and $\delta^{18}\text{O}$ Measurements.....	128
3.5	Discussion.....	130
3.5.1	Clay Mineralogy.....	130
3.5.2	Stable Isotope Composition of Mid-Miocene Meteoric Water.....	137
3.5.3	Modeling temperatures and isotopic composition of potential clay mineral source fluids.....	138
3.5.4	Controls on Clay Mineral Formation.....	146
3.5.5	Comparison to Previous Petrographic Interpretations.....	146
3.6	Conclusions.....	147
3.7	References.....	148
4	Revisiting the origin of the Ries graded suevite: implications for plume fallback preservation and early post-impact sedimentary deposition.....	107
4.1	Introduction.....	162
4.2	Background.....	164
4.3	Methodology.....	167
4.4	Results.....	168
4.4.1	Stratigraphy.....	170
4.4.2	Alteration and Secondary Mineralization in the Graded Unit (331.5–314.3 m).....	174
4.5	Discussion.....	180
4.5.1	Deposition of the Ries Graded Unit.....	180

4.5.2	Hydrothermal Alteration of the Ries Graded Unit.....	185
4.5.3	Comparison to the Wörnitzostheim Drill Core.....	186
4.5.4	Comparison with Ejecta Plume Deposit Preservation at the Bosumtwi Crater, Ghana .....	187
4.6	Conclusions.....	188
4.7	References.....	189
5	Discussion and Conclusions.....	162
5.1	Introduction.....	196
5.2	Reconciling Early Lacustrine Processes within and beyond the Ries Central Basin .....	197
5.3	The Interface Between Post-Impact Lake Systems and Impact Generated Hydrothermal Systems.....	199
5.4	Applications to Astrobiology and Mars Exploration .....	200
5.5	Conclusion .....	202
5.6	Future Work .....	202
5.7	References.....	203
	Curriculum Vitae .....	284

# List of Tables

## Chapter 1

Table 1. 1: Summary of key parameters pertaining to the context and characteristics of five impact crater lakes. .... 24

## Chapter 2

Table 2. 1: Sample record and analytical techniques applied to each sample. ....58

Table 2. 2: Unit mineralogy. ....61

**Table 2. 3:** Averaged WDS results of micas and feldspars from conglomerate units.

..... **Error! Bookmark not defined.**

## Chapter 3

Table 3. 1: Samples and analytical techniques. ....116

Table 3. 2: Summary of averaged WDS analysis of clay minerals.....123

Table 3. 3:  $\delta^{18}\text{O}$  and  $\delta^2\text{H}$  results for the 2–0.2, <2 and <0.2  $\mu\text{m}$  size-fractions.....129

Table 3. 4: Clay mineral abundances\* for the Ca-EG saturated <0.2  $\mu\text{m}$  size-fractions.133

Table 3. 5: Isotope geothermometers for modeling clay mineral source water compositions. ....141

Table 3. 6: Weighted isotopic compositions of hypothetical 20 °C source waters\*. ....143

# List of Figures

## Chapter 1

Figure 1. 1: A geological map of the Ries impact crater. ....	3
Figure 1. 2: A diagram outlining the excavation and modification stages of the impact cratering process as labelled on the diagram .....	6
Figure 1. 3: The distribution of impact generated hydrothermal deposits within the context of a typical complex crater. ....	8
Figure 1. 4: The distribution of the post-impact lacustrine rocks at the Ries impact structure.....	12
Figure 1. 5: Carbonate facies of the northeastern margin of the Ries lake. ....	14
Figure 1. 6: Geological map of the Bosumtwi Lake impact structure. ....	16
Figure 1. 7: Geological map of the Lonar Lake impact structure .....	18
Figure 1. 8: Simplified cross section of the Boltysk post-impact deposits.....	20
Figure 1. 9: Simplified geological map of the western side of the Haughton impact structure.....	22
Figure 1. 10: The general structure of a 2:1 layer clay mineral with interlayer material distinguishing it from the tetrahedral sheet of another clay mineral .....	27

## Chapter 2

Figure 2. 1: Simplified geological map and cross section of the Ries impact structure ...	54
Figure 2. 2: Stratigraphic column for the Wörnitzostheim 1965 drill core.....	60
Figure 2. 3: Common alteration and groundmass textures in the pink melt-bearing breccia (unit 15), sampled from 32 m depth.....	64

Figure 2. 4: Degassing pipe sample observed at 27.50 – 27.70 m depth.....	66
Figure 2. 5: Quench and immiscibility textures in glasses and groundmass of unit 14....	67
Figure 2. 6: Ternary diagrams of feldspar and mica mineral compositions .....	70
Figure 2. 7: Back-scattered electron images of mineral textures from unit 13.....	72
Figure 2. 8: Representative core sample of unit 11 .....	74
Figure 2. 9: Back-scattered electron images from unit 8.....	76
Figure 2. 10: Core sample of unit 9 from 12.74 m depth.....	79
Figure 2. 11: Cross-polarized and plane-polarized optical microscope images of thin-section samples of unit 5.....	82
Figure 2. 12: Cross sectional and top view of the white-toned material from unit 6, sub-parallel layering, load structures and pseudo-polygonal mud cracks..	84
Figure 2. 13: Graphical representation of the upper 32 m of the Wörnitzostheim 1965 drill core based on the descriptions in Förstner’s (1967) original log. ....	86
Figure 2. 14: A diagram illustrating the likely deposition environment represented by the Wörnitzostheim drill core .....	95

### **Chapter 3**

Figure 3. 1: A geological map of the Ries impact structure .....	111
Figure 3. 2: The stratigraphy of the Wörnitzostheim 1965 drill core .....	114
Figure 3. 3: Back-scattered electron and WDS images of clay minerals occurring in unit 13 and unit 11.....	122
Figure 3. 4: Metal oxide abundances (wt.%) of interstitial and void-filling clay minerals as determined by WDS spot analyses .....	124

Figure 3. 5: Diffraction patterns collected from the <math><2 \mu\text{m}</math> size-fraction. ....	127
Figure 3. 6: $\delta^{18}\text{O}$ and $\delta^2\text{H}$ of samples collected from melt-bearing breccias, main conglomerates, sandstone conglomerates, and marlstones. ....	130
Figure 3. 7: Values of $\delta^2\text{H}$ vs $\delta^{18}\text{O}$ for <math><0.2 \mu\text{m}</math> size-fraction samples from the Wörnitzostheim drill core plotted against calculated water and clay mineral compositions. ....	145
<b>Chapter 4:</b>	
Figure 4. 1: A schematic representation of the process by which a cloud of impact-generated material settles back into the bounds of the impact structure.....	163
Figure 4. 2: A geological map of the Ries impact structure .....	166
Figure 4. 3: Simplified stratigraphy of the Nördlingen 1973 drill core. ....	169
Figure 4. 4: The stratigraphy of the Ries graded unit .....	171
Figure 4. 5: Transmitted light photomicrographs of glass clasts .....	172
Figure 4. 6: Photomicrographs hydrothermal mineral textures .....	176
Figure 4. 7: Zoned alteration feature from 322.0 m depth.....	178
Figure 4. 8: A section of a granitoid lithic clast showing sericitic alteration to clay minerals in the feldspars .....	180

## List of Appendices

Appendices.....	209
Appendix A: Chapters 2 & 3 Supplementary Data.....	209
A.1 Wörnitzostheim Drill Core Log.....	209
Standards for WDS Analysis.....	217
WDS Data Tables.....	218
Raw Oxygen and Hydrogen Isotope Results.....	<b>Error! Bookmark not defined.</b>
<i>p</i> XRD Scans of Wörnitzostheim Core Samples.....	240
Appendix B: Nördlingen Drill Core Log.....	248
Appendix C: Preliminary $\mu$ XRD results and In-Situ X-Ray Diffraction (ISXRD) Research Contributions.....	273

## List of Abbreviations

°C	Degrees Celsius
° 2θ	Degrees two theta
μXRF	Micro X-ray fluorescence
‰	Permil
%	Percent
Ab.	Albite
An.	Anorthite
BGMN	Bergman
Bi.	Biotite
BSE	Back scattered electron
Cal.	Calcite
Chl.	Chlorite
cm	Centimetres
Dol.	Dolomite
EDS	Energy Dispersive Sepctroscopy
EG	Ethylene Glycol
Eqn.	Equation
EVA	DIFFRAC PLUS Evaluation software
FBN73	Nördlingen 1973 drill core
Fe-Do.	Ferroan dolomite
FE-EPMA	Field Emission Electron Probe Micro- Analyzer
GADDS	General Area Detector Diffraction System
GC	Gas chromatography
GMWL	Global meteoric water line
Gyp.	Gypsum
ICDD	International Center for Diffraction Data
Ill.	Illite

IRMS	Isotope Ratio Mass Spectrometry
ISXRD	In-Situ X-Ray Diffraction
Kfs.	Potassium feldspar
Kln.	Kaolinite
km	Kilometres
KTB	German Continental Deep Drilling
kV	Kilovolts
Ky.	Kyanite
Lam.	Lamination
LSIS	Laboratory for Stable Isotope Science
m	Metres
mA	Mili-Amps
mm	Milimetres
Ms.	Muscovite
nA	Nano-Amps
nm	Nanometres
Opx.	Orthopyroxene
Ph.	Phlogopite
Pl.	Plagioclase
PPL	Plane Polarized Light
<i>p</i> XRD	Powder X-Ray Diffraction
Py.	Pyrite
Qz.	Quartz
Ref.	Reference
RH	Relative Humidity
RT	Room Temperature
SE	Secondary Electron
Sme.	Smectite
TC-EA	Thermal Combustion Elemental Analyzer
USGS	United States Geological Survey
VSMOW	Vienna Standard Mean Ocean Water

WDS	Wavelength Dispersive Spectroscopy
Wt%	Weight Percent
XPL	Cross Polarized Light
XRD	X-Ray Diffraction
ZERIN	Ries Impact Crater Museum
$\delta^{18}\text{O}$	Delta Oxygen-18
$\delta^2\text{H}$	Delta Hydrogen-2
$\lambda$	Wavelength
$\mu\text{m}$	Micrometres
$\mu\text{XRD}$	Micro X-Ray Diffraction

# 1 Introduction and Literature Review

## 1.1 Introduction

The goal of this thesis is to enhance our understanding of the early depositional processes associated with impact crater lake environments and the evolution of their early stages. As possible host environments for early forms of life and as high-resolution record keepers of climate change and aqueous history over time, the deposits of lakes hosted by impact craters have been the subject of significant interest both on Earth and on Mars (e.g., Hickey et al., 1988; Newsom et al., 1996; Cabrol and Grin, 1999; 2001; Arp et al., 2013a; Osinski et al., 2013; 2020; Cockell et al., 2020). During early lacustrine deposition, interaction between water and latent heat from melt-bearing impactites can generate hydrothermal systems capable of creating potentially suitable conditions for early life forms (Osinski et al., 2013; 2020; Cockell et al., 2020).

The ~24 km diameter, ~14.8 Ma Ries impact structure, Germany, hosts several styles of post-impact lacustrine deposits (e.g., Füchtbauer et al., 1977; Riding, 1979; Pache et al., 2001; Arp, 2006; Arp et al., 2013a; 2017; Christ et al., 2018), and evidence of impact generated hydrothermal alteration is well documented and spatially variable (Arp et al., 2013b; Caudill et al., 2021; Newsom et al., 1986; Osinski, 2005; Osinski et al., 2004; Sapers et al., 2017). As such, this structure provides an optimal site to study early post-impact lacustrine sedimentation, and the effects of impact generated hydrothermal alteration on crater lake evolution. This thesis contributes a case study of the Ries impact structure, Germany, with the aim of characterizing the early crater lake environment to frame early post-impact ecological recovery on Earth and establishing a renewed understanding for the exploration of Mars. This thesis focuses on two main drill cores: the Nördlingen 1973 drill core, and the Wörnitzostheim drill core, which sample lake deposits in the central basin of the impact structure and an outer basin, respectively. Key mineralogical products formed from impact generated hydrothermal systems in early post-impact lacustrine deposits are highlighted with an emphasis on clay minerals; providing insight on the mechanisms of lacustrine formation, the temperature and compositional evolution of early lacustrine fluids, the sources and availability of water at the Ries, and the effect of water availability on the

record of other post-impact processes. Additionally, this thesis contributes the first comprehensive study of secondary alteration products in early post-impact sedimentary deposits at the Ries impact structure. Overall, the goals of this thesis are as follows:

- Outline possible depositional environments recorded in sedimentary rocks from distinct settings within the impact structure.
- Characterize any hydrothermal mineral assemblages present in the post-impact sedimentary deposits.
- Reconcile differences in lacustrine and hydrothermal environments between the distinct settings investigated in this thesis.

## 1.2 Geological Setting of the Ries Impact Structure

The ~24 km diameter, ~ 14.8 Ma Ries impact structure in southern Germany (Fig. 1.1; Schmieder et al., 2018) is a complex impact structure that occurs in a mixed target rock of Hercynian age gneissic crystalline rocks overlain by Jurassic limestones and Triassic sandstones, siltstones and conglomerates. The Ries impact structure is characterized by a tectonic outer rim delineated by a roughly circular ring of highlands and a ~12 km diameter central basin bound by a so called “inner ring” that lacks any modern topographical expression. The displacement, melting and recrystallization of the target material resulted in the formation and emplacement of the Ries’ impactites; rocks created or modified by a hypervelocity impact event (Grieve and Therriault, 2013). The impact event generated a series of impact melt bearing breccias which comprise a continuous ~600 m thick crater fill deposit situated within the central basin, and a discontinuous series of melt-bearing breccias ejected from the central basin (hereafter, melt bearing ejecta) scattered outside the bounds of the central basin that are up to ~80 m thick (Förstner, 1967; Pohl et al., 1977; Stöffler et al., 2013). The crater-fill melt-bearing breccias host pervasive secondary alteration, likely owing to the presence of an overlying lacustrine system (Osinski, 2005). The melt-bearing ejecta typically present secondary hydrothermal mineralization that is generally limited to fillings and linings within fractures and voids (Osinski, Grieve and Spray, 2004; Osinski, 2005; Sapers et al., 2017). The concentration of hydrothermal mineralization in these melt-bearing deposits indicates that they likely contributed a major source of heat, fueling the impact generated hydrothermal system at the Ries (Osinski et al., 2004; Osinski, 2005).

Approximately 400 m of lacustrine deposits directly overly pervasively altered melt-bearing breccias within the central basin, and up to 20 m of lacustrine deposits occur directly overlying some melt-bearing ejecta (Förstner, 1967; Pohl et al., 1977; Stöffler et al., 2013). The direct abutment of melt-bearing breccias with post-impact lacustrine deposits indicates that the impact generated hydrothermal system could have vented into the overlying lacustrine system (Osinski et al., 2013); however, mineralogical evidence of hydrothermal venting into the Ries crater lake has not been documented in detail, hence the motivation for the current study.

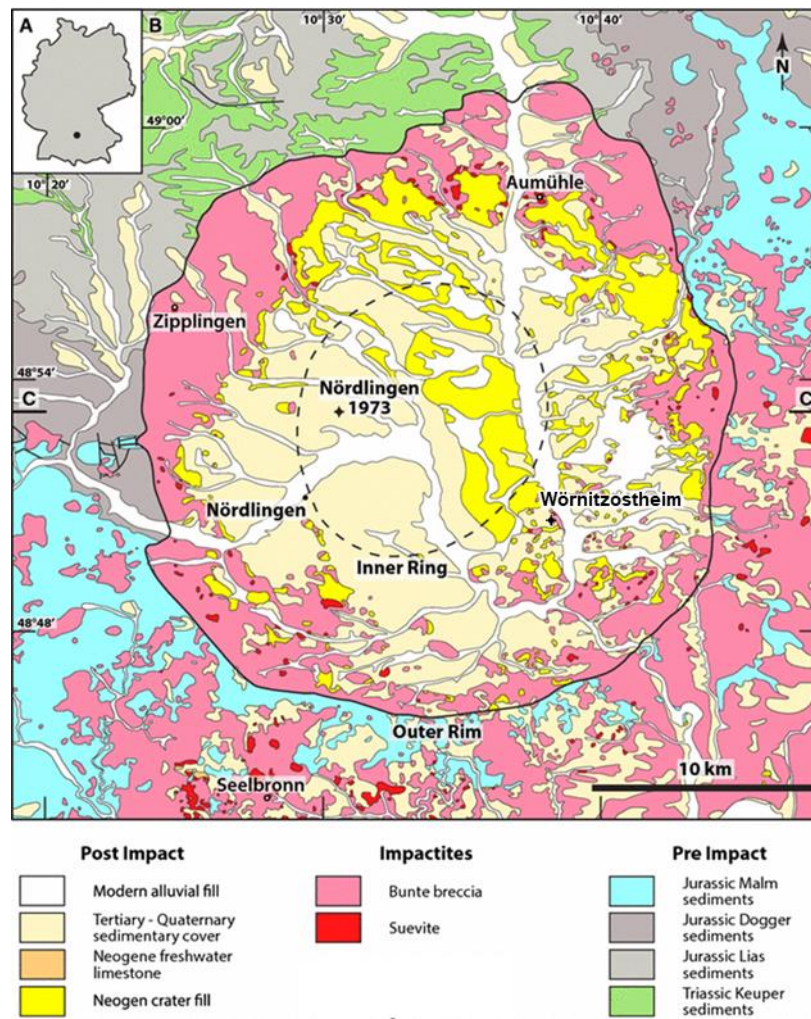


**Figure 1. 1:** A geological map of the Ries impact crater highlighting (A) the location of the impact structure with respect to Germany, and (B) major post-impact deposits, impactites and pre-impact lithologies (Erickson et al., 2017) based on the work of Pohl et al. (1977).

The solid black line outlines the extent of the tectonic outer rim of the impact structure, and the dashed line outlines the approximate extent of the central basin. Additionally, this map highlights the location of the Nördlingen and Wörnitzostheim drill cores.

### 1.3 The Impact Cratering Process

Impact cratering and the formation of impactites is a geological process at the foundation of this thesis. Historically, the impact cratering process has been characterized by three loosely defined stages (Fig. 1.2): (1) contact and compression, (2) excavation and (3) modification (Gault et al., 1968). These stages are briefly discussed below.

The contact and compression stage is characterized by immediate transmission of kinetic energy from a hypervelocity projectile ( $>3,000$  m/s) to the target rock, thereby generating an initial shockwave that compresses the target with several hundred gigapascals of pressure and generates temperatures in excess of 10,000 K (Melosh, 2013). Melosh (2013) contextualizes the pressure-temperature conditions triggered by impact events with a comparison to that of the Earth's core, which are  $\sim 350$  GPa and  $\sim 5,000$  K, respectively. These shockwaves also propagate through the impactor as rarefaction waves and, with sufficient shock pressures, can cause the complete vaporization of the projectile itself (Gault et al., 1968; Melosh, 1989; 2013). The transition to the excavation stage is defined by the complete vaporization of the projectile; however, the transition between stages exists as a continuum.

The excavation stage is characterized by the complex interactions between the impact-generated shockwave and the target material as the shockwave radially propagates from the point of impact. Impact induced rarefaction waves also propagate downward from the point of impact creating an "interference zone" where shockwaves and rarefaction waves interact (Melosh, 1989; 2013). The interaction of shock and rarefaction waves in the interference zone creates an excavation flow-field (Fig. 1.2) which outlines zones where target material is likely to be displaced or excavated from the point of impact (Dence, 1968; Grieve and Cintala, 1982). The excavation of target material results in the formation of a transient cavity. Excavated target rock is ballistically ejected beyond the forming transient cavity and deposited as a continuous ejecta blanket (Oberbeck, 1975; Pohl et al., 1977) whereby

material from the upper zone of the target at the point of impact achieves a proximal emplacement (Stöffler et al., 1975), and deeper target material is emplaced at more distal locations. The pressure gradient triggered by the impact is such that deeper target material is subjected to higher pressures; so, when material is rapidly excavated, the decompression from high shock pressures combined with the initial high temperatures and pressures of the impact event causes melting (Osinski et al. 2011). The cooling melt and newly formed breccias comprise impact generated rocks (Osinski et al., 2018). It was experimentally determined that material within the displaced zone generally does not leave the transient cavity (Stöffler et al., 1975); however, observations from terrestrial impact craters indicates that some material from the displaced zone (Fig. 1.2) can be transported beyond the crater during a secondary phase of ejecta emplacement (Osinski et al., 2011). Impact melt-bearing rocks line the interior of the transient cavity, which later settle in what becomes the crater interior and form “crater-fill deposits”. Observations from terrestrial impact craters indicate that impact melt-bearing material can also be ejected beyond the crater rim as ground-hugging flows that incorporate fragments of the target rock (Osinski, 2004; Osinski et al., 2011). The end of the excavation stage is marked by the point where propagating shockwaves and rarefaction waves are no longer able to eject or displace material.

The modification stage is largely controlled by the size of the transient cavity and the physical properties of the target rock (Melosh and Ivanov, 1999). Simple craters are formed at diameters of ~3 km on Earth and ~6 km on Mars where the transient cavity exhibits relatively little modification to its approximate bowl shape, which is by extension transitive to the shape of the final crater (Pike, 1980; Osinski et al., 2022). At diameters that exceed that of the simple crater size “limit”, the transient cavity is unstable and gravitational settling of impacted material results in the formation of a complex impact structure (Dence, 1968). Central uplifts are triggered by the movement of material in the floor of the transient cavity (Melosh, 1989). The movement of material in the crater floor can also result in the formation of central peak basins to peak ring basins in the place of a central uplift with increasing diameter of the crater. The modification stage never truly ends as it encompasses post-impact processes such as weathering and erosion.

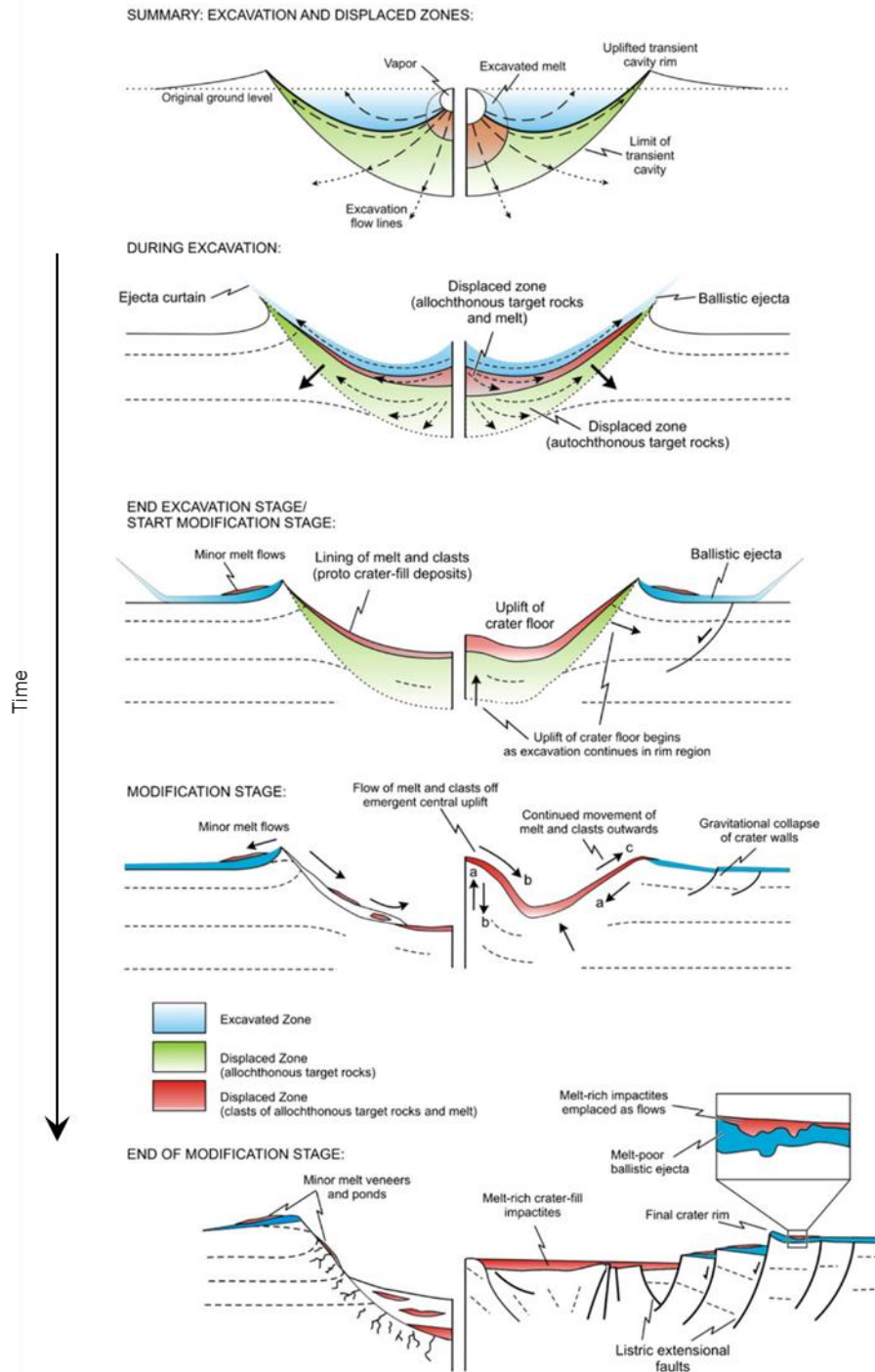


**Figure 1. 2:** A diagram outlining the excavation and modification stages of the impact cratering process as labelled on the diagram (Osinski et al., 2011). This model depicts the emplacement of impact generated melt in the case of both simple (left panel) and complex (right panel) impact structures. Letter and arrow labels present in the modification stage

indicate different stages in time (a–c). The first stage (a) represents the initial collapse of the crater walls and the central uplift, followed by (b) the flow of melt and clasts off the emergent central uplift, and finally (c) continued transport of clasts and melt-bearing material upon the collapse of the crater wall.

## 1.4 Impact Generated Hydrothermal Systems

Hydrothermal alteration is defined as a chemical weathering processes whereby rock-forming minerals interact with fluids at temperatures that are higher than expected considering the geothermal gradient of the given area (Kirsimäe and Osinski, 2013). The formation of any hydrothermal system requires the presence of a heat source, a source of H<sub>2</sub>O and a pathway to facilitate fluid circulation (e.g., faults and fractures). The generation of hydrothermal systems as a product of impact cratering is a well-documented phenomenon, which has been reported from ~70 of the ~200 known impact craters studied on Earth (Naumov, 2005; Kirsimäe and Osinski, 2013; Osinski et al., 2013). The faulting, fracturing and general disaggregation of target material can provide potential fluid pathways for hydrothermal circulation. The shock heating of the target material by the propagation of shockwaves and uplifting of warm deep seated rocks during the formation of a central uplift provides two notable sources of heat that could partly fuel an impact generated hydrothermal system; however, the primary heat source is provided by the impact melt rocks and melt-bearing impactites, in particular the continuous melt “sheet” hosted in annular depressions or central basin (Abramov and Kring, 2004; 2007). Primary fluid sources vary depending on the host region of the impact structure, but impact generated hydrothermal systems are generally fed by either meteoric water or seawater (Naumov, 2005). During the evolution of these hydrothermal systems, source fluids become more alkaline due to the hydrolysis of unstable, shocked (alumino-) silicates and impact-generated glass. The dissolution of this material creates a supersaturation of silica, which enables Fe-Mg clay minerals and zeolites to readily precipitate, as evident by their prevalence as main hydrothermal alteration phases in impact generated systems hosted in silicate target rocks (Naumov, 2005).

Three stages of hydrothermal alteration were broadly defined for impact generated hydrothermal systems based on petrographic observations and dominant fluid environment

regimes: (1) a vapor dominated stage characterized by potassium metasomatism of silicates, followed by (2) an intermediate stage of vapor to liquid-dominated alteration characterized by chlorite–smectite–zeolite mineralization, and lastly (3) a liquid dominated stage characterized carbonate–sulfide / oxyhydrate mineralization (Osinski et al., 2001; Versh et al., 2005).

Six general locations have been distinguished where impact generated hydrothermal deposits can occur (Fig. 1.3; Osinski et al. 2013): (1) crater-fill melt rocks and melt-bearing breccias; (2) the interior of central uplifts; (3) the exterior of central uplifts; (4) the crater rim; (5) post-impact crater lake deposits; (6) ejecta deposits (Osinski et al., 2013). The formation of these deposits, and the extent to which they form, generally correlates with the available heat sources and the geometry of the impact generated fracture network.

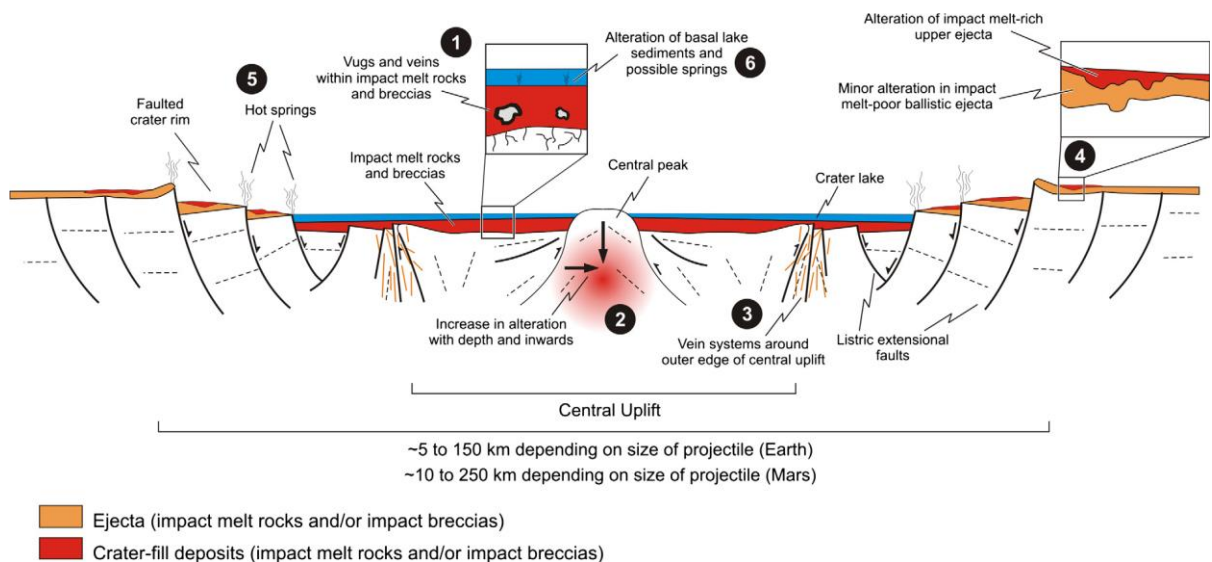


**Figure 1. 3:** The distribution of impact generated hydrothermal deposits within the context of a typical complex crater. Approximate limits to the scale of impact structures to which this model is primarily applicable are indicated in addition to the general location of various syn- and post-impact deposits (Osinski et al. 2013).

At the Ries impact structure, hydrothermal deposits are generally concentrated in the melt-bearing breccias. As indicated by the presence of impact generated glass, initial emplacement temperatures of the melt-bearing breccias was likely 750–900 °C or greater, which then rapidly cooled (Newsom et al., 1986; Osinski, 2005). Ries melt-bearing deposits

likely occur both as crater-fill deposits and ejecta (Osinski, 2004), and the hydrothermal deposits are variable between the two deposits, as suggested by their locations (Osinski et al., 2013). Crater-fill melt-bearing breccias exhibit pervasive alteration characterized by K-feldspar, albite, clay minerals, chlorite, zeolites, calcite, and additional minor phases such as pyrite, goethite, barite and siderite (Osinski, 2005). This mineral assemblage represents an initial stage of K-metasomatism concomitant with albitization and chloritization at 200–300 °C followed by intermediate argillic alteration and zeolitization (Osinski, 2005).

This alteration assemblage is notably different to that of the melt bearing ejecta where alteration is typically limited to smectitic clay minerals, Ba-phillipsite, quartz and calcite which lines and fills vesicles, fractures and voids (Osinski, 2005). This assemblage of secondary minerals reflects low temperature 100–130 °C alteration (Osinski, 2005). The alteration of melt-bearing ejecta is a more contentious subject and neither their original emplacement mechanism (Osinski, 2004; Stöffler et al., 2013) nor their alteration history (Newsom et al., 1986; Osinski, 2003; 2005; Osinski et al., 2004; Muttik et al., 2008; Muttik et al., 2010; Sapers et al., 2017; Caudill et al., 2021) are fully agreed upon. The lack of consensus with respect to the origin hydrothermal alteration history of the melt-bearing ejecta is largely owing to uncertainties pertaining to the origin of clay minerals which comprise >70 vol% of the groundmass (Osinski, Grieve and Spray, 2004). Oxygen and hydrogen isotope studies of clay minerals broadly present in the <2  $\mu\text{m}$  size fraction of the ejected melt-bearing breccias suggest that the clay minerals of the ejected melt-bearing breccias were formed by aqueous, low-temperature weathering processes following the deposition of the rock (Muttik et al., 2008; Muttik et al., 2010). Conversely, it has been shown that the clay minerals of the ejected melt-bearing breccias are highly complex (Newsom et al., 1986; Osinski, Grieve and Spray, 2004) and some are not consistent with surficial weathering or hydrothermal alteration, and instead, could have formed from the recrystallization / devitrification of metastable impact melt (Osinski et al., 2004). The ejected melt-bearing breccia exhibit variable hydrothermal alteration products comprising mixed layer illite-smectite, calcite, chlorite, zeolite and K-feldspar (Osinski et al., 2004; Sapers et al., 2017), and present platy clay mineral (montmorillonite) textures that are consistent with hydrothermal origins (Newsom et al., 1986; Osinski et al., 2004).

The duration of the Ries hydrothermal system is not well constrained but estimates have been made using cooling models (Daubar and Kring, 2001), which indicate that a 25 km diameter crater, with a 200 m thick melt sheet cooling from 800°C to 160°C could persist for approximately 3,000 years. Using a separate model, Pohl (1977) calculated that the cooling of a 200 m thick melt sheet from 800°C to 100°C would take several thousand years. Arp et al. (2013b) stratigraphically correlated a hydrothermal spring mound with late-stage lacustrine deposits, suggesting that the Ries' hydrothermal system was active 250,000 years after the impact event.

## 1.5 Terrestrial Impact Crater Lakes

Crater lakes specific to impact craters are not well understood, so a general model for impact crater lake formation on Earth has not been determined. Volcanic crater lakes and impact crater lakes share some similar scientific value. Volcanic crater lakes analogous to impact crater lakes, such as maar and caldera lakes, can record subtle environmental changes over longer periods of time than most other lake types, with some crater-lakes persisting for several million years (Cohen, 2003). The longevity of a crater-lake's life cycle is attributed to the steep crater walls and relatively small catchment area, which result in moderately high sedimentation rates (Cohen, 2003). Their small catchment size minimizes the influence of distal fluid sources and minimizes the number of potential lithologies influencing the watershed. These lake deposits are valuable because they preserve high resolution records of climate change over long periods of time (Cohen, 2003). Similarly, impact crater lake deposits were historically utilized largely for their climatological archives (Talbot and Johannessen, 1992; Gurov et al., 2006; Shanahan et al., 2006; 2009; Brigham-Grette et al., 2007; Melles et al., 2012); however, with the discovery of potential crater lake deposits on Mars (Forsythe, 1990; Forsythe and Zimbelman, 1995; Cabrol and Grin, 1999; Fassett and Head, 2005; 2008a; 2008b), impact crater lakes on Earth became the subject of special interest owing to their value as potential analogues for the sedimentary, hydrochemical, and paleobiological evolution of Martian paleolakes.

A review of crater lake deposits has been conducted for Martian craters (Newsom et al., 1996; Michalski et al., 2022), and the potential significance of crater lakes to the impact related biosphere and impact generated hydrothermal environment are generally noted

(Cabrol et al., 1999; Osinski, 2005; Osinski et al., 2013; 2020; Grotzinger et al., 2014; Cockell et al., 2020); however, a comprehensive review of impact crater lakes on Earth has not been conducted to date. As a precursor to such a contribution, a short review of a few post-impact crater lakes is provided here, with an emphasis on the Ries, and briefly discuss their common properties. This literature review outline the background for each impact structure and note traits such as location, age, size, target rock, and evidence of past or present ecosystems. We also briefly discuss the extent of hydrothermal deposits, the climate at the time and region of the impact event, and lacustrine evolution where applicable. We note whether the impact structures host a modern lake system or only paleolake deposits, whether there was any record of overflow, whether there is evidence of inlets and / or outlets, and whether the lake was or is hydrologically closed or open. For the purposes of this review, we focus mostly on crater lakes that are relatively well-studied and exclude large impact craters such as the ~180 km diameter Chicxulub impact structure, Mexico, and the ~250 km diameter Sudbury impact structure, Canada. In addition to the Ries impact structure, we discuss the Bosumtwi impact structure, Ghana, the Lonar Lake impact structure, India, the Boltysh impact structure, Ukraine, and the Haughton impact structure, Canada.

### 1.5.1 Ries Impact Structure, Germany

The sedimentary record of the Ries impact crater accounts for an approximately 1.2 Ma long period of time (Pohl et al., 1977) during the transition from the Mid-Miocene Climatic Optimum to a cooler climate influenced by the growth of the Antarctic ice sheet from ~14–13 Ma (Flower and Kennett, 1994; Shevenell et al., 2004; Westerhold et al., 2005; Holbourn et al., 2007). The immediate post-impact climate of the Ries is in alignment with the end of the Mid-Miocene Climatic Optimum (14.7 Ma) and is characterized by warm–subtropical conditions at ~20 °C with high, but seasonally variable levels of precipitation (Böhme, 2003; 2010; Böhme et al., 2006; 2011; Holbourn et al., 2007; Ivanov and Böhme, 2011). Two general post-impact lacustrine lithofacies formed, cumulatively comprising the Ries lake deposits: (1) the basin center siliciclastics, and (2) the basin margin deposits (Arp et al., 2017).

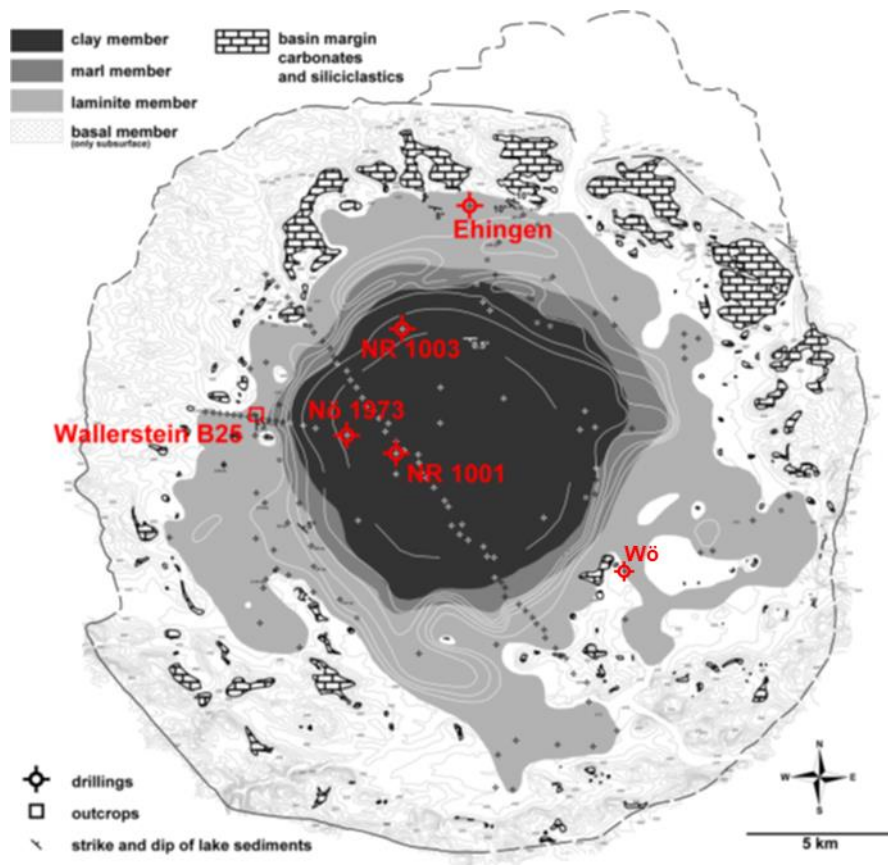


**Figure 1. 4:** The distribution of the post-impact lacustrine rocks as determined based on Pohl et al. (1977) highlighting different post-impact lacustrine units (Jankowski, 1981), and the location of major borehole drilling sites (Arp et al., 2021). Locations of the Nördlingen 1973 and Wörnitzostheim drill cores are marked by the crosshairs labelled Nö 1973 and Wö, respectively.

The Ries’ basin center units comprise a ~350 m thick sequence of siliciclastic sedimentary rocks. These rocks record four major stages in the evolution of the Ries crater-lake as it transitioned from (1) an alluvial playa setting to (2) a stratified, alkaline and saline lake, to (3) an unstratified and less saline lake, and finally to (4) a freshening lake with coal swamps (Füchtbauer et al., 1977; Jankowski, 1981; Arp et al., 2013a; 2017). Füchtbauer et al. (1977) described the sedimentary packages that recorded these environmental changes, where they denoted the packages as units A, B, C and D, from deepest to shallowest, respectively (Fig. 1.4). Unit A (basal member) is comprised of sandstones and breccias derived from “reworked suevite”, which transitions into the bituminous shales of unit B

(lamine member). Unit C (marl member) is comprised of marls and unit D (clay member) is comprised of claystones with intercalated lignites (Füchtbauer et al., 1977; Jankowski, 1977a; 1981; Arp G., 2006).

The basin margin deposits generally represent the final stages of the Ries lake system where the central basin filled with sediment and the marginal carbonates were deposited on its slopes (Jankowski, 1977a; 1981). The eventual establishment of Pleistocene river systems cross-cutting the Ries area eroded approximately 100 m of the youngest lake sediments; leaving the marginal carbonates deposited on the slopes of the inner ring the only modern expression of their sequence (Arp, et al., 2013; Arp, 1995; Füchtbauer et al., 1977). The basin margin carbonates have an approximate vertical extent of 50 m and comprise travertines, packstones, palustrine limestones and dolomitic algal bioherms (Fig. 1.5; Arp, 1995; Arp G., 2006; Riding, 1979). The marginal carbonates also constitute streamer carbonates and travertines at the Erbisberg spring mound (Arp, et al., 2013). The occurrence of these facies types were indicative of a subaerial hydrothermal origin of the mound and stratigraphically correlated with late stage sediments in the lacustrine basin center deposits (Arp, et al., 2013). This suggested that the Ries hydrothermal system could have persisted for approximately 250,000 years after the impact and potentially influenced the evolution of the lake system during the late deposition of the lamine member outlined in Jankowski (1981). The work of Arp et al. (2013b) was subsequently revisited (Arp et al., 2019), where direct evidence of travertines interfingering with lacustrine mudstones was documented, and results of  $^{87}\text{Sr} / ^{86}\text{Sr}$  indicated that the Erbisberg spring mound stratigraphically correlated with the timing of the early, rather than late, lamine member deposition.

In addition to the basin margin carbonates, coarse-siliciclastics comprising conglomerates and sandstones exist along the marginal regions of the lake, mainly in the north-western region of the Ries basin (Arp G., 2006; Arp et al., 2019b). The conglomeritic units are variable with some forming lenticular beds with poor cross-stratification, and others locally interfingering with clay-rich sandstones and sandy dolomite beds (Arp G., 2006). The Ries crater was, at least initially, a hydrologically closed lake (Arp, et al., 2013, 2017; Füchtbauer et al., 1977; Jankowski, 1981), that potentially transitioned into an open

lake system via a lake outlet (Wolff and Füchtbauer, 1976). While there is evidence of fluvial activity (Arp, 2006; Arp et al., 2019; Füchtbauer et al., 1977; Jankowski, 1981), no clear evidence of an inlet, breach flood, or an outlet at the Ries impact structure has been presented to date. It was more recently suggested that the clay member does not represent a final stage of freshwater conditions but rather represents a temporary decline in salinity (Arp et al., 2017), so a transition to hydrologically open conditions might not be necessary to explain this trend with salinity.

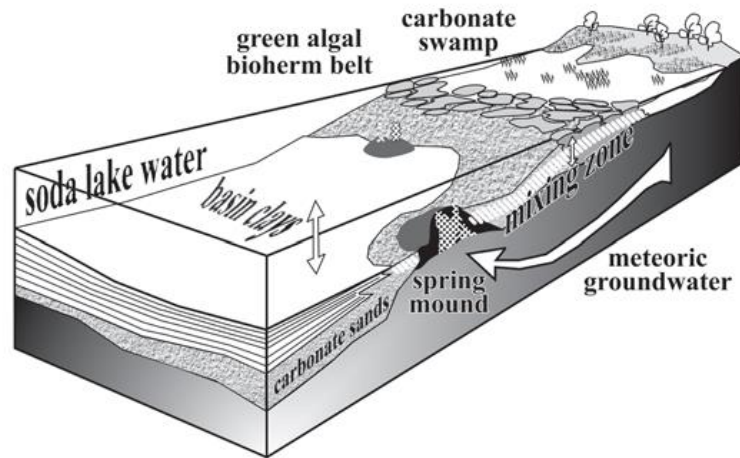


**Figure 1. 5:** A graphic of the northeastern margin of the Ries lake depicting the approximate distribution of carbonate facies with respect to the main lake system (Arp, 1995).

### 1.5.2 Bosumtwi Impact Structure, Ghana

The  $10.5 \pm 0.5$  km diameter Bosumtwi impact structure is a complex impact structure with a central uplift (Jones et al., 1981; Karp et al., 2002; Scholz et al., 2002) and an age of 1.07 Ma (Schnetzler et al., 1967; Koeberl et al., 1997). The target material was the greenschist facies metasediments of the 2.1–2.2 Ga Birimian Supergroup (Fig. 1.6; Wright et al., 1985). The Birimian Supergroup is traditionally divided into the Lower Birimian, which is comprised of metagraywackes, quartzite graywackes, shales and slates, and the Upper Birimian; comprised of altered, basic intrusives with intercalated metasediments (Jones et al., 1981; Koeberl et al., 1998; Reimold et al., 1998; Wagner et al., 2002). The Bosumtwi impact structure is completely filled with the modern Lake Bosumtwi (~45 m

depth); however, the age of the impact structure indicates that initial conditions were dry, and that early lake deposition was largely controlled by precipitation and evaporation (Beuning et al., 2003; Shanahan et al., 2006; 2009). Hydrothermal deposits constituting alteration veining and matrix material of  $2M_1$ -muscovite and secondary chlorite were reported in samples from the melt-bearing impactites, lapilli-bearing fallback deposits, and lithic breccias (Petersen et al., 2007); however, the extent of the alteration was limited generally to fracture fillings.

The Bosumtwi crater lake is hydrologically closed with no reported connection the regional groundwater aquifer, nor is there an inlet or stream inflow (Turner et al., 1996). Local groundwater compositions were controlled by the incongruent dissolution of aluminosilicates and, to a lesser extent, the weathering of carbonates; thereby causing a transition from Na-Mg-HCO<sub>3</sub> water at the upper catchments to Ca-Mg-HCO<sub>3</sub> water within the crater (Loh et al., 2016). The post-impact lake deposits at the Bosumtwi impact structure are diverse and consist of interlayering units of fluviodeltaic gravels and beach sands, and lacustrine silts and clay (Shanahan et al., 2006). Final lake high stands are marked by stromatolite mounds and stromatolitic surface coatings on rocks (Talbot and Delibrias, 1977). The Bosumtwi paleolake deposits records several lake level fluctuations controlled by climate, which in turn was strongly influenced episodes of glaciation (Talbot and Johannessen, 1992; deMenocal, 1995; 2004; Turner et al., 1996; Shanahan et al., 2006). The evolution of lake Bosumtwi has been studied with respect to the last few thousand years (Talbot and Delibrias, 1977; Talbot and Johannessen, 1992; Beuning et al., 2003; Shanahan et al., 2006); however, there have been no reports on the timing of initial lacustrine deposition. Arid environmental conditions surrounding the initial formation of Lake Bosumtwi are inferred based on climatological studies of West Africa (deMenocal, 1995; 2004). Throughout the last several thousand years, evidence of one instance of overflow conditions was recorded which would have funnelled out of the crater through the spillway / crater outlet located ~110 m above the modern lake surface (Turner et al., 1996).

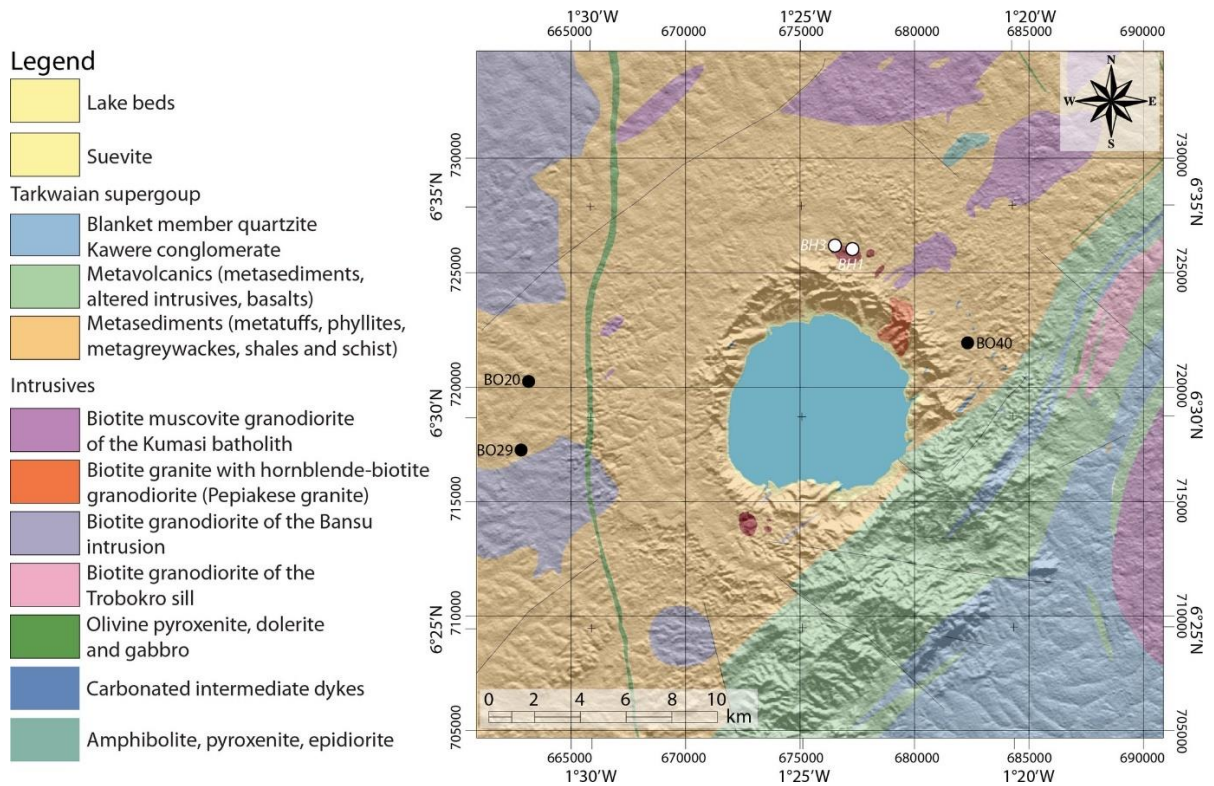


**Figure 1. 6:** Geological map of the Bosumtwi Lake impact structure depicting major host rock and impactite lithologies. Solid black lines highlight main fault systems. (Baratoux et al., 2019).

### 1.5.3 Lonar Lake Impact Structure, India

The Lonar Lake crater, presently host to a ~6 m deep hydrologically closed lake, is a ~1.9 km diameter, simple impact structure located in southwestern India, emplaced entirely in the Deccan basaltic traps (Nayak, 1972; Fredriksson et al., 1973; Maloof et al., 2010). The age of the Lonar Lake impact structure is somewhat contentious; multiple ages have been reported from ~12 Ka (Maloof et al., 2010) to  $570 \pm 47$  Ka (Jourdan et al., 2011), which complicates the application of relevant climatological studies. At least during the Holocene, the climate was characterized by a period of high monsoon activity from ~13 to 8 Ka, which was followed by a period of low monsoon activity with increasing aridity from ~5 to 0.5 Ka (Anoop et al., 2013; Menzel et al., 2013; Prasad et al., 2014; Misra, Tandon and Sinha, 2019). The paleolake deposits of Lonar Lake record the climatic fluctuations from high monsoon activity to aridity. High lacustrine aquatic productivity, increased

detrital input and calcareous clay mineral deposits mark periods of high monsoon activity, whereas evaporative gaylussite ( $\text{Na}_2\text{Ca}(\text{CO}_3)_2 \cdot 5\text{H}_2\text{O}$ ) marks periods of aridity (Prasad et al., 2014). Major sources of water for Lonar Lake currently comprise monsoon precipitation, perennial freshwater springs and streams (Maloof et al., 2010). Groundwater input into the lake is effective during periods of high and low monsoon activity, which themselves largely control lake level fluctuations (Komatsu et al., 2014). There is no stream outlet from Lonar Lake; however, groundwater discharges as springs occurring along the inner walls of the crater rim where the basaltic rock is vesicular or where proximal impactites are deposited (Komatsu et al., 2014). The crater rim presents several signs of subaqueous erosion and deposition such as gullies, debris flows, and the Dhar valley incision into the rim, which is associated with a fan delta (Komatsu et al., 2014). The lake is saline (~0.4 % NaCl), alkaline (pH ~10), eutrophic and permanently anoxic to sub-anoxic below 4 m depth (Joshi et al., 2008; Antony et al., 2013; Komatsu et al., 2014). Over the last several decades, the salinity of Lonar Lake has been progressively decreasing with continued input from fresh water (Joshi et al., 2008).

While there have been no biogenic carbonate deposits documented at Lonar Lake, the lake ecosystem hosts species of blue-green algae (Siddiqi, 2008), which are a similar type of organism to those responsible for the stromatolitic mounds and bioherms present at the Bosumtwi impact structure (Talbot and Delibrias, 1977), and the Ries impact structure (Riding R., 1979; Arp, 1995), respectively. There is currently no evidence of a lacustrine overflow event at the Lonar Lake impact structure.

Although water at the Lonar Lake impact structure was at least intermittently present in this potentially ~12 Ka impact structure, the presence of an impact generated hydrothermal system has generated some debate (Hagerty and Newsom, 2003; Newsom et al., 2005; Maloof et al., 2010). Putative impact generated hydrothermal deposits at Lonar lake constitute saponitic clay minerals, celadonite and calcite, which are pervasive in melt-bearing impactites (Hagerty and Newsom, 2003; Newsom et al., 2005). Additionally, groundwater heated by remnant energy imparted by the impact was proposed as a potential fluid source for an impact generated hydrothermal system at Lonar Lake (Nayak, 1996). It has, however, been argued that these hydrothermal deposits described in Hagerty and

Newsom (2003) and Newsom et al. (2005) are not a result of impact generated hydrothermal activity, but instead represent pre-impact alteration of basaltic flow tops that were highly comminuted (Malooof et al., 2010).

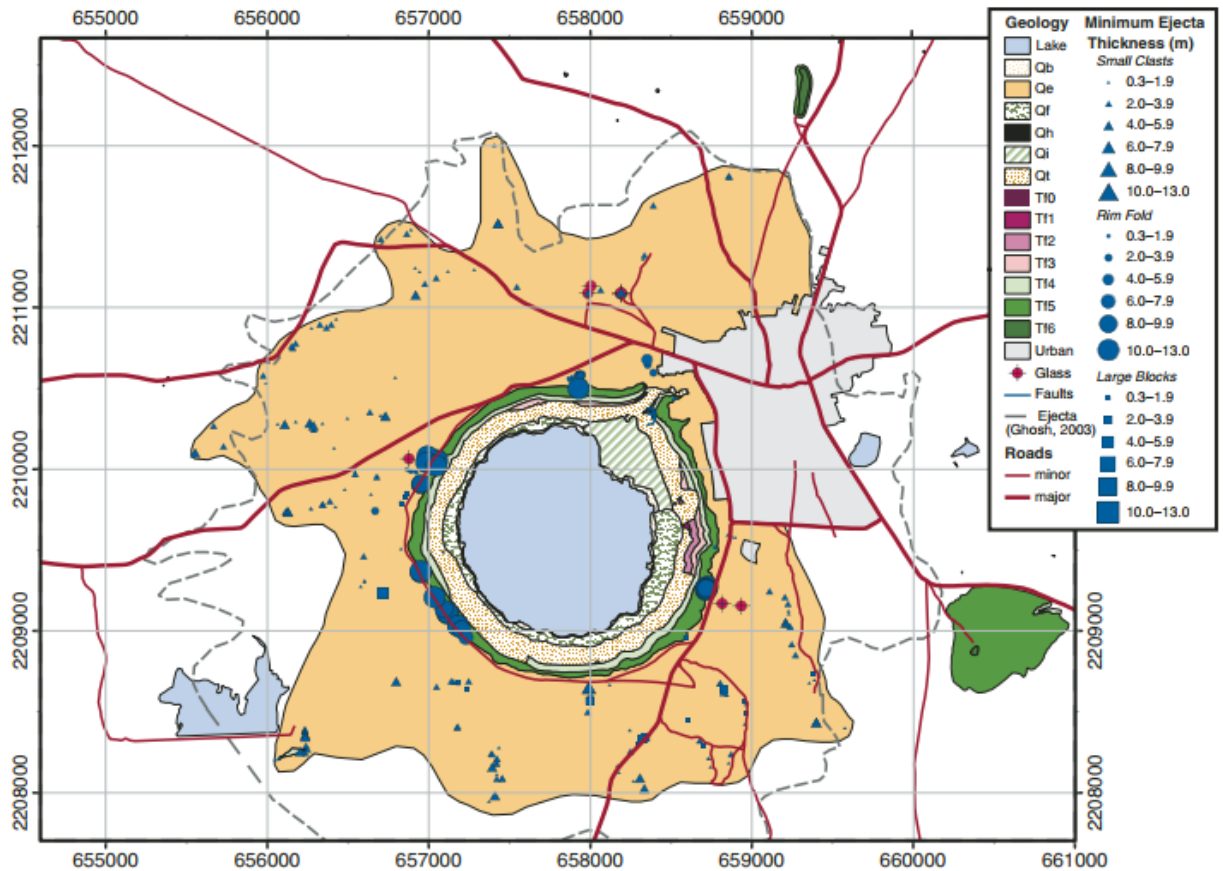


**Figure 1. 7:** Geological map of the Lonar Lake impact structure highlighting major geological units. The dashed grey line delineates the extent of the continuous ejecta blanket. Quaternary units are colored as indicated on the legend. Abbreviations are as follows: Qb–beach unit; Qe–ejecta unit; Qf–forest unit; Qh–histosol unit; Qi–irrigated alluvial fan; Qt–talus (Malooof et al., 2010).

#### 1.5.4 Boltysch Impact Structure, Ukraine

The ~24 km diameter Boltysch impact structure is a complex impact structure with a ~6 km diameter central uplift (Grieve et al., 1987). The Boltysch impact structure currently has minimal surface expression and is largely buried by up to 30 m of Quaternary sediments (Gurov et al., 2006). The target rock comprises a complex mixture of ~ 1550 Ma

Proterozoic porphyritic, aplitic granites associated with migmatites, locally known as Kirovograd type, and older biotite gneiss aged 1850–2220 Ma (Shcherbak et al., 1978; Grieve et al., 1987). The impact event occurred on the northeastern margin of the Tethys Ocean at  $65.39 \pm 0.14 / 0.1$  Ma; a time during ecological recovery from the Cretaceous–Paleogene (K-Pg) extinction (Pickersgill et al., 2021). The impact event generated melt-bearing breccias in addition to impact melt rocks which both occur as crater-fill deposits within the annular depressions of the impact structure (Grieve et al., 1987). Approximately 10–100 m of impact melt-bearing breccias overlie a ~150–220 m thick sheet of impact melt rocks (Gurov, Shekhunova and Permiakov, 2011). The impact melt rocks can be generally separated into two distinct units comprising (1) a lower unit of glassy impact melt rocks with a glassy matrix, and feldspar and orthopyroxene microliths, and (2) an upper unit of microcrystalline melt rocks with microliths of feldspar and chloritized orthopyroxene (Grieve et al., 1987; Gurov et al., 2011). The chloritization of orthopyroxene and the crystalline structure of the matrix present in the upper melt rocks were attributed to interactions with meteoric water during hydrothermal alteration (Gurov et al., 2006; Gurov et al., 2015). Aggregates of apatite and pyrite-apatite hosted in hydrothermal veins comprise the hydrothermal deposits in the melt-bearing breccias (Gurov et al., 2015) in addition to pervasive alteration to smectitic clay minerals (Williams et al., 2013).

The Boltysk impact structure contains ~580 m of post-impact sedimentary rock overlying the melt-bearing breccias (Fig. 1.8). The collapse of material from the crater rim and the inner slopes of the crater deposited the earliest post-impact sedimentary rocks in the impact structure and comprise sandstones and sedimentary breccias with some macrofossils (Gurov et al., 2006; Ebinghaus et al., 2017). Studies of  $\beta\beta$  hopanes indicated that the bottom 10 m of these initial post impact deposits were potentially subjected to short-lived, and low temperature heating (Gilmour et al., 2013); however, an unconformity between the melt-bearing breccias and post-impact lacustrine deposits (Gurov et al., 2006; Ebinghaus et al., 2017) indicates that the duration of hydrothermal heating could have been longer than initially proposed. The initial lake system was hydrologically closed and exhibited lake level fluctuations controlled by surface run-off (Ebinghaus et al., 2017). Water influx and early fresh-water conditions were maintained by continuous groundwater flow and seasonally controlled precipitation (Ebinghaus et al., 2017). Lacustrine siltstones,

claystones and oil shales represent deposition from a primarily a freshwater lake that was biologically active (Gurov et al., 2006; Ebinghaus et al., 2017). The lake was initially inhabited by populations of ostracods and mollusks, which were later replaced during an episode of anoxic conditions where blue-green algae were dominant (Gurov et al., 2006); however, salinity and alkalinity levels subsequently varied (Ebinghaus et al., 2017). Marine transgression during the Middle Eocene caused the flooding of the impact structure with sea water, which deposited sandstones, claystones and marlstones. The sediments deposited as a result of this marine transgression record a period extending to the late Eocene. A final stage of freshwater conditions was recorded by Neogene claystones and sandstones that are up to 100 m thick.

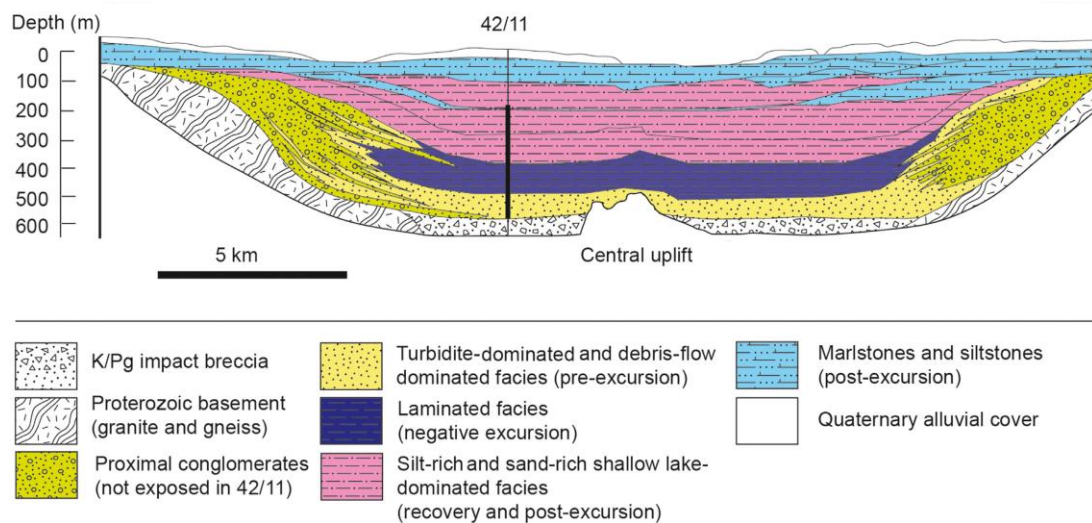


**Figure 1. 8:** Simplified cross section of the Boltysh post-impact deposits. The cross section highlights major lithologies and the location of a drill core used to establish the relationships depicted here (Ebinghaus et al., 2017).

### 1.5.5 The Houghton Impact Structure, Canada

The ~31 km apparent diameter (Osinski et al., 2005b; Erickson et al., 2021) and  $31.04 \pm 0.37$  Ma (Erickson et al., 2021) Houghton impact structure located on Devon Island, Canada, hosts the Neogene and Quaternary sediments of the Houghton Formation (Hickey, Johnson and Dawson, 1988); remnant deposits of a post-impact crater lake system (Fig.

1.9). The Haughton impact structure is complex with a central uplift and is hosted in an approximately 1,880 m thick sequence of Lower Paleozoic sedimentary rocks of the Arctic Platform, which overlie the Precambrian metamorphic rocks that comprise the Canadian shield (Osinski et al., 2005; Stockwell, 1982). The Lower Paleozoic sedimentary rocks are comprised of dolomite and limestone with some evaporites, minor shales and sandstones (Osinski et al., 2005; Stockwell, 1982). The volumetrically dominant crater fill lithology is a clast-rich impact melt rock that comprises a silicate-carbonate-anhydrite groundmass that exhibits immiscibility textures with sedimentary and crystalline clastic material derived from the target rock (Osinski et al., 2001; Osinski et al., 2005; Osinski & Spray, 2003). Hydrothermal deposits occur in cavity and fracture fillings within crater-fill impact melt-bearing breccias, breccias comprising the central uplift, fractures fillings near the central uplift, and in hydrothermal pipe structures and fault surfaces in the crater rim region (Osinski et al., 2001; Osinski et al., 2005). The main alteration assemblage constitutes calcite and selenite with minor marcasite, quartz and goethite (Osinski et al., 2001; Osinski et al., 2005).

Field studies of the Haughton Formation indicate that it was deposited ~8–10 Ma after impact (Osinski and Lee, 2005). The crater-wide unconformity that marks the contact between the base of the Haughton formation and pristine, unweathered clast-rich impact melt rocks indicates that the Haughton formation was deposited after a period of glaciation erosion removed an upper section of the clast-rich impact melt rocks (Osinski & Lee 2005). The Haughton formation has preserved an assemblage of pollen, plant microfossils and early Neogene arctic vertebrates, including fish, which can be used as a vector for paleoclimatological study (Hickey et al. 1988). The preservation of delicate fossils, lack of current scouring and or ripple marks in the post-impact lacustrine deposits indicates deep water conditions in a climate that was characterized by a mean annual temperature range of 16–28 °C (Hickey et al., 1988), although this temperature regime is based on age estimates for the Haughton formation that have since been revised (Osinski and Lee, 2005). No information regarding the physiochemical evolution or micro-ecology of the Haughton Formation paleolake has been reported to date. Additionally, no evidence of a rim-breaching event associated with the Haughton formation has been presented; however, a

breaching event of the crater rim occurred in association with the Haughton River, possibly triggered by the uplift of the Devon Plateau (Hickey et al., 1988).

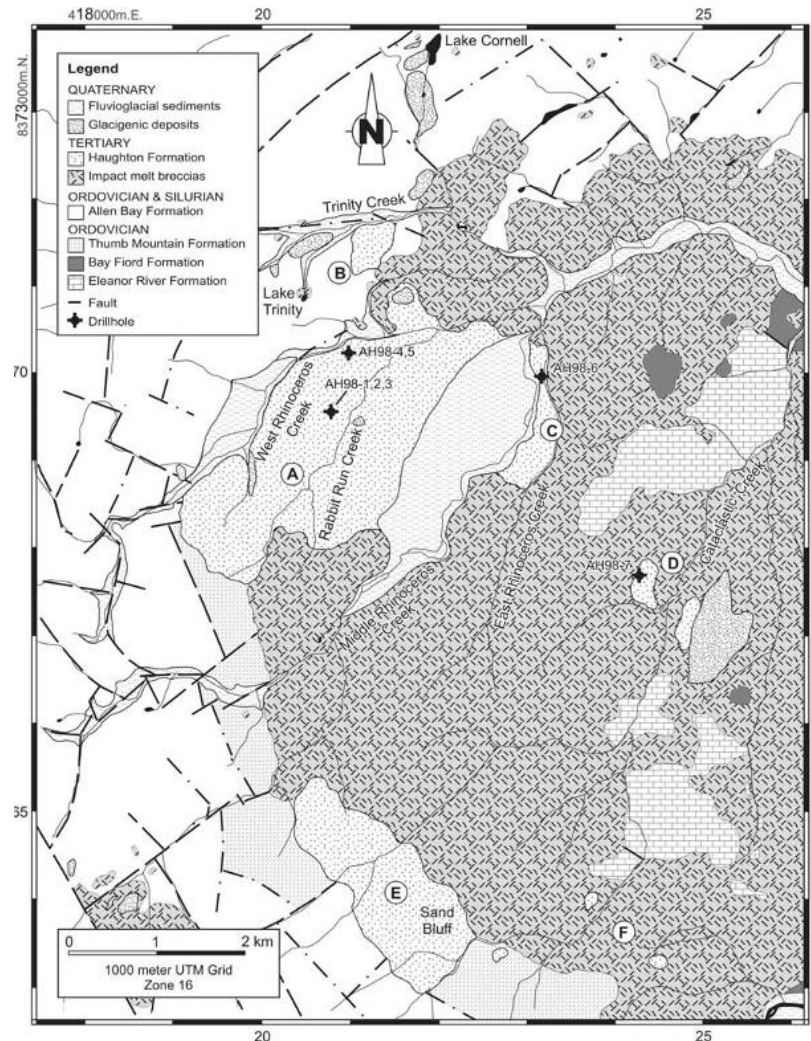


**Figure 1. 9:** Simplified geological map of the western side of the Haughton impact structure highlighting the post-impact lacustrine sediments of the Haughton formation (Osinski & Lee 2005).

### 1.5.6 Summary

Most of the impact structures reviewed here hosted, at least initially, closed lake systems. Generally, the water supply and main control on lake levels in these lake systems was precipitation. As such, the climate and by extension the latitudinal location of the impact structure, and degree of glacial transgression or regression would influence the

lacustrine environment. The timing of a sufficient post-impact water supply necessary to generate a lacustrine system is still not fully understood for most impact structures; however, in cases where immediate lacustrine infilling is hypothesized, such as the Ries impact structure and the Boltysh impact structure, the crater-fill melt-bearing impactites exhibit pervasive alteration associated with clay minerals. There has been no evidence presented for breach flooding at any of the reviewed impact structures as an event that could have initiated lacustrine formation; however, this process is suspected to have formed the Haughton formation. Most of these lake systems began as shallow saline lakes with the exception of the Boltysh impact structure where a constant supply of groundwater and consistent run-off maintained a fresh-water system. In most cases, water supply was at least temporarily intermittent, which led to temporary dry periods in the cases of Bosumtwi, and Lonar Lake. During deposition from the margins of the lacustrine environment, the formation of stromatolites and / or modern living algae is common to all the impact craters studied here with the exception of the Haughton impact structure where it is unclear whether the Haughton Formation records evidence of the presence of algae. The findings of this limited review of a few properties of five terrestrial impact craters are summarized in table 1.

This brief review comprises a very small sample set of impact crater lakes on Earth and as such does have limitations with respect to temporal resolution, representation of varying latitudes, representation of crater type, representation of both modern and paleolakes, and an in-depth review of the respective biospheres of each crater lake system. There are indeed several outstanding questions such as the cause of the termination of the selected paleolakes, and whether breach events could be triggered from overflow, fluvial activity or other processes such as those outlined in Bamber et al., (2022). Indeed, a geomorphological study of the various and relatively unexplained inlets and outlets present in modern crater lakes would be hugely insightful into the processes that govern their evolution. Finally, gaining a more robust understanding of the formation of stromatolites and other biogenic deposits in the marginal regions of these lakes would be significant to the exploration for evidence of life on Mars where the Perseverance rover is set to explore putative lacustrine carbonate deposits in the margins of Jezero crater (Horgan et al., 2020).

**Table 1. 1:** Summary of key parameters pertaining to the context and characteristics of five impact crater lakes.

Parameter	Ries	Bosumtwi	Lonar Lake	Boltysh	Haughton
Location	Germany 48.8833° N 10.5667° E	Ghana 6.5017° N 1.4145° W	India 19.9758° N 76.5069° E	Ukraine 48.7500° N, 32.1667° E	Canada 75.4319° N 89.8112° W
Impact Structure Age	14.8 Ma	1.07 Ma	12 Ka to 570 Ka	65.39 Ma	23.5 Ma
Diameter of the Impact Structure	24 km	10.5 km	1.9 km	24 km	23 km
Impact Structure Type	Complex	Complex	Simple	Complex	Complex
Target Rock	Mixed: Limestone with amphibolite gneiss	Crystalline: greenschist facies metasediments	Crystalline : Deccan trap basalt	Crystalline: granites and migmatites	Mixed: Limestone with Precambrian metamorphic rocks
Modern / Paleolake	Paleolake	Modern	Modern	Paleolake	Paleolake
Main Impact Generated Hydrothermal Deposits	(Extensive) Smectitic clay minerals, K-feldspar, albite, chlorite, calcite, Baphillipsite in crater-fill impact melt-bearing breccias	(Limited) 2M1-muscovite and secondary chlorite in melt-bearing impactites, fallback deposits and lithic breccias	(Limited) Saponitic clay minerals, celadonite and calcite in melt-bearing impactites (disputed as not impact related)	(Extensive) Chloritized orthopyroxene, pervasive secondary smectite in impact melt rocks and impact melt-bearing breccias	(Limited) Calcite and selenite in impact melt-bearing breccias, central uplift region and crater rim region
Evidence of Impact Generated Hydrothermal Heating in Lake Deposits	Intercalation with hydrothermal spring mounds	Unknown	Unknown	$\beta\beta$ hopane studies consistent with short-lived, low temperature heating	None

Water Source(s) / Lake Level Control	Seasonal precipitation	Precipitation	Monsoon rains	Precipitation / sea-rise	Precipitation?
Lacustrine Physiochemical Evolution	Initially alkaline + saline Progressively shifted to less saline conditions with increasing input from rain	Alkaline + saline water evolving to fresh water	Saline, alkaline, eutrophic with anoxic water bottoms	Fresh water, controlled by groundwater Temporarily shifted to saline due to marine transgression Returned to fresh water	Unknown
Inlet / Outlet	Unknown	Outlet	Inlet (with groundwater discharge through springs)	Unknown	Potentially an inlet
Hydrologically Open / Closed	Closed	Closed	Closed	Closed Shifting to open with sea level rise then returning to closed	Closed?
Ecology	Diverse Stromatolites at basin margins	Diverse Stromatolites at basin margins	Modern algal blooms	Ostracods, molluscs, blue-green algae	Diverse
Water supply	Constant – no complete drying episodes	Intermittent initially Currently constant	Intermittent	Constant	Intermittent?
Timing of lacustrine infilling with respect to impact event	Immediate (?) Hypothesized but no direct evidence	Later (unknown time gap)	Unknown	Immediate (?) Hypothesized, but no direct evidence	8–10 Ma time gap
Deep / Shallow Water	Rhythmic Initially shallow with deep	Initially shallow Deep modern lake	Shallow	Rhythmic Initially shallow with	Deep

	water periods			deep water periods	
Overflow Events	Potentially one	One	None	Potentially multiple	Unknown

## 1.6 Clay Minerals

The Ries impact structure hosts a multitude of lithofacies that are replete with clay minerals (Füchtbauer et al., 1977; Salger, 1977; Jankowski, 1981; Newsom et al., 1986; Osinski, Grieve and Spray, 2004; Osinski, 2005; Muttik et al., 2008; 2010; Sapers et al., 2017; Caudill et al., 2021), and indeed clay minerals comprise a key mineralogical presence in each chapter of this thesis. As such, their formation conditions with respect to the Ries impact structure, and in general, are similarly significant to impact cratering, impact generated hydrothermal systems, and crater lakes.

Clay minerals are generally present in the  $<2 \mu\text{m}$  size fraction of rocks and soils, and typically comprise phyllosilicates classified based on the size and origin of their permanent charges. The permanent charges of these clay minerals are dictated by their crystal structure; alternating sheets of octahedrally and tetrahedrally coordinated cations. Octahedral cations, usually aluminum or magnesium, are generally in coordination with hydroxyl groups and / or oxygen (Brindley and Brown, 1980). Silica, or sometimes aluminum, tetrahedral cations, are coordinated with oxygen (Brindley and Brown, 1980). Sheets of tetrahedra form such that the apical oxygen of tetrahedra are aligned along the same plane (Grim, 1968). The conjoining of one tetrahedral sheet and one octahedral sheet creates 1:1 layer clay minerals such as kaolinite and serpentine, whereas the similar joining of two tetrahedral sheets on either side of an octahedral sheet creates a 2:1 layer clay mineral (Fig. 1.10) such as montmorillonite or illite (Grim, 1968). In the case of 2:1 layer clay mineral, the space between two 2:1 layers (the interlayer space) can be occupied by water, cations, hydroxyl groups, or organics depending on their charge (Moore and Reynolds, 1997). The diverse array of material that can occupy the interlayer causes 2:1 layer clay minerals to have a variety of characteristics and properties. Furthermore, different types of 2:1 layer clay minerals can intercalate with one another, further

diversifying their properties and complicating the interpretation of their precise mineralogy (Brindley and Brown, 1980; Moore and Reynolds, 1997).

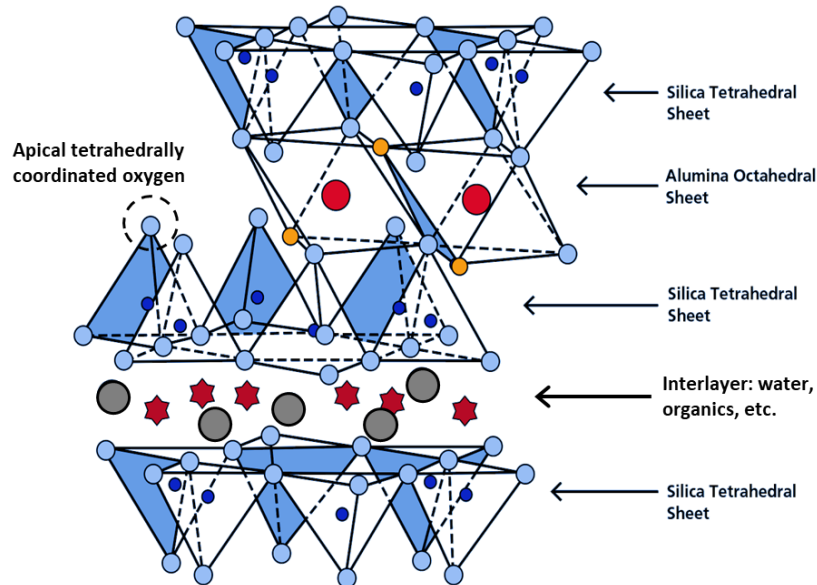


**Figure 1. 10:** The general structure of a 2:1 layer clay mineral with interlayer material distinguishing it from the tetrahedral sheet of another clay mineral. Dark blue circles indicate silica, light blue circles indicate oxygen, orange circles indicate hydroxyl groups, red circles indicate aluminum, grey circles indicate water, red stars indicate various cations; however, other possible constituents of the interlayer are noted (Ghadiri et al., 2015).

The presence of structurally bound hydrogen and oxygen in clay minerals (Brindley and Brown, 1980) has made them attractive targets for isotopic provenance studies. The isotopic composition of clay minerals can provide information about the geological processes that formed them; however, this is only true if they retained the isotopic compositions acquired in the process (Savin and Lee, 1988). In particular, work pertaining to the equilibrium fractionation between clay minerals and water has enabled the approximate reconstruction of the isotopic compositions of clay mineral source fluids; provided that a myriad of conditions such as the likely formation temperature(s), mixed clay mineral intercalation, presence of organics, likelihood of re-equilibration, and possible low-temperature kinetic effects are taken into consideration (Savin, 1967; Sheppard et al., 1969; Savin and Epstein, 1970; Yeh, 1980; Yeh and Epstein, 1981; Savin and Lee, 1988;

Longstaffe and Ayalon, 1990; Capuano, 1992; Sheppard and Gilg, 1996). Research regarding the equilibrium fractionation between clay minerals and water has been instrumental for paleoclimate and palaeohydrological research (Longstaffe, 1991; Gilg et al., 1999; Gilg, 2000). In this thesis, similar approach is used to aid in understanding early post-impact processes at the Ries impact structure.

Clay minerals at the Ries impact structure that occur along the transition from melt-bearing impactites to post-impact sedimentary deposits are a focus of this thesis. These clay minerals are important for their potential to record early post-impact environmental conditions and the early evolution of hydrothermal and lacustrine fluids. Clay minerals were documented throughout lacustrine deposits in the central basin of the Ries impact structure by Füchtbauer et al. (1977) who reports “mixed layer” clay minerals, illite and kaolinite with additional chlorite in basal lacustrine deposits. Salger (1977) also reports occurrences of secondary high temperature montmorillonite clay minerals in the same basal lacustrine deposits described in Füchtbauer et al. (1977). As discussed previously, clay minerals are present in the melt-bearing impactites (see section 1.4: Impact Generated Hydrothermal Systems), and their origins are not fully agreed upon.

## 1.7 Thesis Outline

The following chapters are written as a series of journal articles. The key contributions of each chapter are summarized below.

### 1.7.1 Chapter 2: A mineralogical and textural investigation of the impact melt-bearing breccia to post-impact sedimentary transition in the Wörnitzostheim drill core, Ries impact structure, Germany

The purpose of this chapter is to contribute the first detailed investigation of the post-impact sedimentary deposits sampled by the Wörnitzostheim drill core, catalogue the mineralogical and textural indicators of environmental changes throughout the sedimentary sequence, and outline a potential depositional history. Furthermore, the Wörnitzostheim drill core samples the transition from specifically the ejected melt-bearing breccias to post-impact sedimentary deposits, so this investigation offers additional context for the potential origins of the clay minerals therein and provides the first detailed investigation of post-

impact sedimentary deposits overlying the melt-bearing ejecta at the Ries impact structure. The investigation reported here is focused on the stratigraphy and sedimentary petrology of post-impact sedimentary deposits, and the petrology of melt-bearing impactites; with an additional component of clay mineralogy as determined by powdered X-ray diffraction (*p*XRD). In this chapter, we highlight different depositional processes recorded by the Wörnitzostheim drill core. We additionally constrain an assemblage of alteration minerals within the post-impact sedimentary deposits and estimate potential alteration temperatures.

### 1.7.2 Chapter 3: Tracing the fluid evolution of early post-impact fluvio-lacustrine systems beyond the central basin of the Ries impact structure, Germany

Chapter 3 builds on the results of chapter 2 and aims to characterize the evolutionary sequence of fluids recorded by the Wörnitzostheim drill core. This chapter contributes a detailed investigation of the clay mineralogy preserved in the transition from melt-bearing ejecta to post-impact sedimentary deposits, and additionally contributes the first stable isotopic analysis of 2–0.2 and <0.2  $\mu\text{m}$  size fractions conducted on any deposit at the Ries impact structure. We use temperature estimates determined in chapter 2, and results of previous palaeoclimatological studies of Central Europe and the North Alpine Foreland Basin during the Mid-Miocene as guides to outline potential evolution pathways of fluids during the formation of the basal sedimentary deposits of the Wörnitzostheim drill core. This research further contextualizes the formation of melt-bearing ejecta at the Ries and offers additional insights into their potential origins. Finally, this chapter also offers constraints for possible temperature and fluid composition fluctuations that would frame the immediate ecological recovery following the Ries impact event.

### 1.7.3 Chapter 4: Revisiting the origin of the Ries graded suevite: implications for plume fallback preservation and early post-impact sedimentary deposition.

The original goal of this chapter was to characterize the alteration in the basal post-impact lacustrine deposits sampled by the Nördlingen 1973 drill core (FBN73); however, previous research provided little consensus as to whether the basal sedimentary deposits of FBN73 were deposited subaerially from the ejecta plume (Jankowski, 1977b) or

subaqueously from a turbidity current (Artemieva et al., 2013). A major cause for this debate is the presence of normal grading in the basal sedimentary deposits (hereafter, the graded unit). As such, this chapter aims to contextualize the occurrence of the graded unit in FBN73 using palaeoclimatological studies of Central Europe and the North Alpine Foreland Basin, and by drawing comparisons with similar deposits at the Bosumtwi impact structure, Ghana. This chapter contributes a petrographic study with a main focus on documenting any occurrences of accretionary lapilli and glass spherules throughout the graded unit and the overlying basal unit (unit A) of Jankowski (1981). As additional objectives, this study documents secondary alteration phases present in the graded unit and provides the most detailed log of the basal unit (unit A) and graded unit to date. This research offers insight into the processes that control the preservation of plume fallback deposits within the context of fluvio-lacustrine activity and impact generated hydrothermal alteration. This chapter additionally contributes a new interpretation for the origin of the graded unit that integrates considerations from the present study, previous work, paleoclimate, and processes recorded at other impact structures.

#### 1.7.4 Chapter 5: Discussion and Conclusions

This chapter summarizes the main conclusions of chapters 2 to 4 and outlines the key interpretations of this thesis and addresses objective of reconciling differences between the lacustrine and hydrothermal environments preserved in the Nördlingen drill core and the Wörnitzostheim drill core. This chapter also highlights additional research that was not fully realized or integrated into this dissertation but serves as a vector for future work.

## 1.8 References

- Abramov, O. and Kring, D.A., 2004. Numerical modeling of an impact-induced hydrothermal system at the Sudbury crater. *Journal of Geophysical Research: Planets*, 109(E10007). <https://doi.org/10.1029/2003JE002213>.
- Abramov, O. and Kring, D.A., 2007. Numerical modeling of impact-induced hydrothermal activity at the Chicxulub crater. *Meteoritics & Planetary Science*, [online] 42, pp.93–112. Available at: <<http://meteoritics.org>>.

- Anoop, A., Prasad, S., Krishnan, R., Naumann, R. and Dulski, P., 2013. Intensified monsoon and spatiotemporal changes in precipitation patterns in the NW Himalaya during the early-mid Holocene. *Quaternary International*, 313–314, pp.74–84. <https://doi.org/10.1016/j.quaint.2013.08.014>.
- Antony, Chakkiath.Paul., Kumaresan, Deepak., Hunger, Sindy., Drake, Harold.L., Murrell, J.Colin. and Shouche, Yogesh.S., 2013. Microbiology of Lonar Lake and other soda lakes. *International Society for Microbial Ecology*, 7(3), pp.468–476. <https://doi.org/10.1038/ismej.2012.137>.
- Arp, G., 1995. Lacustrine bioherms, spring mounds, and marginal carbonates of the Ries-impact-crater (Miocene, Southern Germany). *Facies*, 33(1), pp.35–89. <https://doi.org/10.1007/BF02537444>.
- Arp G., 2006. Sediments of the Ries Crater Lake (Miocene, Southern Germany). In: *21st Meeting of Sedimentologists / 4th Meeting of SEPM Central European Section*. pp.216–233.
- Arp, G., Blumenberg, M., Hansen, B.T., Jung, D., Kolepka, C., Lenz, O., Nolte, N., Poschlod, K., Reimer, A. and Thiel, V., 2013a. Chemical and ecological evolution of the Miocene Ries impact crater lake, Germany: A reinterpretation based on the Enkingen (SUBO 18) drill core. *Bulletin of the Geological Society of America*, 125(7–8), pp.1125–1145. <https://doi.org/10.1130/B30731.1>.
- Arp, G., Dunkl, I., Jung, D., Karius, V., Lukács, R., Zeng, L., Reimer, A. and Head, J.W., 2021. A Volcanic Ash Layer in the Nördlinger Ries Impact Structure (Miocene, Germany): Indication of Crater Fill Geometry and Origins of Long-Term Crater Floor Sagging. *Journal of Geophysical Research: Planets*, 126(4). <https://doi.org/10.1029/2020JE006764>.
- Arp, G., Hansen, B.T., Pack, A., Reimer, A., Schmidt, B.C., Simon, K. and Jung, D., 2017. The soda lake—mesosaline halite lake transition in the Ries impact crater basin (drilling Löpsingen 2012, Miocene, southern Germany). *Facies*, 63(1). <https://doi.org/10.1007/s10347-016-0483-7>.

- Arp, G., Kolepka, C., Simon, K., Karius, V., Nolte, N. and Hansen, B.T., 2013b. New evidence for persistent impact-generated hydrothermal activity in the Miocene Ries impact structure, Germany. *Meteoritics and Planetary Science*, 48(12), pp.2491–2516. <https://doi.org/10.1111/maps.12235>.
- Arp, Gernot., Reimer, Andreas., Simon, Klaus., Sturm, Sebastian., Wilk, Jakob., Kruppa, Corina., Hecht, Lutz., Hansen, B.T., Pohl, Jean., Reimold, W.Uwe., Kenkmann, Thomas. and Jung, Dietmar., 2019a. The Erbisberg drilling 2011: Implications for the structure and postimpact evolution of the inner ring of the Ries impact crater. *Meteoritics and Planetary Science*, 54(10), pp.2448–2482. <https://doi.org/10.1111/maps.13293>.
- Arp, Gernot., Schultz, S., Karius, V. and Head, J.W., 2019b. Ries impact crater sedimentary conglomerates: Sedimentary particle ‘impact pre-processing’ transport distances and provenance, and implications for Gale crater conglomerates, Mars. *Icarus*, 321, pp.531–549. <https://doi.org/10.1016/j.icarus.2018.12.003>.
- Artemieva, N.A., Wünnemann, K., Krien, F., Reimold, W.U. and Stöffler, D., 2013. Ries crater and suevite revisited-Observations and modeling Part II: Modeling. *Meteoritics and Planetary Science*, 48(4), pp.590–627. <https://doi.org/10.1111/maps.12085>.
- Bamber, Emily.R., Goudge, Timothy.A., Fassett, Caleb.I. and Osinski, Gordon.R., 2022. Constraining the formation of paleolake inlet valleys across crater rims. *Icarus*, 378(114945). <https://doi.org/10.1016/j.icarus.2022.114945>.
- Baratoux, David., Niang, Cheikh.Ahmadou.Bamba., Reimold, Wolf.Uwe., Sapah, Marian.Selorm., Jessell, Mark.Walter., Boamah, Daniel., Faye, Gayane., Bouley, Sylvain. and Vanderheaghe, Olivier., 2019. Bosumtwi impact structure, Ghana: Evidence for fluidized emplacement of the ejecta. *Meteoritics and Planetary Science*, 54(10), pp.2541–2556. <https://doi.org/10.1111/maps.13253>.
- Beuning, K.R.M., Talbot, M.R., Livingstone, D.A. and Schmukler, G., 2003. Sensitivity of carbon isotopic proxies to paleoclimatic forcing: A case study from Lake Bosumtwi,

- Ghana, over the last 32,000 years. *Global Biogeochemical Cycles*, 17(4).  
<https://doi.org/10.1029/2003gb002072>.
- Böhme, M., 2003. The Miocene Climatic Optimum: Evidence from ectothermic vertebrates of Central Europe. *Palaeogeography, Palaeoclimatology, Palaeoecology*, 195(3–4), pp.389–401. [https://doi.org/10.1016/S0031-0182\(03\)00367-5](https://doi.org/10.1016/S0031-0182(03)00367-5).
- Böhme, M., 2010. Ectothermic vertebrates (Actinopterygii, Allocaudata, Urodela, Anura, Crocodylia, Squamata) from the Miocene of Sandelzhausen (Germany, Bavaria) and their implications for environment reconstruction and palaeoclimate. *Palaontologische Zeitschrift*, 84(1), pp.3–41. <https://doi.org/10.1007/s12542-010-0050-4>.
- Böhme, M., Ilg, A., Ossig, A. and Küchenhoff, H., 2006. New method to estimate paleoprecipitation using fossil amphibians and reptiles and the middle and late Miocene precipitation gradients in Europe. *Geology*, 34(6), pp.425–428.  
<https://doi.org/10.1130/G22460.1>.
- Böhme, Madelaine., Winklhofer, Michael. and Ilg, August., 2011. Miocene precipitation in Europe: Temporal trends and spatial gradients. *Palaeogeography, Palaeoclimatology, Palaeoecology*, 304(3–4), pp.212–218.  
<https://doi.org/10.1016/j.palaeo.2010.09.028>.
- Brigham-Grette, J., Melles, M. and Minyuk, P., 2007. *Overview and significance of a 250 ka paleoclimate record from El'gygytgyn Crater Lake, NE Russia*. *Journal of Paleolimnology*, <https://doi.org/10.1007/s10933-006-9017-6>.
- Brindley, G.W. and Brown, G., 1980. *Crystal Structures of Clay Minerals and their X-Ray Identification*. Mineralogical Society of Great Britain and Ireland.  
<https://doi.org/10.1180/mono-5>.
- Cabrol, N.A. and Grin, E.A., 1999. Distribution, Classification, and Ages of Martian Impact Crater Lakes. *Icarus*, [online] 142, pp.160–172. Available at:  
<http://www.idealibrary.comon>.

- Cabrol, N.A. and Grin, E.A., 2001. The Evolution of Lacustrine Environments on Mars: Is Mars only Hydrologically Dormant? *Icarus*, 149(2), pp.291–328.  
<https://doi.org/10.1006/icar.2000.6530>.
- Cabrol, N.A., Grin, E.A., Newsom, H.E., Landheim, R. and McKay, C.P., 1999. Hydrogeologic Evolution of Gale Crater and Its Relevance to the Exobiological Exploration of Mars. *Icarus*, [online] 139, pp.235–245. Available at:  
<<http://www.idealibrary.comon>>.
- Capuano, R.M., 1992. The temperature dependence of hydrogen isotope fractionation between clay minerals and water: Evidence from a geopressed system. *Geochimica et Cosmochimica Acta*, 56, pp.2547–2554.
- Caudill, C., Osinski, G.R., Greenberger, R.N., Tornabene, L.L., Longstaffe, F.J., Flemming, R.L. and Ehlmann, B.L., 2021. Origin of the degassing pipes at the Ries impact structure and implications for impact-induced alteration on Mars and other planetary bodies. *Meteoritics and Planetary Science*, 56(2), pp.404–422.  
<https://doi.org/10.1111/maps.13600>.
- Christ, N., Maerz, S., Kutschera, E., Kwiecien, O. and Mutti, M., 2018. Palaeoenvironmental and diagenetic reconstruction of a closed-lacustrine carbonate system – the challenging marginal setting of the Miocene Ries Crater Lake (Germany). *Sedimentology*, 65(1), pp.235–262. <https://doi.org/10.1111/sed.12401>.
- Cockell, C. S., Osinski, G.R., Sapers, H.M., Pontefract, A. and Parnell, J., 2020. Microbial life in impact craters. *Current Issues in Molecular Biology*, 38, pp.75–102.  
<https://doi.org/10.21775/cimb.038.075>.
- Cohen, Andrew.S., 2003. *Paleolimnology: The History and Evolution of Lake Systems*. New York, NY: Oxford University Press.  
<https://doi.org/10.1093/oso/9780195133530.001.0001>.
- Daubar, I.J. and Kring, D.A., 2001. Impact-induced hydrothermal systems: Heats sources and lifetimes. In: *32nd Lunar and Planetary Science Conference. (abstract #1727)*.

- deMenocal, P.B., 2004. African climate change and faunal evolution during the Pliocene-Pleistocene. *Earth and Planetary Science Letters*, 220(1–2), pp.3–24.  
[https://doi.org/10.1016/S0012-821X\(04\)00003-2](https://doi.org/10.1016/S0012-821X(04)00003-2).
- deMenocal, Peter.B., 1995. Plio-Pleistocene African Climate. *Science*, 270, pp.53–59.
- Dence, M.R., 1968. Shock zoning at Canadian craters: petrography and structural implications. In: B.M. French and N.M. Short, eds. *Shock Metamorphism of Natural Materials*. Baltimore: Mono Book Corp. pp.169–184.
- Ebinghaus, A., Jolley, D.W., Andrews, S.D. and Kemp, D.B., 2017. Lake sedimentological and ecological response to hyperthermals: Boltys impact crater, Ukraine. *Sedimentology*, 64(6), pp.1465–1487. <https://doi.org/10.1111/sed.12360>.
- Erickson, Timmons.M., Kirkland, Christopher.L., Jourdan, Fred., Schmieder, Martin., Hartnady, Michael.I.H., Cox, Morgan.A. and Timms, Nicholas.E., 2021. Resolving the age of the Haughton impact structure using coupled  $^{40}\text{Ar}/^{39}\text{Ar}$  and U-Pb geochronology. *Geochimica et Cosmochimica Acta*, 304, pp.68–82.  
<https://doi.org/10.1016/j.gca.2021.04.008>.
- Erickson, T.M., Pearce, M.A., Reddy, S.M., Timms, N.E., Cavosie, A.J., Bourdet, J., Rickard, W.D.A. and Nemchin, A.A., 2017. Microstructural constraints on the mechanisms of the transformation to reidite in naturally shocked zircon. *Contributions to Mineralogy and Petrology*, 172(1). <https://doi.org/10.1007/s00410-016-1322-0>.
- Fassett C. I. and Head J. W., 2008. Valley network-fed, open-basin lakes on Mars: Distribution and implications for Noachian surface and subsurface hydrology. *Icarus*, 198, pp.37–56. <https://doi.org/10.1029/2004JE002287>.
- Fassett, C.I. and Head, James.W., 2008. The timing of Martian valley network activity: Constraints from buffered crater counting. *Icarus*, 195(1), pp.61–89.  
<https://doi.org/10.1016/j.icarus.2007.12.009>.

- Fassett, C.I. and Head, J.W., 2005. Fluvial sedimentary deposits on Mars: Ancient deltas in a crater lake in the Nili Fossae region. *Geophysical Research Letters*, 32(14), pp.1–5. <https://doi.org/10.1029/2005GL023456>.
- Flower, Benjamin.P. and Kennett, James.P., 1994. The middle Miocene climatic transition: East Antarctic ice sheet development, deep ocean circulation and global carbon cycling. *Palaeogeography, Palaeoclimatology, Palaeoecology*, 108, pp.537–555.
- Förstner, U., 1967. Petrographische Untersuchungen des Suevit aus den Bohrungen Deiningen und Wörnitzostheim im Ries von Nördlingen. *Contributions to Mineralogy and Petrology*, 15, pp.281–308.
- Forsythe, R.D., 1990. A case for Martian salars and saline lakes during the Noachian. *Abstracts of the Lunar and Planetary Science Conference*, 21, pp.379–380.
- Forsythe, R.D. and Zimbelman, J.R., 1995. A case for ancient evaporite basins on Mars. *Journal of Geophysical Research*, 100(E3), pp.5553–5563.
- Fredriksson, K., Dube, A., Milton, D.J. and Balasundaram, M.S., 1973. Lonar Lake, India: An Impact Crater in Basalt. *Science*, 80, pp.862–864.
- Füchtbauer, H., Brellier, von der, G., Dehem, R., Förstner, U., Gall, H., Höfling, R., Hoefs, J., Hollerbach, H., Jankowski, B., Jung, W., Malz, H., Mertes, H., Rothe, P., Salger, M., Wehner, H. and Wolf, M., 1977. Tertiary lake sediments of the Ries, research borehole Nördlingen 1973-A summary. *Geologica Bavarica*, 75, pp.13–19.
- Gault, D.E., Quaide, W.L. and Oberbeck, V.R., 1968. Impact cratering mechanics and structures. In: B.M. French and N.M. Short, eds. *Shock Metamorphism of Natural Materials*. Baltimore, USA: Mono Book Corp. pp.87–99.
- Ghadiri, M., Chrzanowski, W. and Rohanizadeh, R., 2015. Biomedical applications of cationic clay minerals. *RSC Advances*, 5(37), pp.29467–29481. <https://doi.org/10.1039/c4ra16945j>.

- Gilg, H.A., 2000. D-H evidence for the timing of kaolinization in Northeast Bavaria, Germany. *Chemical Geology*, [online] 170, pp.5–18. Available at: <www.elsevier.com/locate/chemgeo>.
- Gilg, H.A., Hülmeier, S.H., Miller, H. and Sheppard, S.M.F., 1999. Supergene origin of the Lastarria kaolin deposit South-Central Chile and paleoclimate implications. *Clays and Clay Minerals*, 47(2), pp.201–211.
- Gilmour, I., Jolley, D.W., Watson, J.S., Gilmour, M.A. and Kelley, S.P., 2013. Post-impact heating of a crater lake. In: *European Planetary Science Congress*. p.107.
- Grieve, R.A.F. and Cintala, M.J., 1982. A method for estimating the initial impact conditions of terrestrial cratering events, exemplified by its application to Brent crater, Ontario. In: R.B. Merrill and R. Ridings, eds. *In Lunar and Planetary Science Conference Proceedings*. pp.1607–1621.
- Grieve, R.A.F., Reny, G., Gurov, E.P. and Ryabenko, V.A., 1987. The melt rocks of the Boltsh impact crater, Ukraine, USSR. *Contributions to Mineralogy and Petrology*, 96, pp.56–62.
- Grieve, R.A.F. and Therriault, A.M., 2013. Impactites: their characteristics and spatial distribution. In: G.R. Osinski and E. Pierazzo, eds. *Impact Cratering: Processes and Products*. Blackwell Publishing Ltd. pp.90–105.
- Grim, R.E., 1968. *Clay Mineralogy*. 2nd ed. New York: McGraw-Hill .
- Grotzinger, J.P., Sumner, D.Y., Kah, L.C., Stack, K., Gupta, S., Edgar, L., Rubin, D., Lewis, K., Schieber, J., Mangold, N., Milliken, R., Conrad, P.G., DesMarais, D., Farmer, J., Siebach, K., Calef III, F., Hurowitz, J., McLennan, S.M., Ming, D., Vaniman, D., Crisp, J., Vasavada, A., Edgett, K.S., Malin, M., Blake, D., Gellert, R., Mahaffy, P., Wiens, R.C., Maurice, S., Grant, J.A., Wilson, S., Anderson, R.C., Beegle, L., Arvidson, R., Hallet, B., Sletten, R.S., Rice, M., Bell III, J., Griffes, J., Ehlmann, B., Anderson, R.B., Bristow, T.F., Dietrich, W.E., Dromart, G., Eigenbrode, J., Fraeman, A., Hardgrove, C., Herkenhoff, K., Jandura, L., Kocurek, G., Lee, S.,

- Leshin, L.A., Leveille, R., Limonadi, D., Maki, J., McCloskey, S., Meyer, M., Minitti, M., Newsom, H., Oehler, D., Okon, A., Palucis, M., Parker, T., Rowland, S., Schmidt, M., Squyres, S., Steele, A., Stolper, E., Summons, R., Treiman, A., Williams, R. and Yingst, A., 2014. A Habitable Fluvio-Lacustrine Environment at Yellowknife Bay, Gale Crater, Mars. *Science*, 343(1242777).
- Gurov, E.P., Shekhunova, S.B. and Permiakov, V. v., 2011. The Boltysk impact structure and its impact melt rocks. *Geofizicheskiy Zhurnal*, 33, pp.66–89.
- Gurov, E.P., Shekhunova, S.B. and Permyakov, V. v., 2015. Accessory and opaque minerals in impact melt rocks of the Boltysk structure, Ukraine. *Meteoritics and Planetary Science*, 50(6), pp.1139–1155. <https://doi.org/10.1111/maps.12457>.
- Gurov, Eugene.P., Kelley, Simon.P., Koeberl, Christian. and Dykan, Natalia.I., 2006. Sediments and Impact Rocks Filling the Boltysk Impact Crater. In: Charles. Cockell, Christian. Koeberl and Iain. Gilmour, eds. *Biological Processes Associated with Impact Events*. Berlin, Heidelberg, New York: Springer. pp.335–358. [https://doi.org/10.1007/3-540-25736-5\\_15](https://doi.org/10.1007/3-540-25736-5_15).
- Hagerty, J.J. and Newsom, H.E., 2003. Hydrothermal alteration at the Lonar Lake impact structure, India: Implications for impact cratering on Mars. *Meteoritics and Planetary Science*, 38(3), pp.365–381. <https://doi.org/10.1111/j.1945-5100.2003.tb00272.x>.
- Hickey, Leo.J., Johnson, Kirk.R. and Dawson, Mary.R., 1988. The Stratigraphy, Sedimentology, and Fossils of the Houghton Formation: A Post-Impact Crater-Fill, Devon Island, N.W.T., Canada. *Meteoritics*, 23(3), pp.221–231. <https://doi.org/10.1111/j.1945-5100.1988.tb01284.x>.
- Holbourn, Ann., Kuhnt, Wolfgang., Schulz, Michael., Flores, J.Abel. and Andersen, Nils., 2007. Orbitally-paced climate evolution during the middle Miocene ‘Monterey’ carbon-isotope excursion. *Earth and Planetary Science Letters*, 261(3–4), pp.534–550. <https://doi.org/10.1016/j.epsl.2007.07.026>.

- Horgan, B.H.N., Anderson, R.B., Dromart, G., Amador, E.S. and Rice, M.S., 2020. The mineral diversity of Jezero crater: Evidence for possible lacustrine carbonates on Mars. *Icarus*, 339(113526). <https://doi.org/10.1016/j.icarus.2019.113526>.
- Ivanov, M. and Böhme, M., 2011. Snakes from Griesbeckerzell (Langhian, Early Badenian), North Alpine Foreland Basin (Germany), with comments on the evolution of snake faunas in Central Europe during the Miocene Climatic Optimum. *Geodiversitas*, 33(3), pp.411–449. <https://doi.org/10.5252/g2011n3a2>.
- Jankowski, B., 1977a. Die Postimpakt-Sedimente in der Forschungs-bohrung Nördlingen 1973. *Geologica Bavarica*, 75, pp.21–36.
- Jankowski, B., 1977b. The graded unit on top of the suevite layer in the borehole Nördlingen 1973. *Geologica Bavarica*, 75, pp.155–162.
- Jankowski, B., 1981. Die Geschichte der Sedimentation im Nördlinger Ries und Randecker Maar. *Bochumer geologische und geotechnische Arbeiten*, 6, pp.1–315.
- Jones, W.B., Bacon, M. and Hastings, D.A., 1981. The Lake Bosumtwi impact crater, Ghana. *Geological Society of America Bulletin*, 92, pp.342–349.
- Joshi, Amarja.A., Kanekar, Pradnya.P., Kelkar, Anita.S., Shouche, Yogesh.S., Vani, Aijaz.A., Borgave, Suchitra.B. and Sarnaik, Seema.S., 2008. Cultivable bacterial diversity of alkaline Lonar lake, India. *Microbial Ecology*, 55(2), pp.163–172. <https://doi.org/10.1007/s00248-007-9264-8>.
- Jourdan, F., Moynier, F., Koeberl, C. and Eroglu, S., 2011.  $^{40}\text{Ar}/^{39}\text{Ar}$  age of the Lonar crater and consequence for the geochronology of planetary impacts. *Geology*, 39(7), pp.671–674. <https://doi.org/10.1130/G31888.1>.
- Karp, Tobias., Milkereit, Bernd., Janle, Peter., Danuor, Sylvester.K., Pohl, Jean., Berckhemer, Hans. and Scholz, Christopher.A., 2002. Seismic investigation of the Lake Bosumtwi impact crater: preliminary results. *Planetary and Space Science*, [online] 50, pp.735–743. Available at: <[www.elsevier.com/locate/pss](http://www.elsevier.com/locate/pss)>.

- Kirsimäe, K. and Osinski, G.R., 2013. Impact-induced hydrothermal activity. In: G.R. Osinski and E. Pierazzo, eds. *Impact Cratering: Processes and Products*. Blackwell Publishing Ltd. pp.76–89.
- Koeberl, C., Bottomley, , Richard, Glass, B.P. and Storzer, D., 1997. Geochemistry and age of Ivory Coast tektites and microtektites. *Geochimica et Cosmochimica Acta*, 61(8), pp.1745–1772.
- Koeberl, C., Reimold, W.U., Blum, J.D. and Chamberlain, C.P., 1998. Petrology and geochemistry of target rocks from the Bosumtwi impact structure, Ghana, and comparison with Ivory Coast tektites. *Geochimica et Cosmochimica Acta*, 62(12), pp.2179–2196.
- Komatsu, G., Senthil Kumar, P., Goto, K., Sekine, Y., Giri, C. and Matsui, T., 2014. Drainage systems of Lonar Crater, India: Contributions to Lonar Lake hydrology and crater degradation. In: *Planetary and Space Science*. Elsevier Ltd. pp.45–55. <https://doi.org/10.1016/j.pss.2013.05.011>.
- Loh, Yvonne.Sena.Akosua., Yidana, Sandow.Mark., Banoeng-Yakubo, Bruce., Sakyi, Patrick.Asamoah., Addai, Millicent.Obeng. and Asiedu, Daniel.Kwadwo., 2016. Determination of the mineral stability field of evolving groundwater in the Lake Bosumtwi impact crater and surrounding areas. *Journal of African Earth Sciences*, 121, pp.286–300. <https://doi.org/10.1016/j.jafrearsci.2016.06.007>.
- Longstaffe, F.J., 1991. Mineralogical and O-isotope studies of diagenesis and porewater evolution in continental sandstones, Cretaceous Belly River Group, Alberta, Canada. *Applied Geochemistry*, 6, pp.291–303.
- Longstaffe, F.J. and Ayalon, A., 1990. Hydrogen-isotope geochemistry of diagenetic clay minerals from Cretaceous sandstones, Alberta, Canada: evidence for exchange. *Applied Geochemistry*, 5, pp.657–668.
- Maloof, A.C., Stewart, S.T., Weiss, B.P., Soule, S.A., Swanson-Hysell, N.L., Louzada, K.L., Garrick-Bethell, I. and Poussart, P.M., 2010. Geology of Lonar Crater, India.

*Bulletin of the Geological Society of America*, 122(1/2), pp.109–126.

<https://doi.org/10.1130/B26474.1>.

Melles, M., Brigham-Grette, J., Minyuk, P.S., Nowaczyk, N.R., Wennrich, V., DeConto, R.M., Anderson, P.M., Andreev, A.A., Coletti, A., Cook, T.L., Haltia-Hovi, E., Kukkonen, M., Lozhkin, A. v., Rosén, P., Tarasov, P., Vogel, H. and Wagner, B., 2012. 2.8 Million years of arctic climate change from Lake El'gygytgyn, NE Russia. *Science*, 337(6092), pp.315–320. <https://doi.org/10.1126/science.1222135>.

Melosh, H.J., 1989. *Impact cratering: A geologic process*. New York, NY: Oxford University Press.

Melosh, H.J. and Ivanov, B.A., 1999. Impact crater collapse. *Annual Review in Earth and Planetary Sciences*, [online] 27, pp.385–415. Available at: <[www.annualreviews.org](http://www.annualreviews.org)>.

Melosh, H.J., 2013. The contact and compression stage of impact cratering. In: G.R. Osinski and E. Pierazzo, eds. *Impact Cratering: Processes and Products*. Blackwell Publishing Ltd. pp.33–42.

Menzel, P., Gaye, B., Wiesner, M.G., Prasad, S., Stebich, M., Das, B.K., Anoop, A., Riedel, N. and Basavaiah, N., 2013. Influence of bottom water anoxia on nitrogen isotopic ratios and amino acid contributions of recent sediments from small eutrophic Lonar Lake, central India. *Limnology and Oceanography*, 58(3), pp.1061–1074. <https://doi.org/10.4319/lo.2013.58.3.1061>.

Michalski, J.R., Goudge, T.A., Crowe, S.A., Cuadros, J., Mustard, J.F. and Johnson, S.S., 2022. Geological diversity and microbiological potential of lakes on Mars. *Nature Astronomy*. [online] <https://doi.org/10.1038/s41550-022-01743-7>.

Misra, Pavani., Tandon, S.K. and Sinha, Rajiv., 2019. Holocene climate records from lake sediments in India: Assessment of coherence across climate zones. *Earth-Science Reviews*, 190, pp.370–397. <https://doi.org/10.1016/j.earscirev.2018.12.017>.

Moore, D.M. and Reynolds, R.C., 1997. *X-Ray Diffraction and the Identification and Analysis of Clay Minerals*. 2nd ed. Oxford, New York: Oxford University Press.

- Muttik, N., Kirsimäe, K., Somelar, P. and Osinski, G.R., 2008. Post-impact alteration of surficial suevites in Ries crater, Germany: Hydrothermal modification or weathering processes? *Meteoritics & Planetary Science*, [online] 43, pp.1827–1840. Available at: <<http://meteoritics.org>>.
- Muttik, N., Kirsimäe, K. and Vennemann, T.W., 2010. Stable isotope composition of smectite in suevites at the Ries crater, Germany: Implications for hydrous alteration of impactites. *Earth and Planetary Science Letters*, 299, pp.190–195.  
<https://doi.org/10.1016/j.epsl.2010.08.034>.
- Naumov, Mikhail. v., 2005. Principal features of impact-generated hydrothermal circulation systems: mineralogical and geochemical evidence. *Geofluids*, 5, pp.165–184.
- Nayak, V.K., 1972. Glassy objects (impactite glasses?) A possible new evidence for meteoritic origin of the Lonar Crater, Maharashtra State, India. *Earth and Planetary Science Letters*, 14, pp.1–6.
- Nayak, V.K., 1996. A hypothesis for the salinity of lake water and economic potential of the Lonar impact crater, India. In: *Proceedings of the NIPR Symposium on Antarctic Meteorites 21*. pp.136–137.
- Newsom, H.E., Brittelle, G.E., Hibbitts, C.A., Crossey, L.J. and Kudo, A.M., 1996. Impact crater lakes on Mars. *Journal of Geophysical Research: Planets*, 101(E6), pp.14951–14955. <https://doi.org/10.1029/96JE01139>.
- Newsom, H.E., Graup, G., Sowards, T. and Keil, K., 1986. Fluidization and hydrothermal alteration of the Suevite deposit at the Ries Crater, West Germany, and implications for Mars. *Journal of Geophysical Research*, 91(B13), pp.E239–E251.  
<https://doi.org/10.1029/jb091ib13p0e239>.
- Newsom, H.E., Nelson, M.J., Shearer, C.K., Misra, S. and Narasimham, V., 2005. Hydrothermal alteration at Lonar Crater, India and elemental variations in impact crater clays. In: *Lunar and Planetary Science XXXVI*. p.1143.

- Oberbeck, V.R., 1975. The Role of Ballistic Erosion and Sedimentation in Lunar Stratigraphy. *Review of Geophysics and Space Physics*, pp.337–362.
- Osinski, Gordon.R., Grieve, Richard.A.F., Ferrière, Ludovic., Losiak, Ania., Pickersgill, Annemarie.E., Cavosie, Aaron.J., Hibbard, Shannon.M., Hill, Patrick.J.A., Bermudez, Juan.J., Marion, Cassandra.L., Newman, Jennifer.D. and Simpson, Sarah.L., 2022. Impact Earth: A review of the terrestrial impact record. *Earth-Science Reviews*, 232(104112). <https://doi.org/10.1016/j.earscirev.2022.104112>.
- Osinski, G.R., 2003. *Impact glasses in fallout suevites from the Ries impact structure, Germany: An analytical SEM study*. [online] *Meteoritics & Planetary Science*, Available at: <<http://meteoritics.org1641>>.
- Osinski, G.R., 2004. Impact melt rocks from the Ries structure, Germany: An origin as impact melt flows? *Earth and Planetary Science Letters*, 226(3–4), pp.529–543. <https://doi.org/10.1016/j.epsl.2004.08.012>.
- Osinski, G.R., 2005. Hydrothermal activity associated with the Ries impact event, Germany. *Geofluids*, 5, pp.202–220.
- Osinski, G.R., Cockell, C.S., Pontefract, A. and Sapers, H.M., 2020. *The Role of Meteorite Impacts in the Origin of Life*. *Astrobiology*, <https://doi.org/10.1089/ast.2019.2203>.
- Osinski, G.R., Grieve, R.A.F., Bleacher, J.E., Neish, C.D., Pilles, E.A. and Tornabene, L.L., 2018. *Igneous rocks formed by hypervelocity impact*. *Journal of Volcanology and Geothermal Research*, <https://doi.org/10.1016/j.jvolgeores.2018.01.015>.
- Osinski, G.R., Grieve, R.A.F. and Spray, J.G., 2004. *The nature of the groundmass of surficial suevite from the Ries impact structure, Germany, and constraints on its origin*. *Meteoritics & Planetary Science*, .
- Osinski, G.R. and Lee, P., 2005. Intra-crater sedimentary deposits at the Houghton impact structure, Devon Island, Canadian High Arctic. *Meteoritics & Planetary Science*, [online] 40, pp.1887–1899. Available at: <<http://meteoritics.org>>.

- Osinski, G.R., Lee, P., Parnell, J., Spray, J.G. and Baron, M., 2005a. A case study of impact-induced hydrothermal activity: The Haughton impact structure, Devon Island, Canadian High Arctic. *Meteoritics & Planetary Science*, [online] 40, pp.1859–1877. Available at: <<http://meteoritics.org1859>>.
- Osinski, G.R., Lee, P., Spray, J.G., Parnell, J., Lim, D.S.S., Bunch, T.E., Cockell, C.S. and Glass, B., 2005b. Geological overview and cratering model for the Haughton impact structure, Devon Island, Canadian High Arctic. *Meteoritics & Planetary Science*, [online] 40, pp.1759–1776. Available at: <<http://meteoritics.org>>.
- Osinski, G.R. and Spray, J.G., 2003. Evidence for the shock melting of sulfates from the Haughton impact structure, Arctic Canada. *Earth and Planetary Science Letters*, 215(3–4), pp.357–370. [https://doi.org/10.1016/S0012-821X\(03\)00420-5](https://doi.org/10.1016/S0012-821X(03)00420-5).
- Osinski, G.R., Spray, J.G. and Lee, P., 2001. Impact-induced hydrothermal activity within the Haughton impact structure, arctic Canada: Generation of a transient, warm, wet oasis. *Meteoritics and Planetary Science*, 36(5), pp.731–745. <https://doi.org/10.1111/j.1945-5100.2001.tb01910.x>.
- Osinski, G.R., Spray, J.G. and Lee, P., 2005. Impactites of the Haughton impact structure, Devon Island, Canadian High Arctic. *Meteoritics & Planetary Science*, [online] 40, pp.1789–1812. Available at: <<http://meteoritics.org>>.
- Osinski, G.R., Tornabene, L.L., Banerjee, N.R., Cockell, C.S., Flemming, R., Izawa, M.R.M., McCutcheon, J., Parnell, J., Preston, L.J., Pickersgill, A.E., Pontefract, A., Sapers, H.M. and Southam, G., 2013. Impact-generated hydrothermal systems on Earth and Mars. *Icarus*, 224(2), pp.347–363. <https://doi.org/10.1016/j.icarus.2012.08.030>.
- Osinski, G.R., Tornabene, L.L. and Grieve, R.A.F., 2011. Impact ejecta emplacement on terrestrial planets. *Earth and Planetary Science Letters*, 310(3–4), pp.167–181. <https://doi.org/10.1016/j.epsl.2011.08.012>.

- Pache, M., Reitner, J. and Arp, G., 2001. Geochemical Evidence for the Formation of a Large Miocene 'Travertine' Mound at a Sublacustrine Spring in a Soda Lake (Wallerstein Castle Rock, Nördlinger Ries, Germany). *FACIES*, 45, pp.211–230.
- Petersen, M.T., Newsom, H.E., Nelson, M.J. and Moore, D.M., 2007. Hydrothermal alteration in the Bosumtwi impact structure: Evidence from 2M 1-muscovite, alteration veins, and fracture fillings. *Meteoritics & Planetary Science*, [online] 42, pp.655–666. Available at: <<http://meteoritics.org>>.
- Pickersgill, Annemarie.E., Mark, Darren.F., Lee, Martin.R., Kelley, Simon.P. and Jolley, David.W., 2021. The Boltys impact structure: An early Danian impact event during recovery from the K-Pg mass extinction. *Science Advances*, [online] 7, pp.6530–6548. Available at: <<https://www.science.org>>.
- Pike, R.J., 1980. Control of crater morphology by gravity and target type - Mars, earth, moon. In: S.A. Bedini, ed. *Lunar and Planetary Science Conference Proceedings* . pp.2159–2189.
- Pohl, J., Stöffler, D., Gall, H. and Erston, K., 1977. The Ries impact crater. In: Roddy D.J., Pepin R.O. and Merrill R.B., eds. *Impact and Explosion Cratering*. New York: Pergamon Press. pp.343–404.
- Prasad, Sushma., Anoop, A., Riedel, N., Sarkar, S., Menzel, P., Basavaiah, N., Krishnan, R., Fuller, D., Plessen, B., Gaye, B., Röhl, U., Wilkes, H., Sachse, D., Sawant, R., Wiesner, M.G. and Stebich, M., 2014. Prolonged monsoon droughts and links to Indo-Pacific warm pool: A Holocene record from Lonar Lake, central India. *Earth and Planetary Science Letters*, 391, pp.171–182. <https://doi.org/10.1016/j.epsl.2014.01.043>.
- Reimold, Wolf.U., Brandt, D. and Koeberl, C., 1998. Detailed structural analysis of the rim of a large, complex impact crater: Bosumtwi Crater, Ghana. *Geology*, 26, pp.543–546.

- Riding R., 1979. Origin and diagenesis of lacustrine algal bioherms at the margin of the Ries crater, Upper Miocene, southern Germany. *Sedimentology*, 26, pp.645–680.
- Salger, M., 1977. Die Tonminerale der Forschungsbohrung Nördlingen 1973. *Geologica Bavarica*, 75, pp.67–73.
- Sapers, H.M., Osinski, G.R., Flemming, R.L., Buitenhuis, E., Banerjee, N.R., Tornabene, L.L., Blain, S. and Hainge, J., 2017. Evidence for a spatially extensive hydrothermal system at the Ries impact structure, Germany. *Meteoritics and Planetary Science*, 52(2), pp.351–371. <https://doi.org/10.1111/maps.12796>.
- Savin, Samuel.Marvin., 1967. *Oxygen and hydrogen isotope ratios in sedimentary rocks and minerals*. California Institute of Technology.
- Savin, S.M. and Epstein, S., 1970. The oxygen and hydrogen isotope geochemistry of clay minerals\*. *Geochimica et Cosmochimica Acta*, 34, pp.25–42.
- Savin, S.M. and Lee, M., 1988. Isotopic studies of phyllosilicates. In: S.W. Bailey, ed. *Hydrous Phyllosilicates, Reviews in Mineralogy and Geochemistry*. Washington, USA: Mineralogical Society of America. pp.189–223. <https://doi.org/10.1515/9781501508998-012>.
- Schmieder, M., Kennedy, T., Jourdan, F., Buchner, E. and Reimold, W.U., 2018. A high-precision  $^{40}\text{Ar}/^{39}\text{Ar}$  age for the Nördlinger Ries impact crater, Germany, and implications for the accurate dating of terrestrial impact events. *Geochimica et Cosmochimica Acta*, 220, pp.146–157. <https://doi.org/10.1016/j.gca.2017.09.036>.
- Schnetzler, C.C., Philpotts, J.A. and Thomas, H.H., 1967. Rare-earth and barium abundances in Ivory Coast tektites and rocks from the Bosumtwi Crater area, Ghana. *Geochimica et Cosmochimica Acta*, 31, pp.1987–1993.
- Scholz, C.A., Karp, T., Brooks, K.M., Milkereit, B., Amoako, P.Y.O. and Arko, J.A., 2002. Pronounced central uplift identified in the Bosumtwi impact structure, Ghana, using multichannel seismic reflection data. *Geology*, [online] 30(10), pp.939–942.

Available at: <<http://pubs.geoscienceworld.org/gsa/geology/article-pdf/30/10/939/3524154/i0091-7613-30-10-939.pdf>>.

Shanahan, T.M., Overpeck, J.T., Anchukaitis, K.J., Beck, J.W., Cole, J.E., Dettman, D.L., Peck, J.A., Scholz, C.A. and King, J.W., 2009. Atlantic Forcing of Persistent Drought in West Africa. *Science*, 324, pp.337–380. <https://doi.org/10.1126/science.1166352>.

Shanahan, T.M., Overpeck, J.T., Wheeler, C.W., Beck, J.W., Pigati, J.S., Talbot, M.R., Scholz, C.A., Peck, J. and King, J.W., 2006. Paleoclimatic variations in West Africa from a record of late Pleistocene and Holocene lake level stands of Lake Bosumtwi, Ghana. *Palaeogeography, Palaeoclimatology, Palaeoecology*, 242(3–4), pp.287–302. <https://doi.org/10.1016/j.palaeo.2006.06.007>.

Shcherbak, N.P., Zlobenko, V.G., Zhukov, G. v., Kotljvskaya, F.I., Poleyaya, N.I., Komlev, L. v., Kovalenko, N.K., Nosok, G.M. and Pochtarenko, V.I., 1978. *Catalogue of isotopic data of the Ukrainian Shield*. Kiev, Ukraine: Naukova Dumka.

Sheppard, S.M.F. and Gilg, H.A., 1996. Stable isotope geochemistry of clay minerals ‘The story of sloppy, sticky, lumpy and tough’ Cairns-Smith (1971). *Clay Minerals*, 31, pp.1–24.

Sheppard, S.M.F., Nielsen, R.L. and Taylor, H.P., 1969. Oxygen and Hydrogen Isotope Ratios of Clay Minerals from Porphyry Copper Deposits. *Economic Geology*, [online] 64, pp.755–777. Available at: <<https://pubs.geoscienceworld.org/segweb/economicgeology/article-pdf/64/7/755/3483630/755.pdf>>.

Shevenell, A.E., Kennett, J.P. and Lea, D.W., 2004. Middle Miocene Southern Ocean cooling and antarctic cryosphere expansion. *Science*, 305(5691), pp.1766–1770. <https://doi.org/10.1126/science.1100061>.

Siddiqi, S.Z., 2008. Limnological Profile of High-Impact Meteor Crater Lake Lonar, Buldana, Maharashtra, India, an Extreme Hyperalkaline, Saline Habitat. In: *Proceedings of Taal 2007: The 12th World Lake Conference*. pp.1597–1613.

- Stockwell, C.H., 1982. *Proposals for time classification and correlation of Precambrian rocks and events in Canada and adjacent areas of the Canadian Shield; Part 1: A time classification of Precambrian rocks and events*. Ottawa.
- Stöffler, D., Artemieva, N.A., Wünnemann, K., Reimold, W.U., Jacob, J., Hansen, B.K. and Summerson, I.A.T., 2013. Ries crater and suevite revisited-Observations and modeling Part I: Observations. *Meteoritics and Planetary Science*, 48(4), pp.515–589. <https://doi.org/10.1111/maps.12086>.
- Stöffler, D., Gault, D.E., Wedekind, J. and Polkowski, G., 1975. Experimental hypervelocity impact into quartz sand: Distribution and shock metamorphism of ejecta. *Journal of Geophysical Research*, 80(29), pp.4062–4077. <https://doi.org/10.1029/jb080i029p04062>.
- Talbot, M.R. and Delibrias, G., 1977. Holocene variations in the level of Lake Bosumtwi, Ghana. *Nature*, 268, pp.722–724.
- Talbot, M.R. and Johannessen, T., 1992. A high resolution paleoclimate record of the last 27,500 years in tropical West Africa from the carbon and nitrogen isotopic composition of lacustrine organic matter. *Earth and Planetary Science Letters*, 110, pp.23–37.
- Turner, Benjamin.F., Gardner, L.R. and Sharp, W.E., 1996. The hydrology of Lake Bosumtwi, a climate-sensitive lake in Ghana, West Africa. *Journal of Hydrology*, 183, pp.243–261.
- Versh, E., Kirsimäe, K., Jöeleht, A. and Plado, J., 2005. Cooling of the Kärddla impact crater: I. The mineral paragenetic sequence observation. *Meteoritics & Planetary Science*, [online] 40, pp.3–19. Available at: <<http://meteoritics.org3>>.
- Wagner, Rudiger., Reimold, W.Uwe. and Brande, Dion., 2002. Bosumtwi Impact Crater, Ghana: A Remote Sensing Investigation. In: J. Plado and L.J. Pesonen, eds. *Plado J. and Pesonen L. J.* Heidelberg: Springer-Verlag. pp.189–210.

- Westerhold, T., Bickert, T. and Röhl, U., 2005. Middle to late Miocene oxygen isotope stratigraphy of ODP site 1085 (SE Atlantic): New constraints on Miocene climate variability and sea-level fluctuations. *Palaeogeography, Palaeoclimatology, Palaeoecology*, 217(3–4), pp.205–222. <https://doi.org/10.1016/j.palaeo.2004.12.001>.
- Williams, F.A., Kelley, S.P., Jolley, D.W. and Gilmour M., 2013. The Boltysch Impact Crater, Ukraine: Smectites from the Crater-fill Suevites Tectonostratigraphic evolution of East Greenland View project OGA Frontier Basins Rockall Project View project The Boltysch Impact Crater, Ukraine: Smectites from the Crater-fill Suevites. In: *European Planetary Science Congress*. p.305.
- Wolff, M. and Füchtbauer, H., 1976. Die karbonatische Randfazies der tertiären Süßwasserseen des Nördlinger Ries und des Steinheimer Beckens. *Geol Jb D*, 14, pp.3–53.
- Wright, J.B., Hastings, D.A., Jones, W.B. and Williams, H.R., 1985. *Geology and mineral resources of West Africa*. London: George Allen & Unwin.
- Yeh, H.-W., 1980. D/H Ratios and late-stage dehydration of shales during burial. *Geochimica et Cosmochimica Acta*, 44, pp.341–352.
- Yeh, H.-W. and Epstein, S., 1981. Hydrogen and carbon isotopes of petroleum and related organic matter. *Geochimica et Cosmochimica Acta*, 45, pp.753–762.

## 2 A mineralogical and textural investigation of the impact melt-bearing to post-impact sedimentary transition in the Wörnitzostheim drill core, Ries impact structure, Germany

### 2.1 Introduction

Impact cratering is among the most commonly occurring geological processes on rocky and icy bodies in the solar system. On planets like Earth and Mars, meteorite impact craters are commonly capable of hosting lacustrine systems, which are valued for their climatic, geological and possible biological records (Cabrol and Grin, 1999; 2001; Brigham-Grette et al., 2007). Furthermore, hypervelocity impact events forming complex craters are known to produce hydrothermal systems in the presence of sufficient amounts of water (Naumov, 2005a; Kirsimäe and Osinski, 2012; Osinski et al., 2013). If it occurred, the venting of these hydrothermal systems into any overlying lake environments could have provided ideal habitats for microbial life (Cockell et al., 2017; Osinski et al., 2020).

Many impact craters on Earth and Mars preserve evidence for the past and/or present-day (in the case of Earth) presence of intra-crater lakes. In addition, many craters on Earth and a growing number found on Mars, also preserve evidence for past hydrothermal activity (e.g., Osinski et al., 2013). However, the timing of the impact-generated hydrothermal systems with respect to lake initiation is typically not well constrained. Such deposits on Mars would be invaluable targets for sample return, which is particularly relevant and timely for the Mars 2020 *Perseverance* rover mission to Jezero Crater (Farley et al., 2020). Two inlet valleys are present in the north and west crater rim of this crater, as well as an outlet valley on the eastern rim, which implies a standing body of water existed in the basin (Fassett and Head, 2005).

One of the best preserved and accessible examples of post-impact lacustrine sediments in a crater with demonstrated impact-generated hydrothermal activity is provided by the ~24 km diameter Ries impact structure in southern Germany. The ~14.8 Ma Ries impact structure (Schmieder et al., 2018) is one of the world's most well-studied complex impact structures (e.g., see reviews by Pohl et al., 1977, Stöffler et al., 2013, and references therein) and provides a unique opportunity to study post-impact sedimentary deposits in detail (e.g.,

Förstner, 1967; Füchtbauer et al., 1977; Salger, 1977; Riding, 1979; Arp, 2006; Arp et al., 2013a; 2017; 2019; Christ et al., 2018). The impact-generated hydrothermal system at the Ries has also been well studied (e.g., Newsom et al., 1986; Osinski, 2005; Sapers et al., 2017). One study suggested that the Ries hydrothermal system was persistent for 250,000 years following the impact event (Arp, et al., 2013), which would suggest that hydrothermal activity and sediment deposition occurred concomitantly. However, there has been little documentation of any hydrothermal alteration of post-impact lacustrine sedimentary deposits. If such alteration did occur, we would expect it to be recorded in the transition from the impact melt-bearing breccias, the impactites that provided the source of heat to the hydrothermal system (Osinski, 2005), to the post-impact sedimentary deposits. This transition is preserved in the Wörnitzostheim and Nördlingen drill cores, which have not been studied in detail since the 1960's and 1970's (Förstner, 1967). The present study provides a detailed investigation of the transition from impact melt-bearing breccias to post-impact sedimentary rocks as sampled by the Wörnitzostheim 1965 drill core to test this hypothesis.

## 2.2 Background

The Ries impact event penetrated a sequence of Mesozoic sedimentary rocks comprising mainly Jurassic limestones and Triassic siltstones, sandstones and conglomerates of varying thickness, and an underlying basement of Hercynian age crystalline rock (Pohl et al. 1977). The resulting impact structure that exists today is a near-circular region bound by a ring of isolated hills 24 km in diameter, and a buried central basin bound by an uplift of crystalline rocks approximately 12 km in diameter; often called an “inner ring” (Fig. 2.1a, b; Pohl et al. 1977). The buried floor of the impact structure between the outer rim and central basin is relatively flat whereas the transition from the edge of the central basin inwards is stepped and steep (Ernstson, 1974). The impact event generated two main deposits of impact melt-bearing breccias, also known as “suevite”: (1) impact melt-bearing breccias that were deposited as ejecta (Fig. 2.1a); and (2) crater-fill impact melt-bearing breccias confined to the central basin (Fig. 2.1b; e.g., Hörz et al., 1977; Osinski et al., 2004). Impact melt-bearing breccias at the Ries can be broadly distinguished by the degree of secondary alteration in addition to their locality. Alteration in the ejecta deposits is

generally restricted to calcitic cavity and fracture fillings, and replacement of clasts and lining of fractures and cavities by smectitic clay minerals (Osinski, 2005; Sapers et al., 2017). Crater-fill melt-bearing breccias that occur within the inner ring are pervasively altered, with the majority of impact glass replaced by montmorillonite (Osinski 2005). Furthermore, the crater-fill melt-bearing breccias occur as a continuous layer that varies from <100 m in thickness near the inner ring, to up to 300 m in thickness towards the center of the basin (Stöffler et al. 2013); whereas the ejected melt bearing breccias were deposited in topographically higher areas outside the central basin and can be up to 80 m in thickness (Förstner 1967).

The presence of impact glasses in the melt-bearing breccias suggests initial temperatures of >2,000°C, which cooled rapidly to <100–300°C (Osinski 2005). With a structural uplift of approximately 1–2 km and an assumed geothermal gradient of 30°C km<sup>-1</sup>, the uplift possibly contributed approximately 40–70°C as a heat source for the Ries hydrothermal system (Osinski 2005). Heat from the residual kinetic energy of the shockwaves could have made up a minor additional heat contribution, but its magnitude is currently unquantified. Thus, the major heat source for the Ries hydrothermal system was the impact melt-bearing breccia units (Osinski 2005).

The duration of the Ries hydrothermal system is not well constrained but general estimates can be made using Daubar and Kring's (2001) cooling model. A 25 km diameter crater, with a 200 m thick melt sheet cooling from 800 to 160°C could persist for ~3,000 years. Using a separate model, Pohl (1977) calculated that the cooling of a 200 m thick melt sheet from 800 to 100°C would take several thousand years. Arp et al. (2013b) stratigraphically correlated a hydrothermal spring mound with late-stage lacustrine deposits, suggesting that the Ries' hydrothermal system was active 250,000 years after the impact event. Consistent sedimentation in deep impact crater lakes enables them to record subtle environmental changes over longer periods than most other lake types, with some crater-lakes persisting for several million years (Arp et al. 2017).

The sedimentary record of the Ries impact crater accounts for an ~1.2 Ma long period of time (Pohl 1977) during the transition from the Mid-Miocene Climatic Optimum to a cooler climate influenced by the growth of the Antarctic ice sheet (Flower and Kennett,

1994). The lake sediments deposited during this time period can be broadly divided into two groups: (1) the basin center deposits, and (2) the basin margin deposits (Fig. 2.1a; Arp et al. 2013b). The basin center deposits consist of ~350 m of siliciclastic sedimentary rocks. These rocks are interpreted to record the evolution of the Ries crater-lake as it transitioned from an alluvial playa setting to a stratified, alkaline and saline lake, to an unstratified and less saline lake, and finally to progressively freshening lake with coal swamps (Arp et al., 2017). Füchtbauer et al. (1977) described the sedimentary packages that recorded these environmental changes in the 1.2 km deep Nördlingen 1973 drill core, where they denoted the packages as units A to D, from deepest to shallowest. Unit A is a coarse basal unit comprised of sandstones and breccias derived from “reworked suevite”, which transitions into the bituminous shales of unit B. Unit C is comprised of marls and unit D is comprised of claystones with intercalated lignites ((Füchtbauer et al., 1977; Jankowski, 1977; 1981).

In the lake’s final stages, the inner ring filled with sediment and the marginal carbonates were deposited on its slopes (Janowski 1977, 1981). The basin margin carbonates have an approximate vertical extent of 50 m and comprise travertines, carbonate sands, palustrine limestones and dolomitic algal bioherms (Riding 1979; Arp 2006). In addition to the basin margin carbonates, coarse-siliciclastics comprising conglomerates and sandstones exist along the marginal regions of the lake, mainly in the north-western region of the Ries basin (Arp 2006, Arp et al. 2018). The conglomeritic units are variable with some forming lenticular beds with poor cross-stratification, and others locally interfingering with clay-rich sandstones and sandy dolomite beds. The eventual establishment of Pleistocene river systems cross-cutting the Ries area eroded ~100 m of the youngest lake sediments, making the marginal carbonates deposited on the slopes of the inner ring the only modern expression of their sequence (Füchtbauer et al. 1977; Arp et al. 2013b).

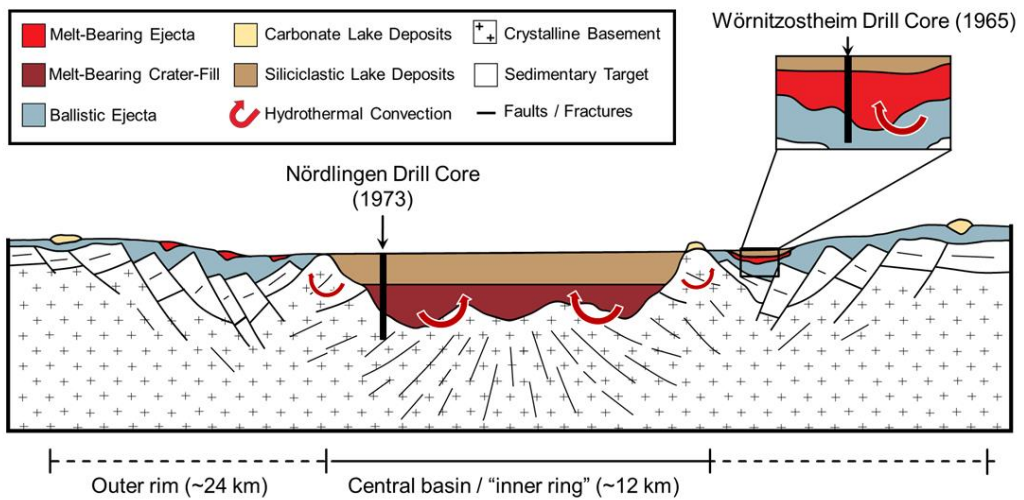
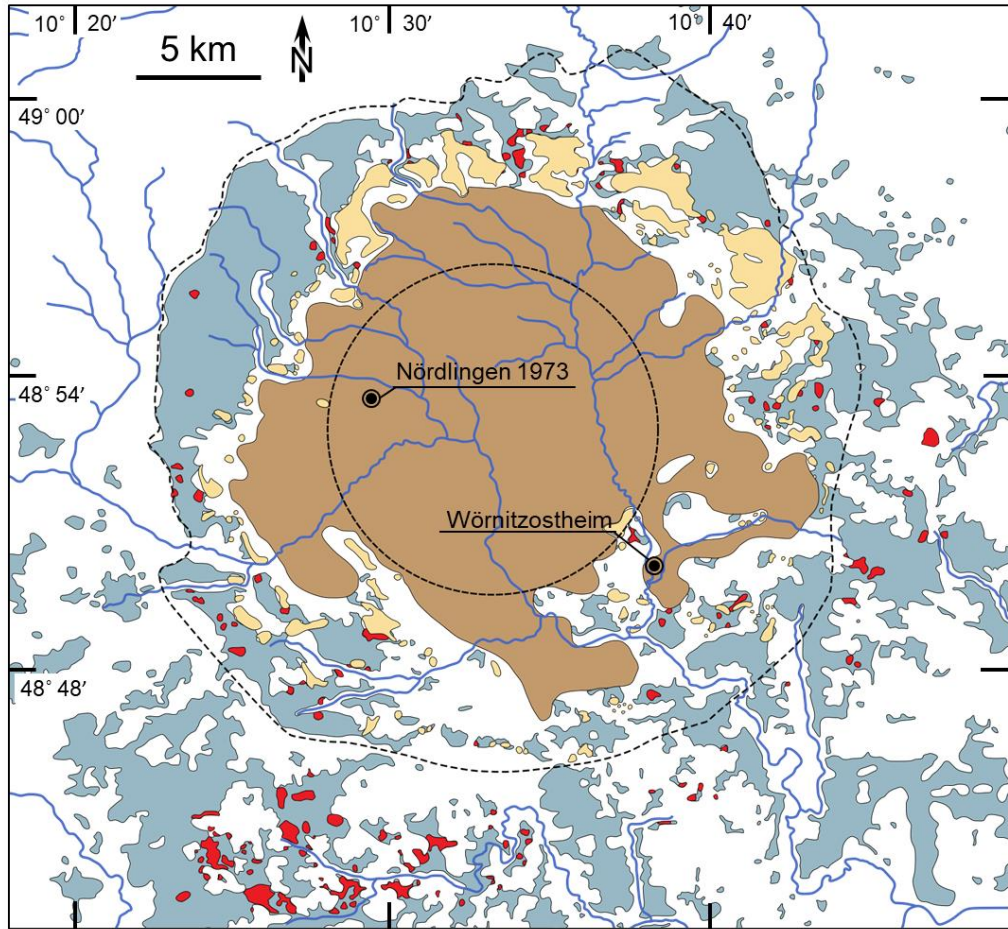


**Figure 2. 1:** (A) Simplified geological map of the Ries impact structure, modified from Sapers et al. (2017) and Arp et al. (2017) highlighting major geological units and drill core locations. The distribution of the post-impact lacustrine rocks as determined based on Pohl

et al. (1977), Ernstson (1974) and Hüttner and Schmidt-Kaler (1999). The cross-section (B) depicts hydrothermal convection cells, and units sampled by the Nördlingen 1973 drill core and Wörnitzostheim 1965 drill core (modified from Sapers et al. 2017). Disclaimer: this cross section is an interpretation of internal structures and relationships between major lithologies and is not intended for use as a to-scale model.

## 2.3 Samples and Analytical Techniques

This study focuses on the transition from the impact melt-bearing breccias to the post-impact sedimentary deposits sampled by the Wörnitzostheim 1965 drill core. The Wörnitzostheim core was drilled ~2 km outside the bounds of the Ries' so-called "inner ring" (Fig. 2.1) and samples approximately 20 m of post-impact sedimentary rocks, which overly approximately 80 m of ejected melt-bearing breccias. In this study, the upper 32 m of the drill core was logged in detail. This upper 32 m segment includes all sedimentary rocks sampled by the Wörnitzostheim drill core in addition to several meters of impact melt-bearing breccias (Fig. 2.2). The lithological units in the core log were distinguished on the basis of macro-scale and microscale textures, such as matrix color and grain-size, abundance of melt fragments, and sedimentary structures. Samples were borrowed from the Ries Impact Crater Museum (ZERN) in the town of Nördlingen, Germany. A summary of all the samples borrowed, and the analyses performed on them to date is provided in Table 2.1.

Representative samples of each unit were characterized using powder X-ray diffraction (*p*XRD) scans of bulk powders, as well as preferentially (00*l*) oriented <2  $\mu$ m separates. All *p*XRD analyses and associated sample preparation were performed at the Laboratory for Stable Isotope Science at the University of Western Ontario. Samples for XRD were prepared by grinding with an agate mortar and pestle to a fine flour. Sample material that was representative of individual components of the rock, such as clast types or matrix material, were preferentially collected where possible. Back-packed mounts of randomly oriented bulk sample powders were analyzed prior to separating the <2  $\mu$ m size-fraction. *p*XRD data of bulk powders was collected from 2–82  $^{\circ}2\theta$  with a 0.02 $^{\circ}$  step size and a scanning speed of 10 $^{\circ}$  per minute using the Rigaku Rotaflex diffractometer. The diffractometer was operated at 45 kV accelerating voltage and a 160 mA tube current with

a Co rotating anode source (Co K $\alpha$ ,  $\lambda = 1.7902 \text{ \AA}$ ). The resultant diffraction patterns were analyzed by hand, and in partial conjunction with the *DIFFRAC.EVA* software package using the International Center for Diffraction Data (ICDD) mineral database and *Profex-BGMN*, an open-source XRD and Rietveld refinement software package (Doebelin and Kleeberg, 2015), using the standard BGMN internal structural reference files. The Rietveld program BGMN was named after its developer, Jörg Bergman, hence BGMN stands for Bergman.

Preferentially (001) oriented  $<2 \mu\text{m}$  separates were prepared by suspension and centrifugation, and then subsequently separated into aliquots that were saturated with CaCl<sub>2</sub> and KCl, respectively. Ca-saturated samples were analyzed from 2–42 °2 $\theta$  after remaining in a 54% relative humidity (RH) desiccation chamber overnight. Ca-saturated samples were subsequently solvated with ethylene glycol (EG) and scanned from 2–82 °2 $\theta$ . K-saturated samples were analyzed from 2–42 °2 $\theta$  at 0% RH (107 °C), 54% RH, and then at 300 °C and 550 °C. All analyses of  $<2 \mu\text{m}$  size fraction separates were collected using the same diffractometer and the same operating conditions as per the bulk samples powders, and all resultant diffractograms were analyzed by hand.

Additionally, thin section offcuts of clastic samples were analyzed using in situ XRD analytical techniques as described in Flemming (2007) to target the mineralogy of particular clasts and to further resolve differences between clast and matrix contributions that would appear in *p*XRD patterns. The in situ XRD data for this study were collected using the Bruker D8 Discover Micro X-Ray Diffractometer ( $\mu$ XRD) with a Co K $\alpha$  X-ray source ( $\lambda = 1.7902 \text{ \AA}$ ) at 35 kV and 45 mA. A Göbel mirror parallel optics system was used with a 300  $\mu\text{m}$  pinhole snout. The  $\theta$ – $\theta$  geometry of the instrument allows for the X-ray source and detector to rotate around the sample location independently while the sample remains stationary. X-rays were detected with a two-dimensional General Area Detector Diffraction System (GADDS) in omega scan mode from 14 to 105 °2 $\theta$ . Omega scan parameters were  $\theta_1 = 14.5^\circ$ ,  $\theta_2 = 20.5^\circ$ ,  $\omega = 10^\circ$ , 60 min duration for frame one, and  $\theta_1 = 40.0^\circ$ ,  $\theta_2 = 40.0^\circ$ ,  $\omega = 10^\circ$ , 90 min duration for frame two with effectively 0.025 °/step. GADDS results were analyzed by hand, and in partial conjunction with the *DIFFRAC.EVA* software package with the same database as described for *p*XRD analyses.

Eighteen polished thin sections were prepared without the use of water to preserve the original texture of any swelling clay minerals. These thin sections were examined using transmitted and reflected light microscopy with plane-polarized light (PPL) and cross-polarized light (XPL), and subsequently analyzed using the JEOL JXA-8530F Field Emission Electron Probe Micro-Analyzer (FE-EPMA) at the Earth and Planetary Materials Laboratory at the University of Western Ontario. Back-scattered electron (BSE) imagery, secondary electron (SE) imagery, and energy dispersive spectroscopy was used to identify mineral species and textures. Wavelength dispersive spectroscopy (WDS) was used to determine the chemical composition of primarily mica and feldspar mineral phases with operational conditions dependent on the phase being targeted for analysis. Micas and feldspars were targeted because they were the most common clast types observed in the sedimentary deposits. The following mineral standards were used for the WDS analysis of feldspar minerals: Albite Amelia, Orthoclase CM Taylor, Anorthite Smithsonian USNM 13704, Diopside Smithsonian USNM 117733. The follow mineral standards were used for micas: Plagioclase Astimex, Orthoclase CM Taylor, Diopside Smithsonian USNM 117733, Fayalite, Rutile, and Rhodonite. Feldspar and micas were analyzed at 15 kV accelerating voltage, 10 nA probe current and a 2  $\mu$ m spot size. The combined average reproducibility was  $\pm 4$  % with  $\pm 5$  % accuracy. Only sample data with totals  $> 90$  % by weight were included in the results (Appendix A).

**Table 2. 1:** Sample record and analytical techniques applied to each sample.

Sample Context					Analytical Techniques						
Lithology	Sample Label	Unit #	Depth (m)	Target Material (for $\mu$ - and $p$ -XRD)	Optical Microscopy	EDS	WDS Spots (Micas)	WDS Spots (Feldspars)	$\mu$ XRD	$p$ XRD (bulk)	$p$ XRD (<2 $\mu$ m)
Mudstones	RW0.9*	1	0.9	Bulk							
	RW1.0	2	1.0	Bulk							
Marlstones	RW2.0	3	2.0	Bulk							
	RW3.0	4	3.0	Bulk							
	RW8.1	4	8.1	Bulk							
Dolomite Packstone	RW8.2	5	8.2	Bulk							
Marlstones	RW9.6A-Wht.**	6	9.60	White material							
	RW9.6B-Gry.	6	9.60	Dar grey material							
	RW10.55	7	10.55	Bulk							
Sandstone	RW10.93	8	10.93	Bulk							
Sandstone Conglomerate	RW12.74	9	12.74	Matrix							
Sandstone	RW13.0	10	13.0	Bulk							
Grey Conglomerate	RW13.2	11	13.2	Matrix							
Altered Grey Conglomerate	RW14.33-ALT	11	14.33	Clasts							
	RW14.33-MTX	11	14.33	Matrix							
Grey Conglomerate	RW14.78	11	14.78	Matrix							
	RW16.16-ALT	11	16.16	Clasts							
	RW16.16-MTX	11	16.16	Matrix							
Light Brown Conglomerate	RW16.85	12	16.85	Matrix							
Pink Conglomerate	RW19A-CLST	13	19.00	Clasts							
	RW19B-MTX	13	19.00	Matrix							
Grey-Toned Melt-Bearing Breccia	RW22	14	22.00	Matrix							
Pink-Toned Melt-Bearing Breccia	RW32	15	32.00	Matrix							

\*Sample naming convention: R: Ries impact structure; W: Wörnitzostheim drill core; [number]: depth location of sample.

\*\* -Wht.: White-toned material; -Gry.: Grey-toned material; -ALT: altered material; -MTX: matrix material; -CLST: clast material.

## 2.4 Results: Drill core, mineral chemistry and petrographic descriptions

This study contributes a new stratigraphic column representing the upper 32 m of the Wörnitzostheim 1965 drill core (Fig. 2.2). Our stratigraphic column highlights features that were previously not reported by Förstner (1967), and is based on notes recorded from direct observation of drill core, not on the tabulated notes contributed by Förstner (1967). As such, our observations of the upper 32 m of drill core represents a key result. The upper 32 m of drill core captures the entirety of the post-impact sedimentary deposits and a portion of the underlying melt-bearing breccias (Fig. 2.2). We identified fifteen distinct units that were distinguished based on their macro-scale textures, color, tone and mineralogical composition (Table 2.2); this approach was similar to the original work of (Förstner, 1967); however, our updated log is based on new detailed textural and mineralogical characterization of micro-scale matrix material, which is discussed in the following sections. Results from *p*XRD analysis are logged in Appendix A and  $\mu$ XRD results are logged in Appendix C. Our classification deviates from Förstner's classification in that the extent of some units differs slightly and additional sub-units are included that were not previously described in detail. Differences between the log in this study and that of (Förstner, 1967) are described in the discussion.

The results of our log indicate that the upper 32 m of the Wörnitzostheim core transitions upward through five distinct unit groups from impact melt-bearing breccias (units 15, 14) to basal conglomerates (units 13–11), to sandstones and the sandstone conglomerate (units 10–8), to marlstones (units 7–3), and then to mudstones (units 2, 1; Fig. 2.2). The nature of the transition between the breccias and some overlying sedimentary units is not always preserved in drill core; consequently, the extents of the marl and mudstone units are estimated based on assays affiliated with remaining core specimens rather than through direct observation.

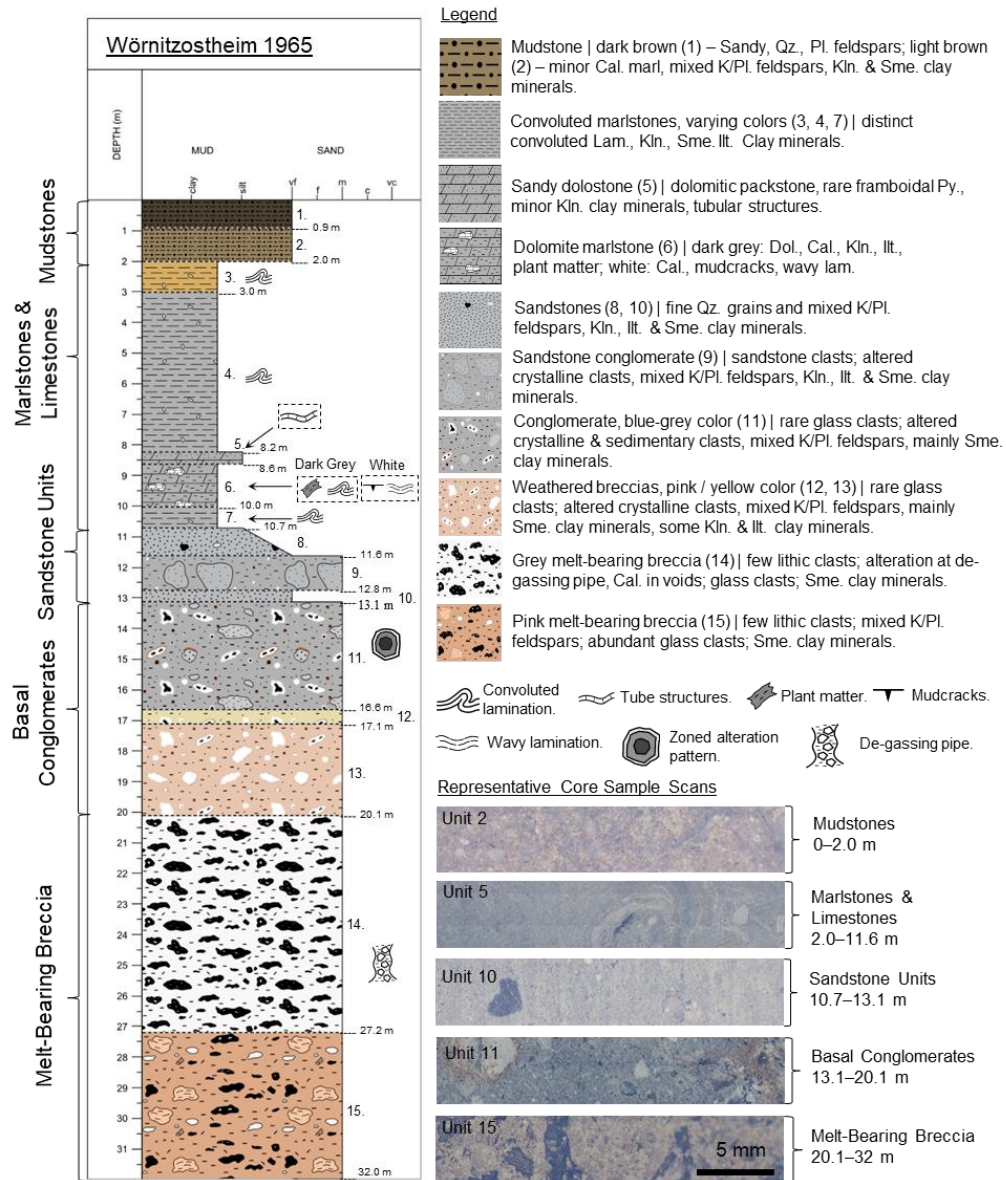


**Figure 2. 2:** Stratigraphic column for the Wörnitzostheim 1965 drill core showing the major lithological units present. The thickness and depth of the units is denoted on the y-axis and the approximate grainsize from clay to very coarse sand is denoted on the x-axis. Grain-sizes were approximated using a grain-size card. Refer to Förstner (1967) for a detailed account of grain-size distribution. Each unit is assigned a number in sequential order starting from the top of the drill core. Representative core scans of each major unit are shown at the samples' depth locations. Abbreviations: Qz. – quartz; Pl. – plagioclase; Kln. – kaolinite; Ilt. – illite; Sme. – smectite; Cal. – calcite; Dol. – dolomite; Py. – Pyrite; Lam. – lamination; Sandstone Units – Sandstones and Sandstone Breccias.



### 2.4.1 *Impact melt-bearing breccias (>32 – 20.1 m; units 15 and 14)*

The impact melt-bearing breccias are the deepest units logged in this segment of drill core (Fig. 2.2) and comprise two sub-units distinguished by the nature of their groundmass material and the abundance and composition of different coarse ( $> 100 \mu\text{m}$  diameter) clastic material. As units 15 and 14 are most apparently distinguishable by the color and composition of their groundmass material, unit 15 is hereafter denoted as “pink melt-bearing breccia” and unit 14 is denoted as “grey melt-bearing breccia”. The mineralogy of the impact melt-bearing breccias has previously been described in detail based on samples acquired from quarries throughout the impact structure and drill core (e.g., Osinski et al. 2004; Stöffler et al. 2013; Sapers et al 2017). Generally, the mineralogy of both the pink and grey melt-bearing breccias observed in the present study consistent with previous work (e.g., Osinski et al. 2004; Osinski 2005; Sapers et al. 2017), but with additional details as provided below.

#### 2.4.1.1 Unit 15, pink-toned melt-bearing breccia: (32–27.2 m)

Unit 15 comprises the pink-toned melt-bearing breccia, which extends to ~78.3 m depth (Förstner, 1967; Sapers et al. 2016); however, only the upper 5.2 m were sampled and analyzed in this study. This unit is a poorly sorted breccia that contains cm to mm scale, sub-angular to angular felsic clasts comprised of K-feldspar and plagioclase feldspar (Table 2.2) with sericitic alteration textures at the grain boundaries and along internal fractures. Rare ( $<1\%$  bulk composition,  $<20 \mu\text{m}$  scale), fractured zircon and fluorapatite occur in association with the feldspar clasts, and phillipsite occurs as linings, and fracture fillings in the fluorapatite. Another significant component of the cm to mm scale clasts includes impact-generated glass with calcitic vesicle fillings and well-preserved flow banding and minor alteration at the grain boundaries and along perlitic fractures. Whole rock impact glass (hereafter “impact glass”) occurs as highly convoluted amoeboid shapes with complex textures (Fig. 2.3A).

Finer ( $\sim 100\text{--}20 \mu\text{m}$  scale) clastic material is comprised of plagioclase feldspar, K-feldspar, quartz and impact glass, with characteristics that match their coarser counterparts (Table 2.2). Finer clastic material also included rare biotite clasts ( $<10\%$  bulk composition)

that are kink-banded and commonly exhibit rutile exsolution textures. Calcite and zoned, euhedral ferroan dolomite also occur on the  $\sim 100\text{--}20\ \mu\text{m}$  scale as vesicle linings throughout the unit (Fig. 2.3B).

This study follows the definition of “groundmass” used in previous studies (e.g., Osinski et al. 2004), which describe it as fine-grained material that encloses fragments of shocked and unshocked target material and excludes any mineral or lithic clasts  $>10\text{--}20\ \mu\text{m}$  in diameter. The groundmass of unit 15 comprises clay minerals and exhibits a flaky texture, similar to typical flaky honeycomb textures formed by smectite (Fig. 2.3C); however, they are relatively x-ray amorphous yielding muted peaks in the  $12.5\ \text{\AA}$  region of the diffraction patterns of bulk, untreated samples, which suggests that they could be palagonitic. The impact glass and palagonitic groundmass material create a texture reminiscent of immiscibility (Fig. 2.3A) such that the palagonitic groundmass forms in inclusion-like pockets with sharp contacts with the impact glass.

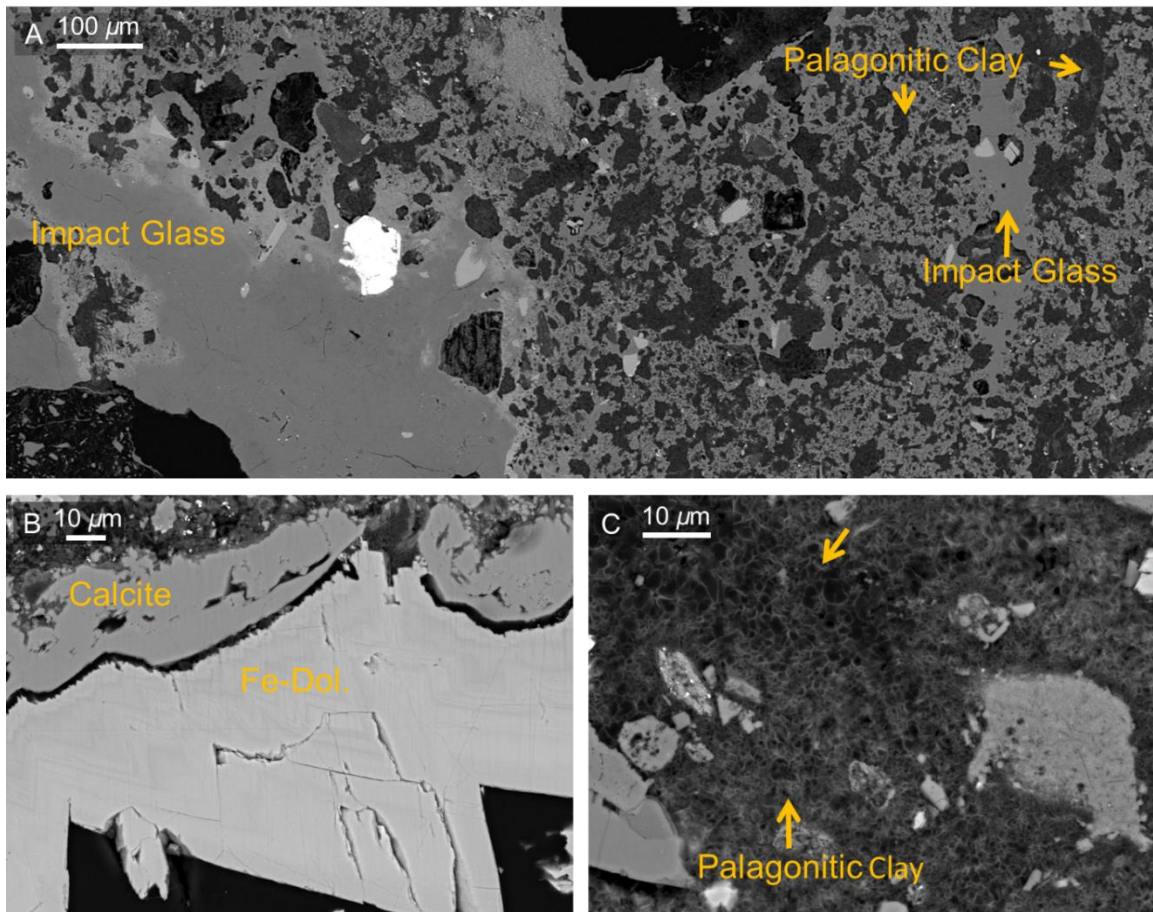


**Figure 2. 3:** Common alteration and groundmass textures in the pink melt-bearing breccia (unit 15), sampled from 32 m depth (sample label RW32). (A) Convoluted impact glass with complex structures and putative immiscibility texture with a palagonitic groundmass. (B) A common vesicle lining texture involving the occurrence of calcite and ferroan dolomite (Fe-Dol.) along the walls of the vesicle. (C) A flaky texture exhibited by the groundmass that is pervasive throughout the sample similar to the honeycomb texture exhibited by smectites.

#### 2.4.1.2 Unit 14, grey-toned melt-bearing breccia (27.2 – 20.1 m)

Unit 14 comprises the grey-toned melt-bearing breccia, which is poorly sorted and mineralogically the most similar unit in this log to the surficial suevite described in previous studies (e.g., Stöffler et al. 1977; Engelhardt and Graup 1984; Osinski et al. 2004). This unit in the Wörnitzostheim 1965 drill core was previously included in the reworked suevite units of Förstner's (1967) log. The grey melt-bearing breccia (Unit 14) can be broadly

distinguished from the pink-colored melt-bearing breccia (Unit 15) by its lesser quantity of quartz and feldspar and greater abundance of calcite. *p*XRD scans of bulk powders shows that unit 14 has its most intense peak at 3.02 Å, suggesting calcite is one of main phases in the rock, and broad ~12.5 Å peaks indicating the presence of clay minerals, while unit 15 exhibits a strong 3.345Å quartz peak and 3.31 Å – 3.16 Å feldspar peaks, muted 12.5 Å clay mineral peaks and 3.02 Å calcite peaks. The mineralogical differences between units 14 and 15 can be distinguished in Figure 5 of Sapers et al. (2017), which also shows that mineralogical similarities exist between the uppermost melt-bearing breccias in the Wörnitzostheim drill core and similar grey-toned melt bearing breccias that underlie unit 15 from 78.3 m to 98.4 m. Figure 2 of Förstner (1967) highlights the distribution of calcite, which shows a similar pattern between unit 14 of this study and the melt-bearing breccias from 78.3 m to 98.4 m depth in Förstner (1967). A significant macro-scale feature that distinguishes unit 14 from 15 is the notable occurrence of a degassing pipe in unit 14 from 27.5 – 27.7 m depth (Fig. 2.4), previously noted by (Caudill et al., 2021).

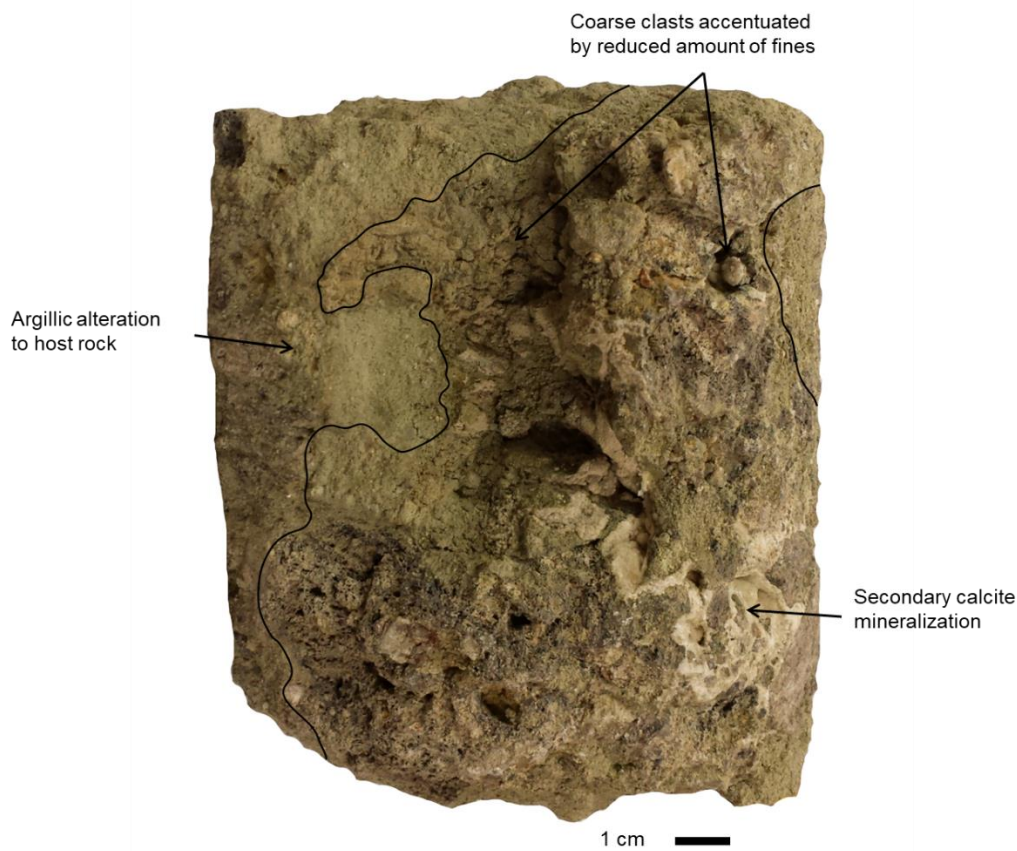


**Figure 2. 4:** Degassing pipe sample observed at 27.50 – 27.70 m depth. The degassing pipe is defined by its characteristic quasi-vertical orientation, and its clast-rich appearance accentuated by its fine-poor nature. Degassing pipes are commonly associated with alteration (e.g., Caudill et al. 2021), which is consistent with the secondary calcite mineralization and pervasive argillic alteration observed here.

The most prominent clast type in unit 14 is cm- to mm-scale, fresh, vesicular glass clasts that occur in irregular and angular shapes with well-preserved flow banding. The glass clasts show minor alteration to smectitic clay minerals along perlitic and quench fractures, and frequently host embedded globules of fresh calcite. Calcite globules form an immiscibility texture with the silicate glasses and where they occur in this setting, the globules of calcite are often rimmed with smectitic clay minerals and exhibit sharp boundaries with other phases, consistent with the observations of Osinski et al. (2004) (Fig. 2.5A). Calcite globules also occasionally hosted spherulites comprised of feldspar and

quartz (Fig. 2.5B). Feldspar and quartz clasts that occur on the cm- to mm-scale in the groundmass occasionally host minor, calcite veining. Feldspar clasts frequently show K-feldspar exsolution textures and host sericitic alteration at their grain boundaries and along internal fractures. Quartz and feldspar clasts are also present at the  $\sim 100 \mu\text{m}$  scale in addition to kink-banded micas and angular, fractured apatite grains.

The groundmass in unit 14 is similar to that reported elsewhere at the Ries (Osinski et al. 2004) and contains fresh skeletal plagioclase with swallow tail terminations (Fig. 2.5C), pyroxene crystallites, quartz, calcite, fluorapatite and ilmenite. Some differences include an absence of garnet crystallites and Ba-phillpsite, and the addition of sub-rounded titanite, and rutile exsolved from micas. Within the groundmass, calcite also occurs as irregular bodies with embayed outlines. Smectitic clay minerals comprise most ( $>50\%$ ) of the groundmass and formed in association with irregular bodies of calcite in the groundmass and exhibit void filling textures.

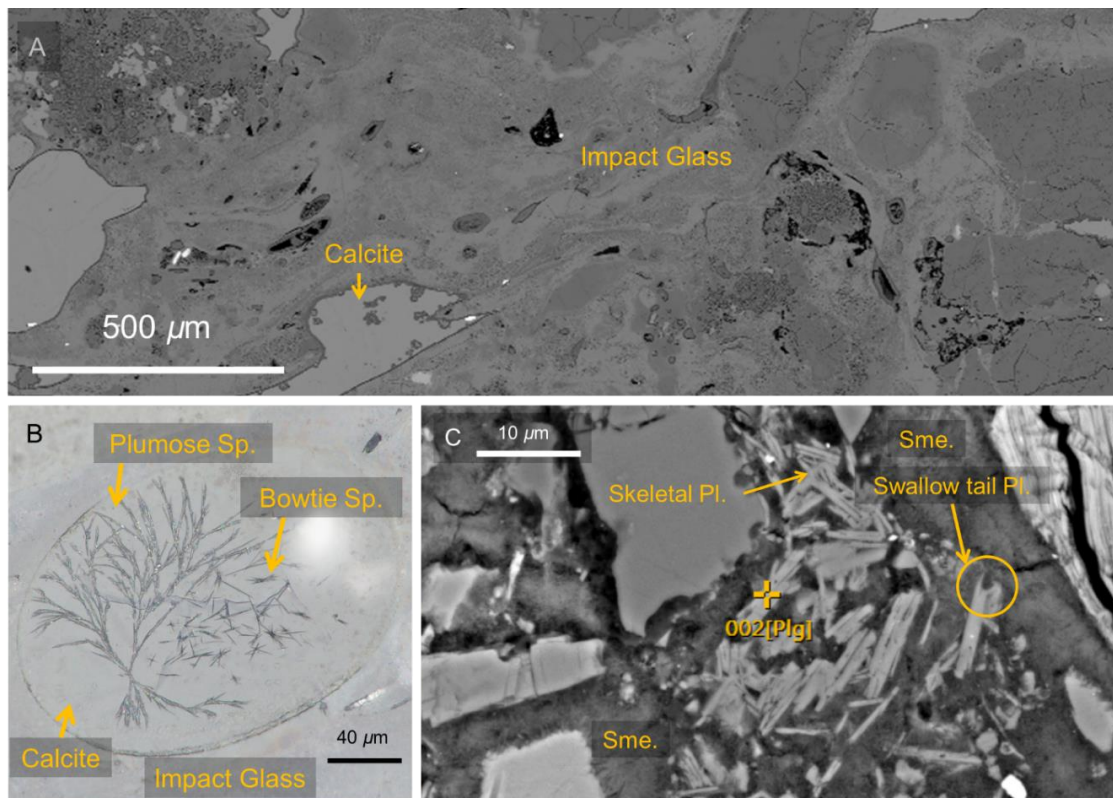


**Figure 2. 5:** Quench and immiscibility textures in the glasses and groundmass of unit 14 from 22 m depth (sample label: RW22). (A) BSE imagery of immiscibility textures

between calcite, and silicate glass (Si. G.) showing clear flow features. (B) A reflected-light image of an immiscible bubble of calcite hosted in a silicate glass showing plumose and bowtie spherulites (Sp.) comprising quartz and feldspar. (C) A BSE image of unit 14 depicting the occurrence of skeletal plagioclase feldspar (Pl.) with rare swallow tail terminations in the smectitic (Sme.) groundmass of the melt-bearing breccia sampled by this unit.

#### 2.4.2 Conglomerates (20.1–13.1 m; units 13, 12 and 11)

The conglomerates comprise 3 sub-units: unit 13 to 11 (Fig. 2.2). These units are generally distinguished from the underlying impact melt-bearing breccias (units 14 and 15) by their sub-rounded cm-scale crystalline, and glass clasts, overall fewer  $>100\ \mu\text{m}$  scale clasts and by a less coherent and more friable matrix. These units are denoted as “conglomerates” instead of “Reworked Breccia” as originally given for the equivalent stratigraphic section in the notes of Förstner (1967) because of the common sub-rounding of the glass clasts, which are typically elongated or irregularly shaped (e.g., Osinski et al. 2004). The mica and feldspar minerals exhibited a range of chemical compositions, which are averaged in Table 2.3 and listed completely in Appendix A. Feldspars occurred as a range of albitic and potassic variants (Fig. 2.6A). Micas showed compositions indicating phlogopite, biotite and chlorite were dominant (Fig. 2.6B). This WDS data was collected from samples RW14.33 and RW19.

Table 2. 3: Averaged WDS results of micas and feldspars from conglomerate units.

Oxide	Chloritic Micas		Biotitic Micas		Phlogopitic Micas		K-Feldspar		Plagioclase Feldspar	
	Mean Wt. %	2 $\sigma$	Mean Wt. %	2 $\sigma$	Mean Wt. %	2 $\sigma$	Mean Wt. %	2 $\sigma$	Mean Wt. %	2 $\sigma$
SiO <sub>2</sub>	36.02	7.52	38.10	2.09	48.94	3.10	65.69	1.31	67.08	2.70
Al <sub>2</sub> O <sub>3</sub>	17.69	2.20	15.09	1.60	30.79	4.81	19.04	0.30	21.63	1.81
Na <sub>2</sub> O	0.14	0.10	0.24	0.12	0.71	0.39	0.96	0.62	10.16	1.44
MgO	11.65	3.29	10.01	2.25	1.85	1.15	0.01	0.03	0.03	0.05
TiO <sub>2</sub>	1.50	0.91	3.56	0.85	0.61	0.26	0.03	0.02	0.01	0.02
CaO	0.65	0.68	0.45	0.89	0.53	0.79	0.03	0.03	1.42	1.72
K <sub>2</sub> O	2.28	1.21	8.21	1.24	7.81	1.85	14.18	1.79	0.58	0.77
FeO	19.79	4.10	18.17	2.72	2.44	1.67	0.15	0.05	0.16	0.09
MnO	0.26	0.17	0.29	0.15	0.02	0.03	0.00	0.01	0.01	0.01
Total	89.96		94.11		93.70		100.10		101.10	
n	30		84		30		28		20	

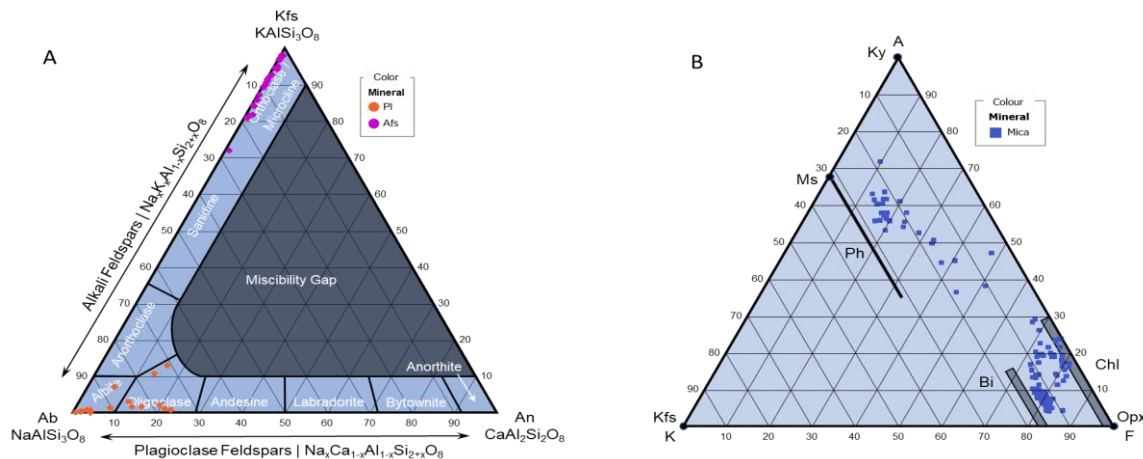


**Figure 2. 6:** Ternary diagrams of (A) feldspar mineral compositions and (B) mica mineral compositions. The values are reported here as oxide Wt. % divided by the molar mass of the oxide and normalized to 100 % using the oxides indicated at the apices of each plot. The apices of the feldspar diagram represent mineral formulas that were calculated after converting from wt. % to molar, and then inputting the resulting values into the following expressions:  $An. = Ca/(2*Al+2*Si)$ ;  $Ab. = Na/(Al+3*Si)$ ;  $Kfs. = K/(Al+3*Si)$ . The apices of the mica diagram represent combinations of measurements as follows:  $A = Al_2O_3 + Fe_2O_3 - Na_2O - K_2O - CaO$ ;  $K = K_2O$ ;  $F = FeO + MgO + MnO + TiO_2$ . Titanium was included in the mica plot to account for the relatively high titanium measurements in the biotitic micas (Table 2), and the association with titanium bearing minerals such as ilmenite and rutile as reported in the individual unit descriptions. Fields associated with specific minerals are highlighted on each plot. Abbreviations: Kfs. – K-feldspar; Ab. – albite; An. – anorthite; Ms. – muscovite; Ph. – phlogopite; Bi. – biotite; Chl. – chlorite; Opx. – orthopyroxene; Ky. – kyanite.

#### 2.4.2.1 Unit 13, pink conglomerate (20.1 – 17.1 m)

Unit 13 is a poorly sorted, matrix-supported conglomerate with cm-scale clasts of fine-grained, white-toned material comprising the only clasts that are distinguishable to the naked eye. These white-toned clasts occasionally occur with black, glassy centers, and are generally comprised of clay minerals. The matrix of unit 13 is made up of clay to very fine sand-sized, clastic matrix material that exhibits a wide range of compositions. The clasts in

the matrix consist of a mixture of K-feldspar and plagioclase feldspar, micas, quartz, calcite, and rare glass fragments (Table 2.2; Table 2.3; Figs. 2.6A, B). The glass fragments have irregular shapes and occasionally enclose rounded pockets of matrix material. The clastic mica grains are compositionally phlogopitic, biotitic and chloritic, and consistently exhibit kink-banding (Fig. 2.6B, Fig. 2.7A). In some cases, rutile, barite and Fe-oxides occur between the kinked bands of the chloritic micas. Quartz occurs as angular to sub-rounded grains and occasionally exhibit PDF's and toasted textures. Calcite generally occurs as 10  $\mu\text{m}$ -scale, featureless grains with irregular shapes and sharp boundaries with the matrix around them. Calcite globules, unlike those observed in unit 14, are rare occurrences that are typically fragmented and lack any smectite borders. Indeed, the 3.02 $\text{\AA}$  *p*XRD peak associated with calcite is notably less intense with respect to the 3.02 $\text{\AA}$  peak observed from unit 14. Uncommon clasts in the matrix include apatite, ilmenite, barite, iron oxides and zircon, which commonly occur as  $\sim 10$   $\mu\text{m}$ -scale, fractured or fragmented grains. Rare subhedral to euhedral ferroan dolomite occurs in voids and empty pockets in the matrix, in a similar manner to unit 15, with rare intergrowths of skeletal plagioclase (Fig. 2.7B).

The interstitial matrix material is mainly comprised of mixed smectitic clay minerals, which exhibit a well-formed honeycomb texture throughout the matrix and occur as void fillings and linings. Smectites occurring as void-fillings and linings appear to be the most well-formed, exhibiting clear honeycomb textures, and occasionally forming ringed structures (Fig. 2.7B). Smectitic clay minerals also form capillaceous growths which nucleated from individual bands of micaceous material (Fig. 2.7C) and “fluffy” growths from feldspar grains such as remnant skeletal plagioclase. Smectitic clay minerals were identified by *p*XRD scans of preferentially oriented  $<2\mu\text{m}$  separates, which yielded peaks at 17.14  $\text{\AA}$  for glycolated, Ca-saturated samples, 15.45  $\text{\AA}$  for hydrated samples (Ca-saturated, 54%RH) and 10.10  $\text{\AA}$  for samples heated to 300  $^{\circ}\text{C}$ ; indicating the expansion and collapse of smectitic material. The consistent occurrence of a relatively broad and weak 10  $\text{\AA}$  peak is consistent with the presence of illitic clay minerals, but suggests they are not abundant in the mixture of clay minerals. Additionally, peaks at 3.56 and 1.48  $\text{\AA}$  collapse at 550  $^{\circ}\text{C}$  indicating the presence of kaolinite due to its characteristic dehydroxylation at elevated temperatures.

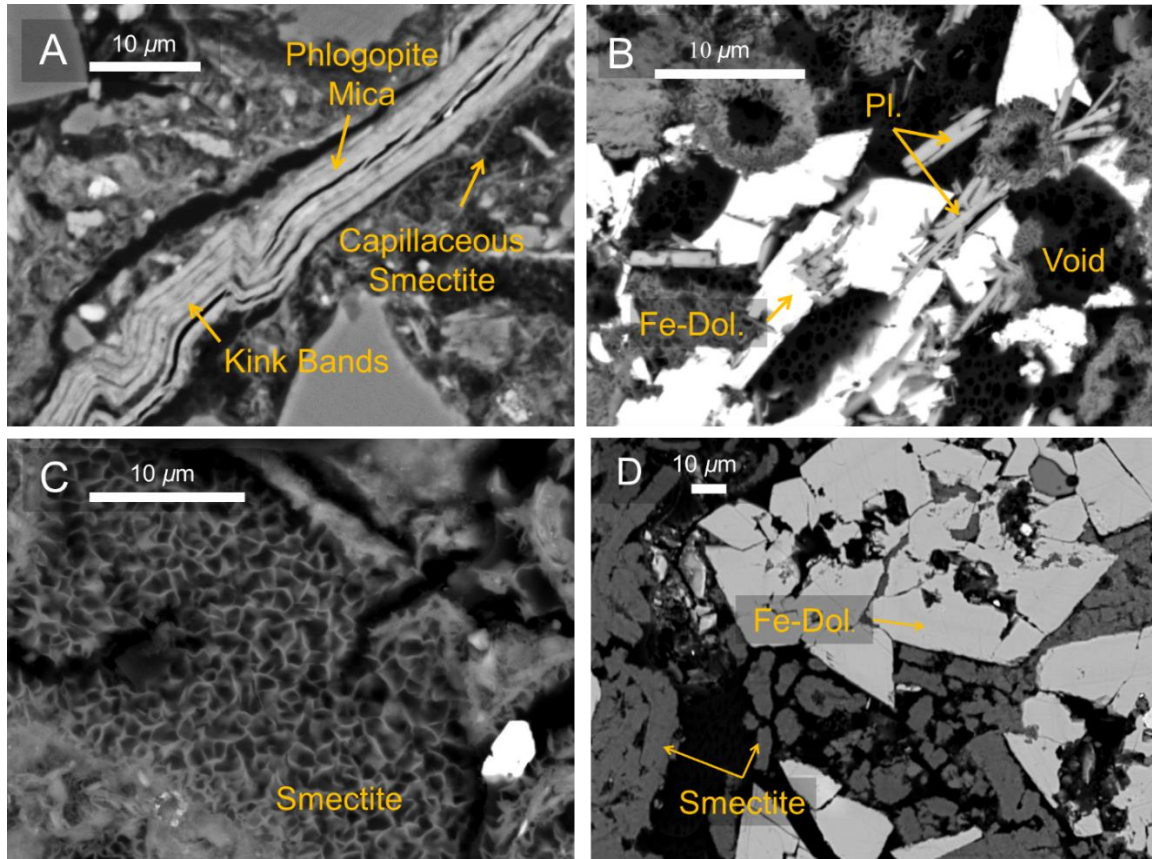


**Figure 2. 7:** Back-scattered electron images of notable mineral textures and occurrences from unit 13 (A, B, C; sample label: RW19) and unit 12 (D; sample label: RW14.78). (A) A phlogopite mica exhibiting a kink-banding texture and capillaceous smectite growths sourced from a strand of micaceous material. (B) A subhedral ferroan dolomite (Dol.) bordering void space and enclosing K-feldspar (Kfs). (C) Honeycomb textures in matrix clay minerals typical of smectites. (D) Smectitic clay minerals exhibiting a “fluffy” texture, and subhedral ferroan dolomite (Fe-Dol.) occurring in void spaces in unit 12.

#### 2.4.2.2 Unit 12, light-brown conglomerate (17.4 – 16.6 m)

Unit 12 is a matrix-supported clastic unit that is poorly sorted and bears a strong resemblance to unit 13 such that the only cm-scale clasts visible to the naked eye are sub-rounded clasts altered to clay minerals. Additionally, the fine clastic matrix in unit 12 consists of the same assemblage of minerals as unit 13: quartz, feldspars, phlogopitic, biotitic and chloritic micas, and glass fragments (Table 1). Bulk diffraction patterns exhibit 10 Å peaks that are stronger than that of unit 13 and muted 3.31Å – 3.21Å peaks typically

associated with K-feldspar. Uncommon  $\sim 10\ \mu\text{m}$ -scale clastic minerals in unit 12 consist of apatite, ilmenite, barite, and zircons. Fragments of rounded calcite globules are absent.

The tone of the matrix material changes from a light red in unit 13 to a light brown in unit 12, which is accompanied by a change in the dominant texture of smectitic clay minerals in the matrix, and a sharper and more intense  $10\ \text{\AA}$  peak. Matrix smectitic clay minerals in unit 12 generally exhibit a tightly packed fluffy texture that form in elongated groups, which curve and clump together (Fig. 2.7D). The smectitic clay minerals in unit 12 are more strongly associated with individual bands of kink-banded chlorites than they are in unit 13 (Fig. 2.7D), and commonly occur in voids, occasionally in association with subhedral ferroan dolomite.

#### 2.4.2.3 Unit 11, grey conglomerate (16.6 – 13.1 m)

Unit 11 is a matrix-supported conglomerate that is poorly sorted with cm-scale clasts similar to those in units 12 and 13 (Table 2.2), that is, mainly sub-rounded clasts of clay material that occasionally have glassy centers. Unlike units 12 and 13, unit 11 additionally hosts sub-rounded cm-scale clasts made up of sandstone, exhibiting faint laminations (Fig. 2.8A), and felsic crystalline rock (Fig. 2.8B). These clasts occur frequently throughout unit 11 and are characterized by red-brown iron oxide staining at their edges. Unit 11 also hosts occurrences of zoned argillic alteration features associated with strong red-brown to yellow discolorations with no distinguishable clast-related origin (Figs. 2.8C, D). These features are reminiscent of epithermal style alteration and are similar in color and zonation pattern to alteration halos associated with glass clasts observed in the graded unit of the Nördlingen 1973 drill core (Chapter 4).

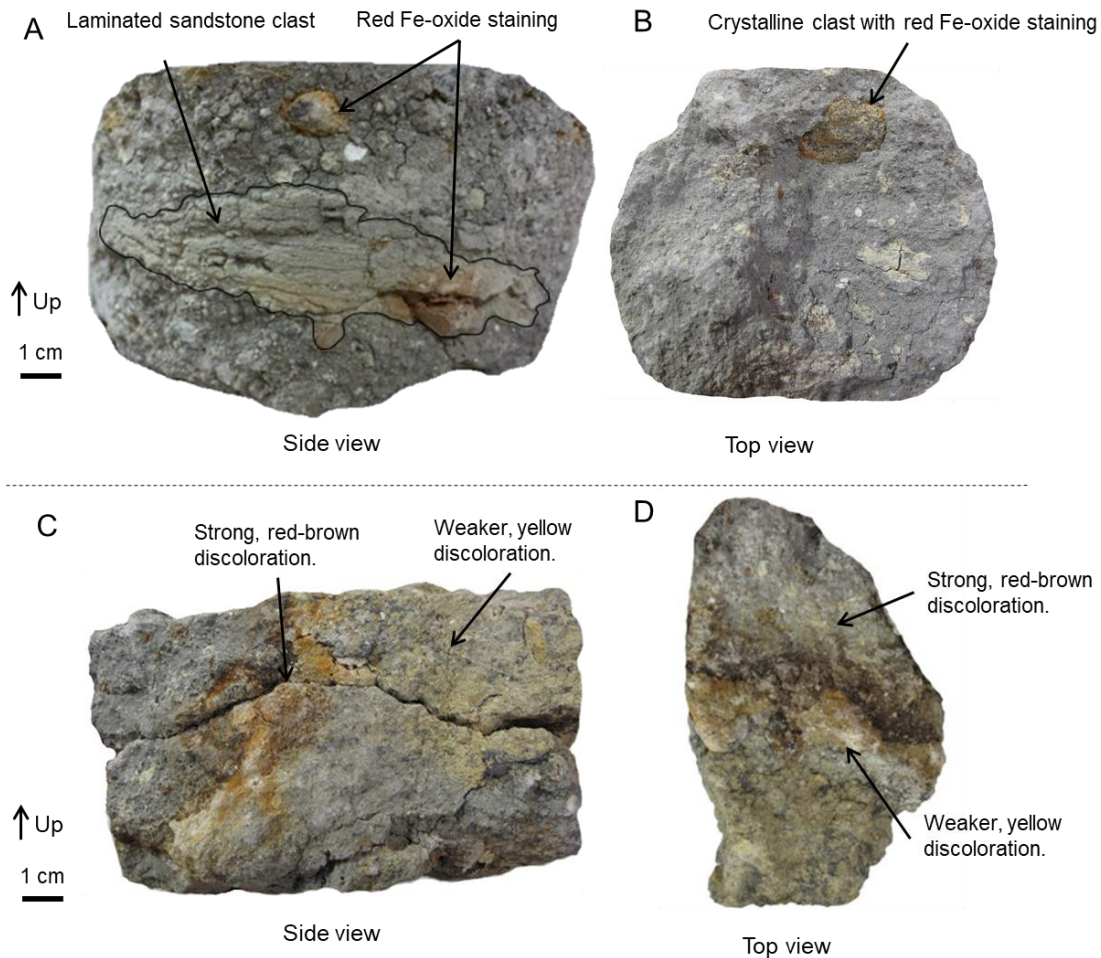


**Figure 2. 8:** A side (A) and top view (B) of a representative sample of unit 11 from a depth of 16.00 m (sample label: RW16.00), which highlights common clast types that are unique among the conglomerates. A side (C) and top view (D) of an argillic alteration feature sampled from unit 8 at a depth of 14.33 m (sample label RW14.33). Strong red-brown discoloration occur adjacent to zones of weaker, yellow discoloration. These zones consistently occur together in weakly concentric patterns; however, no central zone was observed.

The matrix material in unit 11 mainly comprises smectitic clay minerals, and a notably greater abundance of gypsum, anhydrite and pyrite than units 12 and 13 (Table 2.2). Anhydrite and gypsum are difficult to distinguish visually in BSE images. These phases have instead been identified using *p*XRD by the presence of a strong 7.61 Å peak indicating gypsum, and a small 3.50 Å peak indicating anhydrite; the results suggests that gypsum

may be the dominant sulfate phase. Glass clasts occur more frequently and are coarser ( $<10 - >100 \mu\text{m}$ ) in unit 11 than they do in units 12 and 13. Additionally, relatively intact  $\sim 20 \mu\text{m}$ -sized skeletal feldspar and bowtie-like feldspar spherulites occur in rare clusters scattered throughout the matrix (Fig. 2.9A). Coarse ( $>100 \mu\text{m}$  diameter) felsic crystalline clasts show a strong association with gypsum, anhydrite, pyrite and smectite at their borders, and sometimes throughout the internal fractures of the clast. Prominent peaks in the  $3.31\text{\AA} - 3.21\text{\AA}$  range suggest a greater accumulation of plagioclase and K-feldspar in unit 11 than unit 12. Other matrix minerals in unit 11 include rutile, apatite, ilmenite, barite, titanite and zircon.

The clay minerals comprising the matrix of unit 11 are mainly smectitic, and commonly exhibit a fluffy texture that occurs in the same form as in unit 12 (Fig. 2.9B). The fluffy texture of the matrix clay minerals is more distinct in closer proximity to void spaces, whereas clay minerals associated with tightly packed clasts tend to wrap around them. Clay minerals in the matrix also appear to have less clear association with clasts, and do not occur with clear nucleation points associated with clastic material as they did in units 13 and 12. While less prominent than the smectitic clays, and not observed in BSE imagery, illitic clay minerals and kaolinite are indicated by their characteristic  $d(001)$   $p$ XRD peaks in the  $<2 \mu\text{m}$  separates, as described for unit 13. Within the context of the conglomerates, the complexity of the clay mineral mixture increases with depth.

The sulfates and sulfides, comprised of primarily gypsum, anhydrite and pyrite, respectively, are prominent components of the matrix (Table 2.2). Pyrite occurs in three main settings: (1) as clusters of framboids occurring in voids, such as open cavities in the rock linear and voids that conform with the shape of the kink bands in micaceous clasts; (2) clusters of framboids surrounded by gypsum (Fig. 2.9C); and (3) individual cubic growths, which are scattered in close proximity to larger pyrite framboids. In addition to occurring in association with pyrite scattered in the matrix, gypsum commonly occurs as growths between kink bands of micaceous clasts. Pyrite and gypsum are commonly associated with one another and primarily occur as void fillings, occasionally in association with smectitic clay minerals.

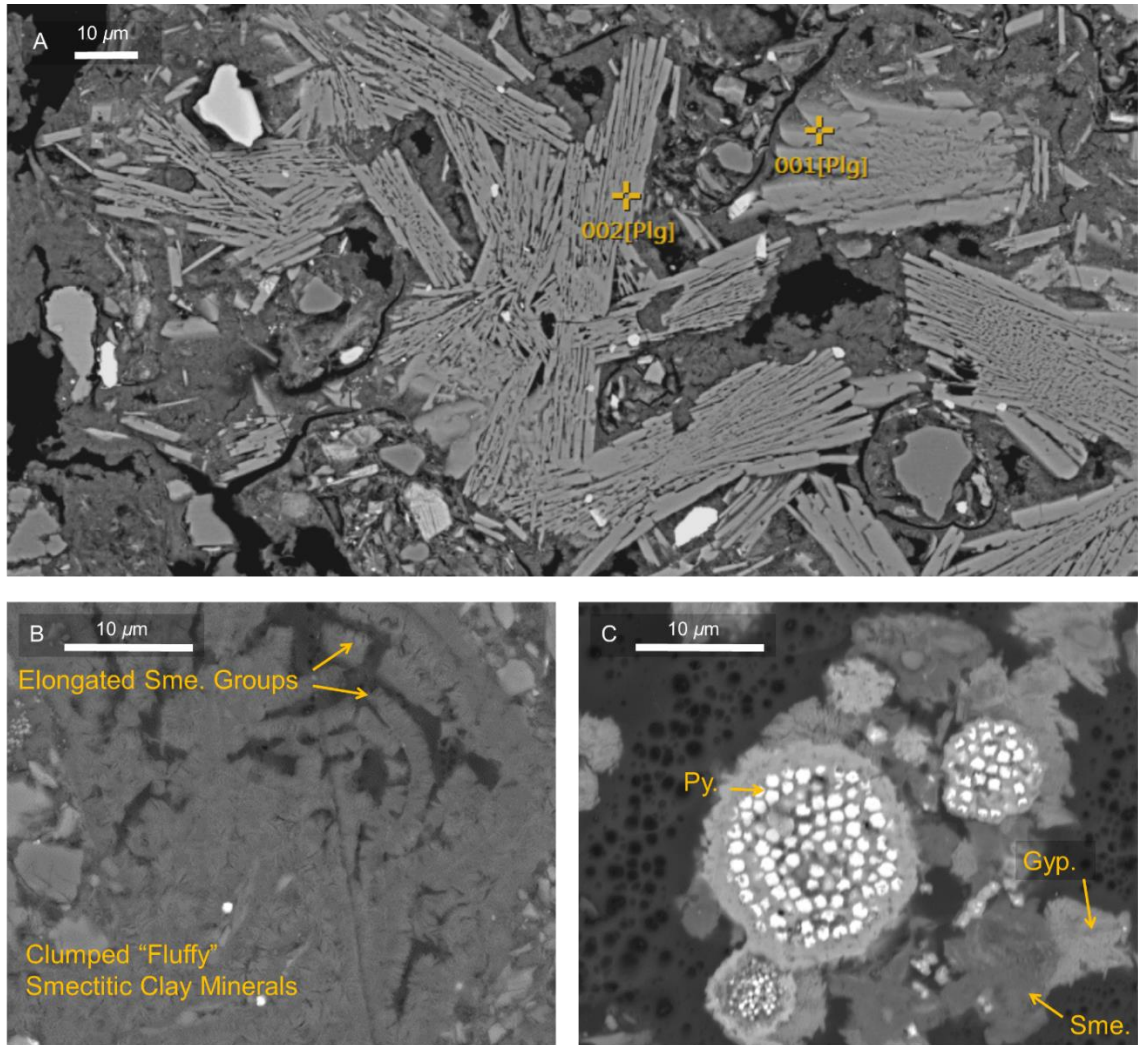


**Figure 2. 9:** BSE images from 14.33 m depth (sample label: RW14.33). (A) Back-scattered electron images from unit 8 depicting occurrences of feldspar bowtie-like spherulites. (B) Clumped and elongated groups of “fluffy” clay minerals. (C) Framboidal pyrite (Py.) is occurs here in voids in association with clumps of fluffy smectitic clays (Sme.), and gypsum (Gyp.).

### 2.4.3 Sandstone Units (13.1 – 10.7 m; units 10, 9 and 8)

The sandstone units include the two sandstones (units 10 and 8) and the sandstone conglomerate (unit 9). Transitions between the sandstone units and the adjacent marlstone and conglomerate units were not observed in this study. Generally, the colour and appearance of the conglomerate matrix and sandstone is consistent with that of the underlying grey conglomerates.

#### 2.4.3.1 Unit 10, sandstone A (13.1 – 13.0 m) and unit 8, sandstone B (11.6 – 10.7 m)

Units 10 and 8 are both massive sandstone units that host rare mm-scale lithic clasts, which are texturally and mineralogically similar enough to be described together. The mm-scale clasts consist of heavily fractured quartz and feldspar grains, and account for ~10% of the total volume of both units 10 and 8 (Table 2.2). The finer grained (a~10  $\mu\text{m}$ -scale material) clastic material in the matrix consists of a complex mixture of muscovite and chloritic mica clasts, heavily fractured quartz clasts, and K-feldspar and plagioclase. Other, less common 10  $\mu\text{m}$  clastic material includes ilmenite, apatite, beryl, rutile and zircon (Table 1). Glass clasts and spherulites observed in the conglomerates (units 11 – 13) are absent in these sandstone units. Gypsum and pyrite occur in similar settings described in unit 11; however, pyrite and gypsum appear to be relatively minor components of these sandstone units, cumulatively comprising ~2% of the overall composition. Smectitic clay minerals make up the main matrix mineralogy with illite and kaolinite comprising ~35% of the clay minerals. These sandstones exhibit less porosity than the conglomerates (units 13 – 11) and unit 9 (porosity was determined by qualitative observations from BSE imagery; porosity data for drill core above ~17 m was not documented in Förstner (1967)). As such, mineralization associated with voids such as ferroan dolomite, some clay mineral occurrence styles and some pyrite occurrence styles is less common. Unit 8 can be distinguished from unit 10 by the gradual reduction in the commonality of mm- scale grains and a subtle overall reduction in grainsize as depth decreases, suggesting that unit 8 exhibits subtle normal grading.

#### 2.4.3.2 Unit 9, sandstone conglomerate (12.8 – 11.6 m)

Unit 9 is a poorly sorted conglomerate that is distinguished from the basal conglomerate unit group (units 13–11) by the occurrence of rounded, > 1 cm diameter lithic clasts comprised of massive, marly sandstone (Fig. 2.10A), and its stratigraphic position between two units of massive sandstone. Conversely, the matrix material of unit 9 is petrographically similar to that of units 13–11 with the notable exception of the phyllosilicate mineralogy comprising the matrix (Table 2.2). Smectitic clay mineral diffractions are muted and illite 001 diffractions are sharper and exhibit greater intensities. Kaolinite d(001) and d(002) diffractions also exhibit greater intensities. K-saturated samples of unit 7 exhibited a broad 14.69 Å peak after heating at 107 °C, indicating incomplete collapse of the smectitic clay mineral structure, and therefore, the likely presence of mixed layering in this phase. Matrix material and the >100 μm-scale clasts exhibit similar textures and mineralogy to that of units 13–11 with the exception that >100 μm-scale micas are more common.

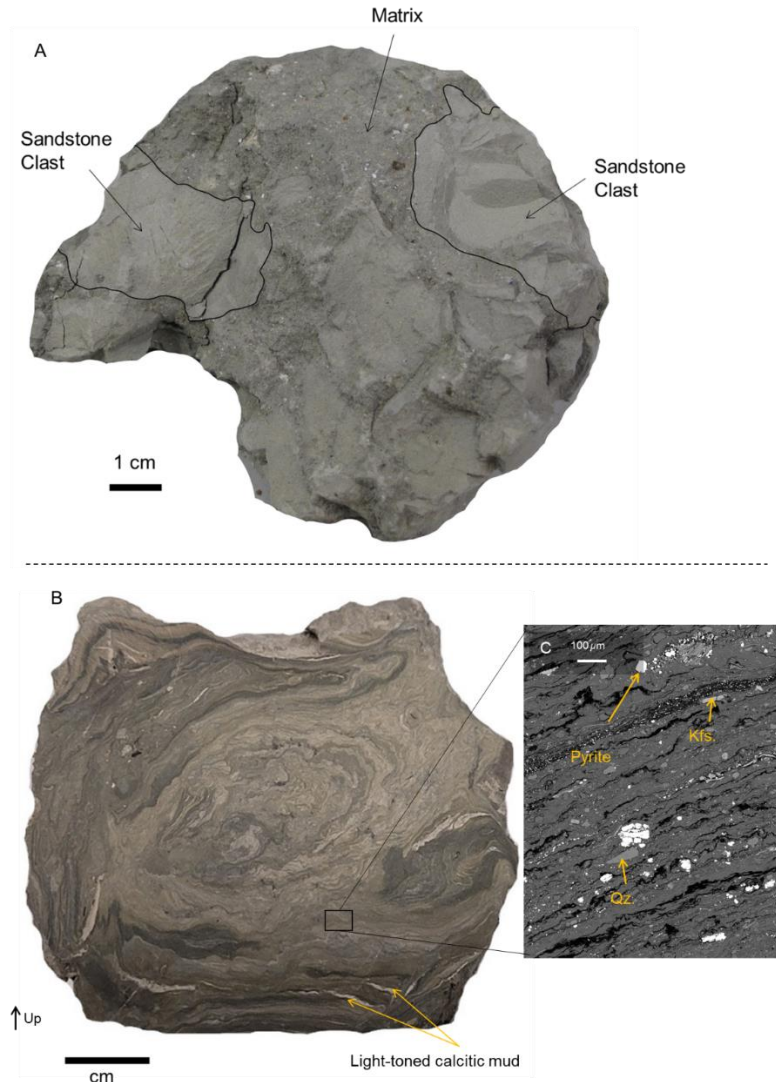


**Figure 2. 10:** (A) Core sample of unit 9 from 12.74 m depth (sample label: RW12.74) where examples of sandstone clasts are outlined. (B) Core sample of unit 4 from 10.55 m depth showing chaotic lamination (sample label RW10.55). (C) Back-scattered electron image shows preferential orientation of clasts within the roughly linear voids and the occurrence of framboidal pyrite within them. The layers consist mainly of clay minerals.

#### 2.4.4 Marlstones and Limestones (10.7–2.0 m; units 7, 6, 5, 4, and 3)

Units 7–3 are distinguished from one another based on changes in the abundances and types of carbonate minerals, and the prevalent sedimentary structures. Units 7, 4 and 3 are each clay-rich, calcitic marlstones with striking convoluted lamination (Fig. 2.10A). Unit

6 is a mixture of dark grey rock that contains embedded plant matter and exhibits chaotic, pseudo-convoluted lamination with a light-toned calcitic rock that has faint mudcracks and wavy, sub-parallel laminations. Unit 5 is comprised of mainly aggregated silt-sized dolomite particles with some clay minerals and rare root fossils. These units are described in detail below.

#### 2.4.4.1 Units 7, 4, and 3, convoluted marlstones A (10.7–10.0 m), B (8.2–3.0 m) and C (3.0–2.0 m), respectively

Units 7, 4 and 3 each exhibit continuous, finely laminated, convoluted bedding structures (e.g., Fig. 2.10B) and disjointed layers of light-toned, calcitic mud occur as rare discontinuous features. The convoluted marlstones are comprised primarily of illitic clay minerals and kaolinite and a mixture of dolomitic and calcitic carbonates. Fine sand-sized clasts in this section consist of mainly K-feldspar, quartz and micas (Table 2.2). These clasts are generally angular to sub-rounded and are aligned along their long-axes with the chaotic bedding and flow textures. Pyrite occurs in abundance along bedding-parallel linear voids and fractures. Pyrite also occurs between bands of kink-banded micaceous clasts in a similar fashion as in units 13, 12 and 11 (Fig 2.10B).

Unit 3 is distinct from units 7 and 4 in that the color of the matrix is light-brown as opposed to the light-grey in the units 7 and 4. This change can be attributed mainly to changes in the dominant matrix mineralogy of the matrix. Units 7 and 4 exhibit stronger 12.5 Å peaks in bulk *p*XRD patterns and host a greater number of feldspars than unit 3. Unit 3 exhibits stronger quartz peaks than unit 7 and 4, which suggests that swelling clay minerals and their common precursors are less prominent. Units 7 and 4 are mineralogically consistent with one another and each exhibit the same sedimentary structures, but are distinguished by their stratigraphic position.

Förstern's (1967) original description of this material includes mention of wavy, alternating limestone / mudstone that was not observed here. Presumably, this alternation is consistent with the observations described in unit 6 below, where alternating light- and dark-toned material with different textures is described. Instead of omitting their presence entirely due to a lack of observation, we assume, based on Förstern's (1967) observations,

that the light-toned limestone layers are less prominent and less common than they are in unit 6.

#### 2.4.4.2 Unit 6 mixed grey dolomite / calcite marlstone and white calcitic limestone (10.0 – 8.6 m)

Unit 6 is a mixture of two different rock types that do not have a clear textural association with each other as contacts between them were not observable in the remaining rock chips available for study. Approximately 70 % of the available material was comprised of a dark-grey toned marlstone with chaotic bedding and scattered clasts of micaceous material. The remaining 30 % is comprised of a white-toned limestone with mudcracks and wavy, sub-parallel lamination.

*Grey-toned dolomite / calcite marlstone:* The grey-toned material in unit 6 is a clast-supported marlstone (15–20 % carbonates) with fine, sand-sized ( $> 100 \mu\text{m}$  scale) mica and sub-rounded to sub-angular dolomite nodules comprising the dominant clastic phases. Unit 6 displays convoluted bedding, but the laminations are commonly discontinuous and disjointed, which is associated with the occurrences of broken and fractured clasts of mica. When crushed and sonicated, bark, stems and other plant debris are exhumed from the rock; however, this plant matter was not observed in further petrographic studies of this unit. The  $> 100 \mu\text{m}$ -scale mica clasts are primarily muscovite with minor biotite and chlorite occurrences (Table 2.2), and exhibit prominent kink-banding (Figs. 2.11A, B). The spaces between the disassociated layers of the kink-banded micas are filled with matrix material (Fig. 10C). The  $> 100 \mu\text{m}$  dolomite particles consist of aggregates of many euhedral dolomite rhomboids, merged together at their crystal boundaries (Figs. 2.11A, B). The matrix is comprised of a complex mixture of mainly  $<10 \mu\text{m}$ -sized muscovite and biotite, sub-rounded calcite clasts, sub-rounded dolomitic clasts, framboidal pyrites, and gypsum. Feldspars are rare, but do occur in the matrix as  $<10 \mu\text{m}$ -sized subhedral grains with sharp grain boundaries.

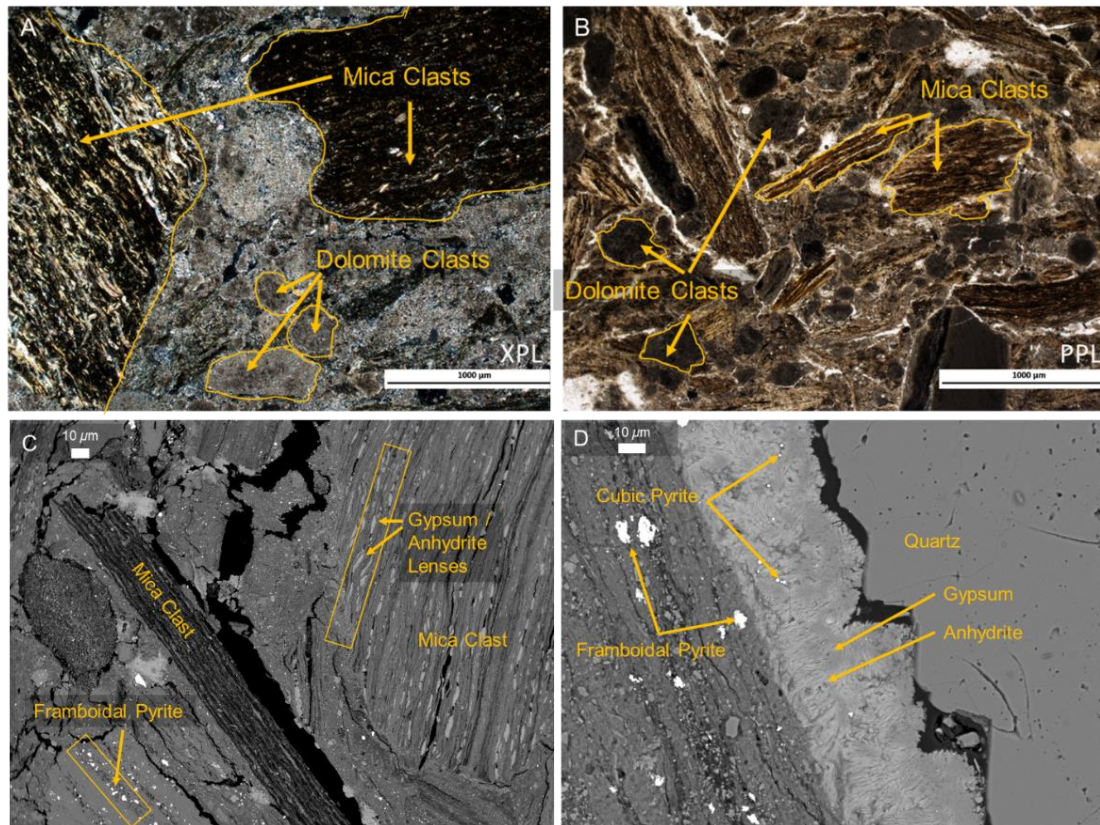


**Figure 2. 11:** (A) Cross-polarized(XPL) and (B) plane-polarized (PPL) optical microscope images of thin-section samples of unit 5, at 9.6 m depth (sample label RW9.6-Gry.). Highlighted in both XPL and PPL photomicrographs are examples of the two major clast types: micaceous and dolomitic. (C) Gypsum, anhydrite and pyrite occur as intergrowths between layers of  $>100\ \mu\text{m}$  scale mica clasts and conform to the shape of the layers. (D) Gypsum and pyrite also occur in linear voids in the matrix and bordering quartz and feldspar grains. Gypsum occurs together with anhydrite around the border of a quartz grain. Gypsum is represented by the slightly darker toned material and is bound by fibrous growths of likely anhydrite (slightly lighter tone). Gry. = grey toned material.

Pyrite and gypsum in the dark-toned material of unit 6 occur in similar settings as described in unit 11, with some exceptions. In addition to the three formation settings described in unit 11, pyrite in unit 6 also occurs as clusters of framboids within sand-sized dolomitic clasts and as clusters of framboids in linear voids that conform with the shape of the kink bands in sand-sized micaceous clasts. While the occurrences of pyrite and gypsum

do appear less common in the marlstone units than in the reworked breccias, they are nonetheless present in similar settings (Figs. 2.11C, D).

Gypsum and anhydrite occur in a similar arrangement to pyrite in that these phases conform with the kink bands of micaceous material, but tend to form as lenses in this setting. In many instances it is difficult to determine whether the observed sulfate is gypsum or anhydrite using BSE images. A strong 3.51 Å peak indicating anhydrite and muted 7.56 Å peak indicating gypsum are used to infer the presence of both minerals. Gypsum and anhydrite also occur extending out from the mixed phyllosilicates in the matrix towards the boundaries of quartz grains, creating a partial rim around the grain (Figs. 2.11D).

Micas and clay minerals are the most abundant minerals in the dark material of unit 6. Clay minerals make up the interstitial material. *p*XRD of preferentially oriented <2 μm separates indicates that the interstitial clay minerals are largely kaolinite and illitic clay minerals, with less prominent smectitic and chloritic components. The sharpness of the 10 Å feature in the *p*XRD scans of preferentially oriented <2 μm separates may suggest that, in addition to illite, muscovite is also likely a component of the clay-sized material.

*White calcitic limestone:* The white calcitic limestone is comprised mainly of muddy layers with wavy, sub-parallel lamination (Fig. 2.12A) and mud cracks (Fig. 2.12B). The muddy layers are structurally distinct and can be generally divided into light- and dark-grey layers, which exhibit wavy structures (Fig. 2.12A), and white-toned layers that exhibit fracturing and faulting (Fig. 2.12A). Clear load structures occur as partially and fully detached intrusions of material into adjacent tonally distinct layers. The tonally distinct layers have varying clay mineralogy and carbonate abundances associated with the colour changes. Dark grey layers are generally dominated by smectitic and kaolin clay minerals and light grey layers are generally dominated by similar clay minerals, but calcite occurs as a more prominent phase. The white-toned material is comprised of a mainly calcite-dominated mud. Generally, framboidal pyrite occurs as clusters within calcitic layers and intrusions of more calcite dominant material into the dark grey layers. Feldspars and quartz minerals are broadly distributed throughout the tonally distinct layers but are rare.

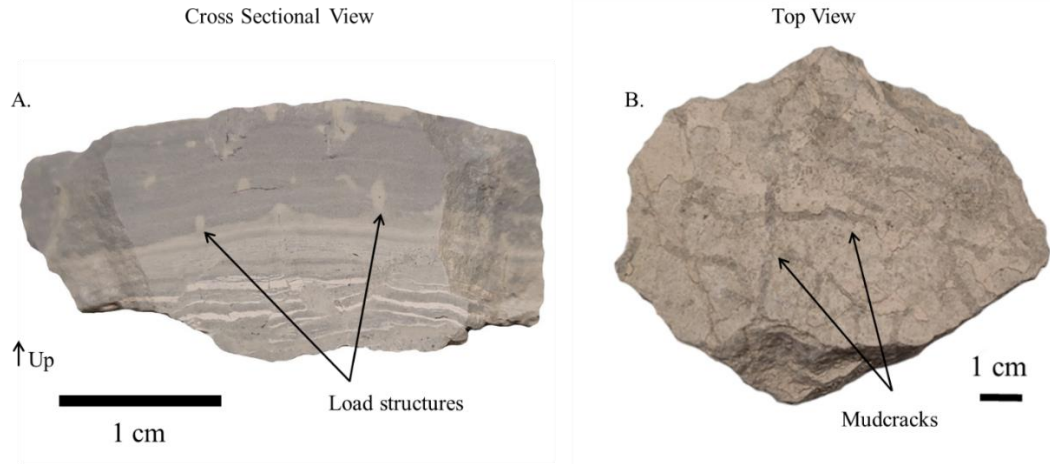


**Figure 2. 12:** Cross sectional (A) and top view (B) of the white-toned material from unit 6 at 9.6 m depth (sample label: RW9.6-Wht.) . (A) Sub-parallel layering and load structures . (B) Pseudo-polygonal mudcracks. Wht. = white toned material.

#### 2.4.4.3 Unit 5, dolomite packstone (8.6 – 8.2 m)

Unit 5 is predominantly (~85 %) comprised of allochems made up of dolomite (Table 1). The allochems are fossiliferous; however, their recrystallized nature impedes accurate identification. Branching tubes with ranging diameters (50 – 150  $\mu\text{m}$ ) and internal veneers of euhedral dolomite rhombs are consistent with descriptions of cladophorites described in Riding (1979), which are common components of bioherms hosted at the Ries impact structure (e.g., Riding 1979; Jankowski 1981). These organisms are proposed to have played a major role in building the bioherms around the Ries structure (Riding 1979). Clay minerals occupy some intergranular spaces between the dolomitic allochems and comprise a mixture of illite and kaolinite. Pyrite was observed as clusters of framboids with a seemingly random distribution throughout the unit. Calcite and quartz were not directly observed using optical microscopy, SE imagery or BSE imagery, but their presence was inferred through the appearance of diagnostic peaks at 3.343 Å (quartz) and 3.02 Å (calcite) in bulk XRD patterns.

#### 2.4.5 Mudstones (3.0 – 0 m; units 2 and 1)

Units 2 and 1 are mudstones, which are distinguished by the prevalence of kaolinite (Table 2.2), and a poorly sorted mixture of silt and sand-sized particles. In both units, the

clastic material is comprised of plagioclase and potassic feldspar, muscovite and quartz. There is a notable change in the color and grain size in unit 2, which has a light-brown tone and some rare well-rounded gravel sized clasts. Unit 1 is texturally similar to unit two but lacks any gravel-sized clasts and has a dark brown tone. These units are further distinguished from the rest of the drill core by the prominence of calcite, which is indicated by a 3.03 Å calcite peak observed in XRD patterns. Calcite peaks are prominent in unit 2, but muted and difficult to distinguish in unit 1. The presence of calcite in the mudstones also marks a major overall shift in the dominant carbonate mineralogy away from dolomite, which was predominant throughout units 10 – 3.

## 2.5 DISCUSSION

### 2.5.1 Comparison with previous work

The Wörnitzostheim drill core was first studied by Förstner (1967) who focused on the mineralogy of the impact melt-bearing breccias. While Förstner's (1967) log did cover the transition from post-impact sedimentary deposits to impact melt-bearing breccias, the nature of this transition was not discussed in detail. The present work thus represents the first detailed study of the transition from post-impact sedimentary deposits to impact melt-bearing breccias. While some notable differences exist between our work and Förstner's (1967) log (Fig. 2.13), some of Förstner's (1967) data regarding the approximate extent of the units was used to fill in gaps in the record where material was missing from the drill core. Mainly, Förstner's (1967) assays were used to determine the extent of units 10 – 8, and 4 (Fig. 2.2) because the contacts associated with these units were not preserved in the drill core.

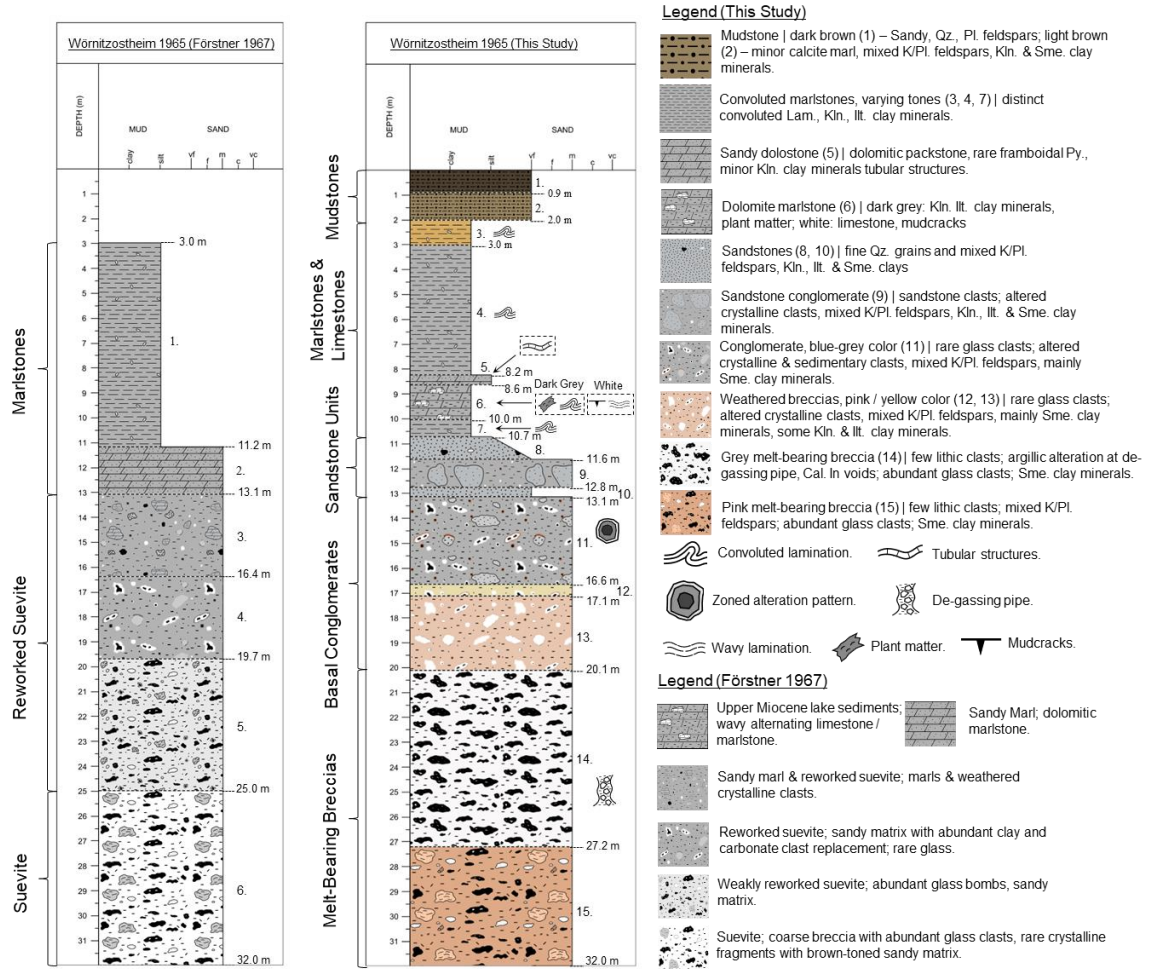


**Figure 2. 13:** We produced a graphical representation of the upper 32 m of the Wörnitzostheim 1965 drill core based on the descriptions in Förschner’s (1967) original log (left) and provided our original log (right) for comparison. The log generated as part of this study (right) was not based on Förschner’s (1967) work, but represents an entirely separate, assessment of the drill core. Förschner’s (1967) log is subdivided into six main units: (1) Upper Miocene Lake Sediments (3.0–11.2 m), (2) Sandy Marl (11.2–13.1 m), (3) Sandy Marl and Reworked Suevite (13.1–16.4 m), (4) Reworked Suevite (16.4–19.7 m), (5) Weakly Reworked Suevite (19.7–25 m), and (6) Suevite (25 – 32m).

The most apparent difference between this work and the work of Förschner (1967) is the inclusion of multiple new sub-units, such as the material logged from 0 m to 3 m (units 1, 2 and 3), which was not included previously. The Upper Miocene lake sediments (3.0–11.2 m) from Förschner’s (1967) log are consistent with the marlstone units of this study. We

divided the marlstone unit into five sub-units based on textural differences described earlier: unit 3 (2.0–3.0 m), unit 4 (3.0–8.2 m), unit 5 (8.2–8.6 m), unit 6 (8.6–10.0 m), and unit 7 (10.0–10.7 m). An additional discrepancy exists in the depth extent of the marlstones (2.0–10.7 m) when compared to Förstner's (1967) Upper Miocene lake sediments (3.0–11.2 m). This difference exists due to the reallocation of material originally included in Förstner's (1967) Upper Miocene lake sediments (10.7–11.2 m) to the sandstones and sandstone breccia units in this study (Fig. 12), and the inclusion of previously unlogged material from 2.0 m to 3.0 m.

The sandy marl unit (11.2–13.1 m) in Förstner's (1967) log is consistent with the sandstones and sandstone breccia units of this study, with the additional documentation of massive sandstone units overlying (unit 8: 10.7–11.6 m) and underlying (unit 10: 12.8–13.1 m) sandstone conglomerate (unit 9: 11.6–12.8 m). Material from 10.7 m to 11.2 m was originally included in the upper Miocene lake sediments unit of Förstner's (1967) but has been reallocated here to the massive sandstone that comprises unit 8. The reallocation of this material in this interval is due to the textural and mineralogical similarities between it and unit 10. Both are comprised of massive sandy material made up of fine, ~10  $\mu\text{m}$ -scale, clastic material that consists of muscovite and chloritic clasts, quartz, and K-feldspar and plagioclase. Unit 7 is texturally and mineralogically similar to the conglomerates in this study (units 13–11) but it was not included in that grouping due to the overlying and underlying sandstone units, and the prominence of cm-scale, marly sandstone clasts.

Förstner (1967) describes three units comprised of "reworked suevite". "Reworked suevite" is a term coined seemingly during the 1960's and 1970's and it is used in several early Ries publications (e.g., Förstner, 1967a; Jankowski, 1977; Stöffler et al., 1977), although its precise origins and meaning is unclear. Its use suggests that it indicates a sedimentary rock that formed from the reworking of impact melt-bearing breccias, presumably through fluvio-lacustrine processes in the Ries basin (e.g., Förstner, 1977, 1967; Füchtbauer et al., 1977; Jankowski, 1977, 1981). The term "reworked suevite" was not used in the present study to avoid assumptions regarding provenance of the sedimentary rocks studied here. The units in Förstner's (1967) log that include "reworked suevite" are: "sandy marl and reworked suevite" (13.1–16.4 m), "reworked suevite" (16.4–19.7 m), and

“weakly reworked suevite” (19.7–25.0 m). The extent of the three “reworked suevite” units from Förstner’s (1967) log refers to most of the same material described in the basal conglomerate unit group of this study, which we have divided into three sub-units: unit 11 (13.1–16.6 m), unit 12 (16.6–17.1 m), and unit 13 (17.1–20.1 m). Förstner’s (1967) log suggests a much deeper extension of the “reworked suevite” (25.0 m) than our study (20.1 m). Our reasoning for this deviation is that the material at 22.0 m depth (e.g., unit 11; 20.1–27.2 m) is petrographically consistent with descriptions of impact melt-bearing breccias elsewhere at the Ries and exhibits similar alteration patterns (e.g., Caudill et al., 2021; Engelhardt et al., 1995; Osinski et al., 2004). Glasses in unit 14 (grey melt-bearing breccia) are typically >100  $\mu\text{m}$ -scale clasts, exhibit distinct flow textures and bear similar mineral associations to the suevite described in Osinski et al. (2004). Glass clasts in unit 14 are associated with calcitic vesicle fillings and globule formations of clay minerals that rim glass clasts and line vesicles. Primary plagioclase crystallites in unit 11 also occur in the groundmass and in the glasses, as documented in Osinski et al. (2004). We further distinguish unit 14 from the basal conglomerates in that the predominant carbonate phase in the conglomerate units is dolomite in contrast to calcite (Table 1), which is the most common carbonate in the grey-toned melt-bearing breccias (unit 14). In addition, occurrences of glass are rare in the conglomerates, whereas they are common in the melt-bearing breccias. There is also a notable difference in how frequently > 100  $\mu\text{m}$  sized clasts occur between the melt-bearing breccias and the conglomerates. Clasts on > 100  $\mu\text{m}$  occur more frequently in the melt-bearing breccias than they do in the conglomerates. Finally, the dominant mineral phase in the matrix of the conglomerates varies between the sub-units, ranging from mainly smectitic to mixed smectitic, kaolinite and illitic clay minerals, whereas the matrix of the melt-bearing breccias is consistently comprised of smectitic clay minerals.

Lastly, we distinguished two types of impact melt-bearing breccias (unit 14: 20.1–27.2 m and unit 15: 27.2 m – end of log) based on the dominant composition of the matrix material and the clasts. This contrasts with the single type of impact melt-bearing breccia allocated for this section of drill core in Förstner (1967). Unit 15 (pink-toned melt-bearing breccia), while still clearly a melt-bearing breccia, displays some notable petrographic distinctions from unit 14 (grey-toned melt-bearing breccia) and the surficial suevite

documented in Osinski et al. (2004). First, the matrix of unit 15 is more uniformly smectitic and clearly exhibits honeycomb textures that are not found in unit 14. Second, Fe-carbonates occur more frequently in unit 15 as zoned, euhedral vesicle fillings (Fig. 3B). Third, *p*XRD patterns indicate a far more quartz and far less calcite in unit 15 relative to unit 14. The greater diversity of clay mineralogy and textures, and the presence of alteration features such as degassing pipes, suggest that unit 14 may be more altered than unit 15. Accordingly, units 14 and 15 should be treated as distinct from one another.

## 2.5.2 Post-impact sedimentation and environmental record

### 2.5.2.1 Topography, and sources of water

The high topographic setting of the units studied here relative to the main series of lake deposits within the central basin of the Ries impact structure suggest that water sources would have been more limited, and that the timing of lacustrine formation recorded by the sedimentary record of the Wörnitzostheim drill core could differ from that of the Nördlingen 1973 drill core, which sampled the central basin. Indeed, it could be possible that isolated bodies of water existed prior to the formation of a large contiguous lake system. Influx of water at the site of the Wörnitzostheim drill core could have been less immediate than it was within the central basin, and different sources of water could have dominated in different regions of the impact structure. Possible sources of water to consider include rainwater, groundwater recharge, and fluvial influx. The main source of water may vary for each of the units described in this study.

### 2.5.2.2 Deposition of the basal conglomerates (units 13 – 11: 20.1 – 13.1 m)

As discussed above, the conglomerates (units 13–11) show signs of mechanical reworking and likely represent the earliest post-impact sedimentary deposition at the Ries, as recorded by the Wörnitzostheim drill core. The transitions between the individual conglomerate units are gradual (Fig. 2.2). The relatively consistent clast mineralogy of specifically units 13 and 12 (K-feldspar, plagioclase, micas, quartz and impact glass) in conjunction with the gradual transition between units suggests they formed from continuous sedimentation of material derived from local impact melt-bearing breccias.

Melt-bearing breccias at the Ries are known to host a small amount (0.4% volume) of sedimentary clasts (Engelhardt, 1997), but 1–4 cm-sized sedimentary clasts occur in unit 11 at a greater (~15 % volume) abundance, which suggests a slightly different, but still local, sediment source than units 13 and 12. The Bunte breccia is a local impact generated breccia which hosts sedimentary clasts (Hörz, Ostertag and Rainey, 1983) and as such, it likely comprises an additional source for clastic material comprising unit 11 (Fig. 2.1). Unit 11 also includes coarse ( $>100\ \mu\text{m}$ ), fresh glass clasts and spherulites (Fig. 8A) derived from the melt-bearing breccias (Fig. 5B, C). While the poor sorting and cm-scale clasts throughout all basal conglomerate units suggests deposition in relatively high energy environments, the greater consistency of  $>100\ \mu\text{m}$ -scale clast occurrences, and the inclusion of clasts up to 4 cm in diameter suggests that unit 11 formed in a higher energy environment than units 13 and 12. As opposed to a Bunte breccia sediment source, unit 11 might represent debris or gravity flow deposition from an outlet breach or overflow flood originating from the central basin. This could provide an alternate explanation for the occurrence of parallel laminated sedimentary clasts, and the general increase in clast size exhibited by unit 11 relative to units 13 and 12; however, this would require an additional focused study to clarify. Considering the commonality of cm-scale clasts in all conglomerate units, in conjunction with the local sediment source, matrix supported nature and nearby topographic highs of the uplifted crystalline ring and the tectonic outer ring of the impact structure, we suggest that the conglomerates (units 13 – 11) likely represent a debris flow or gravity flow of sediment.

The subtle differences in depositional environments between units 13, 12 and 11 are reflected in their micro-scale textures and mineralogy. The well-formed honeycomb texture of the smectitic clay minerals comprising the matrix of unit 13 and their nucleation association with feldspars, micas and impact glass, could indicate that they are primarily authigenic matrix minerals, which precipitated *in situ* from fluids associated with dissolution of feldspars, micas and glass. The densely packed “fluffy” textures of the smectitic clay minerals comprising the matrix of units 12 and 11, and relatively few occurrences of clear nucleation points associated with clastic material, suggests that this matrix material may not be entirely authigenic. The tight packing of the smectitic clay minerals between clasts suggests compaction by settling sediment, which implies a degree

of mechanical reworking, and hence a mixed detrital and authigenic origin. Additionally, by virtue of being matrix supported, the matrix of the conglomerates would have to at least partially consist of detrital clay minerals.

The authigenic clay minerals comprising the matrix of the lower reworked breccia (unit 13) likely formed from a potassium-rich, alkaline fluid derived from K-bearing source materials (K-feldspar, impact glass and muscovitic micas). The presence of alkaline fluids is consistent with interpretations from the Nördlingen 1973 drill core, such that the early stages of the Ries lake system were alkaline with generally low salinity (Füchtbauer et al. 1977; Jankowski 1977, 1981; Arp et al. 2013a). The prevalence of smectitic clay minerals in the basal conglomerates is also consistent with alteration of fine-grained, highly shocked and glassy material in mildly alkaline environments (Bohor and Triplehorn, 1993). This further suggests that the basal conglomerates (units 13–11) represent early post-impact sedimentary deposits; subaerial debris flows which later flooded triggering the formation of authigenic clay minerals.

The increase in the abundance of framboidal pyrite (from <10% in units 13 and 12 to ~10–12 % in unit 11) in unit 11 (Table 1) indicates that substantial sulfur was introduced to the system. Sulfur could have been leached from the sedimentary rocks present in the breccia during weathering or hydrothermal alteration, and / or derived from dissolved organic matter originating from an overlying lacustrine system that travelled downwards in supergene fluids through fractures and voids. In the former scenario, the pervasive mineralization of gypsum and clay minerals throughout unit 11 would require the presence of fluid during deposition of the unit. In the latter scenario, the close relationship between framboidal pyrite, gypsum, anhydrite and void spaces suggests pyrite formation from the reduction of gypsum and anhydrite, which itself formed from fluids traveling through the voids in unit 11 after the breccias had been deposited. We suggest that the presence of a strongly reducing environment led to formation of these framboidal pyrites following deposition of unit 11.

### 2.5.2.3 Deposition of the sandstones and sandstone conglomerate (units 6 – 3: 11.6 – 3.0 m)

We interpret the changing grain-size of the sandstone units (Fig. 2.2) to reflect subtle normal grading that was truncated by an abrupt increase in depositional energy, which produced the sandstone conglomerate (unit 9, Fig. 2.10) bound between the two sandstone units. We interpret the normal grading of the sandstones to indicate progressive aggradation of the alluvial fan, as the basin backfilled with sediment and the crater lake level began to rise. Reverse grading would be expected during normal alluvial aggradation; however, the backstepping of the alluvial fan would result in the normal grading observed in unit 8. Flooding or shifting of the alluvial fan surface during alluvial progradation might have deposited the sandstone conglomerate (unit 9). The grain-size and mineralogy of the marly-sandstone clasts in unit 9 is similar to the sandstones comprising units 8 and 10 (micas, feldspars and quartz clasts with a kaolinite and illitic clay mineral-dominated matrix). Due to this similarity, we suggest that the marly-sandstone clasts in unit 9 were derived from unit 10. The changing dominant clay mineralogy from smectitic in the conglomerates to illitic and kaolinitic in the sandstone and sandstone conglomerate, in addition to the absence of glass clasts and the prominence of feldspars, quartz and micas comprising the clastic material, points to a changing sediment source. Material from increasingly distal locations may have been delivered as the lake system evolved. Sources such as melt-poor impact breccias like the Bunte Breccia or crystalline breccias are likely possibilities.

### 2.5.2.4 Deposition of the marlstones (units 6 – 3: 11.6 – 3.0 m)

The prevalence of kink-banded micas (Fig. 10A, 10B) and illite- / kaolinite-dominant clay mineralogy points to a sediment source that is comprised largely of melt-poor material and that is similar to the source for the sandstones and sandstone conglomerate. This is consistent with the sediment source shifting slightly from the impact melt-bearing breccias to nearby Bunte Breccia ejecta deposits.

The fine grain-size (Fig. 2.2) and the fine laminations (e.g., Fig. 2.10B, C) in units 7, 6, 4 and 3 point to deposition in a low energy environment. The presence of the carbonates comprising the marl sequence could be explained by deposition in a swampy environment where there was a sufficient quantity of aquatic plants to shift the bicarbonate / carbonate

equilibrium towards carbonate through the removal of CO<sub>2</sub> from the water (Boyd, 2015). Plant matter recovered from unit 6 indicates that the presence of aquatic plants is plausible. Another possible explanation for the presence of dolomite and calcite is the incorporation of detrital calcite from the mechanical weathering of proximal impact melt-bearing impactites. Given the close proximity of melt-bearing impactites, and the presence of plant matter, it is plausible that a combination of biologically driven and geologically driven processes led to the deposition of detrital calcite and possibly both detrital and endogenic dolomite in these units; however, dolomite appears to be mainly endogenic.

The convoluted lamination that is prevalent throughout units 7, 6, 4 and 3 can be explained by the gradual slumping of sediment away from the shoreline during post-impact settling and lake infilling. Sediment loading during rapid lacustrine deposition could have produced enough weight to fracture underlying layers before the sediment layers fully lithified. The presence of rare broken mud layers (Fig. 2.10A) indicates that these internal structural failures may have allowed the larger scale partial fluidization and movement of already deposited layers of soft sediment. Similar sedimentary structures produced by slumping have been observed in the Nördlingen drill core (Mertes, 1977).

Due to the preserved plant matter in the dark-toned material in unit 6, we attribute the fracturing and breaking of the convoluted laminations to bioturbation (Fig. 2.11A, B). While there were no fossils directly observed in thin section or under BSE or SE imagery, it could be possible that the dolomitic clasts originated as calcitic growths around fossiliferous nuclei. Fluids carrying cations from Fe-bearing detrital micas possibly led to the subsequent dolomitization. Additionally, the abundance of gypsum between kinked bands of mica (Fig. 2.11C) and between clasts (Fig. 2.11D) points to an increased sulfur content, potentially due to sulfur uptake and concentration by plants. Many plants would have died off during periodic desiccation of the lake, which would have concentrated sulfur in the soil to be available for gypsum mineralization during subsequent wetting periods.

The consistent wavy layering and mud cracks in the calcitic light-toned material of unit 6 suggest that the otherwise swampy lake exhibited a dry period with low deposition rates, which prevented convoluted lamination from forming and caused the formation of mud cracks (Fig. 2.11B) through desiccation. The desiccation and differential loading could

have caused compression fracturing of the mud layers and enabled intrusions of less dense material to migrate into adjacent layers, forming load structures (Fig. 2.12A). Due to the prevalence of convoluted lamination and the presence of fractured, light-toned layers, we interpret the wavy lamination in this unit to be a product of soft sediment deformation caused by differential loading and partial liquefaction as opposed to a primary depositional feature.

The tube structures in unit 5 are mineralogically and texturally consistent with other cladophorite fossil-bearing dolomite packstones around the Ries that are indicative of the transition from a saline to an increasingly fresh lake environment (Arp, 1995, 2006; Arp et al., 2017). The occurrence of this dolomite packstone in local alternation with marlstones bearing polygonal mudcracks suggests that unit 5 represents a lithostratigraphic level equivalent to the Aldesberg-type bioherms described in Arp (1995, 2006), which represent a shallow eulittoral environment and the earliest known algal bioherms of the Ries basin. Alternatively, the tube structures could also represent root networks of aquatic plants as documented elsewhere at the Ries (Arp 1995, 2006), but would similarly indicate eulittoral, shallow water environments (Arp 1995, 2006). With the data presently available, it is unclear which interpretation of the tube structures is the most accurate; whoever, in either case, a shallow eulittoral environment is likely what is represented by unit 5.

#### 2.5.2.5 Deposition of the mudstones (units 2 and 1: 3.0 – 0.0 m)

The distinct mineralogical characteristics of the mudstone units and the change in major carbonate species from dolomite to calcite sets them apart from the other post-impact sedimentary deposits (marlstones, sandstones and sandstone conglomerate, and basal conglomerates) described above. Given the limited amount of sample and contextual information for the mudstone units, it is difficult to suggest a possible origin with confidence. Additionally, without observable contacts and with a distinct shift in mineralogy, and possible sediment source, it is possible that these units represent Quaternary material that was deposited following the erosion of the upper ~50 m of lake deposits towards the end of the Ries lake's lifecycle; however, this cannot be stated with certainty.

### 2.5.2.6 Depositional Environment Summary

The transition between the basal conglomerates, sandstone units, and marlstones and limestone units likely represent the transgression of the lake shoreline (Fig. 2.14). The mudstones are excluded from this interpretation owing to the lack of data available. The early, water-laden debris flows likely represented by the conglomerates could be the early stages of alluvial deposition and the beginnings of fluviolacustrine infilling. The formation of a lake system is represented by marlstones and limestones. The mud cracks potentially represent desiccation in either the shoreline or potentially the entire body of water. The dolomite packstone overlying these marlstones likely represents a shallow eulittoral environment, and the marlstones that subsequently overly it represents the landward transgression of the shoreline as the lake buried the packstone under deeper water sediment.

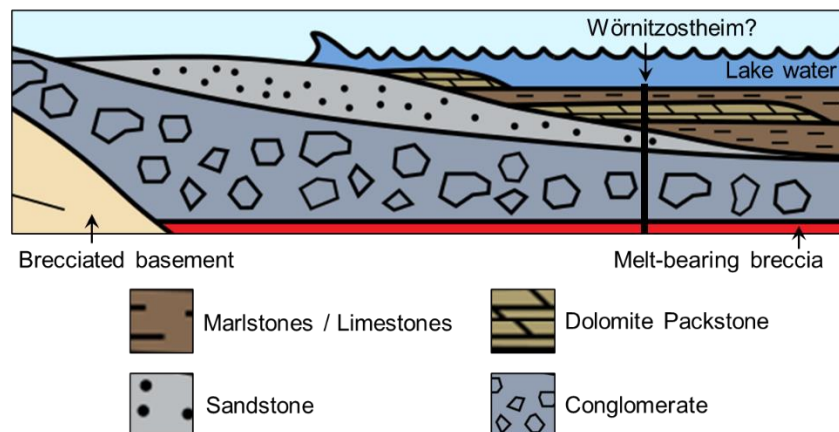


**Figure 2. 14:** A diagram illustrating the likely deposition environment represented by the Wörnitzostheim drill core. Key units are summarized here, with the potential units sampled by the Wörnitzostheim drill core indicated on the diagram. Although depicted as the bottom-most unit here, melt-bearing breccia can drape over some lithologies (Pohl 1977), and as such this illustration does not preclude the possibility of melt-bearing breccias comprising the source of the conglomerates.

### 2.5.3 Hydrothermal activity during early post-impact sedimentation

Impact-generated hydrothermal alteration is well documented in the impact melt-bearing breccias throughout the Ries impact structure (e.g., Caudill et al., 2021; Newsom et al., 1986; Osinski, 2005; Osinski et al., 2004; Sapers et al., 2017). Similar textural and mineralogical occurrences have been observed in the same melt-bearing breccias (units 14 and 15) sampled by the Wörnitzostheim drill core. Indeed, localized occurrences of clay minerals in vugs and voids hosted by glass clasts are common, and the presence of alteration associated with degassing pipes has been described in detail (Caudill et al. 2021). Thus, an impact-generated hydrothermal system was active in the impact melt-bearing breccias at the location sampled by the Wörnitzostheim drill core. Unlike the melt-bearing breccias sampled by the Nördlingen drill core in the central basin of the Ries (Osinski 2005), however, those sampled by the Wörnitzostheim drill core do not show evidence of pervasive hydrothermal alteration. We suggest two possible explanations for this difference. First, the higher elevation of the impactites in the Wörnitzostheim drill core (Fig. 2.1B) may have meant that water was less readily available than deep in the central basin of the Ries impact structure. Additionally, the melt-bearing breccia deposited at the site of the Wörnitzostheim drill core (~80 m) is notably thinner than the crater-fill, melt-bearing breccias (~300 m) sampled by the Nördlingen drill core in the central basin (e.g., Fig. 2.1B), which would have resulted in shorter-lived hydrothermal activity in this region. Thus, the hydrothermal environment of the Wörnitzostheim drill core would have been different from that of the Nördlingen drill core. In a similar fashion, the melt-bearing breccia from quarries and drill cores elsewhere at the Ries exhibit spatially variable hydrothermal environments (Sapers et al. 2017). The question is then whether hydrothermal activity was still ongoing at the time of sediment deposition.

The textures and mineralogy of matrix and void-filling minerals are variable throughout the basal conglomerates. Given the generally subhedral to euhedral form of the void-filling minerals, they are considered secondary, and hence most likely to preserve any signature of a hydrothermal origin (e.g., Fig. 2.7B, D). The matrix of unit 13 consists of smectitic clay minerals with a distinct honeycomb texture (Fig. 2.7C) that are associated primarily with detrital impact glass, mica and feldspar clasts. Clay minerals in units 12 and 11, by

comparison, primarily exhibit densely packed and fluffy textures in the matrix and show few obvious nucleation or growth textures associated with clastic material (e.g., Fig. 2.7D; Fig. 2.8B). Considering the authigenic nature of clay minerals comprising the matrix of unit 13, we suggest they are cogenetic with the void-filling minerals, or at least similar in their timing of formation. As such, the matrix smectitic clay minerals and the void-filling minerals could be part of the same hydrothermal mineral assemblage.

The mineral assemblage of smectitic clay minerals, dolomite and feldspar in unit 13 is mostly consistent with the early to late stages of the principal sequence of mineralization in impact-generated, hydrothermal systems (Kirsimäe and Osinski 2013; Naumov 2005). We suggest that the rare feldspar occurrences within void-filling dolomite represents a brief period of spatially limited  $\sim 300^{\circ}\text{C}$  hydrothermal mineralization, which was followed by quenching, resulting in the spherulitic plagioclase, and rapid cooling to  $\sim 100^{\circ}\text{C}$ . Void-filling clay minerals likely precipitated at these lower temperatures. The upper temperature limit for clay minerals of the melt-bearing breccias is  $130^{\circ}\text{C}$ , as proposed by Newsom (1986), so it is unlikely that fluid temperatures associated with the overlying basal conglomerates exceeded this limit. As such, we suggest a temperature range of  $100\text{--}130^{\circ}\text{C}$  for void-filling clay minerals, or potentially lower. The temperature range for clay minerals cannot yet be stated with certainty based on the results of this study. The prevalence of clay minerals (smectite, illite, kaolinite) and the suggested temperature range ( $\sim 100\text{--}300^{\circ}\text{C}$ ) is typical of argillic alteration (Gifkins, Herrmann and Large, 2005).

The mixed detrital / authigenic nature of the clay minerals comprising the matrix of units 12 and 11 suggests a temporally distinct difference between void-filling minerals and matrix minerals; hence, we cannot approximate the formation temperature of the matrix minerals using the void-filling mineralogy as a proxy. It also remains unclear whether the clay minerals comprising the matrix of units 12 and 11 were formed during hydrothermal activity. Hydrothermal mineralization in unit 12 could have triggered the formation of void-filling dolomite and smectitic clay minerals (Fig. 2.6B, D). Considering the lack of feldspar, and the relatively low abundance of gypsum and pyrite ( $<10\%$ ) we again invoke the principal sequence of mineralization in impact-induced, hydrothermal systems

(Kirsimäe and Osinski 2013; Naumov 2005) to suggest potential hydrothermal alteration at  $\sim \leq 100^\circ\text{C}$ .

The abundant gypsum, anhydrite and pyrite in the voids of unit 11 point to an influx of sulfur, which we suggested above was derived from dissolved organic matter in an overlying lake system (Fig. 2.2) and/or from the alteration of sedimentary clasts that were incorporated into the breccia. As also discussed previously, the lake system that deposited unit 6 contained abundant plant matter and gypsum in the paleolake-bed, which would imply a notable supply of dissolved organics; however, this has not been measured. The mud cracks associated with unit 6 indicates periodic wetting and drying, which would have further concentrated salts and organic matter. In the playa setting recorded in unit 6, sulfur-rich lake water could have percolated through the sandstones (units 10 – 9) into unit 11. Hydrothermal activity affecting unit 11 could have triggered precipitation of hydrothermal gypsum in the voids of the breccia (Fig. 8C), which is consistent with the late, low temperature ( $\sim 100^\circ\text{C}$ ) stages of mineralization in impact-induced, hydrothermal systems (Naumov, 2005; Kirsimäe and Osinski, 2013). The formation of framboidal pyrite from gypsum and anhydrite could occur biogenically through bacterial sulfate reduction of gypsum or anhydrite, as the presence of framboidal pyrites have been considered putative indicators of biogenic mineralization (Love, 1957; Folk, 2005). However, formation of framboidal pyrite during hydrothermal mineralization has also been documented (e.g., Scott et al., 2009; Wilkin & Barnes, 1997). Both hydrothermal and biogenic formation pathways occurring in concert is plausible but requires further investigation.

## 2.6 Conclusions

The results of this study indicate that the upper 20.1 m of rock sampled by the Wörnitzostheim drill core broadly represents deposition of an alluvial fan into a playa lake, and finally into a progressively freshening lake system. Early alluvial sedimentation was affected by venting of an impact-generated hydrothermal system. Presumably shortly after the impact event and the deposition of melt-bearing breccias (units 15 and 14), an influx of freshwater from rain, emergent fluvial systems and groundwater likely reworked and eroded sediment from local melt-bearing breccias. The remnant heat of the transported sediment and the venting of an underlying hydrothermal environment present in the melt-

bearing breccias geothermally modified the composition of the incoming freshwater into a weakly alkaline fluid through the leaching of potassium from clastic material. These alkaline fluids likely precipitated the clay minerals comprising the matrix of unit 13 with well-formed honeycomb textures (Fig. 17a). Venting of hydrothermal fluids in unit 13 shortly after deposition, and subsequent quenching likely triggered the formation of the rare skeletal feldspar in the voids and fractures of unit 13, indicating initial temperatures of  $\sim 300^{\circ}\text{C}$ . Subsequent cooling of the system facilitated mineralization void-filling smectite at  $\sim 100\text{--}130^{\circ}\text{C}$ . Continued fluvial sedimentation of material eroded from local melt-bearing breccias under cooler conditions likely triggered the formation of clay minerals with a “fluffy” texture and a change in the tone of the rock in unit 12. Ongoing hydrothermal mineralization likely triggered the formation of dolomite and smectitic clay minerals in the fractures and voids of unit 12 (Fig. 17b). The progradation of the alluvial fan recorded a period of relatively high energy mass wasting, which eroded sedimentary clasts from additional sediment sources, and coarser clastic material from local melt-bearing breccias during the deposition of unit 11. Sulfur leached from the sedimentary clasts by hydrothermal fluids could have triggered formation of sulfates and sulfides. Alluvial progradation and backfilling towards the sediment catchment area potentially caused burial of the basal conglomerates by the sandstone units. A flooding event or shifting alluvial fan surface likely truncated the record of alluvial backfilling by depositing the sandstone conglomerate (unit 9). Rapid sedimentation in a low energy, lacustrine setting produced marlstones with convoluted laminations, which transitioned to wavy laminations, bioturbation and mud cracks as the system underwent intermittent drying. Lake water carrying sulfur and salt leached from decaying plant matter and sulfates in unit 6 were likely transported into unit 11 where hydrothermal activity from the still warm, reworked breccias triggered formation of hydrothermal gypsum, which was reduced to framboidal pyrite. During the dry periods recorded in unit 6, gypsum converted to anhydrite. Subsequent deepening of the lake triggered the deposition of fossiliferous dolomite packstones and chaotically laminated marlstones as rapid deposition resumed.

This study demonstrates that hydrothermal mineralization during early, post-impact, fluvial-lacustrine sedimentation is possible, even in circumstances where sources of fluid and heat are relatively limited. We suggest that the heat potentially originated from the

sediment itself in conjunction with heat contributed from the underlying melt-bearing breccias. The chemical composition of freshwater can be extensively modified by interaction with warm sediment, and additionally by underlying impact melt-bearing breccias through which it possibly flowed. The deltaic deposits targeted by the *Perseverance* Rover in Jezero crater, Mars may contain similar fluvio-lacustrine deposits (e.g., Fassett & Head, 2005) that, like the basal conglomerates of the Wörnitzostheim drill core, record post-impact hydrothermal interaction with the emerging lake system. The origins of the minerals and their textures recorded in early, post-impact fluvio-lacustrine deposits are indeed difficult to distinguish. Nonetheless, the potential for these features to record a wide array of processes such as hydrothermal mineralization, biomineralization, ecological recovery from the impact event, and climate change, makes their investigation a worthwhile investment.

## 2.7 References

- Arp, G., 1995. Lacustrine bioherms, spring mounds, and marginal carbonates of the Ries-impact-crater (Miocene, Southern Germany). *Facies*, 33(1), pp.35–89.  
<https://doi.org/10.1007/BF02537444>.
- Arp G., 2006. Sediments of the Ries Crater Lake (Miocene, Southern Germany). In: *21st Meeting of Sedimentologists / 4th Meeting of SEPM Central European Section*. pp.216–233.
- Arp, G., Blumenberg, M., Hansen, B.T., Jung, D., Kolepka, C., Lenz, O., Nolte, N., Poschlod, K., Reimer, A. and Thiel, V., 2013a. Chemical and ecological evolution of the Miocene Ries impact crater lake, Germany: A reinterpretation based on the Enkingen (SUBO 18) drill core. *Bulletin of the Geological Society of America*, 125(7–8), pp.1125–1145. <https://doi.org/10.1130/B30731.1>.
- Arp, G., Hansen, B.T., Pack, A., Reimer, A., Schmidt, B.C., Simon, K. and Jung, D., 2017. The soda lake—mesosaline halite lake transition in the Ries impact crater basin (drilling Löpsingen 2012, Miocene, southern Germany). *Facies*, 63(1).  
<https://doi.org/10.1007/s10347-016-0483-7>.

- Arp, G., Kolepka, C., Simon, K., Karius, V., Nolte, N. and Hansen, B.T., 2013b. New evidence for persistent impact-generated hydrothermal activity in the Miocene Ries impact structure, Germany. *Meteoritics and Planetary Science*, 48(12), pp.2491–2516. <https://doi.org/10.1111/maps.12235>.
- Arp, Gernot., Schultz, S., Karius, V. and Head, J.W., 2019. Ries impact crater sedimentary conglomerates: Sedimentary particle ‘impact pre-processing’ transport distances and provenance, and implications for Gale crater conglomerates, Mars. *Icarus*, 321, pp.531–549. <https://doi.org/10.1016/j.icarus.2018.12.003>.
- Bohor, B.F. and Triplehorn, D.M., 1993. Tonsteins: Altered Volcanic-Ash Layers in Coal-Bearing Sequences. *Geological Society of America Special Paper*, (285).
- Boyd, C.E., 2015. pH, Carbon Dioxide, and Alkalinity. In: *Water Quality - An Introduction*, 2nd ed. Switzerland: Springer International Publishing . pp.153–178. [https://doi.org/10.1007/978-3-319-17446-4\\_8](https://doi.org/10.1007/978-3-319-17446-4_8).
- Brigham-Grette, J., Melles, M. and Minyuk, P., 2007. Overview and significance of a 250 ka paleoclimate record from El’gygytgyn Crater Lake, NE Russia. *Journal of Paleolimnology*, 37(1), pp.1–16. <https://doi.org/10.1007/s10933-006-9017-6>.
- Cabrol, N.A. and Grin, E.A., 1999. Distribution, Classification, and Ages of Martian Impact Crater Lakes. *Icarus*, 142(1), pp.160–172. <https://doi.org/10.1006/icar.1999.6191>.
- Cabrol, N.A. and Grin, E.A., 2001. The Evolution of Lacustrine Environments on Mars: Is Mars Only Hydrologically Dormant? *Icarus*, 149(2), pp.291–328. <https://doi.org/10.1006/icar.2000.6530>.
- Caudill, C., Osinski, G.R., Greenberger, R.N., Tornabene, L.L., Longstaffe, F.J., Flemming, R.L. and Ehlmann, B.L., 2021. Origin of the degassing pipes at the Ries impact structure and implications for impact-induced alteration on Mars and other planetary bodies. *Meteoritics and Planetary Science*, 56(2), pp.404–422. <https://doi.org/10.1111/maps.13600>.

- Christ, N., Maerz, S., Kutschera, E., Kwiecien, O. and Mutti, M., 2018. Palaeoenvironmental and diagenetic reconstruction of a closed-lacustrine carbonate system – the challenging marginal setting of the Miocene Ries Crater Lake (Germany). *Sedimentology*, 65(1), pp.235–262. <https://doi.org/10.1111/sed.12401>.
- Cockell, C.S., Lee, P., Ames, N., Field, M., Cockell, C.S. and Lee, P., 2017. The biology of impact craters – a review. (2002), pp.279–310.
- Daubar, I.J. and Kring, D.A., 2001. Impact-induced hydrothermal systems: Heats sources and lifetimes. In: *32nd Lunar and Planetary Science Conference. (abstract #1727)*.
- Doebelin, Nicola. and Kleeberg, Reinhard., 2015. Profex: A graphical user interface for the Rietveld refinement program BGMN. *Journal of Applied Crystallography*, 48, pp.1573–1580. <https://doi.org/10.1107/S1600576715014685>.
- Engelhardt. W. v., Arndt. J., Fecker B. and Pankau H. G., 1995. Suevite breccia from the Ries crater, Germany: origin, cooling history and devitrification of impact glasses. *Meteoritics*, 30, pp.297–293.
- von Engelhardt, W., 1997. Suevite breccia of the Ries impact crater, Germany: Petrography, chemistry and shock metamorphism of crystalline rock clasts. *Meteoritics and Planetary Science*, 32(4), pp.545–554. <https://doi.org/10.1111/j.1945-5100.1997.tb01299.x>.
- Ernstson, Kord., 1974. The structure of the Ries Crater from geoelectric depth soundings. *Journal of Geophysics*, [online] 40, pp.639–659. Available at: <<https://www.researchgate.net/publication/259485112>>.
- Farley, K.A., Williford, K.H., Stack, K.M., Bhartia, R., Chen, A., de la Torre, M., Hand, K., Goreva, Y., Herd, C.D.K., Hueso, R., Liu, Y., Maki, J.N., Martinez, G., Moeller, R.C., Nelessen, A., Newman, C.E., Nunes, D., Ponce, A., Spanovich, N., Willis, P.A., Beegle, L.W., Bell, J.F., Brown, A.J., Hamran, S.E., Hurowitz, J.A., Maurice, S., Paige, D.A., Rodriguez-Manfredi, J.A., Schulte, M. and Wiens, R.C., 2020. Mars 2020

- Mission Overview. *Space Science Reviews*, 216(8). <https://doi.org/10.1007/s11214-020-00762-y>.
- Fassett, C.I. and Head, J.W., 2005. Fluvial sedimentary deposits on Mars: Ancient deltas in a crater lake in the Nili Fossae region. *Geophysical Research Letters*, 32(14), pp.1–5. <https://doi.org/10.1029/2005GL023456>.
- Flemming, R.L., 2007. Micro x-ray diffraction ( $\mu$ XRD): A versatile technique for characterization of earth and planetary materials. *Canadian Journal of Earth Sciences*, 44(9), pp.1333–1346. <https://doi.org/10.1139/E07-020>.
- Flower, Benjamin.P. and Kennett, James.P., 1994. The middle Miocene climatic transition: East Antarctic ice sheet development, deep ocean circulation and global carbon cycling. *Palaeogeography, Palaeoclimatology, Palaeoecology*, 108, pp.537–555.
- Folk, R.L., 2005. Nannobacteria and the formation of framboidal pyrite: Textural evidence. *Journal of Earth Systems Science*, 114, pp.369–374.
- Förstner, v. U., 1977. Geochemische Untersuchungen an den Sedimenten des Ries-Sees (Forschungsbohrung Nördlingen 1973. *Geologica Bavarica*, 75, pp.337–48.
- Förstner, U., 1967. Petrographische Untersuchungen des Suevit aus den Bohrungen Deiningen und Wörnitzostheim im Ries von Nördlingen. *Contributions to Mineralogy and Petrology*, 15(4), pp.281–308. <https://doi.org/10.1007/BF00404198>.
- Füchtbauer, H., Brellie. von der. G., Dehem, R., Förstner, U., Gall, H., Höfling, R., Hoefs, J., Hollerbach, H., Jankowski, B., Jung, W., Malz, H., Mertes, H., Rothe, P., Salger, M., Wehner, H. and Wolf, M., 1977. Tertiary lake sediments of the Ries, research borehole Nördlingen 1973-A summary. *Geologica Bavarica*, 75, pp.13–19.
- Gifkins, C., Herrmann, W. and Large, R., 2005. *Altered volcanic rocks – A guide to description and interpretation*. Hobart: Centre Ore Depos Res, Univ Tasmania.

- Hörz, F., Gall, H., Hüttner, R. and Oberbeck, V.R., 1977. Shallow drilling in the “Bunte Breccia” impact deposits, Ries crater, Germany. In: D.J. Roddy, R.O. Pepin and R.B. Merrill, eds. *Impact and Explosion Cratering* . New York.: Pergamon Press. pp.343–404.
- Hörz, Friedrich., Ostertag, Rolf. and Rainey, D.A., 1983. Bunte Breccia of the Ries: Continuous deposits of large impact craters. *Reviews of Geophysics and Space Physics*, 21(8), pp.1667–1725. <https://doi.org/10.1029/RG021i008p01667>.
- Jankowski, B., 1977. Die Postimpakt-Sedimente in der Forschungs-bohrung Nördlingen 1973. *Geologica Bavarica*, 75, pp.21–36.
- Jankowski, B., 1981. Die Geschichte der Sedimentation im Nördlinger Ries und Randecker Maar. *Bochumer geologische und geotechnische Arbeiten* , 6, pp.1–315.
- Kirsimäe, K. and Osinski, G.R., 2012. Impact-Induced Hydrothermal Activity. *Impact Cratering: Processes and Products*, pp.76–89. <https://doi.org/10.1002/9781118447307.ch6>.
- Kirsimäe, K. and Osinski, G.R., 2013. Impact-induced hydrothermal activity. In: G.R. Osinski and E. Pierazzo, eds. *Impact Cratering: Processes and Products*. Blackwell Publishing Ltd. pp.76–89.
- Love, L.G., 1957. Micro-organisms and the presence of syngenetic pyrite. *Quarterly Journal of the Geological Society*, 113, pp.429–440. <https://doi.org/10.1144/GSL.JGS.1957.113.01-04.18>.
- Mertes, H., 1977. Rutschgefüge in den jungtertiären See-Sedimentender Forschungsbohrung Nördlingen 1973. *Geologica Bavarica*, pp.75–89.
- Naumov, M. V., 2005a. Principal features of impact-generated hydrothermal circulation systems: Mineralogical and geochemical evidence. *Geofluids*, 5(3), pp.165–184. <https://doi.org/10.1111/j.1468-8123.2005.00092.x>.

- Newsom, H.E., Graup, G., Sowards, T. and Keil, K., 1986. Fluidization and hydrothermal alteration of the Suevite deposit at the Ries Crater, West Germany, and implications for Mars. *Journal of Geophysical Research*, 91(B13), pp.E239–E251.  
<https://doi.org/10.1029/jb091ib13p0e239>.
- Osinski, G.R., 2005a. Hydrothermal activity associated with the Ries impact event, Germany. *Geofluids*, 5, pp.202–220.
- Osinski, G.R., 2005b. Hydrothermal activity associated with the Ries impact event, Germany. *Geofluids*, 5(3), pp.202–220. <https://doi.org/10.1111/j.1468-8123.2005.00119.x>.
- Osinski, G.R., Cockell, C.S., Pontefract, A. and Sapers, H.M., 2020. The role of meteorite impacts in the origin of life. *Astrobiology*, 20(9), pp.86–106.  
<https://doi.org/10.1089/ast.2019.2203>.
- Osinski, G.R., Grieve, R.A.F. and Spray, J.G., 2004. *The nature of the groundmass of surficial suevite from the Ries impact structure, Germany, and constraints on its origin. Meteoritics & Planetary Science*, .
- Osinski, G.R., Tornabene, L.L., Banerjee, N.R., Cockell, C.S., Flemming, R., Izawa, M.R.M., McCutcheon, J., Parnell, J., Preston, L.J., Pickersgill, A.E., Pontefract, A., Sapers, H.M. and Southam, G., 2013. Impact-generated hydrothermal systems on Earth and Mars. *Icarus*, 224(2), pp.347–363.  
<https://doi.org/10.1016/j.icarus.2012.08.030>.
- Pohl, J., Stöffler, D., Gall, H. and Erston, K., 1977. The Ries impact crater. In: Roddy D.J., Pepin R.O. and Merrill R.B., eds. *Impact and Explosion Cratering*. New York: Pergamon Press. pp.343–404.
- Riding, R., 1979. Origin and diagenesis of lacustrine algal bioherms at the margin of the Ries crater, Upper Miocene, southern Germany. *Sedimentology*, 26, pp.645–680.
- Salger, M., 1977. Die Tonminerale der Forschungsbohrung Nördlingen 1973. *Geologica Bavarica*, 75, pp.67–73.

- Sapers, H.M., Osinski, G.R., Flemming, R.L., Buitenhuis, E., Banerjee, N.R., Tornabene, L.L., Blain, S. and Hainge, J., 2017a. Evidence for a spatially extensive hydrothermal system at the Ries impact structure, Germany. *Meteoritics and Planetary Science*, 52(2), pp.351–371. <https://doi.org/10.1111/maps.12796>.
- Sapers, H.M., Osinski, G.R., Flemming, R.L., Buitenhuis, E., Banerjee, N.R., Tornabene, L.L., Blain, S. and Hainge, J., 2017b. Evidence for a spatially extensive hydrothermal system at the Ries impact structure, Germany. *Meteoritics and Planetary Science*, 52(2), pp.351–371. <https://doi.org/10.1111/maps.12796>.
- Schmieder, M., Kennedy, T., Jourdan, F., Buchner, E. and Reimold, W.U., 2018. A high-precision  $^{40}\text{Ar}/^{39}\text{Ar}$  age for the Nördlinger Ries impact crater, Germany, and implications for the accurate dating of terrestrial impact events. *Geochimica et Cosmochimica Acta*, 220, pp.146–157. <https://doi.org/10.1016/j.gca.2017.09.036>.
- Scott R. J., Meffre S., Woodhead J., Gilbert S. E., Berry R. F. and Emsbo P., 2009. Development of framboidal pyrite during diagenesis, low-grade regional metamorphism, and hydrothermal alteration. *Economic Geology*, 104, pp.1143–1168.
- Stöffler, D., Artemieva, N.A., Wünnemann, K., Reimold, W.U., Jacob, J., Hansen, B.K. and Summerson, I.A.T., 2013. Ries crater and suevite revisited-Observations and modeling Part I: Observations. *Meteoritics and Planetary Science*, 48(4), pp.515–589. <https://doi.org/10.1111/maps.12086>.
- Stöffler, D., Ewald, U., Ostertag, R. and Reimold, W.-U., 1977. Research drilling Nordlingen 1973 (Ries): composition and texture of polymict impact breccias. *Geologica Bavarica*, 75, pp.163–189.
- Wilkin, R.T. and Barnes, H.L., 1997. Formation processes of framboidal pyrite. *Geochimica et Cosmochimica Acta*, 61(2), pp.323–339.

### 3 Tracing the fluid evolution of early post-impact fluvio-lacustrine systems beyond the central basin of the Ries impact structure, Germany

#### 3.1 Introduction

Impact cratering is a ubiquitous process affecting rocky and icy bodies throughout the solar system. In settings on Earth and Mars where there is sufficient water in the target region, impact cratering can potentially trigger the formation of transient hydrothermal systems (Naumov, 2005; Kirsimäe and Osinski, 2012; Osinski et al., 2013) and fluvio-lacustrine systems (Cabrol and Grin, 1999; 2001; Brigham-Grette et al., 2007; Arp et al., 2013a). Latent heat from the kinetic energy of the impact event, heat from melt-bearing impactites, and heat from uplifted geothermal gradients (Naumov, 2005) can trigger the circulation of incoming fluids from a possible mixture of mainly rainwater, groundwater, and fluvial water, thus generating hydrothermal convection cells within the subsurface. Venting of these hydrothermal systems into an emerging lacustrine environment can create potentially ideal habitats for microbial forms of life (Cockell and Lee, 2002; Osinski et al., 2013; 2020; Cockell et al., 2020). Such environments can potentially be generated even in settings where water and heat may be relatively limited (Chapter 2). Due to the high resolution of the environmental record commonly preserved in post-impact sedimentary deposits (Arp et al., 2017), it is possible to trace fluid evolution and generate accurate models of post-impact environmental recovery. Hydrated minerals such as phyllosilicates, which contain OH<sup>-</sup> and H<sub>2</sub>O bound in their crystal structure can reflect the physiochemical environment at the time of their deposition in their textures, layering patterns, bulk chemical composition, and hydrogen ( $\delta^2\text{H}$ ) and oxygen ( $\delta^{18}\text{O}$ ) isotope geochemistry (Brindley and Brown, 1980; Longstaffe and Ayalon, 1990; Libbey et al., 2013). Such phyllosilicates are present in the form of  $<2\ \mu\text{m}$  clay minerals, which commonly occur in post-impact sedimentary deposits (e.g., Salger, 1977; Chapter 2). Thus, clay minerals from early post-impact sedimentary deposits can be used to reconstruct early lacustrine evolution and provide a resource for the detailed characterization of post-impact crater-lake habitability on Earth and Mars.

Clay minerals have been detected in many different localities on Mars (Ehlmann et al., 2011), and the required presence of water for their formation has generated substantial interest in determining their origins. Many different theories for the formation of clay minerals on Mars have been proposed. Some studies suggested that clay minerals on Mars could have formed during the Noachian period at the planet's surface under warm and wet conditions (Poulet et al., 2005; Bibring et al., 2006), as well as in the subsurface under cold and dry conditions (Ehlmann et al. 2011). It has also been suggested that clay minerals on Mars might have formed during the early formation of the planet's crust (Cannon, Parman and Mustard, 2017). Clay minerals could have also formed in aqueous environments like fluviolacustrine systems (Milliken and Bish, 2010; Bristow and Milliken, 2011), or in hydrothermal environments initiated by volcanism (Farmer, 1996) or meteorite impacts (Newsom, 1980; Rathbun and Squyres, 2002; Tornabene et al., 2013). The detection of complex clay minerals in records of impact-generated environments preserved on Earth (e.g., Caudill et al., 2021; Naumov, 2005; Osinski et al., 2013; Simpson et al., 2022; Tornabene et al., 2013) provides the basis for hypotheses that impact cratering can generate similarly complex and potentially widespread clay mineral-bearing deposits on Mars. Current exploration of Mars' surface is focused on impact structures that host clay mineral-bearing units that preserve evidence of post-impact fluviolacustrine deposition such as Gale Crater (e.g., Bristow et al., 2015, 2018; Bristow & Milliken, 2011; Cabrol et al., 1999; Grotzinger et al., 2014, 2015; Rapin et al., 2019) and Jezero Crater (e.g., Goudge et al., 2015, 2017, 2018; Horgan et al., 2020; Schon et al., 2012). Understanding the influence of impact cratering on the early aqueous history, and subsequently the clay mineralogy, of these areas is critical. Using terrestrial analogues, it is possible to better contextualize the observations of the Curiosity and Perseverance rovers (exploring Gale and Jezero crater, respectively) and provide a resource to better prioritize sampling targets as the rovers explore their respective impact structures. Analyses of the many distinct settings in which clay minerals occur in impact structures on Earth can provide further insight into the role of impact cratering, and subsequent modification processes in generating clay minerals.

The Ries impact structure in southern Germany, hosts several clay mineral-bearing units such as melt-bearing breccias (e.g., von Engelhardt, 1997; Osinski, Grieve and Spray, 2004; Osinski, 2005; Sapers et al., 2017; Caudill et al., 2021), melt-poor breccias (e.g., Caudill et

al. 2021), and post-impact sedimentary deposits (e.g., Salger 1977; Chapter 2). Clay minerals preserved in post-impact sedimentary deposits at the Ries impact structure are spatially widespread (Salger, 1977) and early deposits are derived from complex and mineralogically diverse clay-bearing units such as the melt-bearing breccias and melt-poor breccias (Salger et al. 1977; Chapter 2). Smectitic clay minerals are a major mineralogical constituent of the impact melt-bearing breccias (Osinski et al. 2004; Osinski 2005), and early post-impact sedimentary deposits sampled by the Wörnitzostheim drill core at the Ries impact structure (Chapter 2). Thus, the basal sedimentary units of the Wörnitzostheim drill core represented by units 13–11 are an ideal target for the study of the character and origins of clay minerals generated by early interactions between an impact-induced hydrothermal system and post-impact fluviolacustrine system.

In this study we contribute a detailed investigation of the mineralogy, and hydrogen ( $\delta^2\text{H}$ ) and oxygen ( $\delta^{18}\text{O}$ ) isotope geochemistry of  $<2\ \mu\text{m}$ ,  $2\text{--}0.2\ \mu\text{m}$ , and  $<0.2\ \mu\text{m}$  size-fraction separates from melt-bearing breccias and basal alluvial fan deposits sampled by the Wörnitzostheim drill core from the Ries impact structure. Smectite is a phyllosilicate mineral that occurs throughout the  $<2\ \mu\text{m}$  size-fraction of the upper 27 m of the Wörnitzostheim drill core, which encompasses the entirety of the drill core's post-impact sedimentary deposits and an upper section of melt-bearing breccias. We build off previous studies of the crater lake environment at the Ries impact structure and highlight implications for the formation of clay minerals on Mars and the early post-impact fluviolacustrine environment at the Ries impact structure.

## 3.2 Geological Setting

The  $\sim 24$  km diameter, complex Ries impact structure, Germany formed in a compositionally mixed target during the early Miocene ( $\sim 14.8$  Ma; Schmieder et al., 2018). The target rock comprised Hercynian crystalline basement of amphibolites, gneisses, ultrabasic rocks and later granitoid intrusions that are overlain by a Triassic–Jurassic sedimentary package of mainly limestone with some conglomerates, sandstone, siltstone and marlstone contained in the Triassic rocks (Fig. 3.1A, B). The modern expression of the Ries impact structure consists of a tectonic outer ring represented by a roughly circular array of highlands, and a buried central basin ( $\sim 12$  km in diameter, 800 m deep) bound by

uplifted, but still buried, crystalline rocks loosely resembling an inner ring. The ejecta blanket represented by the Bunte breccia was deposited outside the bounds of the so called “inner ring” and extends ~26 km away from the tectonic rim (von Engelhardt, 1990). A series of melt-bearing breccias ejected from the central basin was discontinuously deposited as patchy remnants upon the Bunte Breccia (Fig. 3.1A, B). These ejected melt-bearing breccias exhibit secondary alteration features limited to calcite and smectitic clay minerals lining and filling fractures and voids (Osinski, 2004; 2005; Sapers et al., 2017) and are occasionally overlain by up to 20 m of post-impact sedimentary rocks (Förstner, 1967). Patches of ejected melt-bearing breccias can be up to 80 m thick (Förstner 1967). Crater-fill melt-bearing breccias that were pervasively altered (mainly to smectitic clay minerals with void lining / filling calcite; Osinski 2005) occur as a continuous sheet within the central basin and are overlain by ~400 m of post-impact sedimentary rocks. The thickness of the crater-fill melt-bearing breccias varies from <100 m near the so called “inner-ring” to up to 300 m towards the basin center (Stöffler et al. 2013).

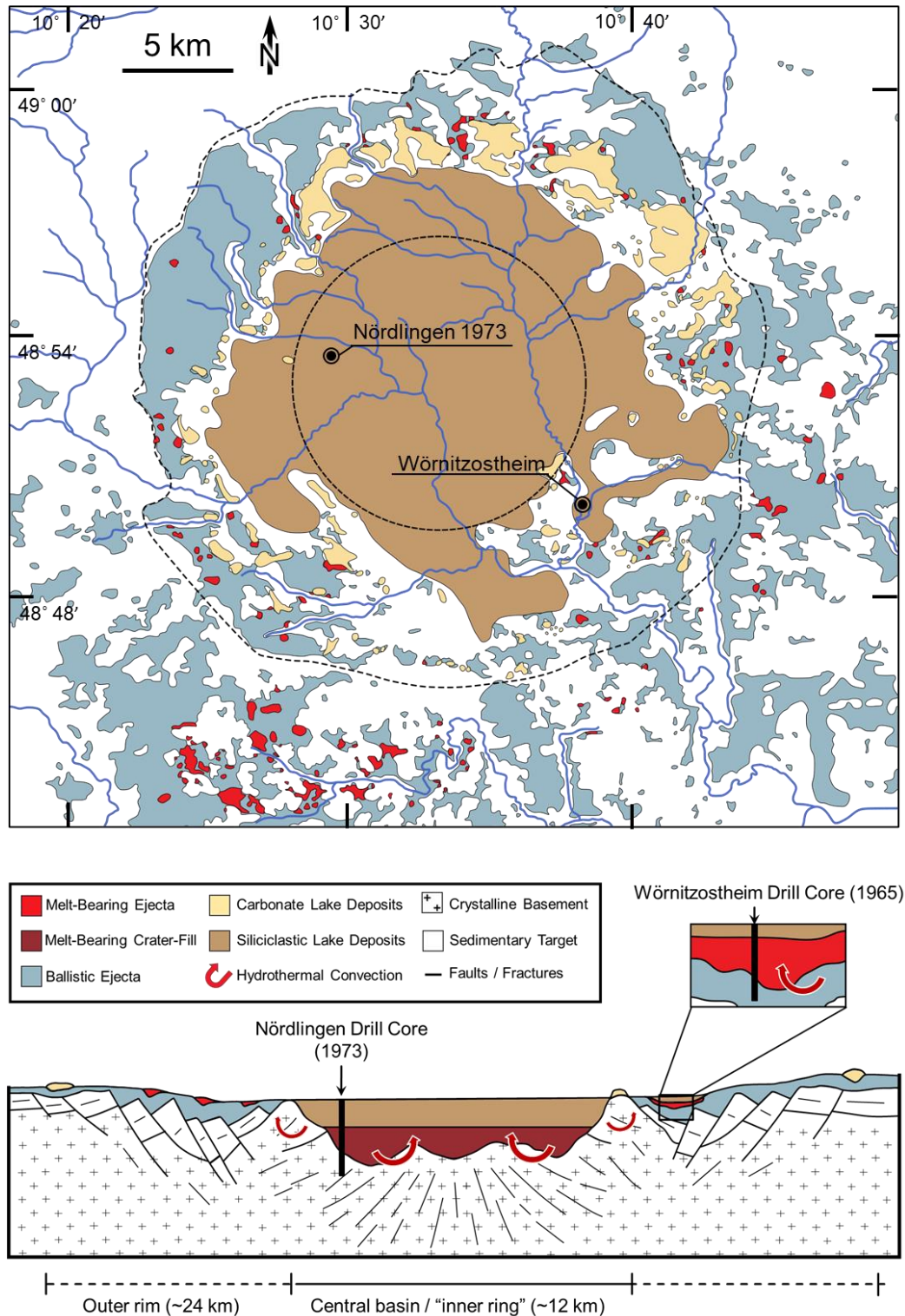


**Figure 3. 1:** (A) A geological map of the Ries impact structure highlighting major clay-bearing units and the locations of the Nördlingen 1973, and Wörnitzostheim drill cores (modified from Sapers et al. 2017 and Arp et al. 2017). Siliciclastic and calcareous

lacustrine deposit distribution is based on the work of (Ernstson, 1974; Pohl et al., 1977; Hüttner and Schmidt-Kaler, 1999). The cross section (B) depicts hypothetical hydrothermal convection cells, interpretations of major structural features, such as the central basin, and units sampled by the Nördlingen 1973 drill core and Wörnitzostheim 1965 drill core (modified from Sapers et al. 2017). This figure is an interpretation and is not intended for use as a 'to-scale' model.

The melt-bearing breccias at the Ries impact structure are likely the main source of heat that drove an impact-generated hydrothermal system (Osinski 2005). Initial temperatures of the melt-bearing breccias were  $\sim 2,000$  °C or higher, which then rapidly cooled to  $\sim 300$  °C (Osinski 2005). Alteration under saturated aqueous conditions triggered the pervasive hydrothermal mineralization observed in the crater-fill melt-bearing breccias (Osinski 2005). Relatively limited or slow water influx in the topographically high regions of the ejected melt-bearing breccias resulted in the concentration of alteration features to fracture and void fillings (Osinski 2005; Sapers et al. 2017; Chapter 2). Additional heat was likely contributed by an uplifted geothermal gradient. Assuming a geothermal gradient of  $30$  °C  $\text{km}^{-1}$ , it is possible that the 1–2 km structural uplift of the Ries geothermal gradient contributed  $\sim 40$ – $70$  °C of heat to drive the Ries hydrothermal system (Osinski 2005).

The length of time during which the Ries hydrothermal system was active has not been well constrained, but Daubar and Kring's (2001) cooling model indicates that a 25 km diameter crater, with a 200 m thick melt-sheet, cooling from 800 to 160 °C could persist for  $\sim 3,000$  years. Pohl (1977) applied a similar cooling model, which suggested that a 200 m thick melt sheet cooling from 800 to 100 °C would take several thousand years. Evidence of hydrothermal alteration in early post-impact sedimentary deposits (Chapter 2) and the occurrence of hydrothermal spring mounds that are stratigraphically correlated with late-stage lacustrine deposits (Arp et al. 2013a) indicate that the duration of the Ries hydrothermal system was sufficiently long-lived to affect post-impact fluvio-lacustrine processes. Additionally, Arp et al. (2013a) indicates that the Ries' hydrothermal system was active for at least 250,000 years after the impact event.

The overall sedimentary succession of post-impact fluvio-lacustrine evolution in the Ries impact structure consists of four major phases as recorded by the Nördlingen 1973 drill

core, which samples post-impact sedimentary deposits from within the central basin (Arp et al., 2013b, 2017, 2021; Füchtbauer et al., 1977; Jankowski, 1977, 1981). These deposits are divided into four main units as follows:

- A. Alluvial fan progradation represented by debrites and reworked melt-bearing breccias intercalated with playa deposits (unit A – basal member).
- B. Soda lake deposition represented by laminites and bituminous shales with authigenic analcime and clinoptilolite zeolites (unit B – laminate member).
- C. Soda – Halite lake transition represented by dolomitic marlstones (unit C – marl member).
- D. Halite lake approaching freshwater compositions with salinity fluctuations represented by alternating claystones, marlstones and limestones (unit D – clay member).

The general sequence of events recorded by units A–D in the Nördlingen 1973 drill core spans an ~1.2 Ma period of time (Pohl 1977; Jankowski 1981), which coincides with the transition from the Mid-Miocene Climatic Optimum to progressively cooler climates with the growing Antarctic ice sheet (Flower and Kennett, 1994). While aspects of this record are useful contextual tools that are generally applicable across the impact structure, stratigraphic correlation of units A–D in the Nördlingen 1973 drill core becomes more difficult with increased distance from the basin center (Arp et al. 2021). Mineralogical and textural studies indicate a good correlation between units in the Wörnitzostheim drill core and unit A, and unit D, from the Nördlingen drill core (Chapter 2). Basal sedimentary deposits from the Wörnitzostheim drill core, which are in contact with underlying melt-bearing breccias, were likely subjected to low temperature alteration ( $\leq 100\text{--}300$  °C; Chapter 2). The sedimentary succession sampled by the Wörnitzostheim drill core (Fig. 3.2) broadly represents the transition from an alluvial-playa setting influenced by early hydrothermal alteration to increasingly fresh lacustrine conditions where the basal units in this drill core represent the early aggradation of a fluvial-dominated alluvial fan (Chapter 2).

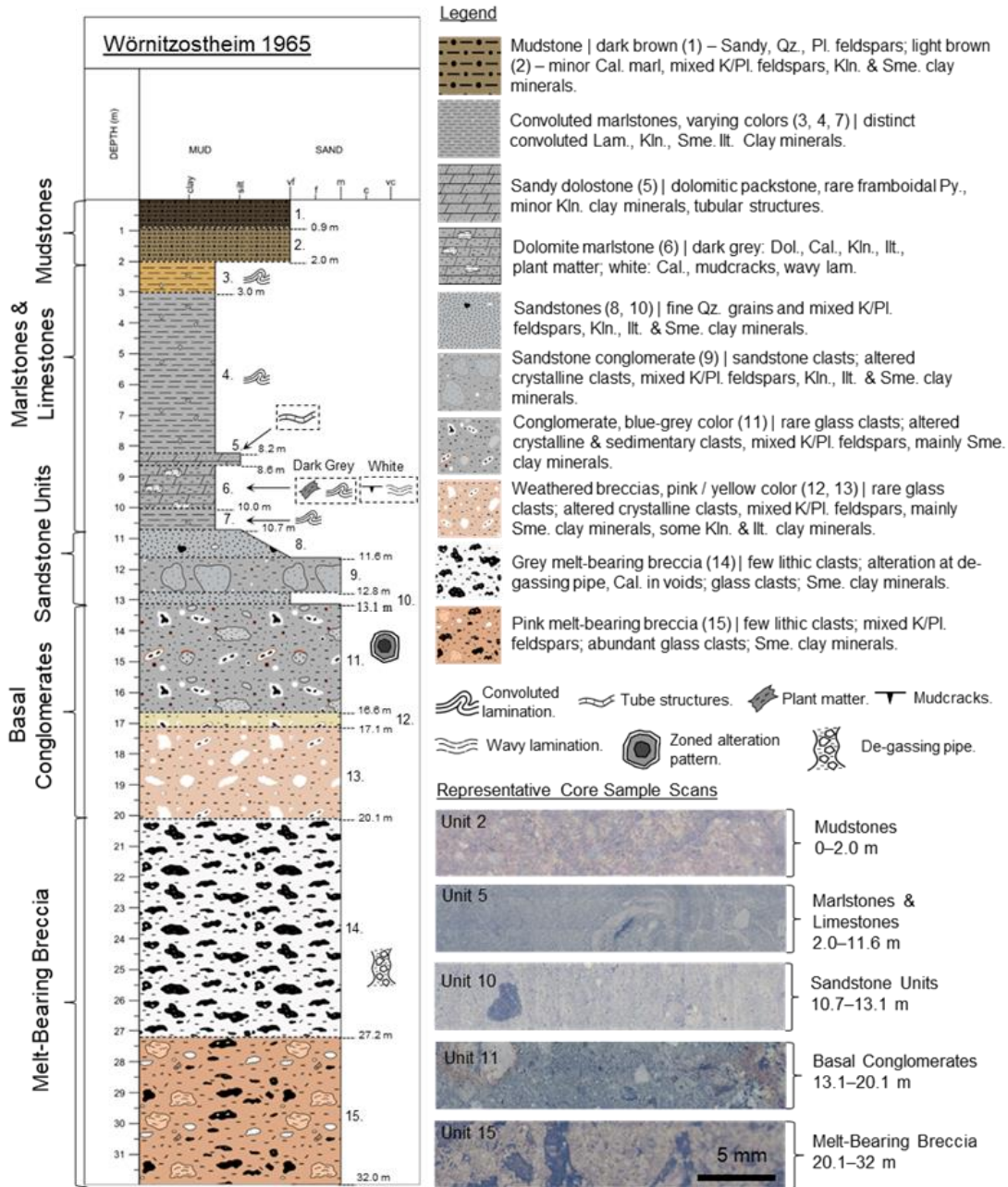


**Figure 3. 2:** The stratigraphy of the Wörnitzostheim 1965 drill core is represented by the above stratigraphic column (Chapter 2), which indicates the extent of major lithologies. The depth and unit groups are denoted on the y-axis of the column, and the approximate grainsize as determined using a grainsize card are indicated by the x-axis. Förstner (1967) reports a detailed record of grainsize changes throughout the Wörnitzostheim 1965 drill core. Illustrations for each unit depicted in the column are specific to each unit and intended to best approximate the appearance and textures. Each distinct unit is assigned a number in

sequential order starting from the top of the drill core. Images of representative core scans of each major unit group is provided below the legend with the depth location of the unit group. Abbreviations used in the symbology descriptions are as follows: Abbreviations: Qz. – quartz; Pl. – plagioclase; Kln. – kaolinite; Ill. – illite; Sme. – smectite; lam. – lamination; Sandstone Units – Sandstones and Sandstone Breccias.

### 3.3 Methodology

Of the 15 units logged in the upper 32m of the Wörnitzostheim drill core (Fig. 2; Chapter 2), 9 units were sampled for the purposes of this study, covering the two melt-bearing breccias (units 15 and 14), the basal conglomerates (units 13–11), the sandstone conglomerates (unit 9), the basal marlstone unit (unit 7), and the marlstone unit bearing mud cracks and bioturbation (dark- and white-toned material from unit 6, respectively). This transect encompasses the transition from melt-bearing breccias to lacustrine marlstones with a sampling focus on the main conglomerate units (units 13–11). In total, 13 samples were studied for the purposes of detailed analyses by field emission electron probe micro-analyzer (FE-EPMA), powder X-ray diffraction (*p*XRD), and hydrogen ( $\delta^2\text{H}$ ) and oxygen ( $\delta^{18}\text{O}$ ) measurements. Multiple samples were taken from the units outlined in Chapter 2, such that material was collected from the clasts and matrix separately. The suite of samples analyzed and applied analytical techniques used in this study are summarized in Table 3.1.

**Table 3. 1: Samples and analytical techniques.**

Lithology	Sample Context		Depth (m)	WDS (Clay Minerals) Spots Map	pXRD	$\delta^{18}\text{O}$ (‰, VSMOW*)	$\delta^2\text{H}$ (‰, VSMOW)
	Sample Label	Unit # Material					
Marlstones	RW9.6A-Whit.**	6 White material	9.60	—	—	—	—
	RW9.6B-Gry.	6 Dar grey material	9.60	—	—	—	—
	RW10.55-Gry.	7 Dark grey material	10.55	—	—	—	—
Sandstone Conglomerates	RW12.74	9 Matrix	12.74	—	—	—	—
Altered Grey Conglomerates	RW14.33-ALT	11 Clasts	14.33	—	—	—	—
	RW14.33-MTX	11 Matrix	14.33	—	—	—	—
Grey Conglomerates	RW14.78	11 Matrix	14.78	—	—	—	—
	RW16.16-MTX	11 Matrix	16.16	—	—	—	—
	RW16.16-ALT	11 Clasts	16.16	—	—	—	—
Pink Conglomerates	RW19-CLST	13 Clasts	19.00	—	—	—	—
	RW19-MTX	13 Matrix	19.00	—	—	—	—
Grey-Toned Melt-Bearing Breccias	RW22	14 Matrix	22.00	—	—	—	—
Pink-Toned Melt-Bearing Breccia	RW32	15 Matrix	32.00	—	—	—	—

\*VSMOW = Vienna Standard Mean Ocean Water

\*\*Sample label convention: R = Ries impact structure; W = Wörnitzosheim; [number] = depth; -Whit. = white-toned material; -Gry. = Grey-toned material; -ALT = altered material; -MTX = matrix material; -CLST = clastic material.

Fourteen polished thin sections were examined using transmitted light microscopy, and subsequently analyzed using the JEOL JXA-8530F Field Emission Electron Probe Micro-Analyzer at the Earth and Planetary Materials Laboratory at the University of Western Ontario. Back-scattered electron (BSE) imagery, secondary electron (SE) imagery, and energy dispersive spectroscopy were used to identify mineral species and textures. Polished thin sections were prepared without the use of water to preserve the original texture of swelling clay minerals as much as possible. Wavelength dispersive spectroscopy (WDS) was used to map the spatial distribution of elements and determine the chemical composition of mineral phases with operational conditions dependent on the phase being targeted for analysis. The following mineral standards were used for the WDS analysis of clay minerals: Albite Amelia, Orthoclase CM Taylor, Anorthite Smithsonian USNM 13704, Diopside Smithsonian USNM 117733. Clay minerals were analyzed at 15 kV accelerating voltage, 10 nA probe current and a 2  $\mu\text{m}$  spot size. Aluminum, magnesium, potassium and iron were targeted due to their common associations with octahedral cation coordination (Al, Mg, and Fe) or interlayer occupation (K, e.g., illite) in clay minerals (Brindley and Brown 1980). The combined average reproducibility was  $\pm 3\%$  with  $\pm 5\%$  accuracy. Only sample data with totals  $> 80$  weight % (wt. %) were included in the results (Appendix A).

X-ray diffraction and isotopic analysis of clay minerals were conducted at the Laboratory for Stable Isotope Science (LSIS) at The University of Western Ontario. Sample material was selected with the goal of isolating clay minerals associated with clasts and matrix material where possible and ground to a fine powder by hand using an agate mortar and pestle. Back-packed mounts of randomly oriented, bulk sample powders and  $<2\ \mu\text{m}$ ,  $2\text{--}0.2\ \mu\text{m}$ , and  $<0.2\ \mu\text{m}$  separates were prepared for analysis by powder X-ray diffraction (pXRD) following the methods of Libbey et al. (2013). A Rigaku Rotaflex RU-200B series X-ray diffractometer, equipped with a Co-rotating anode source (Co  $K\alpha$ ,  $\lambda = 1.7902\ \text{\AA}$ ) and operated at 45 kV accelerating voltage and 160 mA tube current, was used in this study. All XRD scans were conducted at  $10^\circ\ 2\theta$  /min, using a step-size of  $0.02^\circ\ 2\theta$ . Differing scanning ranges were used where appropriate for the various treatments applied to the separates as outlined below.

Bulk powders were gently back-packed into steel sample holders with a glass base and scanned from  $2\text{--}82^\circ 2\theta$ . Initially,  $<2\ \mu\text{m}$  size-fraction separates were prepared by suspension and centrifugation, and then subsequently treated with 6% sodium hypochlorite and set in a water bath at  $65\ ^\circ\text{C}$  for  $\sim 12$  hours. Treatment with sodium hypochlorite was performed to oxidize remnant organics, but also caused  $\text{Na}^+$  to become the dominant exchangeable cation on the clay minerals. Samples were then separated into aliquots that were saturated with 2M  $\text{CaCl}_2$  and KCl, respectively, causing  $\text{Ca}^{2+}$  and  $\text{K}^+$  to become the dominant exchangeable cation in their respective aliquots.

Following the procedures of Ignasiak et al. (1983) and McKay and Longstaffe (2013), a portion of each aliquot was pipetted onto a glass slide to establish a preferred (00 $l$ ) clay mineral orientation, and air-dried. Ca-saturated samples were scanned from  $2\text{--}42^\circ 2\theta$  after remaining in a 54% relative humidity (RH) hydration chamber (achieved using a saturated Mg-nitrate solution) at room temperature (RT) overnight. Ca-saturated samples were subsequently vapour-solvated with ethylene glycol (EG) in a sealed chamber at  $65\ ^\circ\text{C}$  overnight, allowed to further equilibrate at RT for 24 hours, and then scanned from  $2\text{--}82^\circ 2\theta$ . K-saturated samples were analyzed from  $2\text{--}42^\circ 2\theta$  at 0% RH (achieved by drying at  $107\ ^\circ\text{C}$  for 12 h), 54% RH at RT (as for Ca-saturated samples), then at  $300\ ^\circ\text{C}$  (achieved by heating for at least two hours prior to analysis), and finally at  $550\ ^\circ\text{C}$  (achieved by heating for at least 3 hours prior to analysis). These techniques were used because swelling clay minerals such as smectite exhibit characteristic changes in XRD (d(00 $l$ )) behavior that are dependent upon interlayer cation composition, relative humidity and heating (Brindley and Brown, 1980). These techniques were only applied to the full suite of  $<2\ \mu\text{m}$  size-fraction separates, and a smaller subset of the  $2\text{--}0.2$  and  $<0.2\ \mu\text{m}$  size-fraction separates. Front-packed mounts of K-saturated, randomly oriented,  $<2\ \mu\text{m}$ ,  $2\text{--}0.2\ \mu\text{m}$ , and  $<0.2\ \mu\text{m}$  size-fraction separates were scanned from  $58$  to  $78^\circ 2\theta$  at  $2^\circ 2\theta/\text{min}$  to highlight the d(060) peaks, which can indicate whether the present clay minerals are dioctahedral or trioctahedral.

The diffraction patterns obtained from *p*XRD data of bulk powders were analyzed by hand, and in partial conjunction with the *DIFFRAC.EVA* software package using the International Center for Diffraction Data (ICDD) mineral database, and *Profex-BGMN*, an

open source XRD and Rietveld refinement software package (Doebelin and Kleeberg, 2015), using the standard Bergman (BGMN) internal structural reference files. Diffraction patterns resulting from analyses of preferentially oriented separates were analyzed strictly by hand with interpretations guided using Brindley and Brown (1980) and Moore & Reynolds (1997).

Oxygen and hydrogen isotope analyses were performed at LSIS at The University of Western Ontario. K-saturated separates of  $<2 \mu\text{m}$ ,  $2\text{--}0.2 \mu\text{m}$ , and  $<0.2 \mu\text{m}$  from all twelve selected samples were analyzed for  $\delta^2\text{H}$  and  $\delta^{18}\text{O}$ . All oxygen and hydrogen isotope compositions reported here are expressed using the normal  $\delta$ -notation in parts per thousand (‰) relative to Vienna Standard Mean Ocean Water (VSMOW).

Oxygen isotope analyses were performed in accordance with methods developed by Borthwick & Harmon (1982) and Clayton & Mayeda (1963). Prior to analyses, samples in which carbonates were detected by *p*XRD were mixed with 2 mL of 1 M HCl and were allowed to react for 2 hours at room temperature. An additional 1 mL of 1 M HCl was subsequently added, and the sample observed for fizzing prior to being allowed to react overnight. If fizzing was observed, an additional 1 mL of 1 M HCl was added the following day, and the process repeated.

Approximately 7.5 mg of each sample was heated at 150 °C for 12 hours to expel water adsorbed to the surface of the sample and held in smectite interlayers. Internal laboratory standards (quartz: ORX, and kaolinite: KGa-1) were heated under vacuum alongside the samples under the same conditions. Samples and standards were then heated at 150 °C for an addition 3 hours after transferring to a nickel reaction vessel to maximize the removal of interlayer and surface water. Cryogenic transfer by  $\text{N}_{2(l)}$  was used to add a stoichiometric excess of  $\text{ClF}_3$  and the reaction vessels were exposed to vacuum conditions again to expel non-condensable gases. The vessels were then sealed and reacted overnight at 550 °C. Liquid nitrogen was used to separate oxygen from the waste reagent and other compounds. Oxygen was subsequently converted to  $\text{CO}_2$  for use in isotopic analysis by exposure to carbon heated to temperatures in excess of 550 °C to produce a red iridescence. A VG Optima triple-collecting, dual-inlet isotope-ratio mass-spectrometer (IRMS) was used to obtain oxygen isotope analyses. The combined average reproducibility for the  $<2$ ,  $2\text{--}0.2$ ,

and  $<0.2 \mu\text{m}$  samples was  $\pm 0.15 \text{ ‰}$  ( $n=7$ ). Internal laboratory standards calibrated to VSMOW-SLAP, quartz (ORX), kaolinite (KGa-1) and gas standard  $\text{CO}_2$  yielded  $+11.70 \pm 0.17 \text{ ‰}$  (average,  $n=5$ ),  $+21.07 \pm 0.55 \text{ ‰}$  (average,  $n = 5$ ), and  $+10.11 \pm 0.05 \text{ ‰}$ , respectively, showing good agreement with their accepted values of  $+11.5 \text{ ‰}$ ,  $+21.5 \text{ ‰}$ , and  $+10.2 \text{ ‰}$ , respectively.

Hydrogen isotope analyses were performed in accordance with best practices outlined by Bauer and Vennemann, (2014), Kanik et al. (2022), Qi et al. (2017), Sharp et al. (2001) and Vandevelde & Bowen (2013). Sample portions treated with HCl for the removal of carbonates were not used for hydrogen isotope analysis. Approximately 1.5 mg of each sample, 2.5 mg of USGS 58 (muscovite) and 3.5 mg of each of USGS 57 (biotite) and GBS (internal biotite standard) were gently packed into 5 x 3.5 mm silver capsules. The powders were heated at  $220 \text{ }^\circ\text{C}$  under vacuum for 24 hours to expel adsorbed and interlayer water. The samples were then transferred into a Costech Zero Blank autosampler. All samples were then transferred into the autosampler in less than four minutes to minimize contamination from atmospheric moisture. The autosampler was then sealed and purged with He gas for a minimum of 10 minutes. Powders deposited in the autosampler were then combusted at  $1450 \text{ }^\circ\text{C}$  in a Thermo Scientific<sup>TM</sup> Thermal Combustion Elemental Analyzer (TC-EA), which generated a  $\text{H}_2$  gas to be subsequently purified using a 1 m-long gas chromatographic (GC) column, which was heated to  $120 \text{ }^\circ\text{C}$  and contained 0.5 nm molecular sieves.  $\text{H}_2$  gas from the samples and standards were transported in He gas, using the TC-EA's continuous flow function, to a Thermo Scientific Delta XL Plus<sup>TM</sup> IRMS. The combined average reproducibility of the  $2\text{--}0.2$  and  $<0.2 \mu\text{m}$  size-fractions was  $+1.9 \text{ ‰}$  ( $n = 8$ ). Internal laboratory standards were calibrated to VSMOW-SLAP using USGS57 (biotite) and USGS58 (muscovite), which have accepted  $\delta^2\text{H}$  of  $-91.5 \text{ ‰}$  and  $-28.4 \text{ ‰}$ , respectively (Qi et al. 2017), and were reproducible to  $\pm 0.8 \text{ ‰}$  (SD,  $n = 4$ ) and  $\pm 1.0 \text{ ‰}$  (SD,  $n = 4$ ), respectively. Accuracy was evaluated using the GBS biotite internal laboratory standard, calibrated to VSMOW-SLAP, which yielded a  $\delta^2\text{H}$  of  $-63.4 \pm 1.0 \text{ ‰}$  (SD,  $n = 12$ ) as compared to its accepted value of  $-64 \pm 2 \text{ ‰}$ . Hydrogen isotope measurements were performed in duplicate and those values averaged for use in this study.

## 3.4 Results

### 3.4.1 Clay Mineral Chemistry

Maps of the relative elemental abundances (counts) and spatial distribution of the clay minerals in the basal conglomerates, determined by WDS mapping, show a strong association of the clay minerals with aluminum and a lesser association with iron and magnesium. The association between clay minerals in the basal conglomerates and mainly aluminum is consistent, regardless of the changing clay mineral textures (Fig. 3.3A–D). Further semi-quantitative analyses by WDS show that the oxide content (in wt.%) of aluminum in clay minerals is typically ~10–20 % across the transition from melt-bearing breccias to marlstones (Fig. 3.4A; Table 3.2). Potassium, usually associated with illitic clay minerals, exhibits a range of compositions from  $K_2O = \sim 0.8\text{--}2\%$  in the melt-bearing breccias and basal conglomerates. The potassium content gradually increases up-section through the sandstone conglomerate and marlstones to ~2.5–3.5 % (Fig. 3.4B). The oxide weight percent of iron generally decreases along the transition from melt-bearing breccias to marlstones. The lower basal conglomerates (RW19 MTX) and melt-bearing breccias have iron oxide weight % of ~5 %, which decrease towards the upper reworked breccias, sandstone breccia and marlstones to ~4.2–3.5 % (Fig. 3.4C). The oxide weight percent of magnesium in clay minerals shows little change throughout the transition, yielding values of ~2.5–3.2 % (Fig. 3.4D). The chemical composition of the clay minerals is averaged in Table 3.2, and fully documented in Appendix A. Smectitic clay minerals with honeycomb textures (Chapter 2; Fig. 3.3A) typically yielded chemical totals <80 %, so only 4 / 51 points could be included in the results. This cut-off was selected to isolate the highest possible totals with the data available, as most totals were ~80–85% with some <70 %.

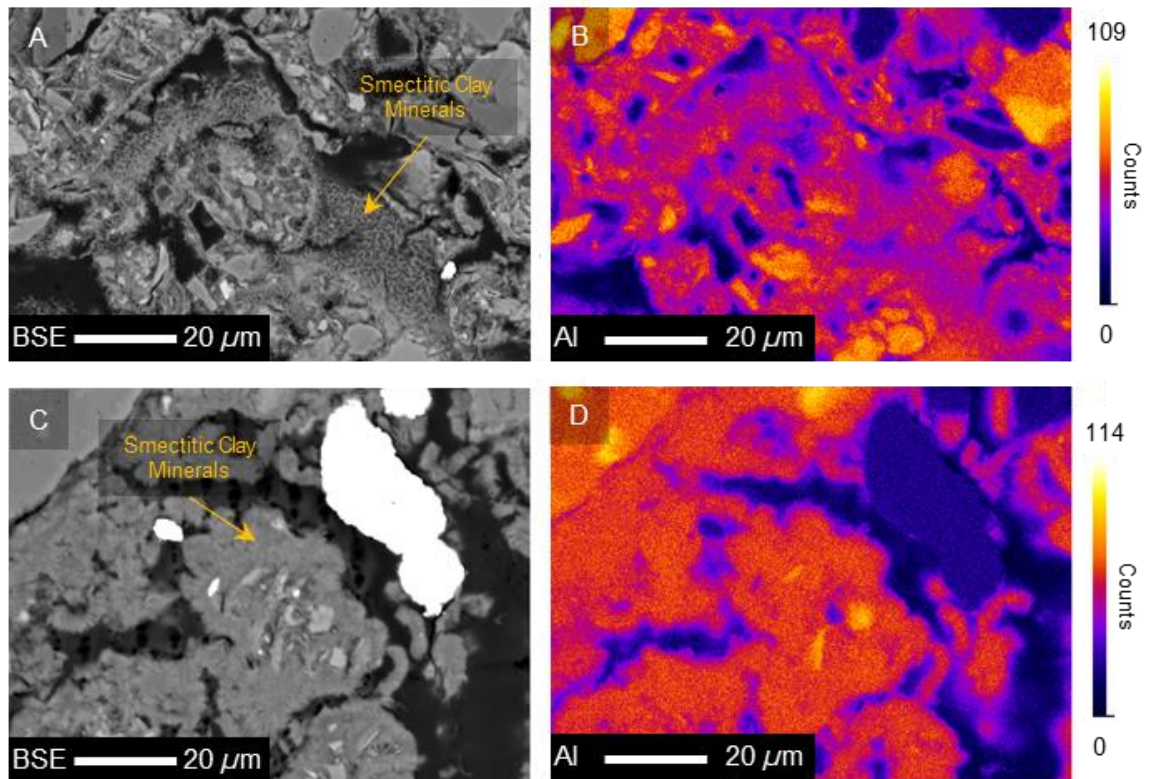


**Figure 3. 3:** Back-scattered electron and WDS images of clay minerals occurring in unit 13 (A, B, respectively; sample label: RW19) and unit 11 (C, D, respectively; sample label RW14.78). False color WDS maps highlight the distribution of aluminum throughout the area pictured in the accompanying BSE images.

**Table 3. 2:** Summary of averaged WDS analysis of clay minerals.

Oxide	Grey Toned Melt-Bearing Breccia (Unit 14, RW22)		Pink Conglomerate (Unit 13, RW19)*		Grey Conglomerate (Unit 11, RW14.33)		Sandstone Conglomerate (Unit 9, RW12.74)		Marlstone (Units 6. RW9.6 Gry.**)	
	Mean Wt. %	2 $\sigma$	Mean Wt. %	2 $\sigma$	Mean Wt. %	2 $\sigma$	Mean Wt. %	2 $\sigma$	Mean Wt. %	2 $\sigma$
SiO <sub>2</sub>	55.59	2.64	56.10	4.02	54.16	3.42	50.89	4.01	50.94	2.59
Al <sub>2</sub> O <sub>3</sub>	17.07	1.83	15.04	4.04	17.73	2.49	15.83	1.52	21.35	1.96
Na <sub>2</sub> O	1.22	2.27	1.38	1.58	0.63	1.34	0.87	0.84	0.20	0.09
MgO	2.38	0.66	2.03	0.71	3.33	1.03	3.47	0.70	2.81	0.38
CaO	2.40	1.87	1.30	0.55	1.44	1.30	2.91	1.67	1.07	0.91
K <sub>2</sub> O	0.86	0.23	1.29	0.72	1.70	1.38	2.88	0.79	3.33	0.42
FeO	4.91	1.18	4.13	1.05	4.04	1.49	4.32	1.31	4.13	0.52
Total	84.43	5.82	81.27	2.74	83.18	2.73	82.64	2.90	83.84	2.73
n	26		4		27		9		32	

\*Clay minerals in the pink conglomerates generally had honeycomb textures and yielded a low number of usable analyses (n).

\*\*Gry. stands for “grey”, and indicates data collected from the grey-toned material in the marlstone.

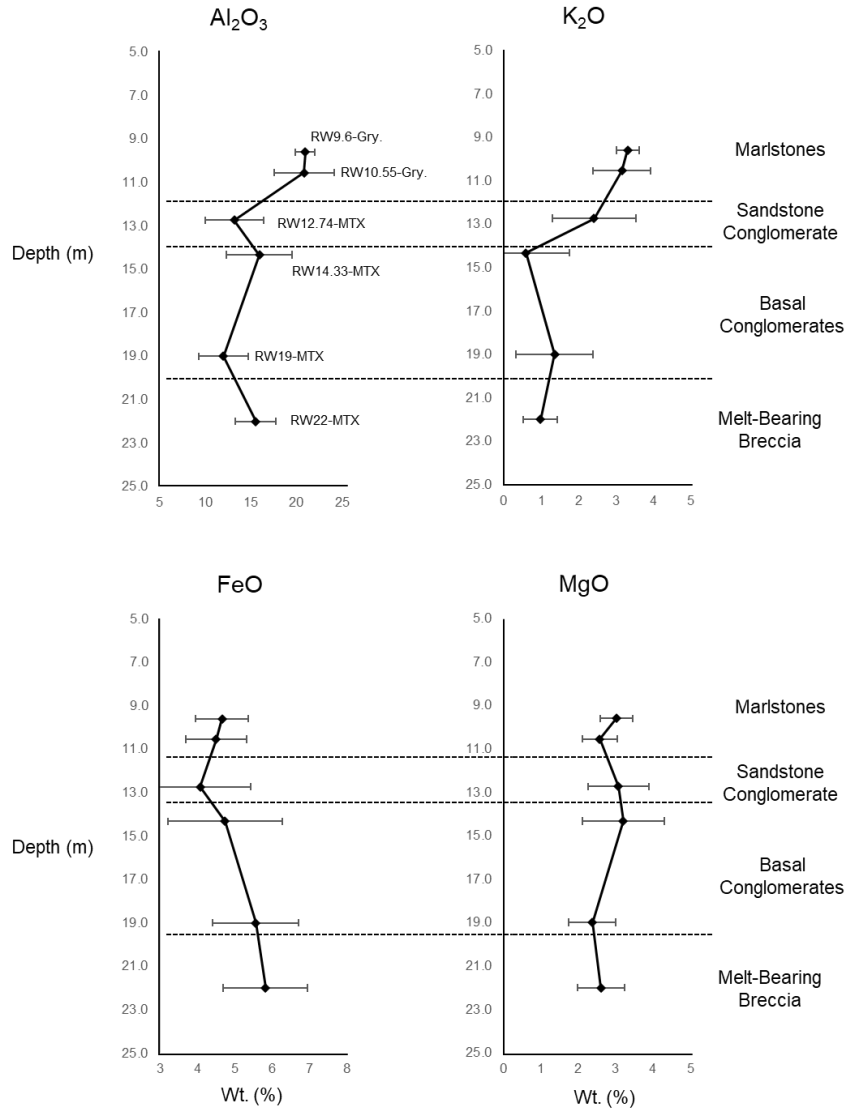


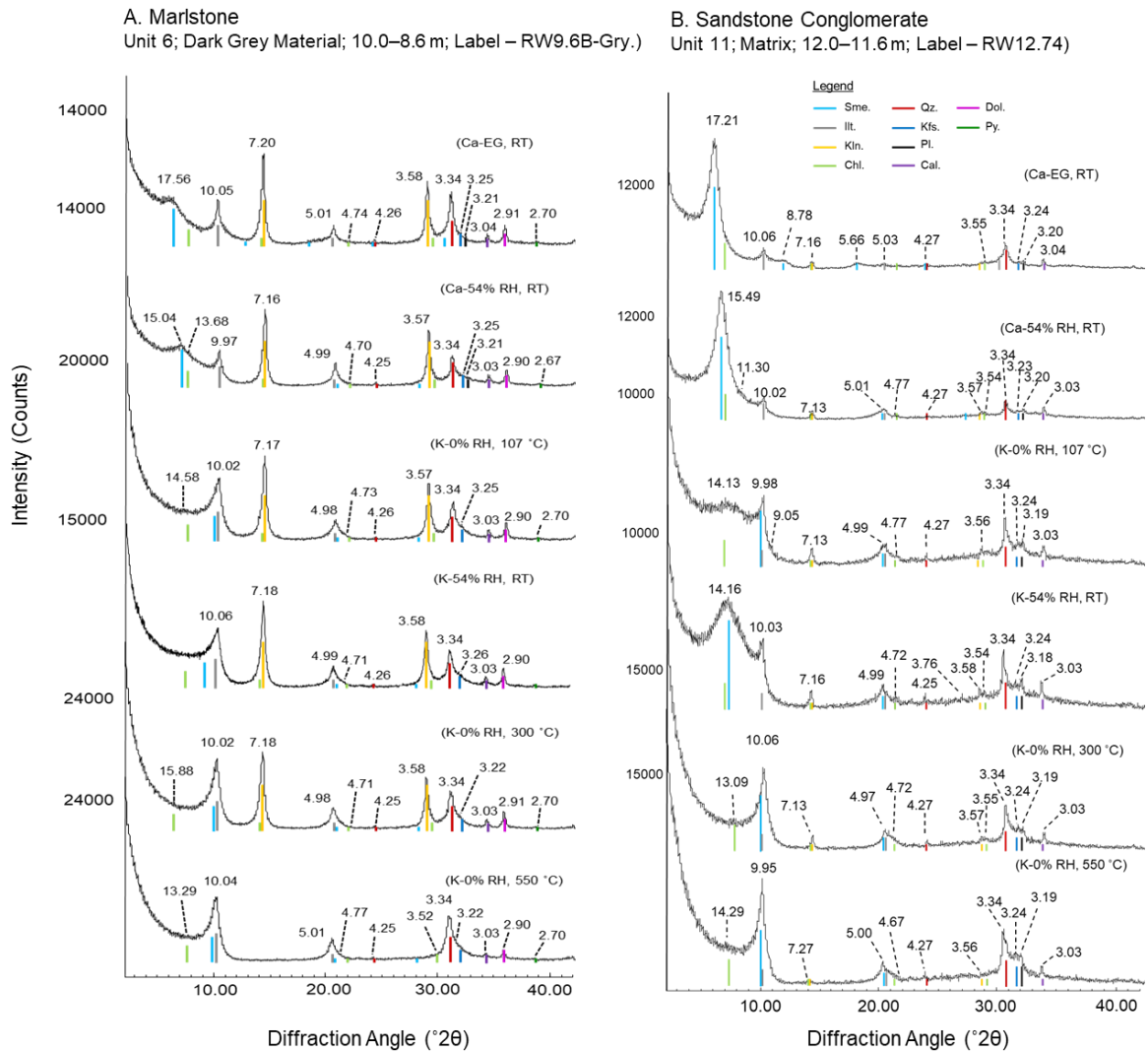
**Figure 3. 4:** Metal oxide abundances (wt.%) of interstitial and void-filing clay minerals as determined by WDS spot analyses. Associated sample labels are denoted next to each point and are applicable to all plots. The points on each diagram comprise an average of multiple spot analyses performed on a single unit. These units are units 14, 13, 11, 9, 7 and 6 from bottom to top, respectively. The number of analyses performed for each unit are as follows: n = 21 (grey-toned melt-bearing breccia; unit 14; RW22-MTX), n = 4 (pink conglomerate; unit 13; RW19-MTX), n = 27 (grey conglomerate; unit 11; RW14.33-MTX), n = 9 (sandstone conglomerate; unit 9; RW12.74-MTX), n = 19 (marlstone; unit 7; RW10.55-Gry.), n = 13 (marlstone; unit 6; RW9.6-Gry.). Error bars represent the standard deviation of the averaged data used to generate each point on the plot.

### 3.4.2 Clay Mineralogy by X-ray Diffraction

Analysis by *p*XRD of the  $<2\ \mu\text{m}$ ,  $2\text{--}0.2\ \mu\text{m}$ , and  $<0.2\ \mu\text{m}$  separates indicated a mixture of clay minerals, quartz, carbonates, and feldspars in all samples. Clay minerals are present in all size-fractions and appear to be the only phase present in the  $<0.2\ \mu\text{m}$  size-fraction (Appendix A). In the absence of more detailed clay mineral analysis of the  $2\text{--}0.2\ \mu\text{m}$ , and  $<0.2\ \mu\text{m}$  separates, the present study focuses on results from *p*XRD scans of the  $<2\ \mu\text{m}$  size-fraction, unless otherwise stated. Generally, upon Ca-saturation and solvation with ethylene glycol (EG), the XRD patterns presented smectitic d(001) peaks at 17.56–17.01 Å (Fig. 3.5). Additionally, illitic d(001) peaks were detected at 10.06–10.00 Å (Ca-EG), and 10.02–9.96 Å (Ca-54% RH; Fig. 3.5). K-saturation, air drying, and heating at 300 °C and 550 °C generally resulted in the collapse of the smectitic d(001)  $\sim$ 17 Å peaks and triggered a notable broadening and shift of peaks at  $\sim$ 10 Å, such that 10.00 Å (Ca-EG) shifted to 9.83 Å (K-550°C), typically with notable asymmetry on the low  $2\theta$  side of the peak (Fig. 3.5). The low  $2\theta$  side of these peaks produce a “saddle” feature that can be typical of interstratified illite-smectite (Inoue et al., 1989). This feature is most prevalent in the conglomerate units (units 13–11). The saddle remains present during heating at 107 °C, 300 °C and 550 °C (Fig. 3.5) – a treatment which additionally reveals peaks ranging from 15.88 Å to 13.29 Å in multiple samples (Fig. 3.5). Additionally, peaks at  $\sim$ 7.15 Å and 3.58 Å consistently disappeared completely at 550 °C, indicating the presence of kaolinite. The occurrence of 3.55 Å peaks with varying degrees of clear distinction from kaolinite d(002) 3.58 Å peaks indicated an additional chlorite component in many samples (Fig. 3.5). Heating to 550 °C does not consistently isolate the chlorite d(004) 3.54 Å peak as it commonly collapses, contributing to a broad, asymmetric 3.32–3.30 Å peak. Peaks at 3.34 Å, 3.23–3.19 Å, 3.03 Å and 2.90 Å indicate the presence of quartz, K- and plagioclase feldspars, calcite and dolomite, respectively. These peaks were detected in the  $<2\ \mu\text{m}$  size-fractions of most samples (Figs. 3.5A–D).

Interpretation of the d(060) region in the  $<2\ \mu\text{m}$  separates was complicated by the presence of a quartz diffraction at  $\sim$ 1.54 Å thus preventing accurate determination of the dioctahedral versus trioctahedral nature of the clay minerals. The few *p*XRD scans obtained of the  $<0.2\ \mu\text{m}$  size-fraction show that they are dominated by clay minerals and are quartz-

free. Analysis of d(060) peaks obtained for these  $<0.2 \mu\text{m}$  separates revealed the dioctahedral nature of the clay minerals present (Appendix A).



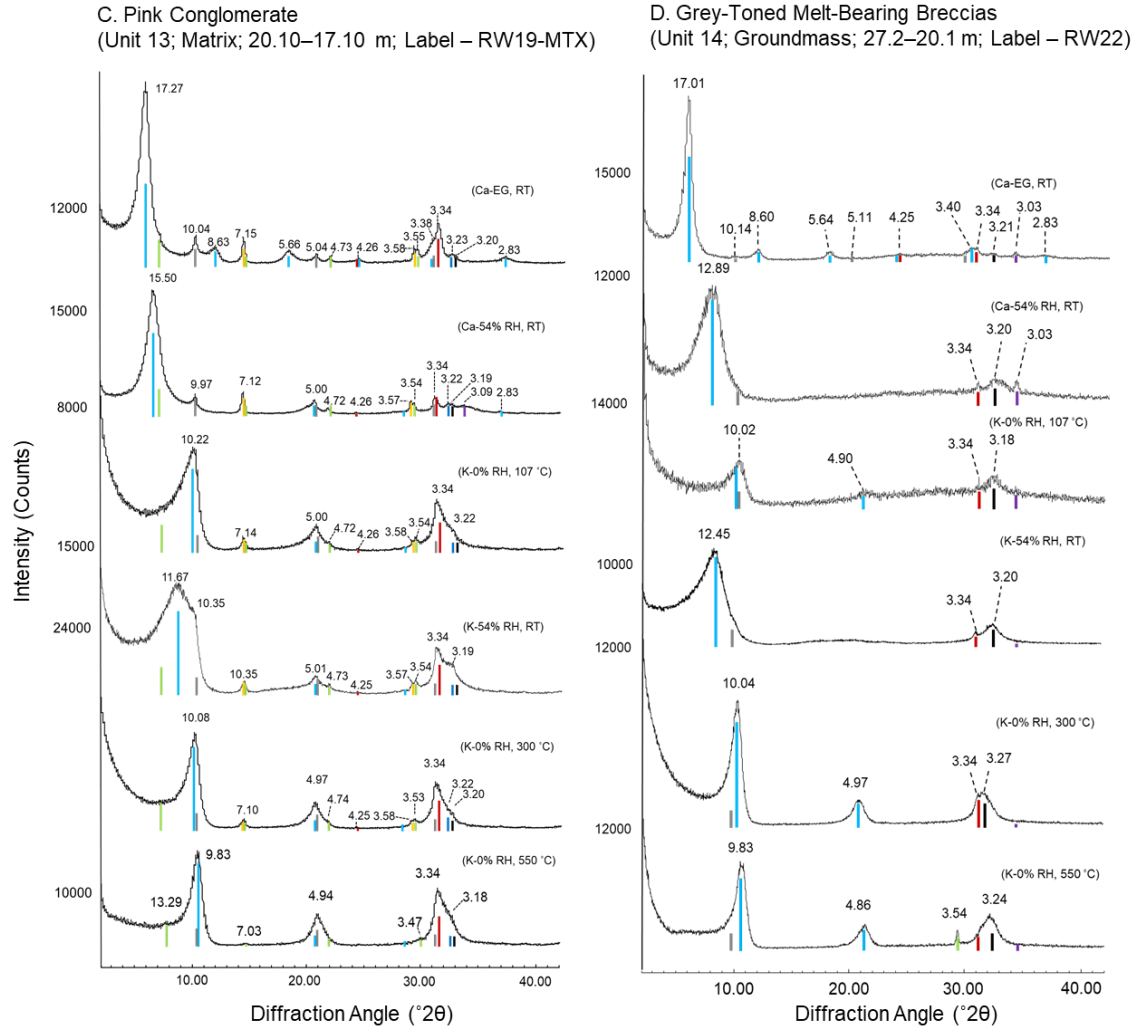


**Figure 3. 5:** Diffraction patterns collected from the  $<2 \mu\text{m}$  size-fraction of specific samples from major unit groups in the upper 32 m of the Wörnitzostheim drill core, stacked for clarity. (A) marlstones, (B) sandstone conglomerate, (C) pink conglomerate (D) grey-toned melt-bearing breccia. Each diffraction pattern was collected from samples with preferred basal orientation after various treatments were applied as labelled on each diagram. Ca = calcium-saturated; K = potassium-saturated; EG = ethylene-glycol saturated; RT = room temperature; RH = relative humidity.

### 3.4.3 $\delta^2\text{H}$ and $\delta^{18}\text{O}$ Measurements

Measurements of  $\delta^{18}\text{O}$  were obtained for  $<2\ \mu\text{m}$ ,  $2\text{--}0.2\ \mu\text{m}$ , and  $<0.2\ \mu\text{m}$  separates, and for  $\delta^2\text{H}$  for  $2\text{--}0.2\ \mu\text{m}$  and  $<0.2\ \mu\text{m}$  separates (Appendix A; Table 3.3). The  $\delta^{18}\text{O}$  of the  $<2\ \mu\text{m}$ ,  $2\text{--}0.2\ \mu\text{m}$ , and  $<0.2\ \mu\text{m}$  separates range from  $+9.8$  to  $+23.4\ \text{‰}$  (Table 3.3; Fig. 3.6). Except for the marlstone samples, the  $\delta^{18}\text{O}$  values of the  $2\text{--}0.2\ \mu\text{m}$  size-fraction are lower than those for the  $<2$  and  $<0.2\ \mu\text{m}$  separates with  $<0.2\ \mu\text{m}$  separates yielding the highest  $\delta^{18}\text{O}$ . The  $\delta^2\text{H}$  values range from  $-129$  to  $-61\ \text{‰}$  (Table 3.3; Fig. 3.6) and display notable differences between size-fractions:  $2\text{--}0.2\ \mu\text{m}$ ,  $-114$  to  $-61\ \text{‰}$ , and  $<0.2\ \mu\text{m}$ ,  $-129$  to  $-98\ \text{‰}$ . The marlstones have distinctly less negative  $\delta^2\text{H}$  than other units studied here and corresponds with a shift in the dominant clay mineralogy from smectite to illite and kaolinite. The  $\delta^2\text{H}$  also trends towards less negative values with depth within the basal conglomerate unit group: ranging from  $-118\ \text{‰}$  ( $<0.2\ \mu\text{m}$ ) at the base of the basal conglomerate unit group (unit 13; 20.1 m) to  $-129\ \text{‰}$  ( $<0.2\ \mu\text{m}$ ) at the top (unit 11; 13.1 m; Table 3.3; Fig. 3.6). Other units generally show little within-unit variation in  $\delta^2\text{H}$ . The  $\delta^2\text{H}$  of the  $<0.2\ \mu\text{m}$  and  $2\text{--}0.2\ \mu\text{m}$  separates follow the same trends within the context of the entire dataset (i.e., if the  $\delta^2\text{H}$  values of the  $<0.2\ \mu\text{m}$  size-fraction increases with depth, so does that of the  $2\text{--}0.2\ \mu\text{m}$ ), except for the pink-toned, melt-bearing breccia sampled at 32 m depth where the  $\delta^2\text{H}$  of the  $2\text{--}0.2\ \mu\text{m}$  size-fraction notably increased.

**Table 3. 3:**  $\delta^{18}\text{O}$  and  $\delta^2\text{H}$  results for the 2–0.2, <2 and <0.2  $\mu\text{m}$  size-fractions.

Sample Context		$\delta^{18}\text{O}$ (‰, VSMOW)			$\delta^2\text{H}$ (‰, VSMOW)*							
Lithology	Sample Label	Unit #	Material	Depth (m)	2–0.2 $\mu\text{m}$	<2 $\mu\text{m}$	<0.2 $\mu\text{m}$	2–0.2 $\mu\text{m}$	<0.2 $\mu\text{m}$	Individual Values	Average	Individual Values
Marlstones	RW9.6A	6	White material	9.60	+17.5	+19.6	+19.5	-61	(-77, -46)	-107	(-105, -109)	
	RW9.6B	6	Dark grey material	9.60	+16.4	+20.7	+19.8	-68	(-68, -68)	-98	(-99, -96)	
Sandstone Conglomerates	RW12.74	9	Matrix	12.74	+15.1	+17.1	+18.7**	-108	(-108, -109)	-129	(-130, -128)	
Altered Grey Conglomerates	RW14.33-CLST	11	Clasts	14.33	+13.3	+15.3	+18.2	-102	(-106, -103)	-129	(-126, -127)	
	RW14.33-MTX	11	Matrix	14.33	+13.6	+16.5	+18.2	-105	(-103, -101)	-126	(-128, -130)	
Grey Conglomerates	RW14.78-MTX	11	Matrix	14.78	+16.2	+18.3	+21.0	-101	(-100, -102)	-124	(-125, -123)	
	RW16.16-MTX	11	Matrix	16.16	+12.2	+18.5	+21.1	-86	(-87, -85)	-121	(-119, -123)	
	RW16.16-CLST	11	Clasts	16.16	+12.5	+19.6	+20.9	-96	(-95, -97)	-119	(-117, -120)	
Pink Conglomerates	RW19-CLST	13	Clasts	19.00	+12.5	+16.5	+19.5	-93	(-92, -93)	-120	(-119, -120)	
	RW19-MTX	13	Matrix	19.00	+13.9	+16.4	+19.8	-90	(-89, -90)	-118	(-117, -119)	
Grey-Toned Melt-Bearing Breccias	RW22	14	Matrix	22.00	+18.4	+19.1	+23.4	-114	(-116, -112)	-125	(-124, -126)	
Pink-Toned Melt-Bearing Breccias	RW32	15	Matrix	32.00	+9.8	+11.8	+18.4	-93	(-90, -96)	-129	(-129, -129)	

\*The  $\delta^2\text{H}$  (‰, VSMOW) averages are utilized in all following diagrams and interpretations.

\*\* The  $\delta^{18}\text{O}$  (‰, VSMOW) reported for 12.74 m depth is an average of three measurements: 18.6, 18.8, and 18.6 ‰.

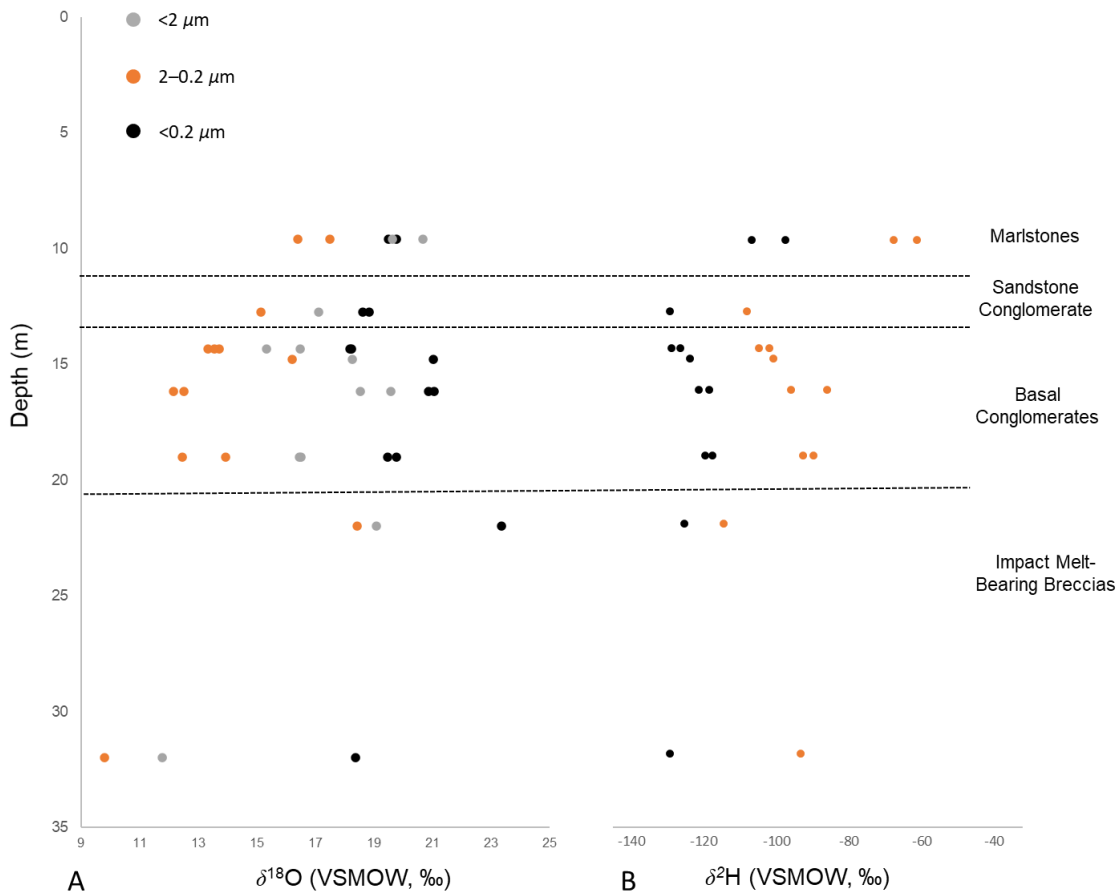


**Figure 3. 6:**  $\delta^{18}\text{O}$  (A) and  $\delta^2\text{H}$  (B) of samples collected from melt-bearing breccias, main conglomerates, sandstone conglomerates, and marlistones.  $\delta^{18}\text{O}$  values are reported for  $<2$ ,  $2\text{--}0.2$  and  $<0.2\ \mu\text{m}$  separates;  $\delta^2\text{H}$  values are reported for  $2\text{--}0.2$  and  $<0.2\ \mu\text{m}$  separates.

## 3.5 Discussion

### 3.5.1 Clay Mineralogy

Generally, the  $<2\ \mu\text{m}$  size-fraction is impure, which is indicated by the *p*XRD results (Figs. 3.5A–D) and reflected in the  $\delta^2\text{H}$  and  $\delta^{18}\text{O}$  results (Fig. 3.6). The  $<2\ \mu\text{m}$  size-fraction typically consists of a heterogeneous mixture of different clay minerals in addition to non-clay minerals such as quartz, feldspars, dolomite and calcite. Detrital phases in the  $<2\ \mu\text{m}$  size-fraction possibly include muscovite and biotite micas (Chapter 2). The few available *p*XRD analyses of the  $2\text{--}0.2\ \mu\text{m}$  size-fraction indicate that non-clay minerals are

concentrated in that size-fraction; this pattern is also reflected in the clear distinction in  $\delta^{18}\text{O}$  between the different size-fractions (Fig. 6). The prevalence of aluminum, as indicated by the WDS spot analyses and WDS maps, and the consistent 1.50 Å d(060) peak, suggests that the dominant smectitic clay mineral throughout this suite of samples could be montmorillonite or beidellite. Illite would exhibit a similar association with aluminum and show a 1.50 Å d(060) peak; however, illite peaks are too muted to indicate its presence as a dominant phase (Figs. 3.5A–D). The Ca-54%-RH treatments show smectite d(001) ranging from 15.50 to 12.89 Å. The geochemical trends shown in Figure 3.4 likely represent stoichiometric differences arising from varying clay mineralogy rather than geochemical trends in the system.

The <2  $\mu\text{m}$  size-fraction of the impact melt-bearing breccias is dominated by smectite. The main clay mineral phase in the post-impact sedimentary deposits, however, is likely not just smectite, given the 15.88–13.29 Å peaks present in several major units (Figs. 3.5A–D), and the consistent incomplete collapse of smectite d(001) peaks during heating. The presence of material interlayered with smectite is likely. The basal d(00 $l$ ) reflections of smectite, illite and kaolinite all produce a rational series of peaks with relatively sharp d(001) peaks (Figs. 3.5A–D), indicating that kaolinite and illite are not likely to comprise the interlayer material (Figs. 3.5A–D; Brindley and Brown 1980). Chlorite peaks are too weak to determine the rationality of its d(00 $l$ ) peaks. Minor chloritic phases would produce peaks in the region of 14.20 Å, so a discrete chloritic clay mineral could potentially be responsible for the 15.88–13.29 Å peaks, and possibly the incomplete collapse of the smectite d(001) peaks upon heating. Similarly, the presence of hydroxy-interlayer material and organics is possible and could be responsible for the incomplete collapse of smectite d(001) peaks. Hydroxy-interlayered material is defined by (Barnhisel & Bertsch (1989) as a solid-solution series between smectite, vermiculite and Al-chloritic end members. The occurrence of smectite d(001) peaks at ~17 and ~15 Å is not necessarily consistent with the presence of hydroxy interlayer material (Barnhisel and Bertsch, 1989; Meunier, 2007) but their presence cannot be definitively ruled out. Most remnant organics would be oxidized by treatment with sodium hypochlorite; however, recalcitrant organic matter could survive on clay mineral surfaces. It is unclear what the exact nature of the interlayered material is; thus, we continue to use “smectite” and “smectitic clay mineral” as the main descriptor of

swelling clay minerals in the discussion below. We use the saddle method described in Inoue et al. (1989) to roughly estimate the % of interlayer material in the smectitic clay mineral. We acknowledge that the saddle method is intended for use with mixed layer illite-smectite; however, without a detailed characterization of the interlayer material, it presently provides the best means of roughly estimating its quantity. The % abundance of interlayered material mixed with the smectitic clay minerals are highlighted in parentheses in Table 3 where applicable.

The % abundance of each clay mineral was estimated using the background-subtracted peak heights of d(001) peaks with weighting factors similar to the methods described in Biscaye (1965). These abundance estimates are primarily used for modeling the isotopic composition of possible waters from which clay minerals formed (hereafter: clay mineral source waters), so pure clay mineral samples are necessary for analysis. The  $<2 \mu\text{m}$  size-fraction of each sample generally contains non-clay mineral contaminants, whereas the few *p*XRD analysis of the  $<0.2 \mu\text{m}$  size-fraction indicate the presence of purely clay minerals. In cases where *p*XRD scans of the  $<0.2 \mu\text{m}$  size-fraction could not be collected, the mineralogy of the  $<2 \mu\text{m}$  size-fraction was used to estimate the  $<0.2 \mu\text{m}$  clay mineralogy. The clay mineralogy of the  $<2 \mu\text{m}$  size-fraction was assumed contain the same clay minerals as the  $<0.2 \mu\text{m}$  size-fraction, and it was assumed that the  $<0.2 \mu\text{m}$  size-fraction would consist of 100 % clay. The abundance of non-clay minerals was estimated using the same method used to estimate the abundance of clay minerals. The abundance of non-clay minerals was subtracted from the overall % composition of the  $<2 \mu\text{m}$  size fraction, and the remainder was normalized to 100 % clay, thus providing an approximation for the  $<0.2 \mu\text{m}$  size-fraction. This approach carries the caveat that some clay minerals could remain in the  $2\text{--}0.2 \mu\text{m}$  size fraction, and that the  $<2 \mu\text{m}$  size-fraction could contain detrital clay minerals that would not appear in the  $<0.2 \mu\text{m}$  size-fraction. These caveats cannot be mitigated presently but are taken into consideration when interpreting the results. The abundances of clay minerals in each sample, normalized to 100 % clay minerals, are summarized in Table 3.4. These estimates are used as a guide for interpreting isotopic data discussed in sections 3.5.3.

**Table 3. 4:** Clay mineral abundances\* for the Ca-EG saturated <0.2  $\mu\text{m}$  size-fractions

Lithology	Label	Depth (m)	Material	% Sme. **	% Chl.	% Ill.	% Kln.
Marlstone	RW9.6B	9.6	Dark grey material	10	0	45	45
	RW9.6A	9.6	White material	5	0	40	55
Sandstone							
Conglomerate	RW12.74	12.74	Matrix	55 (0.4)***	5	35	5
Altered Grey Conglomerate	RW14.33- ALT	14.33	Clast	95 (0.1)	0	5	0
	RW14.33- MTX	14.33	Matrix	85 (0.1)	0	10	5
Grey Conglomerate	RW14.78	14.78	Matrix	80 (0.2)	0	15	5
	RW16.16- ALT	16.16	Clast	80 (0.2)	0	15	5
	RW16.16- MTX	16.16	Matrix	80 (0.2)	0	15	5
Pink Conglomerate	RW19-CLST	19.0	Clast	80 (0.2)	0	15	5
	RW19-MTX	19.0	Matrix	55 (0.2)	5	25	15
Grey-Toned							
Melt-Bearing Breccia	RW22	22.0	Groundmass	100	0	0	0
Pink-toned							
Melt-Bearing Breccia	RW32	32.0	Groundmass	100	0	0	0

\*Clay mineral % abundance is rounded to nearest 5% and normalized to 100%.

\*\*Sme. = smectitic clay mineral as described in section 3.5.1.

\*\*\* (0.X), where indicated, represents the abundance of interlayered material expressed as a decimal fraction, following Inoue et al. (1989).

### 3.5.1.1 Melt-bearing breccias

The melt-bearing breccias are dominated by smectite (Table 3.4) with  $\sim 17.2$  Å d(001) peaks (Ca-EG; Fig. 3.5D). The primary source material for clay mineral formation in the melt-bearing breccia unit group was impact-generated glass in addition to some crystalline clasts and rare sedimentary clasts (Chapter 2). Given the well-formed “fluffy” textures exhibited by these clay minerals (Chapter 2), and the relative symmetry of the smectite d(001) peaks (Figs. 3.5A–D), these clay minerals have been interpreted as being mainly authigenic. The sharpness of the smectite d(001) peaks (Ca-EG; Fig. 5D) indicates relatively high crystallinity (Kübler, 1967; 1968; 1984; Frey, 1987; Kübler and Goy-Eggenberger, 2001), which is also consistent with earlier interpretations of an authigenic origin (Chapter 2). The minor, low  $2\theta$  angle saddle on the smectite d(001) peak could indicate some minor interlayering with chloritic, hydroxy or organic material, but the saddle method indicates essentially 0 % is interlayered with the smectitic clay mineral (Table 3.4).

### 3.5.1.2 Pink conglomerates (unit 13; 20.1–17.1 m)

The pink conglomerates are dominated by smectite with lesser contributions from illite and kaolinite, and only minor peaks indicating chlorite (Table 3.4). The overall symmetry and sharpness of the smectite d(001) peaks (Fig. 3.5C), and the rationality of the smectite, illite and kaolinite, d(00 $l$ ) diffractions from the basal conglomerate unit indicates relatively high crystallinity (Kübler, 1967; 1968; 1984; Frey, 1987; Kübler and Goy-Eggenberger, 2001), which could indicate authigenic origins; consistent with previous work (Chapter 2). A low  $2\theta$  angle saddle on the d(001) peak is more prominent in diffraction patterns from the pink conglomerate than those from the grey-toned melt-bearing breccia, which could indicate interlayering with chloritic, hydroxy or organic material (Table 3.4). The matrix-supported nature of the pink conglomerate (unit 13; Chapter 2) indicates that the origins of the clay minerals might not be entirely authigenic; however, detrital clay minerals emplaced during debris flow deposition (Chapter 2) could have been completely replaced by dissolution and reprecipitation during post-depositional chemical weathering. A likely scenario is that the smectite peaks represent a mixture of detrital and authigenic origins.

Illite and kaolinite present  $d(001)$  peaks with a similar sharpness to that of smectite and rational  $d(00l)$  series, and so we suggest that illite and kaolinite likely represent discrete authigenic clay minerals, like smectite. Kaolinite is more likely to form through in-situ authigenesis because, as a 1:1 layer clay mineral, kaolinite is less capable of existing in states of fine disaggregation and tends to occur as particles composed of relatively large numbers of associated layers (Bradley, 1953). The relatively high intensity of the kaolinite peaks could be indicative of higher  $\text{Al}_2\text{O}_3$  activity, and the illite peaks could similarly indicate higher  $\text{K}_2\text{O}$  activity, and moderate fluid alkalinity (Zhang et al., 2017). Under these conditions, illite and kaolinite could have formed by the dissolution and reprecipitation of similar source material to smectite. We also considered the possibility that chlorite could have formed at the expense of authigenic or detrital smectite. Moderate alkalinity (pH of 8.0–8.5), as potentially indicated by the presence of authigenic of illite, would be ideal for the formation of diagenetic chlorite from smectite by dissolution and reprecipitation through chemical weathering (Bradley, 1953). This chloritic component could have formed as an interlayered phase with smectite, but due to the low amounts of chlorite (Table 3.4, Fig. 3.5C), this possibility cannot be stated with certainty.

### 3.5.1.3 Grey conglomerates (unit 11; 16.6–13.1 m)

Like the pink conglomerates, the smectite  $d(001)$  peaks (Ca-EG) of the grey conglomerates exhibit relatively good overall symmetry and sharpness, and the series of smectite  $d(00l)$  reflections is rational. which indicates relatively high crystallinity (Frey, 1987; Kübler, 1967, 1968, 1984; Kübler & Goy-Eggenberger, 2001), which, by extension, could indicate authigenic formation. The low  $2\theta$  angle saddle on smectite  $d(001)$  peaks (Ca-EG) likely indicates intercalation with some interlayered material (Table 3.4). As was the case with the pink conglomerates, the grey conglomerates are matrix-supported, suggesting that the clay minerals might not be entirely authigenic, and could include some detrital clay minerals. In contrast to the pink conglomerates, however, the lower percentage of illite (Table 3.4) could indicate less alkaline conditions or differing source material for the grey conglomerate (Chapter 2). Similarly, the low percentage of kaolinite (Table 3.4) could indicate that the clay minerals in the grey conglomerates are more comminuted and could have a greater detrital component than that of the pink conglomerates. However, a lack of

kaolinite could also point to a different source of material for the grey conglomerate that results in less  $\text{Al}_2\text{O}_3$  activity (Chapter 2). The clastic material sampled from the altered grey conglomerates sampled from 14.33 m depth are typically comprised of nearly pure smectite with little to no peaks from other clay minerals. These smectitic clay minerals most likely formed from the dissolution and reprecipitation of the original clasts and would have an authigenic origin in that case. By extension, it is likely that the smectitic clay minerals comprising the matrix have at least some authigenic components. Like the pink conglomerate (unit 13), we suggest that the clay minerals of the grey conglomerate (unit 11), have mixed detrital and authigenic origins.

#### 3.5.1.4 Sandstone conglomerate (unit 9; 12.8–11.6 m)

The asymmetry exhibited by the smectite  $d(001)$  peaks ( $17.21 \text{ \AA}$ ; Ca-EG) and the pronounced saddle on the low  $2\theta$  angle side of the smectite  $d(001)$  peak suggests the presence of mixed-layer chlorite-smectite or potentially the presence of hydroxy or organic interlayer material. The material interlayered with smectite could comprise up to 40 % of the smectitic clay mineral (Table 3.4). The smectitic clay mineral, illite, and kaolinite all exhibit a rational series of  $d(00l)$  reflections, which suggests that each aforementioned phase is discrete from the other. The  $14.16 \text{ \AA}$  peak (K-107 °C), and the broad, low  $2\theta$  angle shoulder on the illitic  $d(001)$   $10.00 \text{ \AA}$  peak (K-107 °C) are interpreted as a chlorite  $d(001)$  peak that has possibly shifted slightly from the expected  $14.20 \text{ \AA}$  spacing. The deviation of the chlorite  $d(001)$  peak to a lower  $d$ -spacing and the prominent low  $2\theta$  angle saddle could indicate that chlorite-smectite is more likely present than a smectitic clay mineral interlayered with hydroxy or organic material. The sandstone conglomerate (unit 9) hosts sandstone clasts that do not occur in other units, which suggests a different the sediment source. This could explain the increased abundance of illite and kaolinite. The sharpness of the smectitic clay mineral, illite and kaolinite peaks could indicate higher crystallinity which by extension would indicate that an authigenic component could exist. We suggest that these clay minerals have a mixed authigenic and detrital origin.

### 3.5.1.5 Marlstones (unit 6; 10.0–8.6 m; grey material)

The most abundant clay minerals are illite and kaolinite (Table 3), which both show a rational series of  $d(00l)$  reflections. The asymmetry and broad shape of the smectite  $d(001)$  peak suggest that smectite is relatively minor constituent of this marlstone (unit 6; Table 3). Traces of chlorite may also be present. It is unclear whether the occurrences of these discrete clay mineral phases are associated with specific clast types or with the distinct laminae present in unit 6 (Chapter 2). Some clay minerals could be preferentially associated with dolomitic clasts, and others could be preferentially associated with mica clasts (Chapter 2), but that remains unclear. The relatively high abundance of kaolinite likely is a product of authigenic formation in large numbers of associated layers (Bradley 1953). The formation of authigenic illite from the chemical weathering of mica clasts (Chapter 2) is likely and would be consistent with an alkaline lake system as interpreted in previous work (e.g., Füchtbauer et al., 1977; Jankowski, 1977; 1981; Arp et al., 2013b).

### 3.5.2 Stable Isotope Composition of Mid-Miocene Meteoric Water

The  $\delta^{18}\text{O}$  and  $\delta^2\text{H}$  of water from geothermal systems and hot springs throughout the world indicate that they derive most if not all of their water from meteoric sources (Craig, 1961). The near-surface position of the Ries hydrothermal system likely follows the same pattern, and so meteoric water during the Mid-Miocene is a likely source fluid for clay mineral formation in this study (Chapter 2; Pohl et al., 1977; Osinski, 2005; Stöffler et al., 2013).

The  $\delta^{18}\text{O}$  of mid-Miocene meteoric water for the nearby Steinheim basin determined by Tütken et al. (2006) of  $-5.9 \pm 1.7$  ‰ (VSMOW) is used in the models constructed here. Tütken et al. (2006) calculated the composition of drinking water likely consumed by large mammals (proboscideans, rhinocerotids, equids, cervids, suids) that existed during the mid-Miocene (14.3 to 13.5 Ma) in the region of the Steinheim basin. The Steinheim basin is an impact structure that occurs ~100 km south-west of the Ries impact structure. The hydrogen isotope composition of mid-Miocene meteoric water was determined using the  $\delta^2\text{H}$  of groundwater obtained from the German Continental Deep Drilling site (KTB) by Fritz and Lodemann (1990) who reported values ranging from  $-75$  to  $-65$  ‰. The KTB site is located

in north-eastern Bavaria (~100 km NE of the Ries impact structure) and has been the subject of extensive hydrologic studies (e.g., Fritz and Lodemann, 1990; Lodemann et al., 1990; Möller et al., 1997; Gilg, 2000). A likely meteoric water temperature is indicated by Böhme (2003) who report a mean annual temperature of 17–22 °C for central Europe, which was determined using herpetological, paleobotanical and bauxite formation data. These temperatures are temporally aligned with the Mid-Miocene Climatic Optimum and the Ries impact event. We additionally consider the possibility that meteoric fluids could be geothermally modified. As such, we consider fluid temperatures of up to 130 °C as estimated in Chapter 2, by Newsom et al. (1986) and by Osinski (2005).

Finally, we consider the possibility of groundwater input from river networks transporting low  $\delta^{18}\text{O}$  precipitation from the Alps. In regions of high topographic relief, groundwater can potentially retain its isotopic composition after travelling hundreds of kilometers (e.g., Banner et al., 1989; Musgrove & Banner, 1993), and the Central European Alps are located only ~130 km south of the Ries impact structure. The isotopic composition of precipitation in Central European Alps during the mid-Miocene were reported as  $-14.6 \pm 0.3$  ‰ for oxygen and  $-107 \pm 2$  ‰ for hydrogen (Campani et al., 2012).

### 3.5.3 Modeling temperatures and isotopic composition of potential clay mineral source fluids

Only oxygen and hydrogen isotope measurements from the  $<0.2 \mu\text{m}$  size-fraction were used to model the isotopic composition of possible waters from which clay minerals formed due to the purely clay mineral composition of that size- fraction. The  $<0.2 \mu\text{m}$  size-fraction from a sample of any naturally occurring clay-bearing material generally only contains authigenic clay minerals, so it is unlikely that possible detrital clay minerals as discussed in section 3.5.1 contributed to these results. The isotopic composition of potential clay mineral source fluids was modeled using the geothermometers listed below in equations 1–6 (Table 3.5). These equations were used to calculate the clay mineral-water isotopic fractionation factors.

For hydrogen isotopes, geothermometers presented by Sheppard and Gilg (1996) were used for kaolinite (Eqn. 1), as this geothermometer is suitable for the relatively low

temperature ranges of clay formation expected here. For illite and smectitic clay minerals, the clay-water hydrogen geothermometer presented by Capuano (1992) was used (Eqn. 2). Hypothetical illite and smectitic clay mineral isotope compositions, calculated using Equation 2, based on mid-Miocene meteoric water compositions, were in good agreement with the actual measured clay mineral compositions of samples dominated by illite and smectite. The temperature-dependence of the chlorite-water fractionation factor is not well understood. The fractionation factor may be more strongly controlled by the nature of hydrogen bonding within the chlorite crystal structure as opposed to temperature of chemical composition (e.g., Fe/Mg ratio). Chlorite-water fractionation factors for hydrogen are especially poorly defined at temperatures below 250 °C (Graham, Viglino and Harmon, 1987; Savin and Lee, 1988). The chlorite-water fractionation factor for the lowest temperature estimate (100 °C) available, -40 ‰, was used in the present study (Savin and Lee, 1988).

For oxygen isotopes, geothermometers presented by Sheppard and Gilg (1996) were used for illite, kaolinite and smectite given that the intended temperature range of these geothermometers is similar to possible clay mineral formation temperatures expected here. The smectite geothermometer of Sheppard and Gilg (1996) was used for the smectitic clay minerals present here (Eqns. 3–5), despite possible minor interstratification with other layer types; alternate oxygen isotope geothermometers that account for interlayered material (e.g., Savin & Lee, 1988) did not provide statistically significant different results. This outcome is likely due to the low % abundance of interlayered material, as estimated using the saddle method (Inoue et al., 1989). The low abundance of chlorite (Table 3.4) impeded determination of its chemical composition, making an appropriate geothermometer is difficult to select. Given that the geological context of these samples is similar to that described by Simpson et al. (2022), we elected to use the same chlorite geothermometer (Eqn. 6), originally from Savin and Lee (1988).

Reference lines representing kaolinite, illite and montmorillonite formation, respectively, in the presence of meteoric water at 35 °C were plotted in  $\delta^2\text{H}$  and  $\delta^{18}\text{O}$  space (Fig. 3.7); these lines are based on the work of Capuano (1992), Savin & Lee, (1988), Savin (1967) and Sheppard & Gilg (1996). Such lines are traditionally used in  $\delta^2\text{H}$  and  $\delta^{18}\text{O}$  space

to distinguish supergene versus hypogene origins of clay minerals; the geothermometers used to calculate these lines are listed in Table 3.5. Figure 3.7 also shows the traditional “weathering” lines for kaolinite, illite and montmorillonite in equilibrium with meteoric water at 20 °C (Savin, 1967; Savin and Epstein, 1970), along with the Global Meteoric Water Line of Craig (1961). Supergene / hypogene lines and weathering lines were not plotted for chlorite because of its low abundance, and because of the uncertainty regarding the hydrogen isotope chlorite-water fractionation factor. Mid-Miocene meteoric water plots away from the Global Meteoric Water Line (Fig. 3.7) in  $\delta^2\text{H}$  and  $\delta^{18}\text{O}$  space likely because it represents tropical climatic conditions that characterized the Mid-Miocene Climatic Optimum in central Europe. The position of mid-Miocene meteoric water relative to the GMWL is typical of tropical meteoric water (Sharp, 2017).

**Table 3. 5:** Isotope geothermometers for modeling clay mineral source water compositions.

Isotope	Clay Mineral	Eqn.* Number	Geothermometer	Ref.
Hydrogen	Kaolinite	Eqn. 1	$1000 \ln \alpha_{K-W} = 2.2 \left( \frac{10^6}{T^2} \right) - 7.7$	Sheppard and Gilg (1996)
	Smectite and Illite	Eqn. 2	$1000 \ln \alpha_{C-W} = -45.3 \left( \frac{10^3}{T} \right) + 94.7$	Capuano (1992)
Oxygen	Kaolinite	Eqn. 3	$1000 \ln \alpha_{K-W} = 2.76 \left( \frac{10^6}{T^2} \right) - 6.75$	Sheppard and Gilg (1996)
	Smectite	Eqn. 4	$1000 \ln \alpha_{S-W} = 2.55 \left( \frac{10^6}{T^2} \right) - 4.05$	Sheppard and Gilg (1996)
	Illite	Eqn. 5	$1000 \ln \alpha_{I-W} = 2.39 \left( \frac{10^6}{T^2} \right) - 3.76$	Sheppard and Gilg (1996)
	Chlorite	Eqn. 6	$1000 \ln \alpha_{chl-W} = 0.03 \left( \frac{10^{12}}{T^4} \right) - 0.31 \left( \frac{10^9}{T^3} \right) + 2.5 \left( \frac{10^6}{T^2} \right) + 3.27 \left( \frac{10^3}{T} \right) - 12.62$	Savin and Lee (1988)

\*Abbreviations: Eqn. = Equation; Ref. = reference; W = water; K = kaolinite; S = smectite; I = illite; Chl = chlorite; C = clay.

\*\* $\alpha$  = the fractionation of the element in question (e.g., O or H) between the phases denoted in the expression (e.g., S, W).

The isotopic compositions of the <0.2  $\mu\text{m}$  size-fractions generally plot directly upon, or close to, the smectite “weathering line”, calculated for 20 °C (Fig. 3.7). Additionally, the <0.2  $\mu\text{m}$  size-fractions are consistently offset from the supergene / hypogene lines for smectite, illite and kaolinite at 35 °C, which broadly suggests formation at <35 °C (Fig. 3.7). The isotopic compositions of hypothetical 20 °C source waters (Table 3.6; Fig. 3.7) were calculated using the equations listed in Table 4, as weighted based on the clay mineral

abundances reported in Table 3.4. A temperature of 20 °C was chosen as an appropriate intermediate from the 17–22 °C range reported by Böhme (2003). These hypothetical water compositions show excellent agreement with the isotopic composition of mid-Miocene meteoric water in central Europe (Fig. 3.7).

Water compositions calculated for the pink-toned melt-bearing breccias, altered grey conglomerate and sandstone conglomerate form a distinct group, separate from the grey-toned melt-bearing breccia, pink conglomerate, grey conglomerate, and marlstone (Fig. 3.7). The marlstone is further distinguished by its kaolinite- and illite-dominated clay mineralogy, which sets it apart from the smectite-dominated units. Thus, we define three distinct groups of water compositions (Fig. 3.7): group 1 (pink-toned melt-bearing breccias, altered grey conglomerate and the sandstone conglomerate), group 2 (grey-toned melt-bearing breccia, pink conglomerate and the grey conglomerate), and group 3 (marlstone).

Representative water compositions for each group were additionally calculated for temperatures ranging from 0–300 °C and are indicated by the dashed “source water” lines in Figure 3.7. The source water lines were calibrated for water in equilibrium with hypothetical clay minerals whose isotopic compositions are an average of the samples in each group. Additionally, the mineralogy of these hypothetical clay mineral assemblages was determined by averaging their normalized abundances and the source water compositions were weighted accordingly. These source water lines provide a visual aid of where each group would plot for the formation temperatures indicated along each line.

We suggest that meteoric waters at ~20 °C were likely the dominant source water for most clay minerals in the <0.2 μm size-fractions. The source water lines indicate that compositions influenced by distal precipitation originating in the European Central Alps was unlikely; instead, the source waters were likely relatively local meteoric sources.

**Table 3. 6:** Weighted isotopic compositions of hypothetical 20 °C source waters\*.

Lithology	Label	Depth (m)	Material	Group**	$\delta^{18}\text{O}$ Water (‰, VSMOW)	$\delta^2\text{H}$ Water (‰, VSMOW)
Marlstone	RW9.6B	9.6	Dark grey material	3	-5.3	-47
	RW9.6A	9.6	White material	3	-5.2	-38
Sandstone	RW12.74	12.74	Matrix	1	-5.9	-71
Conglomerate						
Altered Grey Conglomerate	RW14.33-ALT	14.33	Clast	1	-7.1	-69
	RW14.33-MTX	14.33	Matrix	1	-7.1	-67
Grey Conglomerate	RW14.78	14.78	Matrix	2	-4.3	-64
	RW16.16-ALT	16.16	Clast	2	-4.1	-59
	RW16.16-MTX	16.16	Matrix	2	-3.9	-61
Pink Conglomerate	RW19-CLST	19.0	Clast	2	-4.6	-60
	RW19-MTX	19.0	Matrix	2	-4.7	-59
Grey-Toned Melt-Bearing Breccia	RW22	22.0	Groundmass	2	-2.3	-65
Pink-toned Melt-Bearing Breccia	RW32	32.0	Groundmass	1	-7.0	-69

\*Weighted isotopic compositions of hypothetical 20 °C source waters were calculated using the isotope geothermometers (Table 4), weighted for the clay mineral abundances in the <0.2  $\mu\text{m}$  size-fraction.

\*\*The groups of modelled hypothetical water compositions associated by clustering or mineralogy.

Mid-Miocene meteoric water shows particularly good agreement with group 1, which suggests ~20 °C meteoric source waters and high water / rock ratios during alteration of the grey conglomerates and the deposition of the sandstone breccia. Meteoric water temperatures spanning ~18–27 °C for the altered grey conglomerates is consistent the isotopic composition range of mid-Miocene meteoric water; potentially indicating low temperature chemical weathering at up to 27 °C. We also consider the possibility that the good agreement of  $\delta^2\text{H}$  values between mid-Miocene meteoric water and the altered grey conglomerates could indicate post-depositional isotopic re-equilibration with meteoric waters, similar to that described by Longstaffe & Ayalon (1990). Meteoric water percolating through the same fractures that facilitated the localized alteration of the grey conglomerates (Chapter 2) could also have allowed for later fluid flow from meteoric water; however, significantly higher or lower  $\delta^2\text{H}$  values for the clay minerals associated with the altered conglomerates is not consistent with any reasonably possible source water. Interestingly, the single point from the pink-toned melt-bearing breccia, a unit that likely underwent alteration at 100–130 °C according to previous work (Chapter 2; Newsom et al., 1986), also plots in Group 1. An incursion of ~20 °C meteoric water during deposition of the pink-toned melt-bearing breccia could explain the isotopic signature it yields but having only a single data point precludes further speculation.

The hydrogen and oxygen isotope compositions of Groups 2 and 3 are somewhat higher than mid-Miocene meteoric water. The ephemeral lake system represented by the marlstones (Chapter 2) and the water-laden debris flows represented by the pink and grey conglomerates (Chapter 2) could have undergone evaporative isotopic enrichment. The calculated hydrogen isotopic composition of group 3 waters is notable higher than groups 1 and 2. Considering that an evaporative lake environment associated with these rocks, changing lake salinity or changing climate could explain these results, but this cannot be stated with certainty. The single point from the grey-toned melt-bearing breccia, contained in Group 2, is notably enriched in  $^{18}\text{O}$  relative to all other measurements. While interesting, a single data point is difficult to interpret. We consider a likely alteration temperature to have been 100–130 °C (Chapter 2; Newsom et al., 1986), and speculate that the clay minerals associated with the grey-toned melt-bearing breccias may have been affected by more evolved hydrothermal fluids or may have formed at a lower water / rock ratio.

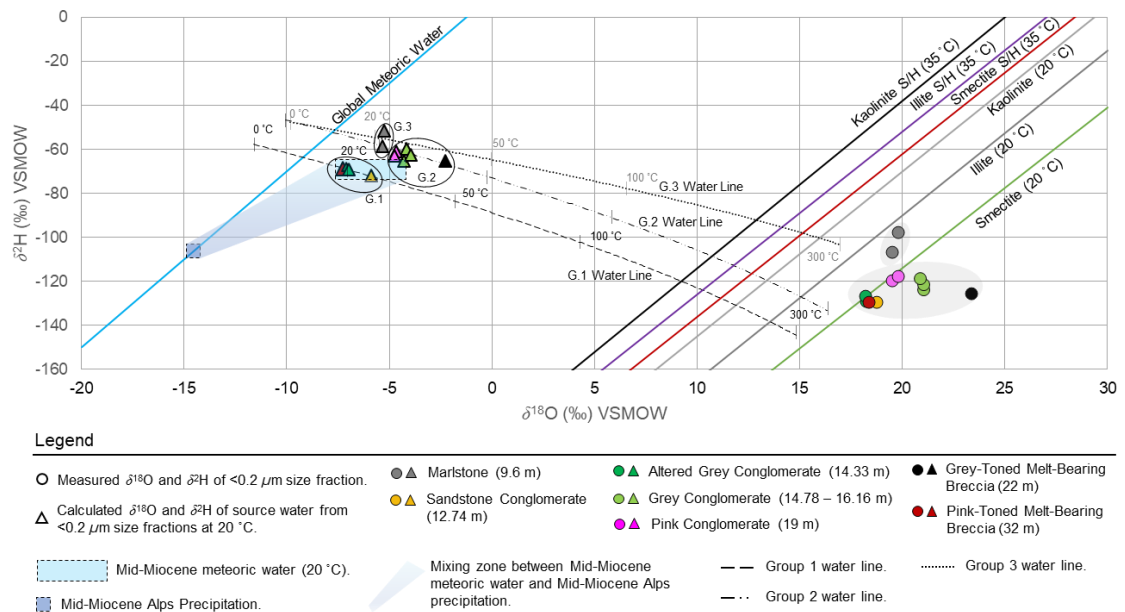


**Figure 3. 7:** Values of  $\delta^2\text{H}$  vs  $\delta^{18}\text{O}$  for  $<0.2 \mu\text{m}$  size-fraction samples from the Wörnitzostheim drill core plotted against calculated water and clay mineral compositions. Symbols (circles, measured  $<0.2 \mu\text{m}$  size-fraction; diamonds, measured 2- $0.2 \mu\text{m}$  size-fraction; triangles, calculated fluid for  $<0.2 \mu\text{m}$  size-fraction at 20 °C) are colour-coded by unit (see legend). A range of calculated possible source water compositions is also shown for temperatures ranging from 0 to 300 °C for Groups 1–3 as indicated by their respective water lines. Also shown are lines dividing supergene from hypogene (S/H) formation of smectite, illite and kaolinite, calculated at 35 °C, and ‘weathering’ lines for smectite, illite and kaolinite formed in equilibrium with meteoric water at 20 °C (Savin 1967; Savin and Lee 1988; Sheppard and Gilg 1996; Capuano 1992). The Global Meteoric Water Line of Craig (1961) is also shown for reference. The estimated isotopic composition of mid-Miocene meteoric water in the Ries region is also shown, along with the calculated source water isotopic compositions for Ries clay mineral formation at 20 °C. The estimated isotopic composition of precipitation from the Central European Alps is shown alongside a “mixing zone” calculated for mixed local meteoric water and Alps meteoric water. Abbreviations: S/H = supergene / hypogene; G. = Group.

### 3.5.4 Controls on Clay Mineral Formation

Clay mineralogy varies between most units in this study (Table 3), yet all hypothetical fluid compositions are roughly consistent with local  $\sim 20$  °C meteoric water (with caveats for the marlstone, and pink-toned and grey-toned melt-bearing breccias as discussed previously; Fig. 7). The varying sediment sources described in Chapter 2 could be exerting a significant influence over the clay mineralogy or the influence of cation activity in the source water could be stronger in different units. We also consider that the clay mineralogy is largely based on interpretations of the  $< 2$   $\mu\text{m}$  size-fraction and could contain detrital phases that are not truly present in the  $< 0.2$   $\mu\text{m}$  size-fraction, from which the isotopic results are derived.

### 3.5.5 Comparison to Previous Petrographic Interpretations

The results of this study indicate that clay minerals comprising the lithologies described in Chapter 2 likely formed at relatively low temperatures from weakly alkaline meteoric water. Conversely, euhedral dolomite and plagioclase spherulites in some fractures and voids of the pink and grey conglomerates suggest the post-impact presence of high temperature fluids (100–130 °C). Higher fluid temperature is also consistent with previous studies of hydrothermal mineral deposits at the Ries impact structure, (e.g., Newsom et al., 1986; Osinski, 2005), and hydrothermal activity is likely to have persisted during post-impact lacustrine deposition (Arp et al., 2013b). We suggest that the high temperature mineral deposits present in the basal conglomerates studied previously (Chapter 2) represent the limited spatial extent of such mineralization, and that input from local meteoric source contributed to the rapid cooling of these hydrothermal fluids, resulting in the spherulitic quench textures, and low temperature ( $\leq 27$  °C) clay mineralization. The widespread clay mineralization likely means that the post-impact depositional environment was similarly characterized by  $\sim 20$  °C meteoric water.

The results of this study also indicate that the clay minerals associated with the impact melt-bearing breccias (units 15 and 14) formed from low temperature meteoric water, which is notably inconsistent with previous studies of impact melt-bearing ejecta (Newsom

et al., 1986; Osinski, Grieve and Spray, 2004). While this conclusion about the nature of these units cannot be stated with certainty based on the data provided in this study, it does warrant further investigation. The melt-bearing breccias likely comprise the sediment source for the post-impact deposition of the conglomerates and marlstones (Chapter 2). It is plausible that some clay minerals contained in the conglomerates and marlstones may have inherited their isotopic composition from the impact melt-bearing breccias. As such, more accurately determining the clay mineralogy and associated hydrogen and oxygen isotope geochemistry of the pink-toned and grey-toned melt-bearing breccias is pertinent to the interpretation of the overlying sedimentary rocks.

Some of the clay minerals in the 2–0.2  $\mu\text{m}$  size-fractions could have formed at higher temperatures; possibly indicated by  $\delta^2\text{H}$  results, which show a clear distinction between the 2–0.2 and <0.2  $\mu\text{m}$  size- fractions (Fig. 6). Unlike  $\delta^{18}\text{O}$ , the  $\delta^2\text{H}$  results from the 2–0.2  $\mu\text{m}$  size-fraction would not be affected by quartz, feldspar, and carbonate contamination. The few *p*XRD results from the 2–0.2  $\mu\text{m}$  size-fraction do indicate that phyllosilicates are present, in addition to non-clay minerals. The origin of phyllosilicates or any other hydrous mineral in the 2–0.2  $\mu\text{m}$  size-fraction is currently unclear. They could originate from higher temperature alteration associated with the impact-generated hydrothermal system, but they could also be of detrital origin, for example, derived from pre-impact granitoid and gneissic rocks. This possibility warrants further investigation.

### 3.6 Conclusions

This study indicates that the source fluids associated with the deposition of the clay minerals in the impact melt-bearing breccias, and post-impact sedimentary deposits sampled by the Wörnitzostheim drill core are likely characterized by local weakly alkaline  $\sim 20^\circ\text{C}$  meteoric water. Smectitic clay minerals with an unknown type of interlayer material are the dominant clay mineral, comprising 55–100 % of the clays reported for all units except for the marlstones, which are dominated by kaolinite and illite. Major changes in clay mineralogy are likely driven mainly by changing sediment sources between units. Oxygen and hydrogen isotope results for <0.2  $\mu\text{m}$  size-fractions of clay minerals from the grey and pink conglomerates suggest that water associated with their authigenic formation

could have been affected by evaporative enrichment. Meteoric water likely percolated into the subsurface during the establishment of the ephemeral lake system represented by the marlstone. Meteoric water in the subsurface then contributed to the low temperature (up to 27 °C) chemical weathering of the grey conglomerates. The eventual drying of the playa lake system resulted in the evaporative isotopic signature recorded in the marlstone; however, the higher hydrogen isotope signature could indicate an associated change in water salinity or climate. It remains unclear whether higher temperature fluids could be indicated by the hydrogen (and perhaps also oxygen) isotope compositions of clay minerals in the 2–0.2  $\mu\text{m}$  size-fraction. Additional investigation of this possibility is warranted.

### 3.7 References

- Arp, G., Kolepka, C., Simon, K., Karius, V., Nolte, N. and Hansen, B.T., 2013a. New evidence for persistent impact-generated hydrothermal activity in the Miocene Ries impact structure, Germany. *Meteoritics and Planetary Science*, 48(12), pp.2491–2516. <https://doi.org/10.1111/maps.12235>.
- Arp, G., Blumenberg, M., Hansen, B.T., Jung, D., Kolepka, C., Lenz, O., Nolte, N., Poschlod, K., Reimer, A. and Thiel, V., 2013b. Chemical and ecological evolution of the Miocene Ries impact crater lake, Germany: A reinterpretation based on the Enkingen (SUBO 18) drill core. *Bulletin of the Geological Society of America*, 125(7–8), pp.1125–1145. <https://doi.org/10.1130/B30731.1>.
- Arp, G., Dunkl, I., Jung, D., Karius, V., Lukács, R., Zeng, L., Reimer, A. and Head, J.W., 2021. A Volcanic Ash Layer in the Nördlinger Ries Impact Structure (Miocene, Germany): Indication of Crater Fill Geometry and Origins of Long-Term Crater Floor Sagging. *Journal of Geophysical Research: Planets*, 126(4). <https://doi.org/10.1029/2020JE006764>.
- Arp, G., Hansen, B.T., Pack, A., Reimer, A., Schmidt, B.C., Simon, K. and Jung, D., 2017. The soda lake—mesosaline halite lake transition in the Ries impact crater basin (drilling Löpsingen 2012, Miocene, southern Germany). *Facies*, 63(1). <https://doi.org/10.1007/s10347-016-0483-7>.

- Banner, J.L., Wasserburg, G.J., Dobson, P.F., Carpenter, A.B. and Moore, C.H., 1989. Isotopic and trace element constraints on the origin and evolution of saline groundwaters from central Missouri\*. *Geochimica et Cosmochimica Acta*, 53, pp.383–398.
- Barnhisel, Richard.I. and Bertsch, Paul.M., 1989. Chlorites and Hydroxy-Interlayered Vermiculite and Smectite. In: J.B. Dixon and S.B. Weed, eds. *Minerals in Soil Environments*, 2nd ed. Madison, WI: Soil Science Society of America. pp.729–788.
- Bauer, Kerstin.K. and Vennemann, Torsten.W., 2014. Analytical methods for the measurement of hydrogen isotope composition and water content in clay minerals by TC/EA. *Chemical Geology*, 363, pp.229–240.  
<https://doi.org/10.1016/j.chemgeo.2013.10.039>.
- Bibring, J.-P., Langevin, Y., Mustard, J.F., Poulet, F., Arvidson, R., Gendrin, A., Gondet, B., Mangold, N., Pinet, P. and Forget, F., 2006. Global Mineralogical and Aqueous Mars History Derived from OMEGA/Mars Express Data. *Science*, [online] 312, pp.400–404. Available at: <<http://science.sciencemag.org/>>.
- Biscaye, Pierre.E., 1965. Mineralogy and sedimentation of recent deep-sea clay in the Atlantic ocean and adjacent seas and oceans. *Bulletin of the Geological Society of America*, 76(7), pp.803–832. [https://doi.org/10.1130/0016-7606\(1965\)76\[803:MASORD\]2.0.CO;2](https://doi.org/10.1130/0016-7606(1965)76[803:MASORD]2.0.CO;2).
- Böhme, M., 2003. The Miocene Climatic Optimum: Evidence from ectothermic vertebrates of Central Europe. *Palaeogeography, Palaeoclimatology, Palaeoecology*, 195(3–4), pp.389–401. [https://doi.org/10.1016/S0031-0182\(03\)00367-5](https://doi.org/10.1016/S0031-0182(03)00367-5).
- Borthwick, James. and Harmon, Russell.S., 1982. A note regarding CIFJ as an alternative to BrF5 for oxygen isotope analysis. *Geochimica et Cosmochimica Acta*, 46, pp.1665–1668.

- Bradley, W.F., 1953. Analysis of Mixed-Layer Clay Mineral Structures. *Analytical Chemistry*, 25(5), pp.727–730.
- Brigham-Grette, J., Melles, M. and Minyuk, P., 2007. Overview and significance of a 250 ka paleoclimate record from El'gygytgyn Crater Lake, NE Russia. *Journal of Paleolimnology*, 37(1), pp.1–16. <https://doi.org/10.1007/s10933-006-9017-6>.
- Brindley, G.W. and Brown, G., 1980. *Crystal Structures of Clay Minerals and their X-Ray Identification*. Mineralogical Society of Great Britain and Ireland. <https://doi.org/10.1180/mono-5>.
- Bristow, T.F., Bish, D.L., Vaniman, D.T., Morris, R. v., Blake, D.F., Grotzinger, J.P., Rampe, E.B., Crisp, J.A., Achilles, C.N., Ming, D.W., Ehlmann, B.L., King, P.L., Bridges, J.C., Eigenbrode, J.L., Sumner, D.Y., Chipera, S.J., Moorokian, J.M., Treiman, A.H., Morrison, S.M., Downs, R.T., Farmer, J.D., des Marais, D., Sarrazin, P., Floyd, M.M., Mischna, M.A. and McAdam, A.C., 2015. The origin and implications of clay minerals from Yellowknife Bay, Gale crater, Mars. *American Mineralogist*, 100(4), pp.824–836. <https://doi.org/10.2138/am-2015-5077CCBYNCND>.
- Bristow, T.F. and Milliken, R.E., 2011. *Terrestrial perspective on authigenic clay mineral production in ancient martian lakes*. *Clays and Clay Minerals*, <https://doi.org/10.1346/CCMN.2011.0590401>.
- Bristow, T.F., Rampe, E.B., Achilles, C.N., Blake, D.F., Chipera, S.J., Craig, P., Crisp, J.A., des Marais, D.J., Downs, R.T., Gellert, R., Grotzinger, J.P., Gupta, S., Hazen, R.M., Horgan, B., Hogancamp, J. v, Mangold, N., Mahaffy, P.R., Mcadam, A.C., Ming, D.W., Morookian, J.M., Morris, R. v, Morrison, S.M., Treiman, A.H., Vaniman, D.T., Vasavada, A.R. and Yen, A.S., 2018. Clay mineral diversity and abundance in sedimentary rocks of Gale crater, Mars. *Science Advances*, [online] 4(eaar3330). Available at: <<http://advances.sciencemag.org/>>.

- Cabrol, N.A. and Grin, E.A., 1999. Distribution, Classification, and Ages of Martian Impact Crater Lakes. *Icarus*, 142(1), pp.160–172.  
<https://doi.org/10.1006/icar.1999.6191>.
- Cabrol, N.A. and Grin, E.A., 2001. The Evolution of Lacustrine Environments on Mars: Is Mars Only Hydrologically Dormant? *Icarus*, 149(2), pp.291–328.  
<https://doi.org/10.1006/icar.2000.6530>.
- Cabrol, N.A., Grin, E.A., Newsom, H.E., Landheim, R. and McKay, C.P., 1999. Hydrogeologic Evolution of Gale Crater and Its Relevance to the Exobiological Exploration of Mars. *Icarus*, [online] 139, pp.235–245. Available at: <http://www.idealibrary.comon>.
- Campani, M., Mulch, A., Kempf, O., Schlunegger, F. and Mancktelow, N., 2012. Miocene paleotopography of the Central Alps. *Earth and Planetary Science Letters*, 337–338, pp.174–185. <https://doi.org/10.1016/j.epsl.2012.05.017>.
- Cannon, K.M., Parman, S.W. and Mustard, J.F., 2017. Primordial clays on Mars formed beneath a steam or supercritical atmosphere. *Nature*, 552(7683), pp.88–91.  
<https://doi.org/10.1038/nature24657>.
- Capuano, R.M., 1992. The temperature dependence of hydrogen isotope fractionation between clay minerals and water: Evidence from a geopressured system. *Geochimica et Cosmochimica Acta*, 56, pp.2547–2554.
- Caudill, C., Osinski, G.R., Greenberger, R.N., Tornabene, L.L., Longstaffe, F.J., Flemming, R.L. and Ehlmann, B.L., 2021. Origin of the degassing pipes at the Ries impact structure and implications for impact-induced alteration on Mars and other planetary bodies. *Meteoritics and Planetary Science*, 56(2), pp.404–422.  
<https://doi.org/10.1111/maps.13600>.

- Clayton, Robert.N. and Mayeda, Toshiko.K., 1963. The use of bromine pentafluoride in the extraction of oxygen from oxides and silicates for isotopic analysis\*. *Geochimica et Cosmochimica Acta*, 27, pp.43–52.
- Cockell, C. S., Osinski, G.R., Sapers, H.M., Pontefract, A. and Parnell, J., 2020. Microbial life in impact craters. *Current Issues in Molecular Biology*, 38, pp.75–102. <https://doi.org/10.21775/cimb.038.075>.
- Cockell, Charles.S. and Lee, Pascal., 2002. The biology of impact craters-a review. *Biological Reviews*, 77, pp.279–310. <https://doi.org/10.1017/S146479310100584X>.
- Craig, H., 1961. Isotopic variations in meteoric waters. *Science*, 133, pp.1702–1703.
- Daubar, I.J. and Kring, D.A., 2001. Impact-induced hydrothermal systems: Heats sources and lifetimes. In: *32nd Lunar and Planetary Science Conference. (abstract #1727)*.
- Doebelin, Nicola. and Kleeberg, Reinhard., 2015. Profex: A graphical user interface for the Rietveld refinement program BGMN. *Journal of Applied Crystallography*, 48, pp.1573–1580. <https://doi.org/10.1107/S1600576715014685>.
- Ehlmann, B.L., Mustard, J.F., Murchie, S.L., Bibring, J.P., Meunier, A., Fraeman, A.A. and Langevin, Y., 2011. *Subsurface water and clay mineral formation during the early history of Mars. Nature*, <https://doi.org/10.1038/nature10582>.
- von Engelhardt, W., 1990. *Distribution, petrography and shock metamorphism of the ejecta of the Ries crater in Germany-a review*. Elsevier Science Publishers B.V.
- von Engelhardt, W., 1997. Suevite breccia of the Ries impact crater, Germany: Petrography, chemistry and shock metamorphism of crystalline rock clasts. *Meteoritics and Planetary Science*, 32(4), pp.545–554. <https://doi.org/10.1111/j.1945-5100.1997.tb01299.x>.

- Ernstson, Kord., 1974. The structure of the Ries Crater from geoelectric depth soundings. *Journal of Geophysics*, [online] 40, pp.639–659. Available at: <<https://www.researchgate.net/publication/259485112>>.
- Farmer, J.D., 1996. Hydrothermal systems on Mars: an assessment of present evidence. In: Bock Gregoy R. and Goode Jamie A., eds. *Ciba Foundation Symposium 202 - Evolution of Hydrothermal Ecosystems on Earth (And Mars?)*. pp.273–299. <https://doi.org/10.1002/9780470514986.ch15>.
- Flower, Benjamin.P. and Kennett, James.P., 1994. The middle Miocene climatic transition: East Antarctic ice sheet development, deep ocean circulation and global carbon cycling. *Palaeogeography, Palaeoclimatology, Palaeoecology*, 108, pp.537–555.
- Förstner, U., 1967. Petrographische Untersuchungen des Suevit aus den Bohrungen Deiningen und Wörnitzostheim im Ries von Nördlingen. *Contributions to Mineralogy and Petrology*, 15, pp.281–308.
- Frey, M., 1987. Very low-grade metamorphism of clastic sedimentary rocks. In: M. Frey, ed. *Low Temperature Metamorphism*. Glasgow: Blackie and Son Ltd. pp.9–58.
- Fritz, P. and Lodemann, M., 1990. Die salinaren Tiefenwässer der KTB-Vorbohrung. *Die Geowissenschaften*, 8, pp.273–278.
- Füchtbauer, H., Brellie. von der. G., Dehem, R., Förstner, U., Gall, H., Höfling, R., Hoefs, J., Hollerbach, H., Jankowski, B., Jung, W., Malz, H., Mertes, H., Rothe, P., Salger, M., Wehner, H. and Wolf, M., 1977. Tertiary lake sediments of the Ries, research borehole Nördlingen 1973-A summary. *Geologica Bavarica*, 75, pp.13–19.
- Gilg, H.Albert., 2000. D-H evidence for the timing of kaolinization in Northeast Bavaria, Germany. *Chemical Geology*, 170, pp.5–18.
- Goudge, T.A., Milliken, R.E., Head, J.W., Mustard, J.F. and Fassett, C.I., 2017. Sedimentological evidence for a deltaic origin of the western fan deposit in Jezero

crater, Mars and implications for future exploration. *Earth and Planetary Science Letters*, 458, pp.357–365. <https://doi.org/10.1016/j.epsl.2016.10.056>.

Goudge, T.A., Mohrig, D., Cardenas, B.T., Hughes, C.M. and Fassett, C.I., 2018. Stratigraphy and paleohydrology of delta channel deposits, Jezero crater, Mars. *Icarus*, 301, pp.58–75. <https://doi.org/10.1016/j.icarus.2017.09.034>.

Goudge, T.A., Mustard, J.F., Head, J.W., Fassett, C.I. and Wiseman, S.M., 2015. Assessing the mineralogy of the watershed and fan deposits of the Jezero crater paleolake system, Mars. *Journal of Geophysical Research: Planets*, 120(4), pp.775–808. <https://doi.org/10.1002/2014JE004782>.

Graham, C.M., Viglino, J.A. and Harmon, R.S., 1987. Experimental study of hydrogen-isotope exchange between aluminous chlorite and water and of hydrogen diffusion in chlorite. *American Mineralogist*, 72(5–6), pp.566–579.

Grotzinger, J.P., Gupta, S., Malin, M.C., Rubin, D.M., Schieber, J., Siebach, K., Sumner, D.Y., Stack, K.M., Vasavada, A.R., Arvidson, R.E., Calef, F., Edgar, L., Fischer, W.F., Grant, J.A., Griffes, J., Kah, L.C., Lamb, M.P., Lewis, K.W., Mangold, N., Minitti, M.E., Palucis, M., Rice, M., Williams, R.M.E., Yingst, R.A., Blake, D., Blaney, D., Conrad, P., Crisp, J., Dietrich, W.E., Dromart, G., Edgett, K.S., Ewing, R.C., Gellert, R., Hurowitz, J.A., Kocurek, G., Mahaffy, P., McBride, M.J., McLennan, S.M., Mischna, M., Ming, D., Milliken, R., Newsom, H., Oehler, D., Parker, T.J., Vaniman, D., Wiens, R.C. and Wilson, S.A., 2015. Deposition, exhumation, and paleoclimate of an ancient lake deposit, Gale crater, Mars. *Science*, 350(6257). <https://doi.org/10.1126/science.aac7575>.

Grotzinger, J.P., Sumner, D.Y., Kah, L.C., Stack, K., Gupta, S., Edgar, L., Rubin, D., Lewis, K., Schieber, J., Mangold, N., Milliken, R., Conrad, P.G., DesMarais, D., Farmer, J., Siebach, K., Calef III, F., Hurowitz, J., McLennan, S.M., Ming, D., Vaniman, D., Crisp, J., Vasavada, A., Edgett, K.S., Malin, M., Blake, D., Gellert, R., Mahaffy, P., Wiens, R.C., Maurice, S., Grant, J.A., Wilson, S., Anderson, R.C.,

- Beegle, L., Arvidson, R., Hallet, B., Sletten, R.S., Rice, M., Bell III, J., Griffes, J., Ehlmann, B., Anderson, R.B., Bristow, T.F., Dietrich, W.E., Dromart, G., Eigenbrode, J., Fraeman, A., Hardgrove, C., Herkenhoff, K., Jandura, L., Kocurek, G., Lee, S., Leshin, L.A., Leveille, R., Limonadi, D., Maki, J., McCloskey, S., Meyer, M., Minitti, M., Newsom, H., Oehler, D., Okon, A., Palucis, M., Parker, T., Rowland, S., Schmidt, M., Squyres, S., Steele, A., Stolper, E., Summons, R., Treiman, A., Williams, R. and Yingst, A., 2014. A Habitable Fluvio-Lacustrine Environment at Yellowknife Bay, Gale Crater, Mars. *Science*, 343(1242777).
- Horgan, B.H.N., Anderson, R.B., Dromart, G., Amador, E.S. and Rice, M.S., 2020. The mineral diversity of Jezero crater: Evidence for possible lacustrine carbonates on Mars. *Icarus*, 339(113526). <https://doi.org/10.1016/j.icarus.2019.113526>.
- Hüttner, R. and Schmidt-Kaler, H., 1999. *Meteoritenkrater Nördlinger Ries*. Munich.
- Ignasiak, Teresa.M., Kotlyar, Luba., Longstaffe, Frederick.J., Strausz, Otto.P. and Montgomery, Douglas.S., 1983. Separation and characterization of clay from Athabasca asphaltene. *Fuel*, 62, pp.353–362.
- Inoue, A., Bouchet, A., Velde, B. and Meunier, A., 1989. Convenient technique for estimating smectite later percentage in randomly interstratified illite/smectite minerals. *Clays and Clay Minerals*, 37(3), pp.227–234.
- Jankowski, B., 1977. Die Postimpakt-Sedimente in der Forschungs-bohrung Nördlingen 1973. *Geologica Bavarica*, 75, pp.21–36.
- Jankowski, B., 1981. Die Geschichte der Sedimentation im Nördlinger Ries und Randecker Maar. *Bochumer geologische und geotechnische Arbeiten* , 6, pp.1–315.
- Kanik, Nadine.J., Longstaffe, Fred.J., Kuligiewicz, Artur. and Derkowski, Arkadiusz., 2022. Systematics of smectite hydrogen-isotope composition: Structural hydrogen versus adsorbed water. *Applied Clay Science*, 216. <https://doi.org/10.1016/j.clay.2021.106338>.

- Kirsimäe, K. and Osinski, G.R., 2012. Impact-Induced Hydrothermal Activity. *Impact Cratering: Processes and Products*, pp.76–89.  
<https://doi.org/10.1002/9781118447307.ch6>.
- Kübler, B., 1967. La cristallinité de l'illite et les zones tout a fait superieures du métamorphisme. In: *Étages tectoniques, Colloque de Neuchâtel 1966, A La Baconniere*. Neuchâtel. pp.105–121.
- Kübler, B., 1968. Evaluation quantitative du métamorphisme par la cristallinité d l'illite. *Bulletin du Centre de recherches, Pau -- S.N.P.A.*, 2, pp.385–397.
- Kübler, B., 1984. Les indicateurs des transformations physiques et chimiques dans la diagenèse, température et calorimétrie. In: M. Lagache, ed. *Thermobarométrie et barométrie géologiques*. Paris: Bulletin de la Société Française de Minéralogie et de Cristallographie. pp.489–596.
- Kübler, B. and Goy-Eggenberger, D., 2001. La cristallinité de l'illite revisitée : un bilan des connaissances acquises ces trented ernières années. *Clay Minerals*, 36, pp.143–157.
- Libbey, R.B., Longstaffe, F.J. and Flemming, R.L., 2013. Clay mineralogy, oxygen isotope geochemistry, and water/rock ratio estimates, Te Mihi area, Wairakei Geothermal Field, New Zealand. *Clays and Clay Minerals*, 61(3), pp.204–217.  
<https://doi.org/10.1346/CCMN.2013.0610304>.
- Lodemann, M., Weise, S.M., Fritz, P., Rauert, W., Trimborn, P., Buheitel, F., Eichinger, L., Hurst, S., Baumann, M., Faber, E., Whiticar, M.J., Schultz, R., Schellenschmidt, R., Ruhland, H. and Meier, M., 1990. Isotope hydrology and chemistry of groundwaters in the surroundings of the KTB drilling site: the Weiden borehole. *KTB Rep*, 90–4(573).

- Longstaffe, F.J. and Ayalon, A., 1990. Hydrogen-isotope geochemistry of diagenetic clay minerals from Cretaceous sandstones, Alberta, Canada: evidence for exchange. *Applied Geochemistry*, 5, pp.657–668.
- McKay, Jennifer.L. and Longstaffe, Frederick.J., 2013. Tracking fluid movement during cyclic steam stimulation of clearwater formation oil sands using stable isotope variations of clay minerals. *Clays and Clay Minerals*, 61(5), pp.440–460. <https://doi.org/10.1346/CCMN.2013.0610504>.
- Meunier, A., 2007. Soil hydroxy-interlayered minerals: A re-interpretation of their crystallochemical properties. *Clays and Clay Minerals*, 55(4), pp.380–388. <https://doi.org/10.1346/CCMN.2007.0550406>.
- Milliken, R.E. and Bish, D.L., 2010. Sources and sinks of clay minerals on Mars. *Philosophical Magazine*, 90(17–18), pp.2293–2308. <https://doi.org/10.1080/14786430903575132>.
- Möller, P., Weise, S.M., Althaus, E., Bach, W., Behr, H.J., Borchardt, R., Bräuer, K., Drescher, J., Erzinger, J., Faber, E., Hansen, B.T., Horn, E.E., Huenges, E., Kämpf, H., Kessels, W., Kirsten, T., Landwehr, D., Lodemann, M., Machon, L., Pekdeger, A., Pielow, H.U., Reutel, C., Simon, K., Walther, J., Weinlich, F.H. and Zimmer, M., 1997. Paleofluids and recent fluids in the upper continental crust: Results from the German Continental Deep Drilling Program (KTB). *Journal of Geophysical Research: Solid Earth*, 102(B8), pp.18233–18254. <https://doi.org/10.1029/96jb02899>.
- Moore, D.M. and Reynolds, R.C., 1997. *X-Ray Diffraction and the Identification and Analysis of Clay Minerals*. 2nd ed. Oxford, New York: Oxford University Press.
- Musgrove, M. and Banner, J.L., 1993. Regional Ground-Water Mixing and the Origin of Saline Fluids: Midcontinent, United States. *Science*, 259, pp.1877–1882.

- Naumov, M. V., 2005a. Principal features of impact-generated hydrothermal circulation systems: Mineralogical and geochemical evidence. *Geofluids*, 5(3), pp.165–184.  
<https://doi.org/10.1111/j.1468-8123.2005.00092.x>.
- Naumov, Mikhail. v., 2005b. Principal features of impact-generated hydrothermal circulation systems: mineralogical and geochemical evidence. *Geofluids*, 5, pp.165–184.
- Newsom, H.E., 1980. Hydrothermal Alteration of Impact Melt Sheets with Implications for Mars. *ICARUS*, 44, pp.207–216.
- Newsom, H.E., Graup, G., Sowards, T. and Keil, K., 1986. Fluidization and hydrothermal alteration of the Suevite deposit at the Ries Crater, West Germany, and implications for Mars. *Journal of Geophysical Research*, 91(B13), pp.E239–E251.  
<https://doi.org/10.1029/jb091ib13p0e239>.
- Osinski, G.R., 2004. Impact melt rocks from the Ries structure, Germany: An origin as impact melt flows? *Earth and Planetary Science Letters*, 226(3–4), pp.529–543.  
<https://doi.org/10.1016/j.epsl.2004.08.012>.
- Osinski, G.R., 2005. Hydrothermal activity associated with the Ries impact event, Germany. *Geofluids*, 5, pp.202–220.
- Osinski, G.R., Cockell, C.S., Pontefract, A. and Sapers, H.M., 2020. The Role of Meteorite Impacts in the Origin of Life. *Astrobiology*, 20(9), pp.1121–1149.  
<https://doi.org/10.1089/ast.2019.2203>.
- Osinski, G.R., Grieve, R.A.F. and Spray, J.G., 2004. *The nature of the groundmass of surficial suevite from the Ries impact structure, Germany, and constraints on its origin. Meteoritics & Planetary Science*, .
- Osinski, G.R., Tornabene, L.L., Banerjee, N.R., Cockell, C.S., Flemming, R., Izawa, M.R.M., McCutcheon, J., Parnell, J., Preston, L.J., Pickersgill, A.E., Pontefract, A., Sapers, H.M. and Southam, G., 2013a. Impact-generated hydrothermal systems on

Earth and Mars. *Icarus*, 224(2), pp.347–363.

<https://doi.org/10.1016/j.icarus.2012.08.030>.

Pohl, J., Stöffler, D., Gall, H. and Erston, K., 1977. The Ries impact crater. In: Roddy D.J., Pepin R.O. and Merrill R.B., eds. *Impact and Explosion Cratering*. New York: Pergamon Press. pp.343–404.

Poulet, F., Bibring, J.P., Mustard, J.F., Gendrin, A., Mangold, N., Langevin, Y., Arvidson, R.E., Gondet, B., Gomez, C., Berthe, M., Erard, S., Forni, O., Manaud, N., Poulleau, G., Soufflot, A., Combes, M., Drossart, P., Encrenaz, T., Fouchet, T., Melchiorri, R., Bellucci, G., Altieri, F., Formisano, V., Fonti, S., Capaccioni, F., Cerroni, P., Coradini, A., Korablev, O., Kottsov, V., Ignatiev, N., Titov, D., Zasova, L., Pinet, P., Schmitt, B., Sotin, C., Hauber, E., Hoffmann, H., Jaumann, R., Keller, U. and Forget, F., 2005. Phyllosilicates on Mars and implications for early martian climate. *Nature*, 438(7068), pp.623–627. <https://doi.org/10.1038/nature04274>.

Qi, Haiping., Coplen, Tyler.B., Gehre, Matthias., Vennemann, Torsten.W., Brand, Willi.A., Geilmann, Heike., Olack, Gerard., Bindeman, Ilya.N., Palandri, Jim., Huang, Li. and Longstaffe, Fred.J., 2017. New biotite and muscovite isotopic reference materials, USGS57 and USGS58, for  $\delta^2\text{H}$  measurements—A replacement for NBS 30. *Chemical Geology*, 467, pp.89–99. <https://doi.org/10.1016/j.chemgeo.2017.07.027>.

Rapin, W., Ehlmann, B.L., Dromart, G., Schieber, J., Thomas, N.H., Fischer, W.W., Fox, V.K., Stein, N.T., Nachon, M., Clark, B.C., Kah, L.C., Thompson, L., Meyer, H.A., Gabriel, T.S.J., Hardgrove, C., Mangold, N., Rivera-Hernandez, F., Wiens, R.C. and Vasavada, A.R., 2019. An interval of high salinity in ancient Gale crater lake on Mars. *Nature Geoscience*, 12(11), pp.889–895. <https://doi.org/10.1038/s41561-019-0458-8>.

Rathbun, J.A. and Squyres, S.W., 2002. Hydrothermal systems associated with martian impact craters. *Icarus*, 157(2), pp.362–372. <https://doi.org/10.1006/icar.2002.6838>.

Salger, M., 1977. Die Tonminerale der Forschungsbohrung Nördlingen 1973. *Geologica Bavarica*, 75, pp.67–73.

- Sapers, H.M., Osinski, G.R., Flemming, R.L., Buitenhuis, E., Banerjee, N.R., Tornabene, L.L., Blain, S. and Hainge, J., 2017. Evidence for a spatially extensive hydrothermal system at the Ries impact structure, Germany. *Meteoritics and Planetary Science*, 52(2), pp.351–371. <https://doi.org/10.1111/maps.12796>.
- Savin, Samuel.Marvin., 1967. *Oxygen and hydrogen isotope ratios in sedimentary rocks and minerals*. California Institute of Technology.
- Savin, S.M. and Epstein, S., 1970. The oxygen and hydrogen isotope geochemistry of clay minerals\*. *Geochimica et Cosmochimica Acta*, 34, pp.25–42.
- Savin, S.M. and Lee, M., 1988. Isotopic studies of phyllosilicates. In: S.W. Bailey, ed. *Hydrous Phyllosilicates, Reviews in Mineralogy and Geochemistry*. Washington, USA: Mineralogical Society of America. pp.189–223.  
<https://doi.org/10.1515/9781501508998-012>.
- Schmieder, M., Kennedy, T., Jourdan, F., Buchner, E. and Reimold, W.U., 2018. A high-precision  $^{40}\text{Ar}/^{39}\text{Ar}$  age for the Nördlinger Ries impact crater, Germany, and implications for the accurate dating of terrestrial impact events. *Geochimica et Cosmochimica Acta*, 220, pp.146–157. <https://doi.org/10.1016/j.gca.2017.09.036>.
- Schon, S.C., Head, J.W. and Fassett, C.I., 2012. An overfilled lacustrine system and progradational delta in Jezero crater, Mars: Implications for Noachian climate. *Planetary and Space Science*, 67(1), pp.28–45.  
<https://doi.org/10.1016/j.pss.2012.02.003>.
- Sharp, Z.D., 2017. *Principles of Stable Isotope Geochemistry*. Open Educational Resources.
- Sharp, Z.D., Atudorei, V. and Durakiewicz, T., 2001. A rapid method for determination of hydrogen and oxygen isotope ratios from water and hydrous minerals. *Chemical Geology*, [online] 178, pp.197–210. Available at: [www.elsevier.com/locate/chemgeo](http://www.elsevier.com/locate/chemgeo).

- Sheppard, S.M.F. and Gilg, H.A., 1996. Stable isotope geochemistry of clay minerals 'The story of sloppy, sticky, lumpy and tough' Cairns-Smith (1971). *Clay Minerals*, 31, pp.1–24.
- Simpson, S.L., Longstaffe, F.J., Osinski, G.R., Caudill, C.M. and Kring, D.A., 2022. A low-temperature, meteoric water-dominated origin for smectitic clay minerals in the Chicxulub impact crater upper peak ring, as inferred from their oxygen and hydrogen isotope compositions. *Chemical Geology*, 588. <https://doi.org/10.1016/j.chemgeo.2021.120639>.
- Stöffler, D., Artemieva, N.A., Wünnemann, K., Reimold, W.U., Jacob, J., Hansen, B.K. and Summerson, I.A.T., 2013. Ries crater and suevite revisited-Observations and modeling Part I: Observations. *Meteoritics and Planetary Science*, 48(4), pp.515–589. <https://doi.org/10.1111/maps.12086>.
- Tornabene, L.L., Osinski, G.R., McEwen, A.S., Wray, J.J., Craig, M.A., Sapers, H.M. and Christensen, P.R., 2013. An impact origin for hydrated silicates on Mars: A synthesis. *Journal of Geophysical Research: Planets*, 118(5), pp.994–1012. <https://doi.org/10.1002/jgre.20082>.
- Tütken, T., Vennemann, T.W., Janz, H. and Heizmann, E.P.J., 2006. Palaeoenvironment and palaeoclimate of the Middle Miocene lake in the Steinheim basin, SW Germany: A reconstruction from C, O, and Sr isotopes of fossil remains. *Palaeogeography, Palaeoclimatology, Palaeoecology*, 241(3–4), pp.457–491. <https://doi.org/10.1016/j.palaeo.2006.04.007>.
- Vandavelde, Justin.H. and Bowen, Gabriel.J., 2013. Effects of chemical pretreatments on the hydrogen isotope composition of 2:1 clay minerals. *Rapid Communications in Mass Spectrometry*, 27(10), pp.1143–1148. <https://doi.org/10.1002/rcm.6554>.
- Zhang, Zhi.Yi., Huang, Li., Liu, Fan., Wang, Ming.Kuang., Fu, Qing.Ling. and Zhu, Jun., 2017. The properties of clay minerals in soil particles from two Ultisols, China. *Clays and Clay Minerals*, 65(4), pp.273–285. <https://doi.org/10.1346/CCMN.2017.064064>.

## 4 Revisiting the origin of the Ries graded suevite: implications for plume fallback preservation and early post-impact sedimentary deposition.

### 4.1 Introduction

Craters formed from hypervelocity impact events can host deposits that represent a variety of post-impact processes, such as lacustrine, biological, hydrothermal, and fluvial activity (e.g., Jankowski, 1977a; Riding, 1979; Osinski, 2005; Koeberl et al., 2007a; Arp et al., 2013; 2019; Osinski et al., 2020). As such, meteorite impact craters can contain valuable paleoenvironmental records and are high-priority targets for the exploration of Mars. Impact cratering has also heavily influenced the evolution of the Earth's surface and could have provided key habitats facilitating the origins of life on Earth and elsewhere in the Solar System (Kring, 2000; Osinski et al., 2020). Despite the importance of understanding the impact cratering process for the exploration of the Earth, Moon and Mars, some aspects of the process remain poorly understood. The emplacement of impactites, in particular crater-fill and ejecta deposits, is one such area of ongoing study. Building on early studies of the Moon that proposed the ballistic emplacement of continuous ejecta blankets (Oberbeck, 1975) and the recognition of overlying impact melt ponds and flows (e.g., Hawke & Head, 1977), Osinski et al. (2011) proposed a working hypothesis for the emplacement of impact melt lithologies, impact ejecta, and crater-fill deposits consisting of 4 main stages: (1) crater excavation and ballistic ejecta emplacement, (2) late excavation–early modification and minor melt-rich flow emplacement, (3) crater modification and “late” melt-rich flow emplacement, and (4) minor fallback. Of these stages, the subaerial deposition of material from ejecta plumes (i.e., fallback) into the crater is least understood and the deposits can be difficult to distinguish from other post-impact depositional products. In fact, relatively few studies have focused on the lithologies formed from the subaerial deposition of material from the ejecta plume. A notable exception is the Bosumtwi impact structure, Ghana, which hosts a normally graded ejecta plume deposit that formed after immediate post-impact modification within hours after the impact (Koeberl et al., 2007a).

Complicating the recognition of subaerial plume deposits is that the early post-impact environment can be inundated with multiple processes, such as impact generated hydrothermal alteration (Naumov, 2005; Kirsimäe and Osinski, 2013; Osinski et al., 2013), lacustrine deposition (e.g., Füchtbauer et al., 1977; Jankowski, 1977b; 1981; Salger, 1977; Arp et al., 2017), and biological activity (e.g., Cockell & Lee, 2002; Osinski et al., 2020) resulting in the formation of highly heterogeneous deposits representing early post-impact deposition. Based on theory and observations, these early fallback deposits are expected to be normally graded and should be situated stratigraphically *above* impact melt-rich crater-fill impactites (i.e., impact melt rocks and/or impact melt-bearing breccias), and *below* post-impact lacustrine deposits (Fig. 4.1; Koeberl et al. 2007a; Osinski et al. 2011). It remains unclear how these deposits vary between different impact structures, and what post-impact processes control the nature of their deposition and their preservation. Thus, it is pertinent to investigate putative fallback deposits in well preserved impact structures to develop a more informed understanding of their formation mechanisms.

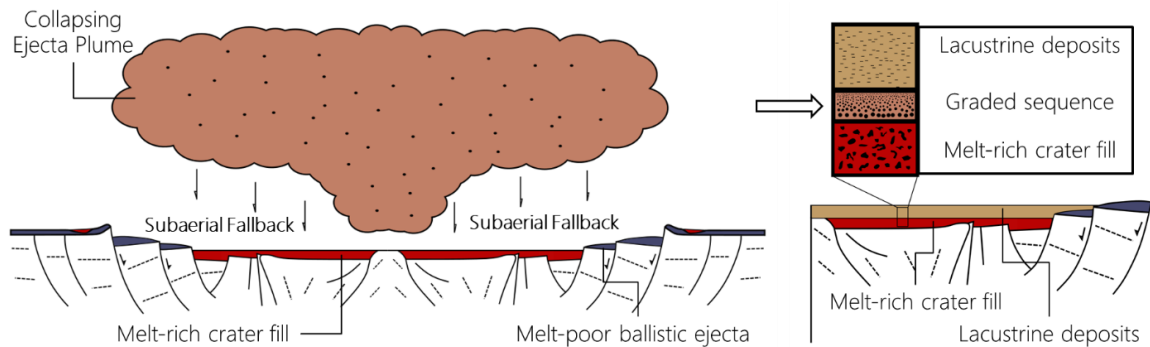


**Figure 4. 1:** A schematic representation of the process by which a cloud of impact-generated material settles back into the bounds of the impact structure and deposits a fining-upward graded “fallback” sequence, which can then be subsequently buried by post-impact lacustrine deposition.

In this study, we revisit the origin of the so-called “graded suevite” unit sampled by the Nördlingen 1973 drill core (FBN73) from the Ries impact structure in southern Germany. The Ries graded unit is ~17 m thick and transitions from a conglomeritic base to fine silt at its top. While the Ries graded unit is interpreted as representative of a single depositional

event (Jankowski, 1977b), there are contradicting interpretations regarding the nature of this event. Jankowski (1977b) suggested that the most probable explanation is that this graded sequence was formed from the fallback of ejecta plume material; although this author does acknowledge the possibility of deposition from a turbidity current and states that such an interpretation would require further study. More recently, Artemieva et al. (2013) modeled the depositional setting of the Ries graded sequence and used a comparison of subaqueous and subaerial settling models to determine the amount of water or air necessary to grade such a mixture of sediment. The results suggested that subaerial deposits were well-mixed, whereas the subaqueous deposits were well-graded. Thus, these authors suggested the subaqueous deposition of the Ries graded unit.

Here, we present the results of the first detailed study of the petrography and sedimentology of the graded unit (331.0–314.3 m) sampled by the FBN73 drill core since 1977. To improve the current geological context for the deposition of the graded unit, we provide an investigation of the overlying post-impact sedimentary rocks (FBN73 Unit A; 314.3–256.0 m), which represent the transition from impact melt-bearing breccias to post-impact lacustrine deposits sampled by FBN73 and compare that transition to that of the Wörnitzostheim drill core (Fig. 4.2; Chapter 2). We also compare the Ries graded unit to the graded unit of a well characterized fallback deposit at the Bosumtwi impact structure, Ghana (Koeberl et al. 2007a). The graded unit at the Bosumtwi impact structure is used as a guide for the classification of subaerial fallback deposits and serves as a starting point to begin interpreting the processes that may control subaerial fallback preservation. It should be noted that, while the term “fallback” has been used to describe melt-bearing breccias often called “suevite” at many impact craters (e.g., fallback suevite), the merits of such terminology has been the subject of some discussion (e.g., Engelhardt. W. v. et al., 1995; Osinski et al., 2004; Stöffler. et al., 1977), so for the purposes of this study subaerial fallback shall specifically refer to graded units.

## 4.2 Background

The ~24 km diameter, ~14.8 Ma (Schmieder et al., 2018) Ries crater in southern Germany is a complex impact structure with a central basin enclosed within the so-called inner ring,

and a tectonic outer ring representing the crater rim. The central basin of the impact structure hosts the majority of the sedimentary deposits from the post-impact crater lake and underlying crater-fill impact melt-bearing breccias that comprised a significant source of heat for the impact generated hydrothermal system (Osinski 2005). The impact melt-bearing breccias and post-impact sedimentary deposits that occupy the central basin were sampled by the FBN73 drill core, with main results presented in the 75<sup>th</sup> volume of the journal *Geologica Bavarica* in 1977 (Pohl et al., 1977). The FBN73 core samples 604.0 m of crystalline basement from 1206.0 to 602.0 m, followed by 270.5 m of altered impact melt-bearing breccias, from 602 to 331.5 m depth. The alteration of the crater-fill impact melt-bearing breccias consists of an early stage of K-metasomatism with minor albitization and chloritization of crystalline basement clasts, which was subsequently followed by argillic alteration and zeolitization (Osinski, 2005). The pervasive nature of the alteration to the crater-fill impact-melt bearing breccias indicated that they were likely the main source of heat for the Ries hydrothermal system (Osinski 2005).

The focus of this study, the “graded unit”, overlies the melt-bearing breccias from 331.5 to 314.3 m depth. The upper and lower contacts of the graded unit are inclined and at least the upper contact is erosional (Füchtbauer et al., 1977). This unit is then overlain by post-impact sedimentary rocks from 314.3 m to the top of the drill core. The basal unit of post-impact sedimentary deposits within the central basin (Unit A of Füchtbauer et al. 1977; Jankowski 1977) records the transition from impact melt-bearing breccias to lacustrine deposits. Füchtbauer et al. (1977)’s Unit A was described as “reworked suevite” and is also referred to as the “basal unit” by other workers (Jankowski, 1977a), and extends from 314.3 to 256.0 m depth. Early studies of the “reworked suevite” interpreted the rocks as flysch type graded beds that were deposited subaqueously (Füchtbauer et al., 1977). These flysch type deposits were interpreted to represent deposition in an arid playa environment (Füchtbauer et al., 1977; Jankowski, 1977a). Overlying units in the sedimentary sequence sampled by FBN73 record soda lake deposition (unit B: laminate member), which transitions into soda to halite lake deposition (unit C: marl member), and finally to halite lake approaching freshwater conditions (unit D: clay member; Füchtbauer et al., 1977; Jankowski, 1981; Arp et al., 2013; 2017; 2021).

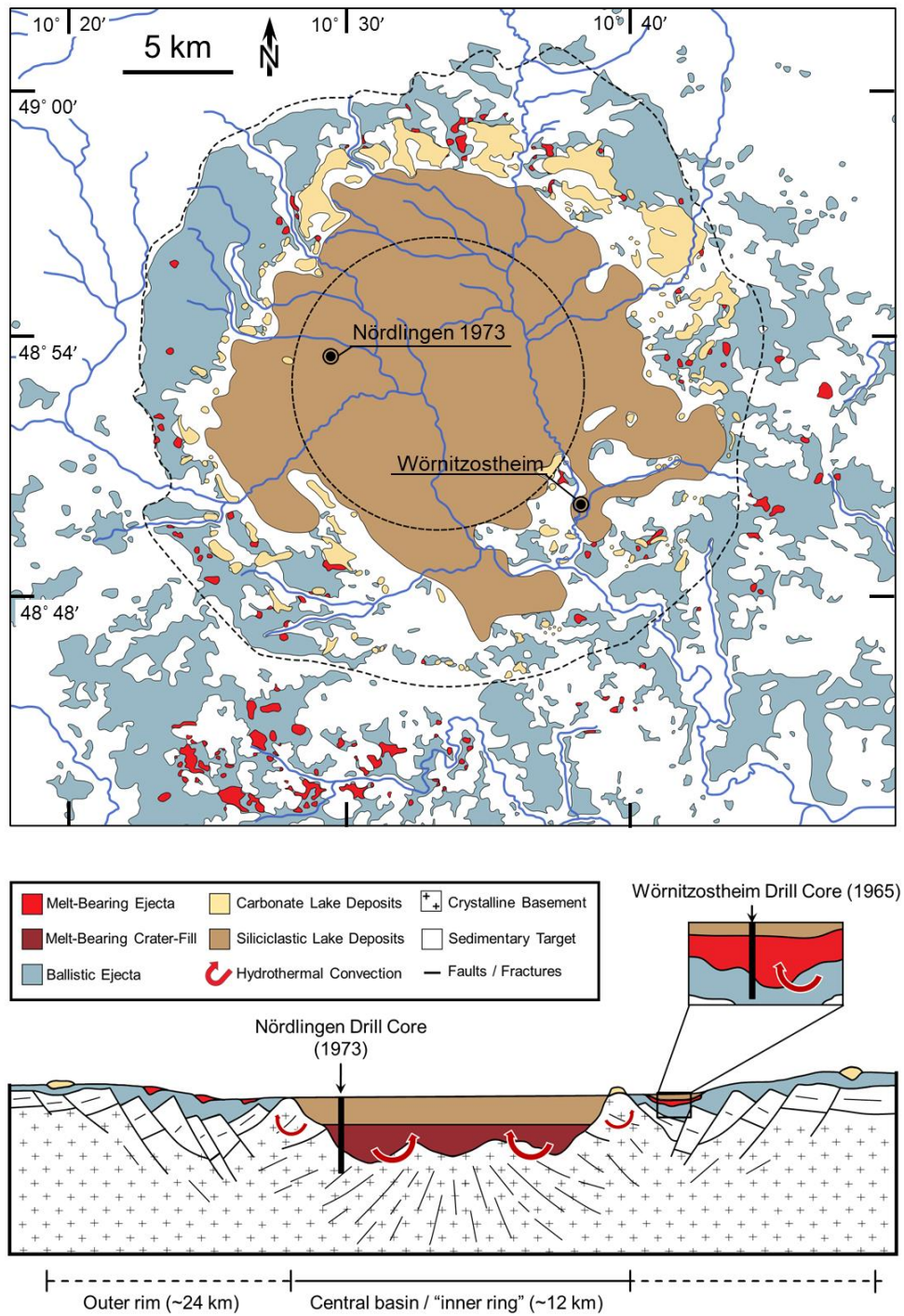


**Figure 4. 2:** (A) A geological map of the Ries impact structure modified from Sapers et al. (2017) and (Arp et al., 2017), which depicts main geological faces and locations of the Nördlingen 1973 borehole. The distribution of the post-impact lacustrine rocks as

determined based on **Ernstson, (1974), Hüttner & Schmidt-Kaler (1999) and Pohl et al., (1977)**. The cross section (B) illustrates the subsurface nature of the main structural components of the Ries impact structure, and main geological faces. Drill core locations and arrows indicating regions of significant hydrothermal alteration are overlain on the cross section.

One of the only other examples of a graded unit within the crater-fill of a complex impact structure is at the ~10.5 km diameter, ~1.0 Ma (Schnetzler et al., 1967; Koeberl et al., 1997) Bosumtwi Crater in southern Ghana. A drilling project under the framework of the International Continental Scientific Drilling Program (ICDP) recovered 16 drill cores from six locations within Lake Bosumtwi, one of which (LB-05) sampled a graded unit between crater-fill the impactites and overlying post-impact lake deposits (Koeberl, et al., 2007a; Koeberl et al., 2007b). This ~30 cm thick graded unit preserves roughly spherical aggregates of clastic material interpreted as accretionary lapilli, and impact glass clasts that display spherical, teardrop, dumbbell and irregular shapes (Koeberl et al. 2007a). The lapilli are most abundant at the top of the graded unit and showed a notable population decrease with depth (Koeberl et al. 2007a).

### 4.3 Methodology

For this study, 142.6 m of the Nördlingen 1973 drill core (FBN73) stored at the Impact Crater Museum (ZERIN) in Nördlingen, Germany, was logged from a depth of 334.6–192.0 m capturing ~80 lithological unit changes and the transition from crater-fill impact melt-bearing breccias to post-impact sedimentary rocks. The ~17 m thick graded unit from FBN73 (314 – 331.5 m) was logged in detail, with 15 representative thin sections made to document the 10 major lithological changes observed along this transect (Fig. 4). Additionally, a set of 38 samples were taken along the 334.6–192.0 m transect and those showing signs of potential secondary mineralization were targeted for focused study. Thin sections were examined using transmitted and reflected light microscopy with plane polarized light (PPL) and cross polarized light (XPL), and subsequently analyzed using the Bruker M4 Tornado micro-X-ray fluorescence ( $\mu$ XRF) instrument with at 17  $\mu$ m spot-size. The  $\mu$ XRF instrument produced false color images, which indicated elemental distribution,

and was used to qualitatively estimate the elemental composition of the most friable material and to contextualize microscale features. Additionally, early optical microscopy and  $\mu$ XRF was used to vet samples for accretionary or glass lapilli, and to establish an analytical baseline for more focused analyses.

## 4.4 Results

The section of drill core investigated in this study (334.6–192 m; Fig. 4.3) records a complex series of lithological changes that are outlined here to provide context for the graded sequence. Altered crater fill impact melt-bearing breccias were documented from 334.6–331.5 m (cf., Osinski, 2005; Stöffler et al., 1977). These impactites show pervasive argillic alteration of impact glass and crystalline clasts, plus calcite and feldspar mineralization primarily in fractures and voids. While not observed in this study, these impact melt-bearing breccias directly abut the graded unit with an angular and sharp contact (Füchtbauer et al. 1977; Pohl pers. comm. 2019). Below, we detail our observations on the units overlying the crater-fill impact melt-bearing breccias.

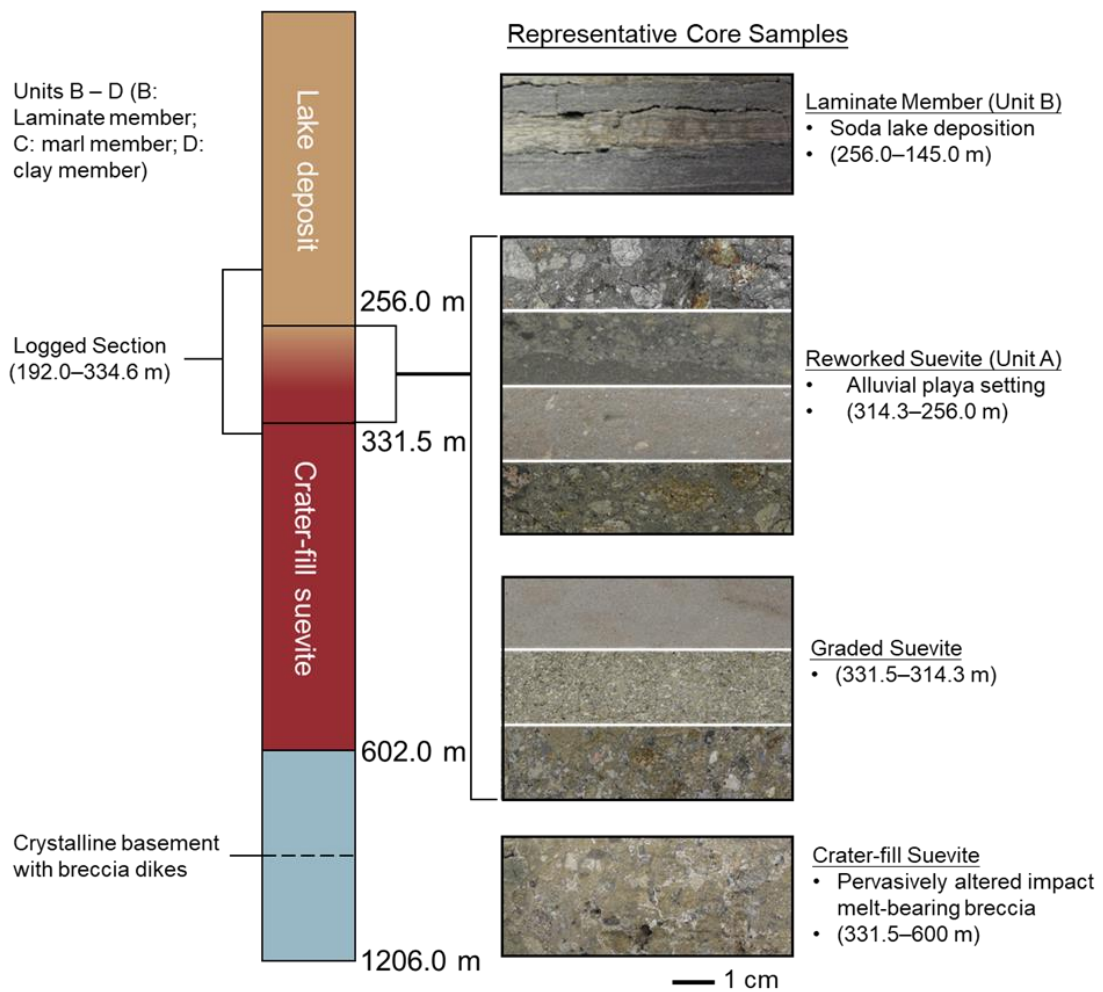


**Figure 4. 3:** Simplified stratigraphy of the Nördlingen 1973 drill core noting the location of the logged section studied here, and representative core images of the major units demarcated in previous studies (e.g., Füchtbauer et al. 1977; Stöffler et al. 1977).

## 4.4.1 Stratigraphy

### 4.4.1.1 Graded Unit 331.5 to 314.3 m depth

The graded unit gradually fines upwards from a coarse, clast-rich, but matrix supported conglomerate at its base (331.5–325.2 m) to clast supported gravelstone (325.2–324.0 m), to clast supported sandstones (324.0–316.3 m), and finally to clast supported siltstones (316.0–314.0 m; Fig. 4.4). This upward transition, demarcated by gradual overall grainsize changes, is intermittently truncated by the abrupt occurrence of pervasively altered breccias at 322.1–322.0 m and 316.3–316.0 m (Fig. 4.4). Each unit logged in the graded sequence is massive and poorly sorted except for the basal gravelstone (325.2 – 324.0 m), which exhibits preferential alignment among most clasts. The contacts between the different units were not preserved in the remaining drill core. Clasts throughout the graded sequence comprise a mixture of sub-rounded to sub-angular granitoid and amphibolite lithic clasts, feldspar and quartz mineral clasts, and impact glass clasts. The granitoid and amphibolite lithic clasts typically occur on mm to cm scales; whereas feldspar and quartz clasts occur on mm to sub-mm scales. Impact glass clasts occur from cm to sub-mm scales and possess irregular shapes (Figs. 4.5A–C). The clast morphology of all aforementioned granitoid, amphibolite, impact glass, feldspar and quartz clasts is does not change throughout the graded sequence.

FBN73: Graded Unit (314 – 331 m)

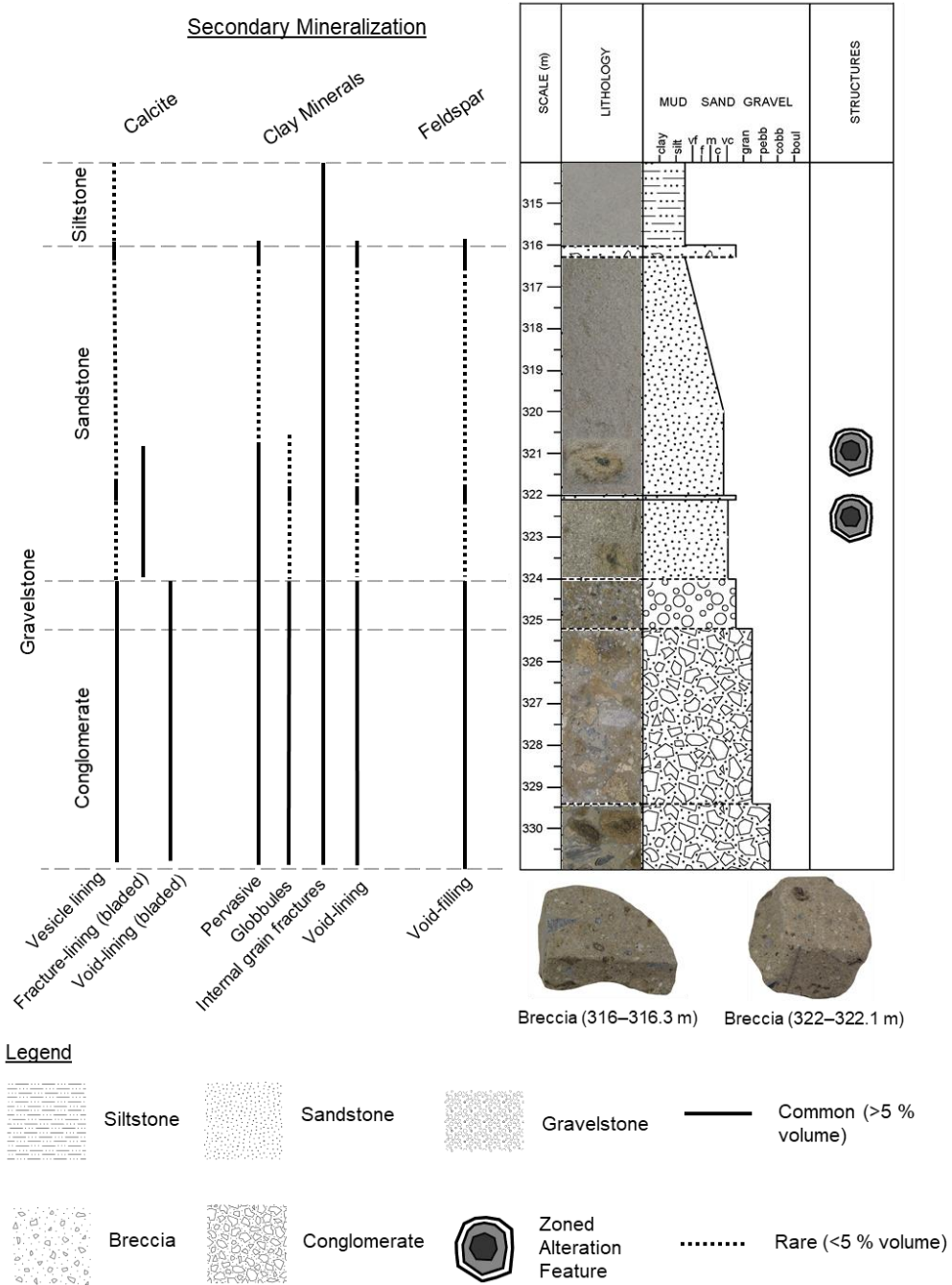


**Figure 4. 4:** The stratigraphy of the Ries graded unit showing the major lithological changes, grain size changes and occurrences of notable features such as cm-scale clasts with alteration halos. Notable alteration mineralogy, mode of occurrence and approximate rarity are described by the basic paragenetic to the left of the stratigraphic column.

The impact glass clasts occurred mainly in the basal sandstones, gravelstone and conglomerates (322.1 – 331.5 m) and most commonly as sub-rounded glass clasts. Additionally, these glass clasts exhibit schlieren textures, and perlitic cracks and vesicles where argillic alteration is sometimes concentrated. Calcite commonly occurs within the glass clasts as globules and often exhibiting liquid immiscibility textures with the glass.  $\mu$ XRF scans of glass clasts showed a strong association with potassium, aluminum, and silica. Perfectly spherical glass clasts or accretionary lapilli as documented in Koeberl et al. (2007a) at the Bosumtwi crater were not observed throughout the Ries graded unit in this study.

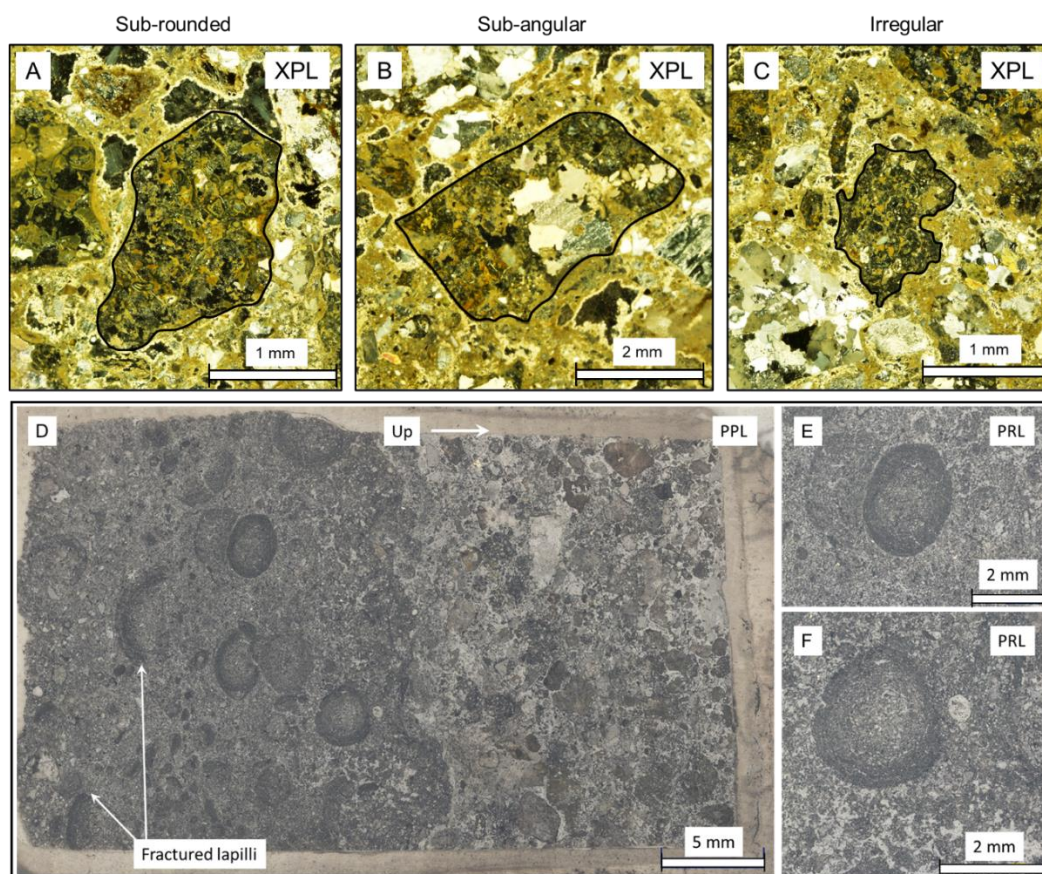


**Figure 4. 5:** Transmitted light photomicrographs of (A) sub-rounded glass clasts, (B) sub-angular glass clasts, and (C) irregularly shaped glass clasts under cross polarized light from

324.0 m depth. (D) A reflected light photomicrograph contact between a post-impact conglomerate overlying a fine mudstone, which hosts a mixture of fractured and well-preserved accretionary lapilli at 282.0 m depth. The long axis of the lapilli is consistently oriented sub-parallel to the contact with the overlying conglomeritic unit. (E, F) Close-up images of individual accretionary lapilli observed in (D). XPL = cross polarized light; PPL = plane polarized light.

#### 4.4.1.2 Reworked Suevite (Unit A): 314.3 to 256.0 m Depth

Overlying the graded unit is a complex 58.3 m thick (314.3–256.0 m), assortment of interstratified conglomerates and fine siltstones (Fig. 4.3; Appendix B). This section of core was originally logged as a series of flysch-type sedimentary rocks called “reworked suevite” by Jankowski (1977b). This author described a series of basal flysch cycles from 314.3 to 305.4 m, with three other overlying major flysch cycles at 305.4–284.0 m, 284.0–272.3 m, and 272.3–257.1 m. Flysch cycles comprise normally graded packages of sedimentary rock that are interpreted as a progression from turbidity flow deposits to shallow water sandstones to claystones (Stow et al., 1996). The results of our study reveal complex and numerous lithological changes that were previously not documented in detail (Appendix B). The conglomerates and gravelstones in this section of the drill core exhibit variations in alteration styles, matrix color, dominant clast type, and style of alteration. Similarly, the fine sandstones and siltstones, which are typically massive, do occasionally exhibit some lamination, and occasional convoluted bedding (Appendix B).

Accretionary lapilli have been reported at 296.0 m and 309.5 m depth in FBN73 by other authors (Figs. 5A–C of Stöffler et al., 2013; Mueller et al., 2018). We also observed similar features at 282.0 m depth (Figs. 4.5D–F), in both well-preserved and fragmented forms. Discussing all the lithological changes in the detail necessary to capture the variability exhibited by these units is not the focus of this current contribution. However, in summary, from 314.3 to 267.5 m we observed a total of ~12 cycles of coarse cm-scale conglomerates transitioning upwards to massive siltstones (Appendix B). These cycles are consistent with observations of flysch type sedimentary rocks from Füchtbauer et al. (1977). Contacts between most units were generally not preserved in drill core with exceptions at 282.0 m

depth, where a sharp, undulating contact exists between a massive siltstone and a conglomerate, and 256.0 m depth, where a sharp, lightly undulating contact exists between a fossil-bearing conglomerate and parallel laminated siltstone. While not explicitly stated in Jankowski (1977b), the contact at 256.0 m depth could mark the upper limit of Unit A. From 267.5 to 256 m, conglomeritic units are interbedded with laminated siltstones and sandstones. Laminations in Unit A siltstones are typically well defined but are more difficult to distinguish in sandstone units. The lithology of the Laminate Member (Unit B) of Jankowski (1977a) is relatively consistent throughout the section of Unit B that was logged in this study (256.0–192.0 m) such that the lithology consists of finely parallel laminated siltstone. There is a notable exception at the base (254.6 m depth) where a siltstone breccia occurs with cm-scale clasts of finely laminated siltstone and a fine silt / clay matrix.

#### **4.4.2 Alteration and Secondary Mineralization in the Graded Unit (331.5–314.3 m)**

Generally, alteration mineralization in the graded sequence is limited to the bottom 11.5 m of the unit (~331.5–320.0 m). Alteration phases present in fine-grained sandstones and siltstones from 321.0 to 314.3 m could not be conclusively distinguished, except for alteration in the interbedded breccia (316.3–316.0 m), and as such, the fine sandstones and siltstones comprising this segment have been excluded for the purposes of assessing alteration mineralogy. The alteration mineralization present in the graded unit of FBN73 can be loosely divided up into three different zones as follows: (1) basal conglomerate / gravelstone alteration zone (331.5– 324.0 m), (2) basal sandstone alteration zone (324.0– 320.0 m), (3) and the interbedded breccia alteration zones (322.1–322.0 m; 316.3–316.0 m). The alteration mineralogy that characterizes these units is discussed below.

#### 4.4.2.1 Basal Conglomerate / Gravelstone Alteration Zone (331.5–324.0 m)

Alteration to the basal conglomerates and gravelstones is characterized mainly by pervasive argillic alteration whereby secondary clay mineralization occurs as fine-grained, brown-colored overprints affecting all clast types and overprinting multiple grain boundaries. Occasionally, clay mineralization exhibits semi-spherical budding and globular textures (Fig. 4.6A). Budding and globular clay mineral textures typically occur in association with glass clasts where clay minerals also commonly occur along perlitic fractures. Feldspar granitoid and amphibolite clasts exhibit argillic (sericitic) alteration to clay minerals along internal fractures and along grain boundaries (Figs. 4.6B, C). Complete replacement of impact glass with clumped aggregates of clay minerals becomes common in the lower 1.5 m (331.5–330.0 m) of the graded unit. Clay minerals also make up a common constituent of the void-filling mineral assemblage. Starting at 324 m depth, secondary clay mineralization commonly occurs as linings and spherical globules within fractures and voids. Pervasive clay mineralization does not overprint void-lining minerals throughout the graded sequence.

Secondary mineralization occurring in addition to the alteration phases in the basal conglomerates / gravelstones are characterized by the occurrence of plagioclase feldspar spherulites as a void-filling phase, and mm to sub-mm scale bladed calcite lining fractures and voids (Figs. 4.6B, C). Plagioclase spherulites typically occurred as sub-spherical radiating aggregates of fibrous material, which nucleate from the void walls and radiate towards the centers of the voids (Figs. 4.6B, C). It was also common for feldspar to radiate from veneers of euhedral calcite crystals that lined the walls of void spaces, and to exhibit polysynthetic twinning at sub-mm scales (Fig. 4.6E). Calcite occurs as bladed mm to sub-mm scale veneers of cm scale void spaces; however, the occurrences of cm-scale voids was restricted to the basal conglomerates (Fig. 4.6F).

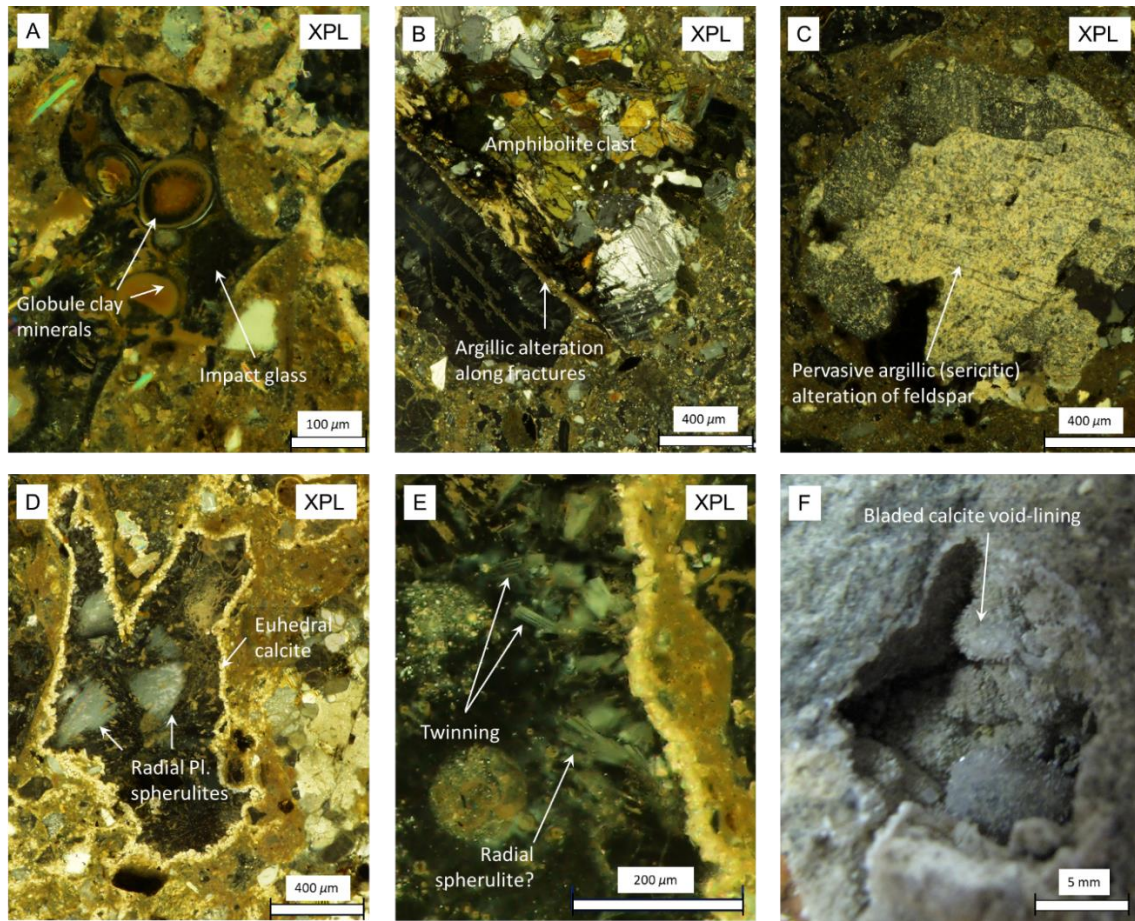


**Figure 4. 6:** (A) Photomicrograph of globular clay mineral textures occurring in association with impact glass (324.0 m). (B) Argillic alteration along an internal fracture of an amphibolite clast (330.0 m). (C) Pervasive argillic alteration to a feldspar clast (330.0 m). (D) Radial textures of feldspar spherulites occurring within a void lined by euhedral calcite crystals (324.0 m). (E) Polysynthetic twinning exhibited by lathes of plagioclase feldspars within a calcite-lined void (324.0 m). (F) Sub-mm scale calcite lining a cm scale void (331.0 m). XPL = cross polarized light.

#### 4.4.2.2 Basal Sandstone Alteration Zone (324.0–320.0 m)

Alteration of the basal sandstones is characterized generally by distinct cm-scale, localized alteration halos that occur concentrically on amphibolite clasts and impact glass clasts. These alteration halos generally occur as three concentric rings that consistently transition inward from a thin outer ring of red-brown material to a thicker ring of yellow-brown material, and lastly to an equally thick ring of white toned material with a clast at the center (Fig. 4.7A). Analyses by  $\mu$ XRF indicates that these glass clasts are associated with Fe- and S-bearing minerals (Fig. 7B). The alteration halos bordering these glass clasts are primarily comprised of clay minerals and are often linked by fractures which host veneers of bladed calcite (Fig. 4.7C).

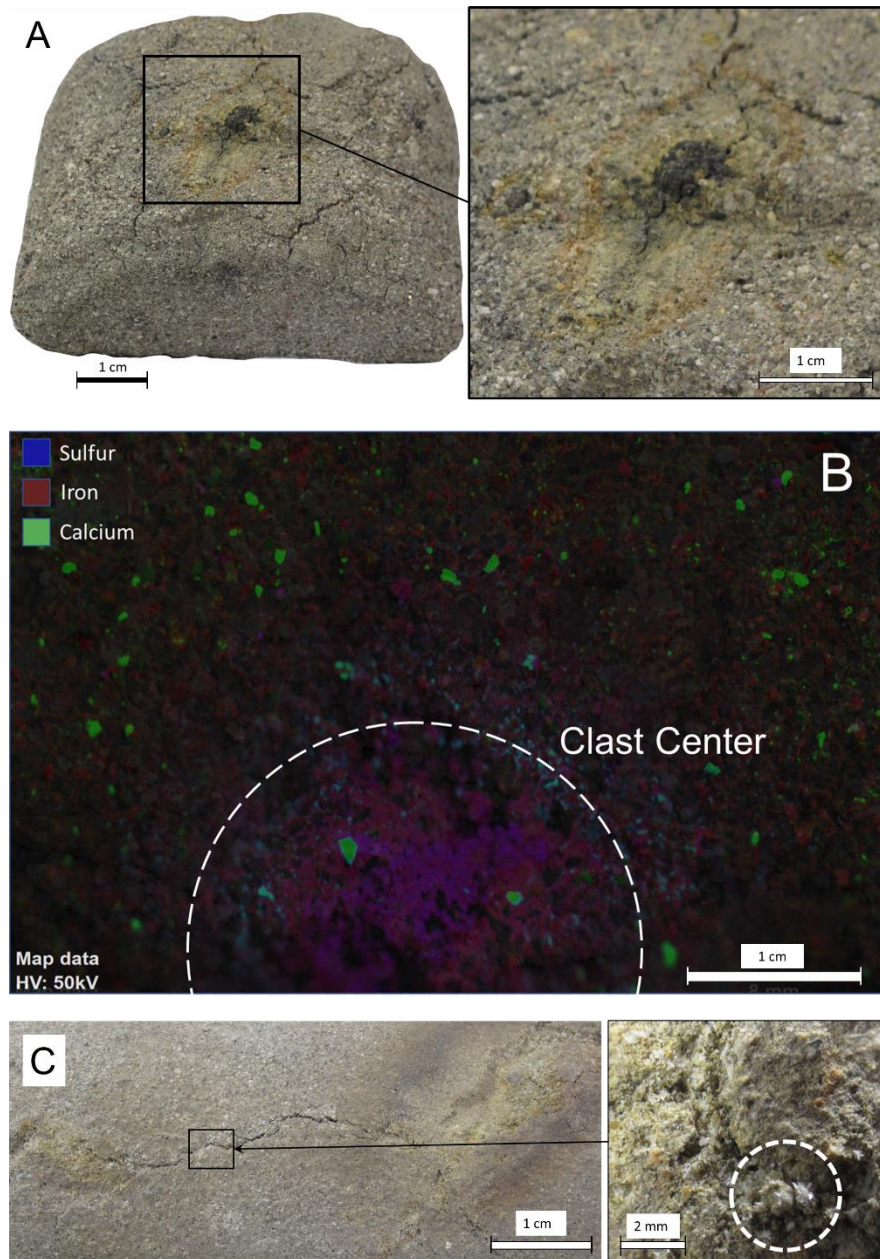


**Figure 4. 7:** (A) Zoned alteration feature from 322.0 m depth showing a full image of the drill core and a close-up image for detail. (B) A  $\mu$ XRF image of the alteration halo from 322.0 m depth showing an association between the central clast and iron, sulfur and calcium. (C) Bladed calcite occurring along a fracture that links two clast-related alteration halos with an close-up image for detail.

The basal sandstone alteration zone also hosts pervasive argillic alteration, but to a lesser degree than occurs in the basal conglomerates and gravelstones. Argillic alteration to the basal sandstones differs to that of the basal conglomerates / gravelstones such that fewer clasts exhibit complete replacement by clay minerals, and alteration along internal fractures of feldspar clasts and amphibolite clasts and along perlitic fractures of impact glass clasts is less common. Additionally, feldspar spherulites occur as void filling phases; however, they occur less frequently than they do in the basal conglomerates, as do void spaces broadly speaking.

#### 4.4.2.3 Interbedded Breccia Alteration Zones (322.1–322.0 m; 316.3–316.0 m)

Alteration to the interbedded breccias is similar to that of the basal conglomerates with the main noticeable difference being the color of the matrix of the interbedded breccias, which tend to take on a pinkish color; whereas the basal conglomerates and gravelstones present a green-grey color (Fig. 4.4). Generally, the clasts in both the basal conglomerates and gravelstones and the interbedded breccias consist of fragmented clasts of amphibolite, feldspars and impact glass. In both cases, this clastic material shows argillic alteration along internal fractures (Figs. 4.8A, B). Additionally, argillic alteration is pervasive in both the interbedded breccias and basal conglomerates / gravelstones, and both alteration zones show similar void filling mineral assemblages that consist of plagioclase feldspar spherulites, clay minerals, and euhedral calcite.

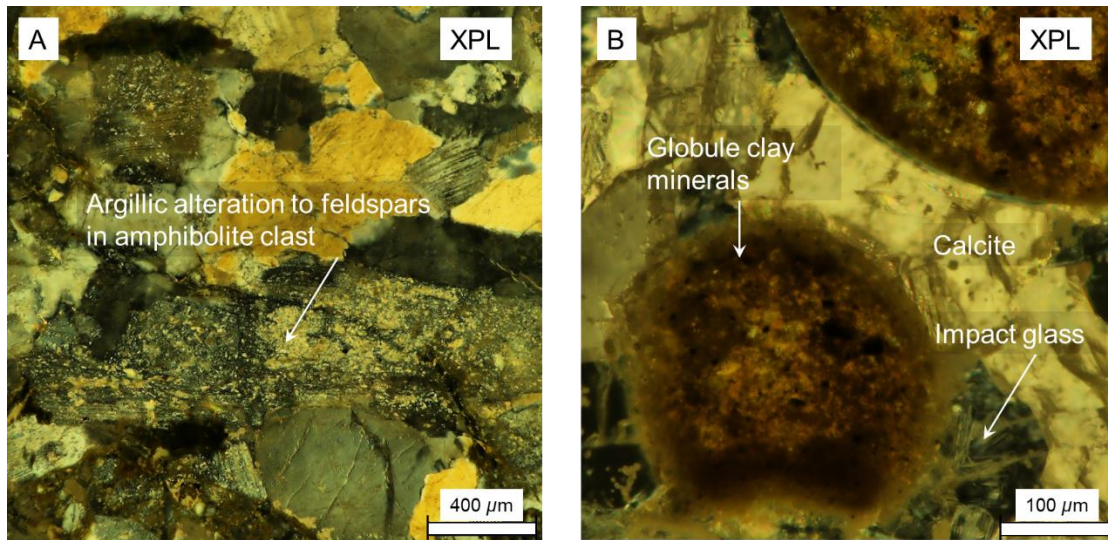


**Figure 4. 8:** (A) A section of a granitoid lithic clast showing sericitic alteration to clay minerals in the feldspars. (B) Vesicle hosted in impact glass filled by clastic material that has been altered to clay minerals. XPL = cross polarized light.

## 4.5 Discussion

### 4.5.1 Deposition of the Ries Graded Unit

The Ries graded unit is a ~17 m thick, normally graded deposit of sub-rounded clastic material from 331.5 to 314.3 m depth, that is interbedded with two distinct breccia units (322.1–322.0 m and 316.3–316.0 m). There are also three main zones of secondary alteration, which are (1) the basal conglomerate / gravelstone zone, (2) the basal sandstone zone, and (3) the interbedded breccia zone.

It is notable that the graded fallback deposit preserved at the Bosumtwi impact structure is many times smaller than the Ries graded unit with a total thickness of ~30 cm (Koeberl et al. 2007a), and secondary mineralization in the Bosumtwi fallback deposit is generally restricted to very thin rim of alteration phases around glass spherules and accretionary lapilli. Although the Bosumtwi impact structure is approximately half the diameter of the Ries (~10.5 km diameter and ~24 km diameter, respectively), this size difference does not provide a satisfactory explanation for the difference in the scale of Ries and Bosumtwi graded units if subaerial deposition is assumed for both deposits. We acknowledge that the

difference in target material potentially influenced the size and make-up of a possible fallback deposit; however, this is speculative. It is therefore plausible, based on the difference in thickness alone, to postulate that the Ries graded unit was not formed by the same processes as the Bosumtwi fallback deposit. The nature and preservation of glass clasts and accretionary lapilli would allow for better distinction between the Bosumtwi fallback deposit and the Ries graded unit.

Impact glass clasts are present in the Ries graded unit from ~331.5 to 322.3 m depth, and only occur rarely from 322.3 to 314.3 m. An important distinction between the glasses in the Ries' graded unit and Bosumtwi crater's fallback deposit is that the Ries glass clasts are sub-rounded to sub-angular (Figs. 4.4A–C); whereas at Bosumtwi the glasses occur with perfectly spherical, teardrop, dumbbell, and irregular shapes. The common morphology of the Ries glasses is consistent with that of the granitoid, amphibolite, feldspar and quartz clasts, and indicates that all aforementioned clasts were subjected to erosive transport; whereas the relatively well-preserved morphology of the glass lapilli observed in the Bosumtwi fallback deposit does not indicate any notable erosion or mechanical reworking. Additionally, the glass present in the Ries graded unit has an inverse population distribution with respect to that of Bosumtwi. The glass clasts are common at the base of the Ries graded unit; whereas they occur in abundance at the top of the Bosumtwi fallback deposit (Koeberl et al. 2007a) as is predicted from theory (Melosh, 1989). In addition, the glass clasts in the Ries graded unit share similar alteration patterns to glass clasts observed in crater-fill impact melt-bearing breccias (Osinski 2005), and to impact melt-bearing breccia ejecta present in the Wörnitzostheim drill core (Chapter 2). In all cases, glass clasts show alteration along perlitic fractures and an association with secondary alteration to clay minerals.

We conclude that the glass observed in the Ries graded unit are not lapilli but are rather detrital glass clasts derived from local impact-melt-bearing breccias. This is supported by the presence of vesicles and schlieren in the glasses in the Ries graded unit, which is consistent with whole rock impact glasses in the underlying crater-fill sequence. While it could be argued that any lapilli at the top of the Ries graded unit could have been eroded

as evident by the erosional contact documented in (Füchtbauer et al. 1977), there are no broken spherical glass clasts. The fact remains that glass clasts are present at the base of the Ries graded unit, whereas they are not present at the base of the Bosumtwi fallback deposit.

Despite the lack of accretionary lapilli and glass lapilli in the graded unit, accretionary lapilli are not absent in the FBN73 drill core, having been documented in Unit A (314.3–256 m), which preserves flysch-type sedimentary rocks (e.g., Mueller et al. 2018; Figs. 8F–H). Prior to this study, accretionary lapilli in FBN73 have been observed at depths of 309.5, (Mueller et al. 2018), 304.0 and 296.0 m (Stöffler et al. 2013). We also noted an additional occurrence at a depth of 282.0 m. Importantly, these accretionary lapilli-bearing units are distinct from the graded unit and record different depositional processes. The mix of fractured and well-preserved accretionary lapilli and their preferential alignment at 282.0 m depth in our study – and at slightly shallower levels in the aforementioned previous studies – suggests they were subject to a degree of erosional transport. Thus, there are, at present, no accretionary lapilli in their primary depositional setting at the Ries impact structure and, therefore, no conclusions about the ejecta plume dynamics and immediate post-impact deposition of fallback material should be drawn. Instead, the occurrence of accretionary lapilli within the flysch type sedimentary deposits of Unit A and the fractured state of some lapilli, indicates that these lapilli were likely deposited elsewhere and transported to their current setting.

Having now ruled out subaerial deposition from an ejecta plume (Jankowski, 1977b), we now turn to the second proposed mechanism for the graded sequence, namely subaqueous deposition from a turbidity current (Artemieva et al., 2013). The notion that the Ries impact structure rapidly filled in with water (e.g., Pohl et al. 1977; Osinski 2005; Stöffler et al. 2013) could support the theory proposed by Artemieva et al. (2013). Indeed, the pervasive alteration to the impact melt-bearing breccias immediately underlying the graded unit was also considered indicative of immediately available source of water in sufficient volumes to trigger such alteration (Osinski 2005). However, the deposition of a turbidity flow deposit and the flysch type sedimentary sequences of Unit A (314.3–256.0

m; Füchtbauer et al. 1977) would require the existence of a *deep* body of water prior to the deposition of both units, and it is unclear what depth could be plausibly achieved during early lacustrine filling. Importantly, no deep-water sedimentary deposits occur stratigraphically below the graded unit, so there is no evidence that a sufficiently deep body of water required to deposit a ~17 m thick turbidity flow, as suggested by Artemieva et al. (2013), and the overlying flysch cycles was present prior to the deposition of the graded unit. The sharp contact at the base of the graded unit (Füchtbauer et al. 1977) does, however, indicate that such deposits could have been eroded. Additionally, the absence of deep-water deposits does not necessarily preclude the rapid formation of a deep body of water. Framing the climatic setting at the time of the Ries impact event could indicate whether the formation of a body of water capable of forming a ~17 m thick turbidity current deposit prior to subaerial fallback deposition is plausible.

The age of the Ries impact structure (~14.8 Ma; Schmieder et al. 2018) indicates that the impact event occurred during the Mid-Miocene Climatic Optimum, and Böhme (2003) reported on migration events of vertebrates adapted to a dry climate towards central Europe at the time of the Ries impact event (~14.7–14.5 Ma), which suggests that water availability was highly seasonal (Böhme 2003). Paleoclimate studies of central Europe also indicate relatively high amounts of rain with a mean annual precipitation of ~828–1362 mm (Böhme, Bruch and Selmeier, 2007), which is supported by further isotopic studies that show meteoric water, likely precipitation, was a major component of early fluids at the Ries, at least in the nearby periphery of the central basin (Chapter 3). While torrential rains should not be ruled out, there is currently no evidence for immediate post-impact formation of a deep body of water of the central basin. Groundwater influx into the newly lowered hydrologic head created by the impact event could provide a major source of fluid in the central basin. One could also speculate that the evaporation of incoming groundwater caused by hot impact melt-bearing breccias and the evaporation of volatiles bound in sedimentary target rocks in the melt-bearing breccias themselves could generate a transient humid atmosphere, which likely contributed to subsequent precipitation events upon cooling of the airmass. Given the highly seasonal nature of precipitation at the time of the Ries impact event (Böhme, 2003), we suggest that it is highly unlikely that groundwater

influx in conjunction with immediate torrential rains triggering the formation of a large enough body of water to accommodate a ~17 m thick subaqueous turbidity flow within hours after impact is a realistic explanation for the occurrence of the graded unit.

Based on our observations, we suggest an alternative depositional setting whereby the Ries graded unit was deposited by water-laden, subaerial debris or gravity flows during alluvial fan-delta formation, triggered by post-impact modification and precipitation-driven weathering and erosion of local impact melt-bearing breccias. Deposition by water-laden alluvial processes could similarly explain the sub-rounding of the clasts in the Ries graded unit, and the pervasive alteration present at the base of the graded unit. Additionally, the location of the Nördlingen drill core is towards the periphery of the central basin and would sample the fining upwards sequence produced by a backstepping alluvial fan. Indeed, the original work of Füchtbauer et al. (1977) and Jankowski (1977a) suggests that the basal sedimentary deposits (~256.0–314.3 m) overlying the Ries graded unit represents a progressively drying environment with desiccation cracks and evaporitic minerals. The progression into a dry playa environment would fit well with the evolution of a fluviolacustrine system from an alluvial fan in a climate with highly seasonal precipitation. Torrential rains and subsequent flooding could explain the sharp contact that marks the upper limit of the Ries graded sequence and could explain the occurrence of bodies of water that could trigger the deposition of flysch type sedimentary sequence overlying the graded unit.

The flysch type deposits overlying the graded unit record likely record multiple flooding events and debris flows, consistent with interpretations of Jankowski (1977a). The first occurrence of parallel laminated siltstones, clear indicators of lacustrine deposition, occurs at 267.5 m depth. One final overlying cycle of normally graded sedimentary rocks occurs from 267.2 to 262.6 m, which could represent a turbidity current. Parallel and convoluted laminated siltstones representing continued lacustrine deposition comprise the main lithology of FBN73 from 267.6 m and upward; however, the limit of Unit A is marked by the final occurrence of a conglomerate bearing fossils of shelly fauna at 256.0 m (Appendix B; Füchtbauer et al. 1977; Jankowski 1977a). We suggest that the alteration features present

in the conglomerates throughout Unit A likely have detrital origins and indicate alteration from a previous setting rather than their current one.

#### 4.5.2 Hydrothermal Alteration of the Ries Graded Unit

There are four main styles of secondary mineralization throughout the graded unit, that are distributed across the three alteration zones: basal conglomerate / gravelstone zone (331.5–324.0 m), basal sandstone zone (324.0–320.0 m) and the interbedded breccia zone (322.1–322.0 m; 316.3–316.0 m). The styles are: (1) alteration halos associated with coarse, cm-scale glass and granitoid and amphibolite lithic clasts, (2) bladed calcite occurring along fractures and cm-scale vugs, (3) clay minerals, plagioclase feldspar spherulites and calcite occurring as void-lining and /or void-filling minerals, and (4) pervasive secondary clay mineralization with varying degrees of replacement of lithic and glass clast.

The bladed calcite present in sandstones throughout this subsection indicates that boiling occurred during secondary mineralization (Simmons and Christenson, 1994). The radial pattern exhibited by plagioclase feldspar spherulites have been experimentally reproduced at ~ 1 atm with a 100–200 °C undercooling (Muncill and Lasga, 1988); however, this is dependent on the composition of the feldspar, which is not known here. While it cannot be said with certainty, we suggest that the presence of both radial spherulites and bladed calcite indicate that fluid temperatures of ~100–200 °C should be considered. Provided that the dominant source of fluids for the Ries hydrothermal system was likely dominated by meteoric water (Chapters 2 and 3), a fluid temperature of at least 100 °C is likely. As such, this comprises the best evidence to date for >100 °C alteration to post-impact lacustrine deposits in an impact structure.

The association of impact glass and crystalline clasts with both alteration halos and bladed calcite alteration styles suggests that the origin and timing for both styles of alteration were similar. The sharp contrast between the breccias and sandstones suggest differing depositional origins; however, both the breccias and the basal conglomerates and gravelstones of the graded sequence exhibit pervasive alteration to secondary clay minerals. The exclusion of void-lining minerals from the assemblage of material that are overprinted

by secondary clay mineralization suggests that void-filling minerals formed either at the same time as the pervasive clay mineralization or sometime after. Additionally, the occurrence of alteration halos overprinting pervasive clay mineralization suggests that both alteration styles 1 and 2 occurred after pervasive alteration to secondary clay minerals. Thus, the timing of the varying secondary mineralization styles was such that there was a period of pervasive alteration to secondary clay minerals (4), which occurred concomitantly or prior to void filling mineralization, possibly at 100 to 200 °C (3). Continued alteration due to the presence of cm-scale granitoid and glass clasts triggered the continued formation of secondary clay minerals in the form of concentric alteration halos (1). Fractures and voids associated with the coarser clastic material were lined with bladed calcite (2) during the formation of the alteration halos.

#### 4.5.3 Comparison to the Wörnitzostheim Drill Core

The Wörnitzostheim drill core was acquired from the south-eastern edge of the Ries central basin (Fig. 2A), and samples the transition from impact melt-bearing breccias to post-impact lacustrine deposits at a ~200 m higher elevation than that of FBN73 (Fig. 2B; Stöffler et al. 2013). The alteration to the impact melt-bearing breccias that were transported beyond the bounds of the Ries central basin show limited alteration features that are generally restricted to fracture and void-filling minerals (Osinski et al. 2004; Osinski 2005). These melt-bearing breccias are characterized by rapid cooling to 100–130 °C (Osinski 2005), which is additionally supported by the presence of plagioclase feldspar spherulites (Chapter 2); a texture of plagioclase that indicates quenching from relatively high temperatures. A relatively small, normally graded sandstone unit occurs from 13.1–10.7 m in the Wörnitzostheim drill core (Chapter 2); however, no accretionary or glass lapilli have been observed (e.g., Chapter 2; Förstner, 1967). Many of the original contacts between the different units sampled by the Wörnitzostheim drill core have not been preserved, so it is unknown whether any graded fallback deposits from the ejecta plume were deposited and then eroded, or never deposited in the first place. The graded sandstone of the Wörnitzostheim drill core is underlain by a series of conglomerates (16.6–13.1 m; Chapter 2). Together, the sandstones and conglomerates sampled by the Wörnitzostheim

drill core are interpreted to represent the progradation and back-stepping of an alluvial fan, where the conglomerates represent early debris flow deposits.

The alluvial debris flow deposits of the Wörnitzostheim drill core are similar to the conglomerates of the graded unit sampled by FBN73 but exhibit fewer hydrothermal alteration features. Hydrothermal alteration in the debris flow deposits of the Wörnitzostheim drill core are limited to  $\mu\text{m}$ -scale fillings of voids and fractures scattered throughout the conglomerate units (Chapter 2); whereas that of the conglomerates in the FBN73 graded unit is generally more pervasive, and comprises multiple styles of alteration, some of which extend into the overlying sandstones. We suggest that the more abundant and earlier presence of water in the central basin of the Ries impact structure likely was a major cause of pervasive alteration occurring in the basal conglomerates and gravelstones of the graded unit sampled by FBN73. Water was likely to be less readily available at the higher elevation of the Wörnitzostheim drill core location.

The different hydrothermal environments represented by the debris flows of FBN73 and that of the Wörnitzostheim drill core could create different ecological niches for endolithic and endogenic organisms. These basal lacustrine habitats can enable the establishment of stable microbial communities and preserve bio-signatures and organics that could indicate their origins (Meyers and Ishiwatari, 1993). Indeed, there is significant potential for the preservation of diverse ecological systems influenced by impact-generated processes, warranting further exploration of ecological niches provided by early debris flow deposits and weathered impact melt-bearing breccias (Chapter 2).

#### 4.5.4 Comparison with Ejecta Plume Deposit Preservation at the Bosumtwi Crater, Ghana

Accretionary lapilli have not been observed in their primary setting at the Ries impact structure, but rather interbedded in the overlying Reworked suevite. Additionally, the glass that is present in the Ries graded unit is distributed inversely relative to the Bosumtwi fallback deposit, and they typically exhibit sub-rouded morphologies that are consistent with other clast types. We propose that the Ries does not possess primary fallback deposits.

The complex interaction between concurrent hydrothermal alteration, fluviolacustrine deposition, and ejecta plume deposition in a likely humid atmosphere are all likely contributing factors causing accretionary lapilli to occur in unexpected settings at the Ries impact structure. The complex interplay of ongoing processes comprises an important distinction between the Ries impact structure and the Bosumtwi impact crater with respect to the preservation of a distinct plume fallback deposit. The age of the Bosumtwi impact crater suggests it occurred during arid episodes that marked the terminal Pliocene (~1.0 Ma; Koeberl et al., 1997; Schnetzler et al., 1967), and that precipitation and evaporation in a predominantly dry atmosphere had a greater influence on its early lacustrine processes (Shanahan et al., 2006). In contrast, a greater availability of water at the Ries impact structure likely mitigated the preservation of a distinct plume fallback deposit and redistributed the constituents of such a deposit throughout early fluviolacustrine deposition.

## 4.6 Conclusions

Due to the gravity-controlled nature of subaerial deposition, it is likely that ejecta plume deposits would exhibit normal grading (Osinski, Tornabene and Grieve, 2011). As the name suggests, the graded unit at the Ries impact structure possesses this characteristic; however, within the context of impact generated ejecta plume deposits, the occurrence of other characteristic features would be expected, specifically accretionary and glass lapilli (e.g., Koeberl et al. 2007a), which, despite detailed petrographic analysis of the Ries graded unit sampled by FBN73, were not observed in this study. Conversely, the graded unit at the Bosumtwi impact structure, possesses distinct glass lapilli in spherical, teardrop and dumbbell shapes, in addition to accretionary lapilli (Koeberl et al. 2007a). Active fluviolacustrine deposition combined with ongoing hydrothermal activity and subaerial deposition under a warm and humid atmosphere are likely processes that impeded the preservation of subaerial fallback from the Ries ejecta plume. At the Bosumtwi impact structure, the arid climate and relatively limited influx of water could have resulted in better preserved fallback deposits. Poor fallback deposit preservation at the Ries impact structure is further suggested by the presence of accretionary lapilli as preferentially aligned and fractured detrital material in sedimentary units stratigraphically above the Ries graded unit.

Hypothetically, if glass lapilli were in fact present in the Ries graded unit, but not observed in this study, then in addition to the notable reworking and redistribution of material from the ejecta plume, the extensive hydrothermal alteration of glass clasts observed in the graded unit suggests that lapilli would be heavily altered. At the very least, it is highly unlikely that the Ries graded unit solely represents deposition of airborne “fallback” material. We suggest a more likely scenario is that the Ries graded unit represents early water-laden debris flows from early alluvial fan deposition and fluviolacustrine processes controlled by precipitation. While formation of the Ries graded unit from a turbidity flow cannot be completely ruled out based on this study, we suggest debris flow deposition represents a simpler explanation as it does not invoke the presence of a deep body of water; for which evidence is yet to be observed. A follow-up study of the clay mineralogy and hydrogen and oxygen isotope composition would aid in establishing a more accurate understanding of the depositional environment.

This study has conclusively shown that the Ries graded unit is notably different to the fallback deposit preserved at the Bosumtwi impact structure and that the Ries graded unit likely did not form from the subaerial deposition of ejecta plume material. There remains some debate regarding whether there are any “true” ejecta plume fallback deposits at the Ries impact structure (e.g., Stöffler et al., 1977; Graup, 1981; Osinski, 2004; Meyer C., 2012; Artemieva et al., 2013). But the results of this study suggests that a distinct and discrete deposit that solely represents ejecta plume fallback does currently not exist at the Ries impact structure, and that the inclusion of a normally graded fallback deposit as a fundamental component of impact structures might not be consistently necessary or accurate. While the presence of lapilli in post-impact sedimentary deposits are undoubtedly likely, the context and nature of their occurrence can be a strong indicator of the complex processes that shaped the post-impact environment.

## 4.7 References

Arp, G., Blumenberg, M., Hansen, B.T., Jung, D., Kolepka, C., Lenz, O., Nolte, N., Poschlod, K., Reimer, A. and Thiel, V., 2013. Chemical and ecological evolution of the Miocene Ries impact crater lake, Germany: A reinterpretation based on the

- Enkingen (SUBO 18) drill core. *Bulletin of the Geological Society of America*, 125(7–8), pp.1125–1145. <https://doi.org/10.1130/B30731.1>.
- Arp, G., Dunkl, I., Jung, D., Karius, V., Lukács, R., Zeng, L., Reimer, A. and Head, J.W., 2021. A Volcanic Ash Layer in the Nördlinger Ries Impact Structure (Miocene, Germany): Indication of Crater Fill Geometry and Origins of Long-Term Crater Floor Sagging. *Journal of Geophysical Research: Planets*, 126(4). <https://doi.org/10.1029/2020JE006764>.
- Arp, G., Hansen, B.T., Pack, A., Reimer, A., Schmidt, B.C., Simon, K. and Jung, D., 2017. The soda lake—mesosaline halite lake transition in the Ries impact crater basin (drilling Löpsingen 2012, Miocene, southern Germany). *Facies*, 63(1). <https://doi.org/10.1007/s10347-016-0483-7>.
- Arp, G., Reimer, A., Simon, K., Sturm, S., Wilk, J., Kruppa, C., Hecht, L., Hansen, B.T., Pohl, J., Reimold, W. Uwe., Kenkmann, T. and Jung, D., 2019. The Erbisberg drilling 2011: Implications for the structure and postimpact evolution of the inner ring of the Ries impact crater. *Meteoritics and Planetary Science*, 54(10), pp.2448–2482. <https://doi.org/10.1111/maps.13293>.
- Artemieva, N.A., Wünnemann, K., Krien, F., Reimold, W.U. and Stöffler, D., 2013. Ries crater and suevite revisited—Observations and modeling Part II: Modeling. *Meteoritics and Planetary Science*, 48(4), pp.590–627. <https://doi.org/10.1111/maps.12085>.
- Böhme, M., 2003. The Miocene Climatic Optimum: Evidence from ectothermic vertebrates of Central Europe. *Palaeogeography, Palaeoclimatology, Palaeoecology*, 195(3–4), pp.389–401. [https://doi.org/10.1016/S0031-0182\(03\)00367-5](https://doi.org/10.1016/S0031-0182(03)00367-5).
- Böhme, Madelaine., Bruch, Angela.A. and Selmeier, Alfred., 2007. The reconstruction of Early and Middle Miocene climate and vegetation in Southern Germany as determined from the fossil wood flora. *Palaeogeography, Palaeoclimatology, Palaeoecology*, 253(1–2), pp.91–114. <https://doi.org/10.1016/j.palaeo.2007.03.035>.

- Cockell, Charles.S. and Lee, Pascal., 2002. The biology of impact craters-a review. *Biological Reviews*, 77, pp.279–310. <https://doi.org/10.1017/S146479310100584X>.
- Engelhardt. W. v., Arndt. J., Fecker B. and Pankau H. G., 1995. Suevite breccia from the Ries crater, Germany: origin, cooling history and devitrification of impact glasses. *Meteoritics*, 30, pp.297–293.
- Ernstson, Kord., 1974. The structure of the Ries Crater from geoelectric depth soundings. *Journal of Geophysics*, [online] 40, pp.639–659. Available at: <<https://www.researchgate.net/publication/259485112>>.
- Förstner, U., 1967. Petrographische Untersuchungen des Suevit aus den Bohrungen Deiningen und Wörnitzostheim im Ries von Nördlingen. *Contributions to Mineralogy and Petrology*, 15, pp.281–308.
- Füchtbauer, H., Brellie. von der. G., Dehem, R., Förstner, U., Gall, H., Höfling, R., Hoefs, J., Hollerbach, H., Jankowski, B., Jung, W., Malz, H., Mertes, H., Rothe, P., Salger, M., Wehner, H. and Wolf, M., 1977. Tertiary lake sediments of the Ries, research borehole Nördlingen 1973-A summary. *Geologica Bavarica*, 75, pp.13–19.
- Graup, G., 1981. Terrestrial chondrules, glass spherules and accretionary lapilli from the suevite, Ries Crater, Germany. *Earth and Planetary Science Letters*, 55, pp.407–418.
- Hawke, B.R. and Head, J.W., 1977. Impact melt on lunar crater rims. In: D.J. Roddy, R.O. Pepin and R.B. Merrill, eds. *Impact and explosion cratering*. New York: Pergamon Press. pp.815–841.
- Hüttner, R. and Schmidt-Kaler, H., 1999. *Meteoritenkrater Nördlinger Ries*. Munich.
- Jankowski, B., 1977a. Die Postimpakt-Sedimente in der Forschungs-bohrung Nördlingen 1973. *Geologica Bavarica*, 75, pp.21–36.
- Jankowski, B., 1977b. The graded unit on top of the suevite layer in the borehole Nördlingen 1973. *Geologica Bavarica*, 75, pp.155–162.

- Jankowski, B., 1981. Die Geschichte der Sedimentation im Nördlinger Ries und Randecker Maar. *Bochumer geologische und geotechnische Arbeiten*, 6, pp.1–315.
- Kirsimäe, K. and Osinski, G.R., 2013. Impact-induced hydrothermal activity. In: G.R. Osinski and E. Pierazzo, eds. *Impact Cratering: Processes and Products*. Blackwell Publishing Ltd. pp.76–89.
- Koeberl, C., Bottomley, R., Glass, B.P. and Storzer, D., 1997. Geochemistry and age of Ivory Coast tektites and microtektites. *Geochimica et Cosmochimica Acta*, 61(8), pp.1745–1772.
- Koeberl, C., Brandstätter, F., Glass, B.P., Hecht, L., Mader, D. and Reimold, W.U., 2007a. Uppermost impact fallback layer in the Bosumtwi crater (Ghana): Mineralogy, geochemistry, and comparison with Ivory Coast tektites. *Meteoritics & Planetary Science*, [online] 42, pp.709–729. Available at: <<http://meteoritics.org>>.
- Koeberl, C., Milkereit, B., Overpeck, J.T., Scholz, C.A., Amoako, P.Y.O., Boamah, D., Danuor, S.K., Karp, T., Kueck, J., Hecky, R.E., King, J.W. and Peack, J.A., 2007b. An international and multidisciplinary drilling project into a young complex impact structure: The 2004 ICDP Bosumtwi Crater Drilling Project - An overview. *Meteoritics and Planetary Science*, 42(4–5), pp.483–511. <https://doi.org/10.1111/j.1945-5100.2007.tb01057.x>.
- Kring, D.A., 2000. Impact events and their effect on the origin, evolution and distribution of life. *GSA Today*, 10(8), pp.1–7.
- Melosh, H.J., 1989. *Impact cratering: A geologic process*. New York, NY: Oxford University Press.
- Meyer C., 2012. *Sedimentological, Structural and Geochemical Investigations of the Suevite of the Impact Crater Nördlinger Ries, Germany*. Free University of Berlin.

- Meyers, Philip.A. and Ishiwatari, Ryoshi., 1993. Lacustrine organic geochemistry-an overview of indicators of organic matter sources and diagenesis in lake sediments. *Organic Geochemistry*, 20(7), pp.867–900.
- Mueller, S.B., Kueppers, U., Huber, M.S., Hess, K.U., Poesges, G., Ruthensteiner, B. and Dingwell, D.B., 2018. Aggregation in particle rich environments: a textural study of examples from volcanic eruptions, meteorite impacts, and fluidized bed processing. *Bulletin of Volcanology*, 80(4). <https://doi.org/10.1007/s00445-018-1207-3>.
- Muncill, G.E. and Lasga, A.C., 1988. Crystal-growth kinetics of plagioclase in igneous systems: Isothermal H<sub>2</sub>O-saturated experiments and extension of a growth model to complex silicate melts. *American Mineralogist*, 73, pp.982–992.
- Naumov, Mikhail. v., 2005. Principal features of impact-generated hydrothermal circulation systems: mineralogical and geochemical evidence. *Geofluids*, 5, pp.165–184.
- Oberbeck, V.R., 1975. The Role of Ballistic Erosion and Sedimentation in Lunar Stratigraphy. *Review of Geophysics and Space Physics*, pp.337–362.
- Osinski, G.R., 2004. Impact melt rocks from the Ries structure, Germany: An origin as impact melt flows? *Earth and Planetary Science Letters*, 226(3–4), pp.529–543. <https://doi.org/10.1016/j.epsl.2004.08.012>.
- Osinski, G.R., 2005. Hydrothermal activity associated with the Ries impact event, Germany. *Geofluids*, 5, pp.202–220.
- Osinski, G.R., Cockell, C.S., Pontefract, A. and Sapers, H.M., 2020. The Role of Meteorite Impacts in the Origin of Life. *Astrobiology*, 20(9), pp.1121–1149. <https://doi.org/10.1089/ast.2019.2203>.
- Osinski, G.R., Grieve, R.A.F. and Spray, J.G., 2004. *The nature of the groundmass of surficial suevite from the Ries impact structure, Germany, and constraints on its origin. Meteoritics & Planetary Science*, .

- Osinski, G.R., Tornabene, L.L., Banerjee, N.R., Cockell, C.S., Flemming, R., Izawa, M.R.M., McCutcheon, J., Parnell, J., Preston, L.J., Pickersgill, A.E., Pontefract, A., Sapers, H.M. and Southam, G., 2013. Impact-generated hydrothermal systems on Earth and Mars. *Icarus*, 224(2), pp.347–363.  
<https://doi.org/10.1016/j.icarus.2012.08.030>.
- Osinski, G.R., Tornabene, L.L. and Grieve, R.A.F., 2011. Impact ejecta emplacement on terrestrial planets. *Earth and Planetary Science Letters*, 310(3–4), pp.167–181.  
<https://doi.org/10.1016/j.epsl.2011.08.012>.
- Pohl, J., Stöffler, D., Gall, H. and Erston, K., 1977. The Ries impact crater. In: Roddy D.J., Pepin R.O. and Merrill R.B., eds. *Impact and Explosion Cratering*. New York: Pergamon Press. pp.343–404.
- Riding, R., 1979. Origin and diagenesis of lacustrine algal bioherms at the margin of the Ries crater, Upper Miocene, southern Germany. *Sedimentology*, 26, pp.645–680.
- Salger, M., 1977. Die Tonminerale der Forschungsbohrung Nördlingen 1973. *Geologica Bavarica*, 75, pp.67–73.
- Sapers, H.M., Osinski, G.R., Flemming, R.L., Buitenhuis, E., Banerjee, N.R., Tornabene, L.L., Blain, S. and Hainge, J., 2017. Evidence for a spatially extensive hydrothermal system at the Ries impact structure, Germany. *Meteoritics and Planetary Science*, 52(2), pp.351–371. <https://doi.org/10.1111/maps.12796>.
- Schmieder, M., Kennedy, T., Jourdan, F., Buchner, E. and Reimold, W.U., 2018. A high-precision  $^{40}\text{Ar}/^{39}\text{Ar}$  age for the Nördlinger Ries impact crater, Germany, and implications for the accurate dating of terrestrial impact events. *Geochimica et Cosmochimica Acta*, 220, pp.146–157. <https://doi.org/10.1016/j.gca.2017.09.036>.
- Schnetzler, C.C., Philpotts, J.A. and Thomas, H.H., 1967. Rare-earth and barium abundances in Ivory Coast tektites and rocks from the Bosumtwi Crater area, Ghana. *Geochimica et Cosmochimica Acta*, 31, pp.1987–1993.

- Shanahan, T.M., Overpeck, J.T., Wheeler, C.W., Beck, J.W., Pigati, J.S., Talbot, M.R., Scholz, C.A., Peck, J. and King, J.W., 2006. Paleoclimatic variations in West Africa from a record of late Pleistocene and Holocene lake level stands of Lake Bosumtwi, Ghana. *Palaeogeography, Palaeoclimatology, Palaeoecology*, 242(3–4), pp.287–302. <https://doi.org/10.1016/j.palaeo.2006.06.007>.
- Simmons, S.F. and Christenson, B.W., 1994. Origins of calcite in a boiling geothermal system. *American Journal of Science*, 294, pp.361–400.
- Stöffler, D., Artemieva, N.A., Wünnemann, K., Reimold, W.U., Jacob, J., Hansen, B.K. and Summerson, I.A.T., 2013. Ries crater and suevite revisited-Observations and modeling Part I: Observations. *Meteoritics and Planetary Science*, 48(4), pp.515–589. <https://doi.org/10.1111/maps.12086>.
- Stöffler, D., Ewald, U., Ostertag, R. and Reimold, W.-U., 1977. Research drilling Nordlingen 1973 (Ries): composition and texture of polymict impact breccias. *Geologica Bavarica*, 75, pp.163–189.
- Stow, D.A. v, Reading H. G. and Collinson, J.D., 1996. Deep Seas. In: H.G. Reading, ed. *Sedimentary Environments: Processes, Facies and Stratigraphy*, 3rd ed. Blackwell Publishing. pp.395–453.

## 5 Discussion and Conclusions

### 5.1 Introduction

This thesis has provided an extensive investigation of early post-impact sedimentary deposits sampled by the Nördlingen 1973 drill core (FBN73) and the Wörnitzostheim drill core, which sample the transition from impact melt-bearing breccias to post-impact sedimentary deposits within the Ries central basin and just beyond the edge of the central basin, respectively. The ~ 14.8 Ma Ries impact structure (Schmieder et al., 2018) is one of the most well-studied and well-preserved impact structures on Earth; hosting accessible examples of post-impact lacustrine sedimentary rocks (e.g., Förstner, 1967; 1977; Füchtbauer et al., 1977; Riding, 1979; Jankowski, 1981; Arp et al., 2013a; 2017; Christ et al., 2018) in a crater with documented hydrothermal mineral deposits (Newsom et al., 1986; Osinski et al., 2004; Osinski, 2005; Arp et al., 2013b), making it an excellent candidate for the study of early post-impact sedimentation. This thesis establishes an improved understanding of how the Ries crater lake formed, and how an active impact-generated hydrothermal system influenced its early evolution; contributing the first detailed account of the sedimentary deposits sampled by the Wörnitzostheim drill core since the 1970's.

This thesis contributed a characterization of hydrothermal alteration styles, and the depositional environments of the entire sedimentary record preserved by the Wörnitzostheim drill core (Chapter 2). This study has additionally provided a focused mineralogical and geochemical investigation of clay minerals in the Wörnitzostheim drill core's transition from impact melt-bearing breccias to basal lacustrine deposits with implications for early fluid evolution and hydrothermal alteration temperatures in lacustrine settings beyond the Ries central basin (Chapter 3). This research also provides additional context for the determination of the origin of impact melt-bearing breccias emplaced beyond the central basin of the Ries impact structure, which is contentious largely due to uncertainty regarding the origin of clay minerals comprising the groundmass of these rocks (Newsom et al., 1986; Osinski, 2003; 2005; Osinski, Grieve and Spray, 2004; Muttik et al., 2008; Muttik et al., 2010; Sapers et al., 2017; Caudill et al., 2021). Finally, this thesis has contributed a detailed log of the transition from impact melt-bearing breccias to basal

lacustrine deposits sampled by FBN73 and proposed a new origin for the Ries graded unit with implications for ejecta plume fallback preservation, the timing of early lake evolution and hydrothermal alteration styles and temperatures of lacustrine deposits within the Ries central basin (Chapter 4). Overall, this thesis has outlined processes and products of early lacustrine processes at the Ries impact structure and provides a resource to broadly characterize the processes which shape and control the physiochemical evolution of impact crater lakes on Earth, and better understand the different biological niches present in impact crater lake environments. This thesis is concluded with the reconciliation of early lacustrine processes within the central basin of the Ries crater with that of the region just outside the central basin's edge and outline possible avenues for future work.

## 5.2 Reconciling Early Lacustrine Processes within and beyond the Ries Central Basin

The upper 32 m of the Wörnitzostheim drill core represents the transition from impact melt-bearing breccias ejected beyond the central basin to deposits from an alluvial-playa environment. This transition preserves a dolomite packstone which potentially stratigraphically correlates with early eulittoral bioherm deposition at the Ries (Chapter 2; Arp G., 2006). Based on interpretations from this thesis, the transition into a lacustrine environment represented by the Wörnitzostheim drill core is marked by the transition from pristine, relatively unaltered impact melt-bearing breccias to debris flow conglomerates, to massive normally graded alluvial sandstone, to chaotically laminated lacustrine marlstones and massive dolomitic packstones, and finally to mudstones. The presence of feldspars, dolomite and smectitic clay minerals as authigenic void-linings and fillings in the debris flow conglomerates is consistent with early to late stages of the principal sequence of mineralization in impact-generated, hydrothermal systems (Naumov, 2005; Kirsimäe and Osinski, 2013), and indicates localized alteration at temperatures 100–130 °C. The limited spread of alteration in the basal debris flow deposits of the Wörnitzostheim drill core was interpreted as an indicating less available water beyond the edge of the central basin relative to within the central basin. The absence of accretionary lapilli or any fallback deposit

beyond the edge of the central basin could be a result of post-impact erosion; however, there is currently no direct evidence of such erosional events.

The 331.0–256.0 m transect of the Nördlingen 1973 drill core (FBN73) represents the transition from crater-fill impact melt-bearing breccias to parallel laminated lacustrine deposits just within the bounds of the central basin. The transition sampled by FBN73 encompasses the Ries graded unit (331.0–314.3 m depth), and the Reworked Suevite (A.K.A. Unit A; 314.3–256.0 m). The Ries graded unit likely represents water-laden debris flow deposit that formed early after impact (Chapter 4). Similarly, Unit A likely represents flooding events and debris flows (Chapter 2; Füchtbauer et al., 1977; Jankowski, 1977) that are interbedded with erosively emplaced fallback material at 309.5, 304.0, 296.0 and 282.0 m (Chapter 2; Mueller et al., 2018; Stöffler et al., 2013). These deposits could represent early and rapid water-laden alluvial sedimentation occurring just within the edge of the central basin, which then transitioned into a playa lake environment over time (Chapter 4; Jankowski 1977). The immediate presence of water, and an abundant source of heat from the crater-fill melt-bearing breccias likely triggered pervasive alteration in the basal conglomerates, gravelstones and sandstones preserved in the Ries graded unit (Chapter 4). Alteration to graded unit occurred in two main stages consisting of pervasive argillic alteration to the matrix of the basal sedimentary rocks that occurred prior to or concomitantly with the occurrence of void-filling minerals such as clay minerals and calcite. Following the pervasive argillic and void-filling hydrothermal alteration, alteration halos and bladed calcite associated with clasts were deposited comprising a late-stage hydrothermal mineral assemblage (Chapter 4). The boiling indicated by bladed calcite (Simmons and Christenson, 1994) and the likely meteoric fluid composition (Chapter 3), together with the ~100 to 200 °C undercooling temperatures indicated by radial plagioclase spherulites (Muncill and Lasga, 1988), suggests that hydrothermal mineralization likely occurred at 100–200 °C (Chapter 4).

The timing of lacustrine processes in the central basin are expected to be relatively rapid and soon after impact (Chapter 4; Osinski 2005); however, the timing of lacustrine processes preserved in the Wörnitzostheim drill core is unclear as it lacks markers such as

accretionary lapilli (Chapter 4), but could stratigraphically correlate with early bioherm deposition (Chapter 2). The lacustrine processes preserved by the Wörnitzostheim drill core could also represent discrete ponding at higher elevations beyond the edge of the Ries central basin (Chapter 2). Current estimates are based on textural and mineralogical similarities between a dolomite packstone sampled by the Wörnitzostheim drill core (8.6–8.2 m; Chapter 2), and other similar deposits representing early bioherm formation in the Ries lake (Arp, 2006; Arp et al., 2013a). Additionally, it was speculated that parallel laminated sedimentary clasts in basal debris flow deposits of the Wörnitzostheim drill core (16.6–13.1 m) could have potentially originated from pre-existing crater-lake sedimentary rocks. If these sedimentary clasts do originate from pre-existing post-impact lake deposits, it would constitute evidence of the establishment of an outlet breach or overflow event. As such, the Ries lake system might not have necessarily been continuous across the impact structure during its early evolutionary stages (Chapter 2). Conclusive identification of multiple paleolake systems within an impact structure is yet to be reported, but such a conclusion could imply that impact crater lake systems have the potential to host more environmentally diverse biological niches than previously thought. Overall, the early lacustrine evolution both within and beyond the Ries central basin are characterized by similar alluvial playa settings but differ strongly in the degree of hydrothermal alteration, and the availability of water.

### **5.3 The Interface Between Post-Impact Lake Systems and Impact Generated Hydrothermal Systems**

This thesis has shown, for the first time, that post-impact sedimentary rocks can preserve mineral evidence of hydrothermal venting into an emerging fluviolacustrine environment in multiple settings. In both FBN73 and the Wörnitzostheim drill cores, early lacustrine deposits preserve hydrothermal mineralization (Chapters 2–4). The alteration to early lacustrine deposits in both FBN73 and the Wörnitzostheim drill core are characterized by temperatures of ~100 to at least 130 °C (Chapters 2–4) and fluids dominated by local, weakly alkaline meteoric water (Chapter 3; Osinski 2005); however, this alteration is far more limited in the environmental setting represented by the Wörnitzostheim drill core,

where hydrothermal mineral deposits are locally restricted to euhedral  $\mu\text{m}$ -scale void-lining minerals, and mm- to cm-scale alteration halos (Chapter 2). Despite the lack of abundant fluids, hydrothermal activity still affected the early lacustrine evolution preserved by the Wörnitzostheim drill core (Chapter 2).

The pervasive alteration present in the graded unit, and the abundant debris flow deposits throughout the 331.0–256.0 m transition preserved by FBN73 indicates an abundant and immediately available source of water in the central basin, and points to relatively high sedimentation rates. Comparatively, the upper 32 m of the Wörnitzostheim drill core shows limited alteration mineralogy in the early post-impact debris flow deposits, an overall smaller size of the debris flow deposits likely indicates less abundant and less immediately available water sources.

In both FBN73 and the Wörnitzostheim drill core hydrothermal mineral deposits are concentrated in the basal conglomerates of each respective sequence of post-impact sedimentary rocks (Chapters 2–4). In both cases, these mineral deposits are mainly characterized by euhedral or bladed carbonates (dolomite / calcite) associated with voids and fractures. These carbonate minerals are typically associated with euhedral plagioclase spherulites, which could indicate that these carbonates were deposited by a relatively hot  $\sim 100\text{--}130\text{ }^{\circ}\text{C}$  fluid that exhibited quenching. While the clay minerals present in the basal conglomerates of the graded unit in FBN73 are pervasive, and their possible water compositions have not yet been explored, similar analyses of the basal conglomerates of the Wörnitzostheim drill core indicate that the main composition of water was local meteoric water. A similar source of water to that of the Wörnitzostheim drill core is likely for the clay minerals sampled by the basal conglomerates of FBN73; however, this cannot be stated with certainty.

## 5.4 Applications to Astrobiology and Mars Exploration

Impact crater lakes have a demonstrated history of preserving evidence of complex ecosystems on Earth (e.g., Riding, 1979; Hickey et al., 1988; Arp, 1995); however, the earliest signs of ecological recovery in any impact structure have not yet been conclusively

identified. It is possible that the subsurface environments affected by impact generated hydrothermal alteration could be the best candidates to record such signs (Cockell and Lee, 2002; Cockell et al., 2002; 2020; Osinski et al., 2020). The sandstones, gravelstones and conglomerates that record early fluviolacustrine evolution provide a porosity and permeability that enables the flow of relatively high temperature fluids (Chapters 2–4), which could be ideal for the transport of potentially key compounds for microbial metabolism. Minerals like the framboidal pyrite in the grey conglomerates of the Wörnitzostheim drill core could potentially be indicators of such processes (Svensson et al., 2022). As such, these deposits make for ideal candidates to explore the possibility of life's emergence on Earth and potentially on Mars in similar environments.

The improved understanding of the processes and products of post-impact crater lake deposits provided by this thesis could be relevant in guiding rover-based exploration of impact crater lake deposits on Mars. Further exploration of the characteristics of the Ries lake deposits can help to answer key questions about the origins of putative lake deposits on Mars (e.g., Svensson et al., 2021). Specifically, the exploration of Jezero crater, Mars, has resulted in the potential identification of crater lake carbonates at the margins of the crater (Horgan et al., 2020). Jezero crater is an approximately 45 km diameter impact structure located at 18.9°N 77.5°E in the Nili Fossae region of Mars, which is currently being explored by the Mars 2020 Perseverance Rover. The origin of carbonate-bearing units in the marginal regions of Jezero crater has been the subject of some debate (e.g., Ehlmann et al., 2008, 2009; Goudge et al., 2015, 2017; Horgan et al., 2020; Tarnas et al., 2021), specifically pertaining to whether these carbonates have lacustrine origins. Until recently, the inlets, outlets and fan deposits were considered the primary evidence of lacustrine activity (Fassett and Head, 2005; Schon et al., 2012; Goudge et al., 2017). Horgan et al. (2020) generated new maps of Jezero using hyperspectral data collected by CRISM in concert with imagery captured by HiRISE. They found a greater spectral diversity and a more distinct morphology in carbonates that exist between the western delta and the crater rim than previously thought and hypothesized that these carbonates could be associated with precipitation from the water column at the paleolake margins. A comparison between the lacustrine carbonate distribution at the Ries and the distribution of the possible

lacustrine carbonates at Jezero could contribute to discussions regarding Jezero's marginal carbonates.

## 5.5 Conclusion

This thesis has shown evidence of spatially diverse lacustrine processes during early sedimentary deposition and has documented the first mineralogical evidence of hydrothermal alteration at temperatures of  $\sim 100$  °C or greater in early post-impact sedimentary deposits in an impact structure on Earth. The potential microbial habitat provided during immediate post-impact lacustrine evolution can then be characterized by fresh, weakly alkaline meteoric waters fueled mainly by precipitation and local groundwater at temperatures of 100–200 °C, depending on the locality, which would have then cooled to 18–27 °C. This thesis comprises a foundational contribution to the growing body of literature focused on impact-crater lake systems and comprises a key steppingstone towards understanding the role of impact crater lake systems as potential “cradles” for the genesis of life on Earth and potentially Mars. With impact cratering being a ubiquitous geological process on rocky bodies across the solar system, it was likely influential during the early evolution of Earth's crust. For this reason, the significance of impact craters on Earth to understanding the potential origins of life cannot be understated, and comprehensive investigations of additional terrestrial impact crater lakes should be prioritized.

## 5.6 Future Work

This thesis prompts several questions and hypotheses that warrant further investigation. Additionally, several potential chapters were excluded from the final version of this thesis but are noted here. Here, we briefly discuss eight proposed investigations as follows: (1) additional constraints for the chemical evolution and clastic provenance of the Wörnitzostheim lake deposits; (2) the origins of potentially biogenic framboidal pyrite in preserved in the basal debris flow deposits of the Wörnitzostheim drill core and FBN73; (3) characterization of the post-impact lacustrine deposits at the Ries Wengenhausen outcrop; (4) a detailed investigation of the complex flysch deposits preserved in the

“Reworked Suevite” / Unit A of FBN73; (5) a detailed investigation of hydrothermal alteration mineralogy in the Ries graded unit sampled by FBN73 with a special focus on clay minerals; (6) investigating the utility of in-situ X-ray diffraction (ISXRD) as a tool to better refine the identification of clay minerals during rover-based exploration; (7) a terrestrial analogue study between the carbonate deposits of the Ries impact structure and the marginal carbonate unit at Jezero crater; (8) as comprehensive a review as possible of impact crater lakes on Earth, expanding on the review provided in Chapter 1.

## 5.7 References

- Arp, G., 1995. Lacustrine bioherms, spring mounds, and marginal carbonates of the Ries-impact-crater (Miocene, Southern Germany). *Facies*, 33(1), pp.35–89.  
<https://doi.org/10.1007/BF02537444>.
- Arp G., 2006. Sediments of the Ries Crater Lake (Miocene, Southern Germany). In: *21st Meeting of Sedimentologists / 4th Meeting of SEPM Central European Section*. pp.216–233.
- Arp, G., Blumenberg, M., Hansen, B.T., Jung, D., Kolepka, C., Lenz, O., Nolte, N., Poschlod, K., Reimer, A. and Thiel, V., 2013a. Chemical and ecological evolution of the Miocene Ries impact crater lake, Germany: A reinterpretation based on the Enkingen (SUBO 18) drill core. *Bulletin of the Geological Society of America*, 125(7–8), pp.1125–1145. <https://doi.org/10.1130/B30731.1>.
- Arp, G., Kolepka, C., Simon, K., Karius, V., Nolte, N. and Hansen, B.T., 2013b. New evidence for persistent impact-generated hydrothermal activity in the Miocene Ries impact structure, Germany. *Meteoritics and Planetary Science*, 48(12), pp.2491–2516.  
<https://doi.org/10.1111/maps.12235>.
- Arp, G., Hansen, B.T., Pack, A., Reimer, A., Schmidt, B.C., Simon, K. and Jung, D., 2017. The soda lake—mesosaline halite lake transition in the Ries impact crater basin (drilling Löpsingen 2012, Miocene, southern Germany). *Facies*, 63(1).  
<https://doi.org/10.1007/s10347-016-0483-7>.

- Caudill, C., Osinski, G.R., Greenberger, R.N., Tornabene, L.L., Longstaffe, F.J., Flemming, R.L. and Ehlmann, B.L., 2021. Origin of the degassing pipes at the Ries impact structure and implications for impact-induced alteration on Mars and other planetary bodies. *Meteoritics and Planetary Science*, 56(2), pp.404–422. <https://doi.org/10.1111/maps.13600>.
- Christ, N., Maerz, S., Kutschera, E., Kwiecien, O. and Mutti, M., 2018. Palaeoenvironmental and diagenetic reconstruction of a closed-lacustrine carbonate system – the challenging marginal setting of the Miocene Ries Crater Lake (Germany). *Sedimentology*, 65(1), pp.235–262. <https://doi.org/10.1111/sed.12401>.
- Cockell, C. S., Osinski, G.R., Sapers, H.M., Pontefract, A. and Parnell, J., 2020. Microbial life in impact craters. *Current Issues in Molecular Biology*, 38, pp.75–102. <https://doi.org/10.21775/cimb.038.075>.
- Cockell, Charles.S. and Lee, Pascal., 2002. The biology of impact craters-a review. *Biological Reviews*, 77, pp.279–310. <https://doi.org/10.1017/S146479310100584X>.
- Cockell, C.S., Lee, P., Osinski, G., Horneck, G. and Broady, P., 2002. Impact-induced microbial endolithic habitats. *Meteoritics and Planetary Science*, 37(10), pp.1287–1298. <https://doi.org/10.1111/j.1945-5100.2002.tb01029.x>.
- Ehlmann, B.L., Mustard, J.F., Fassett, C.I., Schon, S.C., Head, J.W., des Marais, D.J., Grant, J.A. and Murchie, S.L., 2008. Clay minerals in delta deposits and organic preservation potential on Mars. *Nature Geoscience*, 1(6), pp.355–358. <https://doi.org/10.1038/ngeo207>.
- Ehlmann, B.L., Mustard, J.F., Swayze, G.A., Clark, R.N., Bishop, J.L., Poulet, F., des Marais, D.J., Roach, L.H., Milliken, R.E., Wray, J.J., Barnouin-Jha, O. and Murchie, S.L., 2009. Identification of hydrated silicate minerals on Mars using MRO-CRISM: Geologic context near Nili Fossae and implications for aqueous alteration. *Journal of Geophysical Research: Planets*, 114(10). <https://doi.org/10.1029/2009JE003339>.

- Fassett, C.I. and Head, J.W., 2005. Fluvial sedimentary deposits on Mars: Ancient deltas in a crater lake in the Nili Fossae region. *Geophysical Research Letters*, 32(14), pp.1–5. <https://doi.org/10.1029/2005GL023456>.
- Förstner, v. U., 1977. Geochemische Untersuchungen an den Sedimenten des Ries-Sees (Forschungsbohrung Nördlingen 1973. *Geologica Bavarica*, 75, pp.337–48.
- Förstner, U., 1967. Petrographische Untersuchungen des Suevit aus den Bohrungen Deiningen und Wörnitzostheim im Ries von Nördlingen. *Contributions to Mineralogy and Petrology*, 15, pp.281–308.
- Füchtbauer, H., Brellwiler, G., Dehem, R., Förstner, U., Gall, H., Höfling, R., Hoefs, J., Hollerbach, H., Jankowski, B., Jung, W., Malz, H., Mertes, H., Rothe, P., Salger, M., Wehner, H. and Wolf, M., 1977. Tertiary lake sediments of the Ries, research borehole Nördlingen 1973-A summary. *Geologica Bavarica*, 75, pp.13–19.
- Goudge, T.A., Milliken, R.E., Head, J.W., Mustard, J.F. and Fassett, C.I., 2017. Sedimentological evidence for a deltaic origin of the western fan deposit in Jezero crater, Mars and implications for future exploration. *Earth and Planetary Science Letters*, 458, pp.357–365. <https://doi.org/10.1016/j.epsl.2016.10.056>.
- Goudge, T.A., Mustard, J.F., Head, J.W., Fassett, C.I. and Wiseman, S.M., 2015. Assessing the mineralogy of the watershed and fan deposits of the Jezero crater paleolake system, Mars. *Journal of Geophysical Research: Planets*, 120(4), pp.775–808. <https://doi.org/10.1002/2014JE004782>.
- Hickey, Leo.J., Johnson, Kirk.R. and Dawson, Mary.R., 1988. The Stratigraphy, Sedimentology, and Fossils of the Haughton Formation: A Post-Impact Crater-Fill, Devon Island, N.W.T., Canada. *Meteoritics*, 23(3), pp.221–231. <https://doi.org/10.1111/j.1945-5100.1988.tb01284.x>.

- Horgan, B.H.N., Anderson, R.B., Dromart, G., Amador, E.S. and Rice, M.S., 2020. The mineral diversity of Jezero crater: Evidence for possible lacustrine carbonates on Mars. *Icarus*, 339(113526). <https://doi.org/10.1016/j.icarus.2019.113526>.
- Jankowski, B., 1977. The graded unit on top of the suevite layer in the borehole Nördlingen 1973. *Geologica Bavarica*, 75, pp.155–162.
- Jankowski, B., 1981. Die Geschichte der Sedimentation im Nördlinger Ries und Randecker Maar. *Bochumer geologische und geotechnische Arbeiten*, 6, pp.1–315.
- Kirsimäe, K. and Osinski, G.R., 2013. Impact-induced hydrothermal activity. In: G.R. Osinski and E. Pierazzo, eds. *Impact Cratering: Processes and Products*. Blackwell Publishing Ltd. pp.76–89.
- Mueller, S.B., Kueppers, U., Huber, M.S., Hess, K.U., Poesges, G., Ruthensteiner, B. and Dingwell, D.B., 2018. Aggregation in particle rich environments: a textural study of examples from volcanic eruptions, meteorite impacts, and fluidized bed processing. *Bulletin of Volcanology*, 80(4). <https://doi.org/10.1007/s00445-018-1207-3>.
- Muncill, G.E. and Lasga, A.C., 1988. Crystal-growth kinetics of plagioclase in igneous systems: Isothermal H<sub>2</sub>O-saturated experiments and extension of a growth model to complex silicate melts. *American Mineralogist*, 73, pp.982–992.
- Muttik, N., Kirsimäe, K., Somelar, P. and Osinski, G.R., 2008. Post-impact alteration of surficial suevites in Ries crater, Germany: Hydrothermal modification or weathering processes? *Meteoritics & Planetary Science*, [online] 43, pp.1827–1840. Available at: <<http://meteoritics.org>>.
- Muttik, N., Kirsimäe, K. and Vennemann, T.W., 2010. Stable isotope composition of smectite in suevites at the Ries crater, Germany: Implications for hydrous alteration of impactites. *Earth and Planetary Science Letters*, 299, pp.190–195. <https://doi.org/10.1016/j.epsl.2010.08.034>.

- Naumov, Mikhail. v., 2005. Principal features of impact-generated hydrothermal circulation systems: mineralogical and geochemical evidence. *Geofluids*, 5, pp.165–184.
- Newsom, H.E., Graup, G., Sowards, T. and Keil, K., 1986. Fluidization and hydrothermal alteration of the Suevite deposit at the Ries Crater, West Germany, and implications for Mars. *Journal of Geophysical Research*, 91(B13), pp.E239–E251.  
<https://doi.org/10.1029/jb091ib13p0e239>.
- Osinski, G.R., 2003. *Impact glasses in fallout suevites from the Ries impact structure, Germany: An analytical SEM study*. [online] *Meteoritics & Planetary Science*, Available at: <<http://meteoritics.org/1641>>.
- Osinski, G.R., 2005. Hydrothermal activity associated with the Ries impact event, Germany. *Geofluids*, 5, pp.202–220.
- Osinski, G.R., Cockell, C.S., Pontefract, A. and Sapers, H.M., 2020. The Role of Meteorite Impacts in the Origin of Life. *Astrobiology*, 20(9), pp.1121–1149.  
<https://doi.org/10.1089/ast.2019.2203>.
- Osinski, G.R., Grieve, R.A.F. and Spray, J.G., 2004. *The nature of the groundmass of surficial suevite from the Ries impact structure, Germany, and constraints on its origin*. *Meteoritics & Planetary Science*, .
- Riding, R., 1979. Origin and diagenesis of lacustrine algal bioherms at the margin of the Ries crater, Upper Miocene, southern Germany. *Sedimentology*, 26, pp.645–680.
- Sapers, H.M., Osinski, G.R., Flemming, R.L., Buitenhuis, E., Banerjee, N.R., Tornabene, L.L., Blain, S. and Hainge, J., 2017. Evidence for a spatially extensive hydrothermal system at the Ries impact structure, Germany. *Meteoritics and Planetary Science*, 52(2), pp.351–371. <https://doi.org/10.1111/maps.12796>.
- Schmieder, M., Kennedy, T., Jourdan, F., Buchner, E. and Reimold, W.U., 2018. A high-precision  $^{40}\text{Ar}/^{39}\text{Ar}$  age for the Nördlinger Ries impact crater, Germany, and

- implications for the accurate dating of terrestrial impact events. *Geochimica et Cosmochimica Acta*, 220, pp.146–157. <https://doi.org/10.1016/j.gca.2017.09.036>.
- Schon, S.C., Head, J.W. and Fassett, C.I., 2012. An overfilled lacustrine system and progradational delta in Jezero crater, Mars: Implications for Noachian climate. *Planetary and Space Science*, 67(1), pp.28–45. <https://doi.org/10.1016/j.pss.2012.02.003>.
- Simmons, S.F. and Christenson, B.W., 1994. Origins of calcite in a boiling geothermal system. *American Journal of Science*, 294, pp.361–400.
- Stöffler, D., Artemieva, N.A., Wünnemann, K., Reimold, W.U., Jacob, J., Hansen, B.K. and Summerson, I.A.T., 2013. Ries crater and suevite revisited-Observations and modeling Part I: Observations. *Meteoritics and Planetary Science*, 48(4), pp.515–589. <https://doi.org/10.1111/maps.12086>.
- Svensson, M.J.O., Osinski, G.R., Goudge, T.A. and Longstaffe, F.J., 2021. The Ries Impact Structure as an analogue for Jezero Crater’s marginal carbonates. In: *Workshop on Terrestrial Analogues for Planetary Exploration*. USGS Astrogeology Science Center.
- Svensson, M.J.O., Osinski, G.R., Longstaffe, F.J. and Sapers, H.M., 2022. Determining the Origin of Framboidal Pyrite in Early Post-Impact Sedimentary Deposits at the Ries Impact Structure, Germany. In: *AbSciCon-2022*. Atlanta: American Geophysical Union (AGU). p.333.
- Tarnas, J.D., Stack, K.M., Parente, M., Koepfel, A.H.D., Mustard, J.F., Moore, K.R., Horgan, B.H.N., Seelos, F.P., Cloutis, E.A., Kelemen, P.B., Flannery, D., Brown, A.J., Frizzell, K.R. and Pinet, P., 2021. Characteristics, Origins, and Biosignature Preservation Potential of Carbonate-Bearing Rocks Within and Outside of Jezero Crater. *Journal of Geophysical Research: Planets*, 126(11). <https://doi.org/10.1029/2021JE006898>.

## Appendices

### Appendix A: Chapters 2 & 3 Supplementary Data

#### A.1 Wörnitzostheim Drill Core Log

This log contains original unrefined notes during field excursions to the Ries impact structure and visits to the Nördlingen Impact Crater Museum, Nördlingen, Germany.

##### **Appendix A. 1:** Wörnitzostheim Drill Core Log

Depth (m)	Lithology	Description
0 – 0.9	Mudstone	Dark brown, highly weathered, muddy lake sediments, essentially soil at this point, parallel lamination is very weakly preserved  Interesting white structures reminiscent of the white bleaching mentioned earlier and the coral at Hainsfarth
0.9 – 2	Mudstone	Brown, highly weathered, muddy lake sediments with weathered out globular structures produced by cladophorites, very minor layering preserved - distorted and incorporated into the weathering profile  abundant silica clasts <1mm to 1mm in size; 10% spatial coverage; sub-rounded to angular clasts possibly incorporated from above - description based off hand sample of core from drawer - gets greyer with depth
2 – 3	Marlstone	Grey - Brown, highly weathered, muddy lake sediments with weathered out globular structures produced by the cladophorites, parallel lamination preserved (could actually just be drill chatter)

3 – 8.2	Marlstone	<p>Light grey clay no distinct clasts, coherent, not chunked in a bag</p> <p>no tube structures, but dominated by the mat structures</p> <p>soft material - can be scratched by a fingernail</p> <p>parallel lamination preserved in the mats, mudstone</p>
8.2 – 8.6	Limestone	<p>Light grey clay with crinkled mats from cladophorites</p> <p>White tone occurring in patches appears to be bleaching the rock</p> <p>Fabric of the crinkled mats are preserved</p> <p>Dark grey coloration is also present</p>
8.6 – 10.0	Limestone?	<p>Light grey clay with crinkled mats from cladophorites</p> <p>White coloring in chunks still occurs - now appears to be associated with a <b>highly altered section of core</b> within the 9.6-9.0 range although it's exact location could not be determined</p> <p>Dark grey clasts with muddy texture and softness occurs in contact with the bleached white areas and the mats</p>
10.0 – 10.7	Marlstone	<p>Light grey, consolidated, muddy clay is the dominant lithology and fractures in the core now occur along planar surfaces indicating very weak parallel lamination or possible influence from cladophorites.</p> <p>Clasts are absent.</p>
10.7 – 11.6	Sandstone	<p>Light grey, consolidated, massive sandstone / siltstone (?)</p> <p>Poorly sorted, subrounded to angular, polymict clasts dominated by a very fine-grained matrix made of light grey, muddy, clay material</p>

---

Contains clasts ranging from <1 mm; generally sharp contact between clasts and matrix, but sometimes fuzzy

**Polymict clasts:** consists of very fine black and white material; difficult to distinguish from groundmass, but possibly the altered glass, more clasts of silica

---

11.6 – Conglomerate Light grey, consolidated, less brittle than suevite, more  
12.8 competent, frequently retains scars from drill

Poorly sorted, subrounded to angular, polymict clasts dominated by a very fine-grained matrix made of light grey, muddy, clay material

**Contains light grey sed clasts** ranging from <1mm to 1.5cm across; generally sharp contact between clasts and matrix, but sometimes fuzzy

Contains additional, 1cm-3cm sized, well rounded, very light grey, soft, irregularly shaped, clay-like fragments within the matrix previously described.

**Polymict clasts:** consists of very fine black and white material difficult to distinguish, but possibly the altered and unaltered glass

Light grey, consolidated, less brittle than suevite, more competent, frequently retains scars from drill

Poorly sorted, subrounded to angular, polymict clasts dominated by a very fine-grained matrix made of light grey, muddy, clay material

---

---

Contains clasts ranging from <1mm to 1.5cm across; generally sharp contact between clasts and matrix, but sometimes fuzzy; glass clasts were observed with **yellow-brown alteration rind** \*picture taken\*

**Polymict clasts:** consists of very fine black and white material (difficult to distinguish, but possibly the altered and unaltered glass

---

12.8 – Sandstone Similar to 10.7 – 11.6: massive, light grey sandstone, but  
13.1 slightly coarser.

**Polymict clasts:** consists of very fine black and white material; difficult to distinguish from groundmass, but possibly the altered glass, more clasts of silica

---

13.1 – Conglomerate Light grey/blueish tinge, moderately unconsolidated,  
16.6 more brittle than suevite, suevite sediments

Poorly sorted, subrounded to angular, polymict clasts supported by a very fine-grained matrix made of light grey, clay-like amorphous material

In general the clasts are much smaller than generally observed in suevite, larger than Wor-kt-17, vernal sharp contact between clasts and matrix, but sometimes fuzzy

**Polymict clasts:** consists of highly altered glassy material, with fuzzy boundaries rimmed by white, powdery amorphous material (50% of the polymict clasts) - **completely replaced by white powder** in some cases. Disjoined, broken down, **muddy clasts are**

---

---

**entrained with parallel lamination** in these suevite seds clearly at **16m (Wor-kt-16)** with **brown-yellow alteration halos**

These cm-scale sedimentary clasts occur again at **15.1m** in 2-4cm size whitened chunks

The mud material is soft, but less brittle thus retaining scars from the drill, but not shattering

Prominent brown-yellow alteration features throughout **14.1-13.8m**

The % abundance and size of the glass clasts undergoes a marked increase at **15.10m**, immediately after the flakey clay clasts (mud rip-ups) were observed. The overall % abundance and size of the glass clasts remains constant until the change in lithology at 16.6m

---

16.6 – Conglomerate Light grey/tan-brown, moderately unconsolidated, more  
17.1 brittle than suevite, denser than suevite, suevite sediments.

Poorly sorted, subrounded to angular clasts supported by very fine-grained, muddy matrix made of a light grey clay-like amorphous material

In general, the clasts are slightly smaller than generally observed in suevite, generally sharp contact between clasts and matrix, but sometimes fuzzy

**Polymict clasts:** glass (<1mm) (<1%); red sediment (shale?), usually angular clasts; rounded globular shell-

---

---

like material possibly derived from the layers of accumulated gastropods in the lake sedimentary rocks (<1mm) (<1%); clasts are comprised primarily of <1mm - 2mm sized chunks of silica(?)

---

17.1 – Conglomerate Pink-grey reworked suevite, gradual transition from light  
20.1 grey/tan-brown material (suevite sediments), possibly reworked by the overlying lake system

Contains polymict clasts supported by an aphanitic pink-grey matrix

**Clasts:** both rimmed (by white amorphous material), non-rimmed glass clasts at a range of sizes from, <1mm to 2cm, rims are usually sharp, but sometimes fuzzy; white clasts - possibly siliceous clasts or glass altered to fine white material

contains, <1mm sized vein-like structures

Light grey reworked suevite (slight pinkish hue); has a weathered appearance: the fines are dominant and crumbly; matrix supported polymict clasts

Poorly sorted, subrounded to angular clasts

**Polymict clasts:** primarily reworked, irregularly shaped glass and melt fragments observed coated in pervasive white amorphous material which has completely replaced the fragments in most cases (20% completely replaced glass fragments, 5% reworked glass fragments), size range of fresher glass = <1mm (most common) to 3mm, size range of replaced clasts is more difficult to

---

---

distinguish = roughly <1mm to 2cm; 2% overall coverage of other clasts <1mm in size so their lithology is difficult to distinguish, typically angular with sharp borders

Appears to have a gradual contact with more coherent, moderate to lightly reworked suevite unit below

---

20.1 – 27.2	Melt-bearing breccia (surficial suevite)	Light grey, moderately reworked suevite(slight white hue); has a weakly weathered appearance, matrix supported poymict clasts  Poorly sorted, subrounded to angular clasts  Matrix is comprised of very fine white-grey amorphous material  <b>Polymict clasts:</b> primarily reworked, irregularly shaped glass and melt fragments observed coated white amorphous material which has completely replaced the fragments in most cases (15% completely replaced glass fragments, 10% reworked glass fragments), size range of fresher glass = <1mm (most common) to 10mm, size range of replaced clasts is more difficult to distinguish = roughly <1mm to 2cm; 10% overall coverage of other clasts <1mm to 3cm in size, typically sub-rounded with sharp borders, sometimes fuzzy, moderate replacement by white powdery material making the primary lithology difficult to distinguish  Appears to have a gradual contact with highly weathered looking, non-reworked suevite unit below
----------------	---	---

---

---

Gradual increase in prominence of melt fragments with depth

Gradual decrease in white powdery replacement

---

27.2 – 32 Melt-bearing breccia (surficial suevite) Light grey-red, moderately reworked suevite; has a surficial weathered appearance on exterior of core, matrix supported polymict clasts

Poorly sorted, subrounded to angular clasts

Matrix is comprised of very fine white-greyish red amorphous material

Very similar to **Nor-73-328**

**Polymict clasts:** primarily reworked, irregularly shaped glass and melt fragments observed coated white amorphous material which has completely replaced the fragments in most cases (15% completely replaced glass fragments, 20% reworked glass fragments), size range of fresher glass = <1mm to 4cm, size range of replaced clasts is more difficult to distinguish = roughly <1mm to 2cm; 10% overall coverage of other clasts <1mm to 3cm in size, typically sub-rounded with sharp borders, sometimes fuzzy, appears to be mainly comprised of sedimentary material

---

## A.2 Standards for WDS Analysis

The standards used during the WDS analyses of different types of minerals are noted in Table 6.1. The results of these analyses are listed in highlighted in Appendix A.2.2.

**Table 6. 1:** Mineral standards used per WDS elemental analysis and corresponding target mineral phase.

Element	Clay Minerals	Micas	Feldspars
Si	Albite Amelia (TAP)*	Plagioclase Astimex (TAP)	Albite Amelia (TAP)
Al	Albite Amelia (TAP)	Plagioclase Astimex (TAP)	Albite Amelia (TAP)
Na	Albite Amelia (TAP)	Albite Amelia (TAP)	Albite Amelia (TAP)
K	Orthoclase CM Taylor (PETH)	Orthoclase CM Taylor (PETH)	Orthoclase CM Taylor (PETH)
Ca	Anorthite Smithsonian USNM 137041 (PETJ)	Plagioclase Astimex (PETJ)	Anorthite Smithsonian USNM 137041 (PETJ)
Mg	Diopside Smithsonian USNM 117733 (TAP)	Diopside Smithsonian USNM 117733 (TAP)	Diopside Smithsonian USNM 117733 (TAP)
Fe	Fayalite (LIFL)	Fayalite (LIFL)	Fayalite (LIFL)
P	Apatite Astimex (PETH)	-	Apatite Astimex (PETH)
Ti	Rutile (PETJ)	Rutile (PETJ)	Rutile (PETJ)
Mn	Rhodonite Astimex (LIFL)	Rhodonite Astimex (LIFL)	Rhodonite Astimex (LIFL)
Sr	Celestite Astimex (PETH)	-	Celestite Astimex (PETH)

\*Analyzing crystals associated with each element are noted in parentheses after the standard used for the same element.

### A.3 WDS Data Tables

This section contains tables of WDS data. For data collected on clay minerals, only totals of ~ 80 % or greater were included for interpretations detailed in Chapter 3. Totals of ~80 % were selected as the acceptable limit because the majority of analyses were above 80 %. The name of the sample analyzed is noted in each table along with the number of spot analyses, an average of the spot analyses, the % error and the standard deviation of the suite of reported values associated with each oxide reported at the top of the tables below. The % error was automatically generated in reference to a standard, and then averaged for each oxide in the tables provided below. The sample associated with the data in each table is indicated by the sample label, e.g., RW22. The sample labels are written such that the number following “RW” corresponds with the depth from which the sample was collected and RW stands for Ries impact structure, Wörnitzostheim drill core.

#### A.3.1 Clay Mineral WDS Data

Clay Minerals								
RW22	Wt. % Oxide							
Spot	SiO <sub>2</sub>	Al <sub>2</sub> O <sub>3</sub>	Na <sub>2</sub> O	MgO	CaO	K <sub>2</sub> O	FeO	Total
1	54.77	16.81	0.12	2.71	0.93	1.01	4.51	80.85
2	58.01	17.66	0.13	3.16	1.27	0.88	4.30	85.40
3	55.55	16.67	0.09	2.65	1.29	0.69	5.42	82.35
4	58.16	17.67	0.13	2.72	1.19	0.76	5.27	85.89
5	54.58	16.78	0.14	2.44	0.88	1.50	4.43	80.75
6	56.93	17.36	0.06	2.80	1.33	0.82	4.32	83.62
7	53.22	15.55	0.14	2.80	2.83	0.51	5.24	80.29
8	53.22	15.55	0.14	2.80	2.83	0.51	5.24	80.29
9	51.99	15.77	0.18	2.14	5.44	0.46	5.12	81.09
10	54.45	16.55	0.14	2.93	1.86	0.42	5.03	81.37

11	54.53	16.29	0.20	2.72	1.10	0.97	4.75	80.54
12	57.26	16.80	0.19	2.50	0.85	1.13	6.24	84.96
13	53.72	15.47	0.16	2.43	0.97	0.93	6.30	79.98
14	58.30	17.05	0.16	2.45	0.96	0.90	6.25	86.08
15	57.96	17.15	0.13	2.55	1.01	0.86	6.31	85.96
16	59.83	17.56	0.13	2.79	1.19	0.84	6.24	88.57
17	53.81	15.11	0.16	2.62	1.65	1.04	5.97	80.36
18	54.20	15.38	0.32	2.97	3.78	0.77	5.49	82.90
19	54.93	15.71	0.15	2.70	1.32	0.72	5.63	81.15
20	52.97	16.89	0.20	2.85	1.46	1.06	4.81	80.23
21	54.88	16.24	0.29	2.92	1.61	0.82	5.27	82.02
Average	55.59	17.07	1.22	2.38	2.40	0.86	4.91	84.43
2 $\sigma$	2.64	1.83	2.27	0.66	1.87	0.23	1.18	5.82
Avg. % Error	0.81	1.45	31.84	4.46	5.28	7.36	3.60	

#### Clay Minerals

RW19	Oxide Wt. %							
Spot	SiO <sub>2</sub>	Al <sub>2</sub> O <sub>3</sub>	Na <sub>2</sub> O	MgO	CaO	K <sub>2</sub> O	FeO	Total
1	56.12	18.29	3.54	1.32	1.86	0.81	2.87	84.79
2	51.89	16.50	1.56	1.63	1.13	2.34	3.71	78.75
3	61.52	9.14	0.13	2.26	0.60	1.20	4.65	79.50
4	54.88	16.24	0.29	2.92	1.61	0.82	5.27	82.02
Average	56.10	15.04	1.38	2.03	1.30	1.29	4.13	81.27
2 $\sigma$	4.02	4.04	1.58	0.71	0.55	0.72	1.05	2.74

Avg. % Error	0.78	1.56	19.10	4.59	6.61	6.07	3.91
--------------	------	------	-------	------	------	------	------

Clay Minerals Continued

RW14.78	Wt % Oxide							
Spot	SiO <sub>2</sub>	Al <sub>2</sub> O <sub>3</sub>	Na <sub>2</sub> O	MgO	CaO	K <sub>2</sub> O	FeO	Total
1	53.66	16.38	2.26	2.27	0.95	1.16	3.28	80.38
2	52.68	16.50	0.18	2.95	2.38	0.66	4.67	80.71
3	54.71	16.71	0.14	3.47	1.32	0.55	4.98	83.96
4	56.06	17.55	0.34	3.37	0.99	0.59	3.40	82.77
Average	54.28	16.78	0.73	3.01	1.41	0.74	4.08	81.96
2 $\sigma$	1.45	0.53	1.02	0.54	0.67	0.29	0.87	1.71
Avg. % Error	0.79	1.42	22.58	3.61	6.22	8.08	3.90	

Clay Minerals Continued

RW14.33	Wt % Oxide							
Spot	SiO <sub>2</sub>	Al <sub>2</sub> O <sub>3</sub>	Na <sub>2</sub> O	MgO	CaO	K <sub>2</sub> O	FeO	Total
1	51.34	17.63	0.08	3.58	1.34	2.46	6.05	82.48
2	51.79	17.05	0.12	4.75	1.91	2.96	6.96	85.55
3	63.79	10.07	0.04	2.18	3.34	1.45	3.46	84.32
4	51.29	18.71	0.15	4.26	2.80	3.68	6.30	87.18
5	51.21	22.39	0.15	3.06	1.71	4.16	4.31	86.98
6	54.66	18.03	0.11	4.94	0.62	3.76	5.94	88.05
7	50.15	22.16	0.17	4.57	0.51	4.02	6.41	87.98

8	47.60	18.95	0.09	3.91	0.88	2.92	5.05	79.40
9	51.74	20.57	0.09	4.06	1.02	3.42	5.27	86.17
10	56.36	14.77	0.12	2.92	0.68	2.00	3.91	80.77
11	51.40	21.67	0.14	3.75	1.16	3.93	5.06	87.10
12	59.80	13.30	0.09	3.28	0.52	0.90	2.58	80.47
13	55.21	16.95	0.28	3.91	0.83	0.73	3.38	81.28
14	51.15	17.91	4.71	0.90	4.88	1.36	1.37	82.28
15	50.82	18.28	5.09	0.54	5.45	1.39	1.16	82.72
16	58.50	18.65	0.13	3.37	0.95	0.32	3.22	85.13
17	56.22	17.92	0.10	3.38	0.38	0.46	3.15	81.60
18	56.60	17.87	0.13	3.61	0.40	0.47	3.07	82.13
19	56.05	17.53	0.11	3.93	0.33	0.56	3.66	82.16
20	57.21	18.18	0.22	3.69	0.46	0.60	3.51	83.88
21	53.56	17.90	1.96	2.17	1.25	0.99	2.44	80.26
22	53.81	17.69	0.01	3.92	0.77	0.17	3.37	79.73
23	55.07	17.48	0.11	3.17	1.06	0.32	3.09	80.30
Average	52.16	17.22	0.57	3.34	2.37	1.87	4.04	81.58
2 $\sigma$	7.73	3.47	1.35	1.05	3.56	1.37	1.52	6.99
Avg. % Error	0.83	1.44	71.31	3.71	7.22	6.56	4.20	

#### Clay Minerals Continued

RW12.74	Oxide Wt. %							
Spot	SiO <sub>2</sub>	Al <sub>2</sub> O <sub>3</sub>	Na <sub>2</sub> O	MgO	CaO	K <sub>2</sub> O	FeO	Total
1	51.47	16.54	0.92	3.26	3.05	1.17	2.70	79.10

2	57.75	17.19	2.99	2.01	0.92	3.61	1.77	86.23
3	52.71	16.83	0.49	3.71	1.27	2.61	5.53	84.77
4	46.10	15.48	1.15	3.02	2.36	3.69	5.56	78.39
5	50.11	17.47	0.39	4.16	3.68	2.89	4.28	84.55
6	51.06	16.89	0.52	3.96	1.70	3.61	5.12	84.54
7	54.50	14.86	0.45	3.78	2.39	2.36	4.08	83.86
8	49.79	13.15	0.66	3.12	5.93	2.90	4.58	82.92
9	44.54	14.08	0.30	4.18	4.88	3.11	5.24	79.44
Average	50.89	15.83	0.87	3.47	2.91	2.88	4.32	82.64
2 $\sigma$	4.01	1.52	0.84	0.70	1.67	0.79	1.31	2.90
Avg. % Error	0.84	1.50	14.15	3.39	4.48	3.79	3.95	

#### Clay Minerals Continued

RW10.55	Wt. % Oxide							
Spot	SiO <sub>2</sub>	Al <sub>2</sub> O <sub>3</sub>	Na <sub>2</sub> O	MgO	CaO	K <sub>2</sub> O	FeO	Total
1	51.06	19.77	0.13	2.64	0.53	3.17	4.48	81.78
2	55.49	20.80	0.33	2.81	0.68	2.55	3.55	86.20
3	50.62	19.70	0.20	2.83	1.16	3.30	4.84	82.64
4	48.08	20.82	0.33	2.58	0.75	3.47	4.28	80.31
5	53.06	20.44	0.33	2.80	0.55	3.28	4.57	85.02
9	51.83	22.00	0.36	2.90	1.20	3.74	4.38	86.40
10	52.27	21.29	0.39	3.02	0.17	3.38	4.56	85.07
11	50.09	28.44	0.32	1.87	0.54	2.15	2.63	86.05
12	47.13	20.92	0.25	2.55	4.25	3.04	3.50	81.63

14	49.12	20.82	0.16	2.80	1.39	4.31	4.42	83.02
15	49.38	18.12	0.07	2.77	1.88	3.84	4.71	80.77
18	56.75	21.29	0.15	2.89	0.44	3.59	4.33	89.43
19	48.92	20.20	0.15	2.84	1.06	3.56	4.46	81.19
Average	51.06	21.12	0.24	2.71	1.12	3.34	4.21	83.81
2 $\sigma$	2.81	2.40	0.10	0.29	1.05	0.55	0.62	2.76
Avg. % Error	0.83	1.27	28.70	3.74	9.06	3.39	3.84	

#### Clay Minerals Continued

RW9.6	Wt. % Oxide							
Spot	SiO <sub>2</sub>	Al <sub>2</sub> O <sub>3</sub>	Na <sub>2</sub> O	MgO	CaO	K <sub>2</sub> O	FeO	Total
1	51.41	22.61	0.15	2.85	0.55	3.28	4.10	84.94
2	52.29	22.75	0.12	2.97	0.39	3.47	4.35	86.32
3	51.56	23.01	0.15	2.76	0.34	3.44	4.43	85.68
4	55.34	21.36	0.15	2.20	1.43	3.15	3.48	87.11
5	48.28	20.22	0.14	2.68	0.96	3.11	3.78	79.17
6	47.15	20.42	0.18	3.80	2.68	3.30	3.75	81.27
7	51.46	22.18	0.16	3.57	1.12	3.44	4.48	86.40
12	49.90	20.19	0.14	2.88	0.64	3.43	3.93	81.11
13	49.55	22.36	0.16	2.94	0.89	3.31	3.80	83.00
Average	50.77	21.68	0.15	2.96	1.00	3.33	4.01	83.89
2 $\sigma$	2.40	1.15	0.02	0.47	0.72	0.13	0.35	2.84
Avg. % Error	0.84	1.26	34.31	3.69	8.89	3.41	3.91	

### A.3. Mica WDS Data

This section contains tables of WDS data collected from micas as discussed in Chapter 2. Only WDS analyses with totals at ~90 % or greater were included for interpretation. The name of the sample analyzed is noted in each table along with the number of spot analyses, an average of the spot analyses, the % error and the standard deviation. In the name of each sample, the number follow “RW” corresponds with the depth from which the sample was collected.

Micas										
RW19	Wt. % Oxide									
Spot	SiO <sub>2</sub>	Al <sub>2</sub> O <sub>3</sub>	Na <sub>2</sub> O	MgO	TiO <sub>2</sub>	CaO	K <sub>2</sub> O	FeO	MnO	Total
1	34.1	15.9		17.0	1.9		3.2	18.0		91.1
	5	3	0.15	3	9	0.31	8	7	0.22	3
2	40.5	16.8		10.7	1.2		2.6	16.9		91.7
	4	7	0.45	8	2	1.97	9	7	0.20	0
3	47.5	37.9			0.3		7.1			96.8
	5	3	2.06	0.69	2	0.03	0	1.16	0.01	5
4	39.4	17.0			1.5		6.9	17.2		91.9
	7	1	0.23	8.99	4	0.37	0	7	0.13	1
5	39.9	17.0			1.4		7.4	16.8		92.2
	3	6	0.18	8.89	3	0.39	4	0	0.11	3
6	38.7	17.0			1.4		6.8	17.5		91.6
	1	0	0.22	9.25	1	0.53	6	4	0.13	6
7	43.7	27.1			0.3		5.4			92.0
	1	1	0.24	5.72	0	0.27	3	9.15	0.13	5
8	47.6	29.6			0.3		7.7			94.5
	2	1	0.20	4.08	2	0.14	9	4.77	0.06	7
9	41.1	17.8		10.4	2.6		2.7	13.2		88.8
	9	7	0.25	6	2	0.41	2	9	0.07	8
10	41.5	18.0		10.3	1.9		4.2	13.6		90.5
	2	9	0.24	7	8	0.36	2	2	0.10	0

11	55.1 8	14.8 6	0.22	4.71	0.3 3	0.77	1.5 0	12.4 4	0.06	90.0 7
12	53.9 1	13.9 6	0.25	4.06	2.3 1	2.15	1.7 2	11.7 9	0.04	90.1 8
13	56.9 9	14.6 8	0.19	4.30	0.8 3	1.15	1.8 4	12.0 1	0.03	92.0 1
14	31.3 4	20.5 7	0.17	9.24	0.1 1	0.34	1.2 8	25.6 8	0.15	88.8 7
15	30.9 8	20.9 3	0.15	9.73	0.1 3	0.29	1.4 0	26.5 1	0.13	90.2 5
16	37.0 3	20.0 2	0.29	7.16	2.4 4	0.35	5.1 4	20.7 2	0.44	93.5 8
17	38.0 6	19.0 7	0.30	6.39	3.8 7	1.30	5.3 0	18.1 9	0.36	92.8 4
18	37.3 4	20.4 0	0.31	7.35	4.2 5	0.26	6.2 1	20.6 4	0.35	97.1 2
19	52.4 0	31.8 5	0.31	1.95	0.4 4	0.20	7.2 5	2.47	0.02	96.8 9
20	51.5 5	31.5 2	0.44	2.05	0.7 1	0.19	8.3 0	2.30	-0.01	97.0 5
21	51.0 2	26.6 5	0.68	2.05	1.2 4	1.39	6.0 4	3.63	0.02	92.7 1
22	48.7 0	34.2 1	0.85	1.20	0.8 4	0.09	9.4 3	1.78	0.01	97.1 0
23	47.5 3	28.4 1	0.79	1.76	1.2 8	2.23	6.9 4	2.84	0.01	91.7 9
24	47.4 9	29.0 7	0.95	1.46	0.8 1	0.61	7.2 7	2.47	0.02	90.1 5
25	38.8 8	15.9 0	0.35	5.84	2.2 1	0.51	6.7 2	20.0 9	0.23	90.7 2

26	39.3 0	16.1 9	0.21	6.02	2.4 1	0.41	6.2 6	20.4 3	0.25	91.4 8
Average	43.5 4	22.0 3	0.41	6.21	1.4 4	0.65	5.2 7	12.7 9	0.13	92.4 7
2 $\sigma$	7.29	6.97	0.40	3.94	1.1 0	0.64	2.4 4	7.92	0.12	2.59
Avg. % Error	0.85	1.20	15.6 6	3.15	9.6 7	13.7 1	1.4 1	2.31	99.3 4	

Micas Continued

RW16.85	Wt. % Oxide									
Spot	SiO <sub>2</sub>	Al <sub>2</sub> O <sub>3</sub>	Na <sub>2</sub> O	MgO	TiO <sub>2</sub>	CaO	K <sub>2</sub> O	FeO	MnO	Total
1	36.4 3	16.4 6	0.20	7.51	4.0 8	0.04	9.4 4	21.6 9	0.25	96.0 9
2	35.6 9	16.4 2	0.16	7.57	4.1 8	0.01	9.5 9	22.1 1	0.21	95.9 4
3	36.0 0	16.9 2	0.14	7.64	4.2 2	0.01	9.6 0	21.8 8	0.22	96.6 5
4	35.6 3	16.0 4	0.22	11.2 2	4.0 3	0.03	8.9 2	15.9 4	0.07	92.0 9
5	37.7 9	17.1 7	0.21	12.1 1	4.0 4	0.03	9.2 4	16.2 7	0.08	96.9 4
6	36.9 5	16.7 1	0.21	11.8 8	4.1 1	0.02	9.2 3	16.2 8	0.09	95.4 7
7	36.1 1	16.3 0	0.24	11.5 0	4.0 0	0.05	9.0 5	16.0 3	0.09	93.3 7
8	41.3 4	14.9 3	0.41	11.7 4	2.4 0	0.33	7.3 9	14.9 6	0.41	93.9 3
9	39.1 0	15.1 6	0.42	12.0 5	3.0 1	0.12	9.1 0	17.2 4	0.59	96.7 7

10	40.8 7	15.0 9	0.50	11.9 0	2.5 5	0.33	8.2 8	15.9 1	0.49	95.9 2
11	39.7 0	14.9 1	0.68	12.2 8	3.0 4	0.21	8.1 8	17.0 8	0.56	96.6 3
12	39.5 7	14.6 8	0.59	12.0 2	3.0 9	0.15	8.5 0	16.9 4	0.58	96.1 1
13	39.0 7	15.3 4	0.15	11.6 7	3.8 8	0.24	7.9 4	16.0 3	0.28	94.6 0
14	38.4 5	15.3 0	0.16	11.6 2	4.0 3	0.18	8.3 1	16.2 0	0.27	94.5 1
15	36.5 6	14.7 4	0.11	11.2 7	4.1 4	0.19	8.3 4	16.3 8	0.27	91.9 8
16	39.4 9	16.7 2	0.22	7.13	2.6 6	0.19	8.6 9	19.8 2	0.67	95.5 9
17	37.8 2	16.5 6	0.20	7.51	2.8 2	0.11	9.0 7	20.5 8	0.69	95.3 6
18	57.2 9	22.1 2	0.18	4.38	0.2 6	0.53	6.8 0	4.55	0.04	96.1 4
19	37.0 3	14.6 4	0.29	11.6 2	4.7 7	0.05	9.0 1	18.1 9	0.22	95.8 1
20	36.2 7	14.6 2	0.29	11.1 9	4.9 9	0.03	9.0 0	18.1 4	0.24	94.7 8
21	30.7 0	17.9 5	0.09	11.7 7	1.3 5	0.57	2.2 2	24.0 3	0.24	88.9 2
22	31.3 5	17.2 9	0.07	12.3 7	1.7 5	0.09	2.8 5	23.7 0	0.24	89.6 9
23	36.3 1	14.8 9	0.16	11.2 4	3.5 4	0.08	8.4 0	19.5 7	0.38	94.5 7
24	35.9 7	14.5 4	0.14	10.9 6	3.5 8	0.06	8.7 6	19.5 5	0.37	93.9 3

Average	37.9 8	16.0 6	0.25	10.5 1	3.3 5	0.15	8.1 6	17.8 8	0.32	94.6 6
2 $\sigma$	4.82	1.64	0.16	2.20	1.1 2	0.15	1.8 6	3.90	0.19	2.13
Avg. % Error	0.88	1.36	18.2 4	1.90	3.7 8	52.9 8	0.8 6	1.40	21.5 6	

Micas Continued

RW14.78	Wt. % Oxide									
Spot	SiO <sub>2</sub>	Al <sub>2</sub> O <sub>3</sub>	Na <sub>2</sub> O	MgO	TiO <sub>2</sub>	CaO	K <sub>2</sub> O	FeO	MnO	Total
1	39.4 1	14.5 6	0.21	8.51	3.5 5	0.24	8.3 5	20.2 2	0.46	95.9 1
2	40.9 7	14.3 6	0.19	7.38	3.0 3	0.35	7.3 9	17.7 1	0.39	92.4 8
3	39.0 6	13.9 6	0.18	7.61	3.0 8	1.48	7.5 0	17.8 6	0.42	91.7 6
4	39.5 9	14.3 9	0.16	8.83	3.4 9	0.88	8.6 9	20.9 6	0.53	98.3 6
5	38.8 9	13.6 5	0.19	7.35	2.9 5	3.14	7.2 1	16.9 6	0.39	91.2 0
6	33.3 5	12.3 3	0.17	8.11	3.1 5	6.96	7.6 9	18.6 6	0.44	91.4 9
7	37.8 4	14.4 3	0.16	7.69	3.7 3	0.18	8.8 1	21.4 2	0.30	95.2 4
8	35.4 8	13.6 4	0.21	7.43	3.1 5	0.24	7.4 7	21.0 7	0.25	89.3 5
9	36.5 9	14.2 1	0.19	7.97	3.2 9	0.20	8.2 0	22.4 8	0.30	94.0 0
10	37.8 1	14.7 4	0.19	8.56	3.1 5	0.14	8.0 9	21.9 7	0.30	95.6 4

11	40.9 7	15.0 2	0.19	14.7 2	2.7 1	0.28	5.3 6	15.2 7	0.12	94.9 4
12	40.9 1	14.8 3	0.18	13.2 8	2.6 8	0.13	7.9 6	15.0 6	0.10	95.4 5
13	39.7 0	14.9 6	0.27	16.1 6	2.8 2	0.46	4.0 9	15.3 3	0.16	94.3 3
Average	38.5 0	14.2 4	0.19	9.51	3.1 4	1.13	7.4 5	18.8 4	0.32	93.8 6
2 $\sigma$	2.27	0.73	0.03	3.07	0.3 2	1.94	1.3 3	2.68	0.14	2.46
Avg. % Error	0.87	1.44	18.3 2	2.02	3.2 3	11.1 9	0.8 7	1.33	17.3 6	

Micas Continued

RW14.33	Wt. % Oxide									
Spot	SiO <sub>2</sub>	Al <sub>2</sub> O <sub>3</sub>	Na <sub>2</sub> O	MgO	TiO <sub>2</sub>	CaO	K <sub>2</sub> O	FeO	MnO	Total
1	37.4 4	13.7 9	0.09	10.1 5	3.72	0.02	9.1 0	21.0 3	0.18	95.52
2	37.3 7	13.8 0	0.11	10.3 6	3.77	0.02	9.4 8	21.3 7	0.25	96.52
3	32.7 7	18.4 0	0.04	15.1 8	2.05	0.09	2.5 4	19.5 3	0.31	90.91
4	35.2 6	17.5 1	0.09	14.2 9	2.28	0.58	4.8 6	18.0 9	0.25	93.21
5	33.8 8	17.0 0	0.06	13.8 7	2.29	0.06	4.7 2	19.0 6	0.26	91.19
6	29.3 3	22.1 8	0.03	14.8 7	0.07	0.06	0.1 6	22.6 9	0.12	89.51
7	27.4 2	22.0 7	0.01	15.2 1	0.07	0.05	0.0 5	23.7 4	0.14	88.75

8	62.3 6	24.2 8	7.86	0.01	0.02	4.98	0.7 6	- 0.29	100.5 0.01	4
9	48.3 2	33.9 1	0.92	1.15	0.46	0.27	7.8 6	1.42	0.01	94.31
10	49.3 6	30.9 8	1.02	1.55	0.46	0.16	6.8 1	1.87	0.02	92.22
11	36.1 8	18.1 9	0.18	11.1 0	1.71	0.17	3.0 0	19.4 0	0.26	90.18
12	35.7 1	17.6 8	0.21	10.6 1	1.60	2.34	2.9 7	18.3 9	0.24	89.74
13	37.2 6	17.7 0	0.15	10.1 7	1.61	1.03	3.0 1	17.3 9	0.22	88.53
14	37.4 0	18.5 6	0.19	11.0 4	1.77	0.29	3.4 4	19.1 3	0.27	92.09
15	35.8 5	17.5 2	0.17	10.3 4	1.67	1.87	3.1 3	18.1 3	0.23	88.89
16	36.5 5	17.7 3	0.18	10.5 6	1.65	1.46	2.9 6	18.5 0	0.22	89.80
17	30.8 1	17.0 1	0.03	13.6 4	2.24	0.23	1.2 6	22.8 9	0.61	88.71
18	32.2 8	16.4 7	0.03	12.6 8	2.39	0.15	2.7 9	22.4 2	0.56	89.77
19	30.7 3	16.8 0	0.03	13.4 5	2.48	0.38	1.8 3	23.1 4	0.59	89.43
20	31.0 0	16.7 5	0.02	13.2 9	2.69	0.33	1.8 7	23.1 5	0.61	89.70
21	39.1 1	13.9 3	0.19	12.8 4	3.15	n.d.	8.8 0	16.9 2	0.19	95.12
22	38.2 9	13.7 8	0.16	12.7 9	3.39	0.07	9.4 4	17.4 9	0.23	95.64

23	37.2 3	13.5 0	0.18	11.9 9	3.40	0.09	9.3 2	17.4 4	0.20	93.35
24	38.6 2	15.8 9	0.39	14.2 2	3.72	0.00	9.6 3	13.8 4	0.20	96.52
25	38.8 9	16.1 5	0.39	14.1 1	3.77	0.00	9.6 0	13.7 6	0.18	96.84
26	47.3 7	31.3 4	0.44	1.33	0.72	0.23	8.6 7	1.58	0.02	91.70
27	43.6 3	30.6 5	0.45	1.43	0.79	0.25	9.3 7	1.71	0.01	88.29
28	48.8 6	35.6 3	0.32	1.21	0.79	0.02	8.8 2	1.26	0.01	96.89
29	45.7 1	32.4 3	0.48	1.26	0.77	0.07	9.5 7	1.46	0.02	91.75
30	37.1 6	13.5 2	0.13	11.2 8	3.29	0.03	7.1 2	18.3 8	0.28	91.18
31	38.1 8	16.5 5	0.31	7.05	3.30	0.01	8.4 6	21.0 7	0.55	95.47
32	37.6 6	16.1 0	0.28	7.72	3.37	0.04	8.7 2	22.7 1	0.67	97.25
33	36.5 3	15.8 8	0.30	7.50	3.14	0.08	8.7 8	22.3 9	0.59	95.18
34	36.5 8	14.2 6	0.28	12.0 4	4.17	0.03	8.5 3	17.7 8	0.21	93.87
35	38.1 6	14.0 6	0.24	12.2 7	4.03	0.21	8.0 5	16.5 9	0.25	93.85
Average	38.2 6	19.4 8	0.46	9.79	2.19	0.46	5.8 7	15.8 8	0.25	92.64
2 $\sigma$ .	6.80	6.51	1.31	4.83	1.28	0.97	3.3 6	7.77	0.20	3.18

Avg. %			45.8		13.6	193.9	2.1		65.9
Error	0.91	1.31	8	9.26	5	6	7	2.40	4

Micas Continued

RW13.2	Wt. % Oxide									
Spot	SiO <sub>2</sub>	Al <sub>2</sub> O <sub>3</sub>	Na <sub>2</sub> O	MgO	TiO <sub>2</sub>	CaO	K <sub>2</sub> O	FeO	MnO	Total
1	42.2	16.8		11.3	3.7		7.7	13.5		96.5
	2	1	0.54	0	0	0.59	4	1	0.19	9
2	40.5	16.9		11.8	3.9		8.5	14.8		97.5
	2	6	0.53	1	0	0.22	3	4	0.20	2
3	36.6	14.9		11.5	4.1		8.7	14.9		91.6
	0	1	0.50	0	8	0.06	7	1	0.20	2
4	36.5	14.0			5.3		8.4	21.8		95.1
	5	4	0.17	7.98	4	0.36	4	3	0.48	9
5	35.7	13.7			4.0		9.1	22.4		94.2
	7	0	0.17	8.42	6	0.06	8	0	0.53	7
6	36.6	14.3			4.1		9.0	21.4		94.9
	9	6	0.23	8.17	2	0.37	0	6	0.51	1
9	38.2	14.0			4.6		9.4	21.2		97.2
	7	8	0.15	9.09	6	0.04	0	1	0.32	3
10	36.3	13.8			4.9		9.0	22.0		95.4
	0	2	0.13	8.87	1	0.01	6	1	0.35	6
11	37.7	13.9			4.5		9.2	20.9		96.1
	1	5	0.16	9.31	2	0.03	4	6	0.29	6
12	37.3	13.6			4.7		9.3	21.2		96.1
	8	8	0.14	9.25	8	0.04	7	2	0.29	5
13	50.5	34.9			0.7		9.3			99.5
	2	2	0.86	1.57	5	0.09	1	1.54	n.d.	6
14	51.0	35.3			0.7		8.5			99.0
	0	9	0.61	1.37	3	0.06	7	1.27	0.00	0

15	48.6 5	32.9 3	0.90	1.58	0.6 0	0.08	9.1 3	1.33	n.d.	95.1 9
16	48.6 2	34.0 7	0.98	1.53	0.5 9	0.06	9.4 3	1.29	0.01	96.5 9
17	38.3 6	14.0 0	0.10	11.9 8	2.7 2	0.04	9.5 3	19.2 1	0.20	96.1 4
18	38.7 1	13.4 1	0.27	11.4 7	3.5 8	1.34	8.7 2	16.4 4	0.20	94.1 4
19	39.1 2	13.8 3	0.25	11.1 0	3.3 8	1.22	7.8 0	14.6 3	0.12	91.4 4
20	35.3 6	12.5 9	0.33	11.3 5	4.2 9	1.72	8.7 3	16.2 7	0.18	90.8 1
Average	40.4 6	18.7 5	0.39	8.20	3.3 8	0.35	8.8 8	14.8 0	0.25	95.4 4
2 $\sigma$	5.37	8.65	0.29	3.91	1.6 1	0.52	0.5 3	7.94	0.16	2.39
Avg. % Error	0.85	1.32	15.1 0	2.58	4.0 9	48.4 1	0.7 9	2.25	162.4 9	

#### Micas Continued

RW12.74	Wt. % Oxide									
Spot	SiO <sub>2</sub>	Al <sub>2</sub> O <sub>3</sub>	Na <sub>2</sub> O	MgO	TiO <sub>2</sub>	CaO	K <sub>2</sub> O	FeO	MnO	Total
1	45.0 9	29.5 1	0.69	1.41	0.5 2	3.63	8.25	1.55	0.00	90.6 6
2	47.7 2	30.1 3	0.69	1.57	0.5 2	1.21	8.40	1.69	0.01	91.9 3
3	48.1 8	36.4 1	0.68	0.68	0.8 0	0.13	9.39	1.15	nd	97.4 1
4	38.0 9	15.4 1	0.16	12.8 5	3.5 8	0.52	9.12	15.7 6	0.19	95.6 9

5	37.8 9	15.3 9	0.15	12.6 7	3.6 8	0.12	9.36	16.3 2	0.20	95.7 9
6	37.7 0	15.7 8	0.16	12.1 4	3.6 4	0.07	9.46	16.5 8	0.21	95.7 4
7	38.0 5	13.5 8	0.17	12.3 1	4.4 9	0.19	8.68	18.0 3	0.20	95.6 9
8	37.1 8	13.4 2	0.16	12.0 7	4.3 6	1.10	8.90	16.4 9	0.21	93.9 0
9	31.2 2	11.2 8	0.15	10.3 4	3.4 9	0.62	7.05	24.9 1	0.23	89.3 0
10	38.6 1	13.8 8	0.13	12.3 1	4.5 6	0.21	9.03	16.6 3	0.21	95.5 7
11	36.6 8	14.0 7	0.22	10.1 5	5.2 1	0.13	8.91	18.8 8	0.21	94.4 6
12	36.5 6	13.6 7	0.25	8.55	4.1 7	1.37	7.56	16.3 0	0.18	88.6 1
13	37.1 8	14.1 8	0.25	9.74	4.7 6	0.60	8.53	17.8 7	0.21	93.3 2
14	37.3 8	13.9 2	0.34	10.0 8	4.8 3	1.19	8.76	17.8 1	0.22	94.5 3
15	48.5 9	33.3 0	1.13	1.16	0.3 4	0.21	8.54	1.89	0.00	95.1 4
16	48.3 3	33.7 6	1.00	1.07	0.2 5	0.16	9.04	1.81	0.01	95.4 3
17	47.8 7	34.0 0	0.99	0.91	0.3 3	0.17	9.04	1.62	0.00	94.9 2
18	48.8 8	34.0 8	0.26	1.27	0.4 0	0.12	10.3 8	1.84	0.03	97.2 6
19	42.2 3	14.8 9	0.16	12.1 2	3.6 2	0.37	7.95	13.8 9	0.19	95.4 3

Average	41.2 3	21.0 9	0.41	7.55	2.8 2	0.64	8.76	11.6 3	0.14	94.2 5
2 $\sigma$ .	5.55	9.52	0.34	5.14	1.9 2	0.84	0.74	8.11	0.09	2.46
Avg. % Error	0.84	1.24	14.4 7	3.30	6.3 2	13.8 3	0.80	2.66	238.2 8	

## A.4 Feldspar WDS Data

This section contains tables of data representing the WDS analyses of spots on feldspar minerals, which was used in Chapter 2. Only analyses with totals of ~90 % or greater were used for interpretation. The name of the sample analyzed is noted in each table along with the number of spot analyses, an average of the spot analyses, the % error and the standard deviation. In the name of each sample, the number follow “RW” corresponds with the depth from which the sample was collected.

Feldspars										
RW14.78	Wt. % Oxide									
Spot	SiO <sub>2</sub>	Al <sub>2</sub> O <sub>3</sub>	Na <sub>2</sub> O	MgO	TiO <sub>2</sub>	CaO	K <sub>2</sub> O	FeO	MnO	Total
1	69.1 2	20.0 8	12.0 1	0.00	0.03	0.04	0.07	0.15	n.d.	101.50
2	67.9 6	20.0 7	11.5 0	n.d.	n.d.	0.43	0.06	0.12	n.d.	100.14
3	68.6 8	20.1 3	12.2 6	n.d.	0.00	0.17	0.10	0.17	0.00	101.51
4	64.1 1	19.6 7	1.91	0.01	0.10	0.06	12.9 9	0.18	n.d.	99.01
5	63.2 7	19.0 6	1.61	0.03	0.07	0.06	13.7 8	0.19	n.d.	98.06
6	64.0 8	18.9 5	1.03	n.d.	0.04	0.02	13.9 4	0.14	n.d.	98.19
7	64.0 9	18.8 6	1.23	0.01	0.01	0.02	13.2 3	0.21	0.01	97.65
8	65.4 4	22.8 7	9.46	0.07	0.00	1.55	2.10	0.23	n.d.	101.72
9	63.5 6	23.6 4	8.51	0.08	n.d.	1.70	2.40	0.22	0.02	100.12

10	62.6 2	24.4 5	8.09	0.07	n.d.	2.83	2.23	0.25	0.01	100.55
11	68.2 9	20.7 2	11.6 5	0.00	n.d.	0.38	0.13	0.11	n.d.	101.28
12	68.1 1	19.9 6	11.4 9	0.01	0.03	0.15	0.09	0.14	n.d.	99.97
Average	65.7 8	20.7 0	7.56	0.03	0.03	0.62	5.09	0.17	0.01	99.97
2 $\sigma$	2.45	1.89	4.71	0.03	0.03	0.91	6.26	0.05	0.01	1.45
Avg. % Error	0.72	1.27	4.76	544.0 8	425.6 0	59.2 2	16.2 1	34.0 1	472.3 1	1558.1 8

#### Feldspars Continued

RW14.33	Wt. % Oxide									
Spot	SiO <sub>2</sub>	Al <sub>2</sub> O <sub>3</sub>	Na <sub>2</sub> O	MgO	TiO <sub>2</sub>	CaO	K <sub>2</sub> O	FeO	MnO	Total
1	66.1 8	22.1 5	10.0 2	0.04	0.02	2.22	0.47	0.14	0.01	101.2 4
2	66.8 6	18.3 1	0.26	0.04	0.05	0.01	13.7 6	0.26	n.d.	99.54
3	65.7 6	18.6 5	0.43	0.03	0.03	0.07	15.4 0	0.19	0.01	100.5 7
4	64.8 9	18.8 5	0.48	0.10	0.03	0.10	15.1 2	0.21	0.01	99.79
5	65.3 2	18.8 5	0.26	n.d.	0.02	0.03	14.7 4	0.15	0.01	99.37
6	65.2 5	19.4 8	1.78	0.00	0.02	0.14	13.3 4	0.11	0.01	100.1 2
7	66.2 2	19.0 2	1.05	n.d.	0.05	0.03	14.9 8	0.22	n.d.	101.5 7

8	65.9 3	18.8 4	0.10	0.01	n.d.	0.04	12.4 6	0.09	0.02	97.49
9	64.9 2	19.0 0	0.69	0.01	0.02	0.04	14.9 0	0.19	n.d.	99.77
10	67.2 0	22.0 4	10.3 8	0.02	0.02	1.73	0.36	0.14	0.01	101.8 9
11	66.3 5	19.0 2	1.45	0.00	0.04	0.04	14.0 2	0.18	0.01	101.1 2
12	66.1 6	18.9 9	0.56	0.00	0.04	0.02	16.0 5	0.14	n.d.	101.9 6
14	66.5 4	19.3 0	1.17	n.d.	0.00	n.d.	15.4 0	0.17	n.d.	102.5 8
15	66.8 7	21.1 2	10.0 1	0.01	n.d.	1.22	0.59	0.13	n.d.	99.94
16	65.9 6	18.9 1	0.92	n.d.	n.d.	n.d.	15.4 7	0.10	0.03	101.3 8
17	65.4 3	19.3 3	1.75	n.d.	0.04	0.03	11.7 8	0.06	n.d.	98.42
18	66.3 6	18.9 1	0.93	0.01	n.d.	0.02	15.4 1	0.14	n.d.	101.7 6
19	59.7 9	27.0 6	7.09	0.00	0.02	7.75	0.15	0.09	0.02	101.9 6
20	63.8 2	18.6 6	0.17	0.08	0.03	0.01	16.2 1	0.14	n.d.	99.11
22	66.0 0	18.8 6	0.31	0.04	0.03	0.01	16.1 5	0.19	n.d.	101.5 8
23	65.3 0	19.5 7	0.15	0.00	0.07	n.d.	15.9 1	0.09	0.00	101.0 9
24	64.9 2	19.1 7	1.63	n.d.	0.05	0.03	13.8 3	0.18	n.d.	99.80
25	66.9 0	22.3 3	10.2 6	n.d.	n.d.	2.50	0.28	0.15	0.04	102.4 5

26	65.5 2	19.3 5	1.91	0.00	0.04	0.06	13.5 1	0.18	n.d.	100.5 7
27	69.7 0	20.5 5	11.3 1	0.01	0.02	0.39	0.18	0.05	n.d.	102.2 0
28	66.2 3	19.1 6	0.87	n.d.	n.d.	n.d.	15.5 8	0.05	0.01	101.8 8
29	66.1 5	19.4 2	0.97	n.d.	0.03	0.01	15.0 5	0.09	0.01	101.7 3
30	65.7 6	19.1 3	1.14	n.d.	0.02	0.01	15.1 5	0.10	0.01	101.3 2
31	69.9 3	20.6 5	11.4 2	0.00	n.d.	0.30	0.18	0.07	n.d.	102.5 4
32	68.6 0	19.0 4	0.16	n.d.	n.d.	n.d.	10.3 5	0.07	n.d.	98.22
33	71.5 5	20.5 5	9.66	n.d.	0.01	0.17	0.10	0.07	0.01	102.1 2
34	68.4 6	21.6 7	7.78	0.03	0.01	2.08	0.15	0.13	0.03	100.3 3
35	69.4 5	18.8 7	2.10	0.03	0.03	0.05	8.52	0.12	n.d.	99.17
36	67.8 8	22.0 5	10.4 8	0.04	0.02	1.44	0.36	0.17	0.02	102.4 5
37	67.4 7	20.5 5	9.94	0.08	0.02	0.64	1.29	0.33	n.d.	100.3 1
38	65.8 7	19.9 6	9.99	0.21	0.08	0.79	0.27	0.38	0.01	97.57
Average	66.4 3	19.9 3	3.88	0.03	0.03	0.71	9.65	0.15	0.01	100.6 9
2 $\sigma$	1.98	1.67	4.38	0.05	0.02	1.50	6.84	0.07	0.01	1.43
Avg. % Error	0.72	1.30	11.6 8	811.4 5	525.7 2	135.5 9	6.47	46.7 6	397.8 9	

## A.5 Key *p*XRD Scans of Wörnitzostheim Core Samples

This section contains representative bulk *p*XRD patterns of samples from the Wörnitzostheim drill core. Representative diffraction patterns of relevance to the discussion of Chapter 2 are shown in their respective unit groups in Figures A.5.1–A.5.5. An example of the differences between the *p*XRD scans of the <0.2 and 2–0.2  $\mu\text{m}$  size-fractions are shown for the grey material in the marlstones (Fig. A.5.6). Scans of for d(060) peaks are shown in Figure A.5.7, highlighting an example from the clastic and matrix material from the pink conglomerate (19 m depth). The following abbreviations are used in Figures 6.1–6.7: Qz. – quartz, Pl. – plagioclase, Kfs. – K-feldspar, Clay – clay minerals (e.g., smectite, illite, kaolinite, chlorite; these peaks often overlap in diffraction patterns from non-oriented samples), Cal. – calcite, Dol. – dolomite, Py. – pyrite, and Msc. – muscovite.

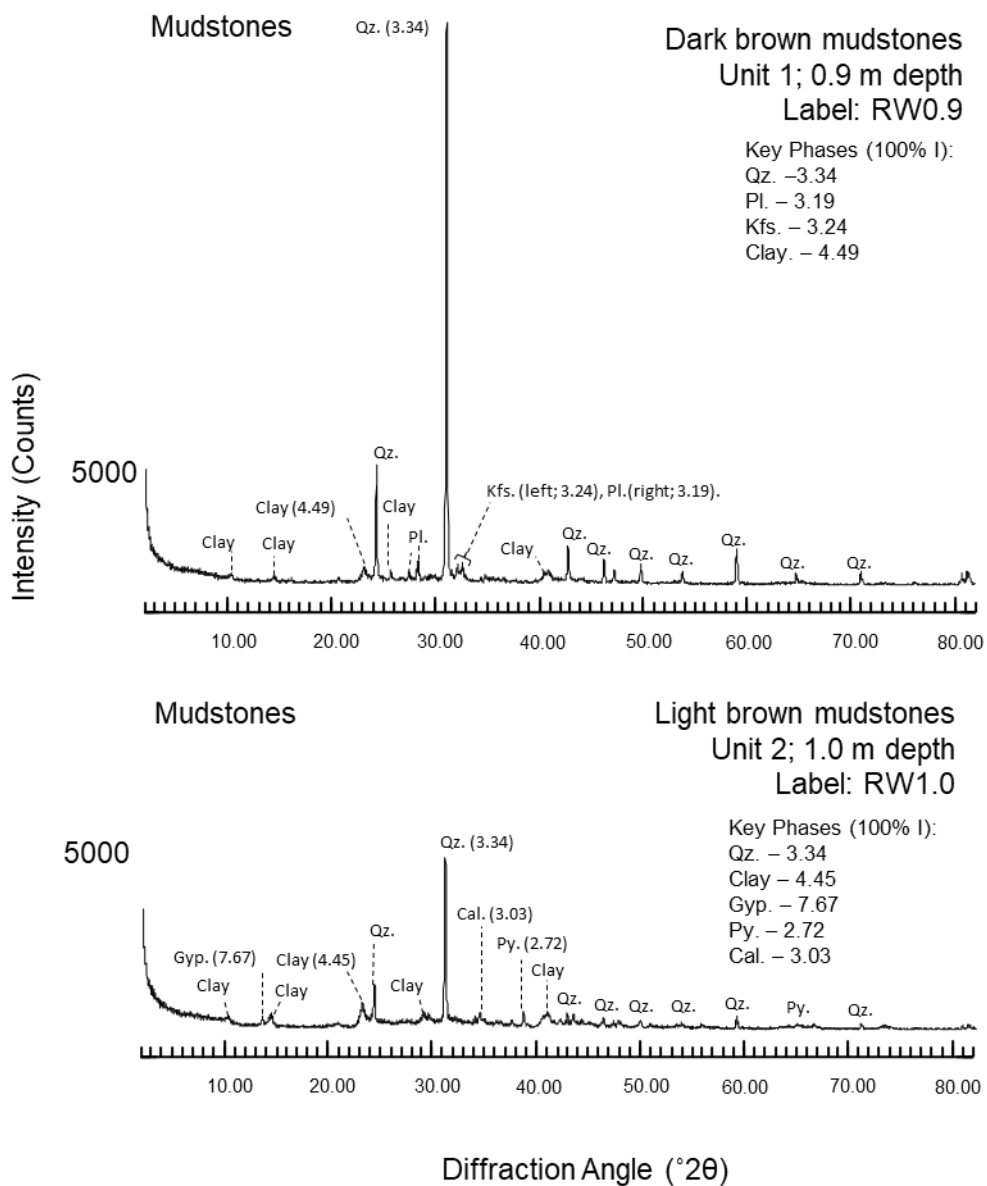


**Figure A.5. 1:** Bulk *p*XRD diffraction patterns of the dark brown and light brown mudstones as labelled. The most intense (100 % I), diagnostic peak of each mineral is indicated next to each pattern.

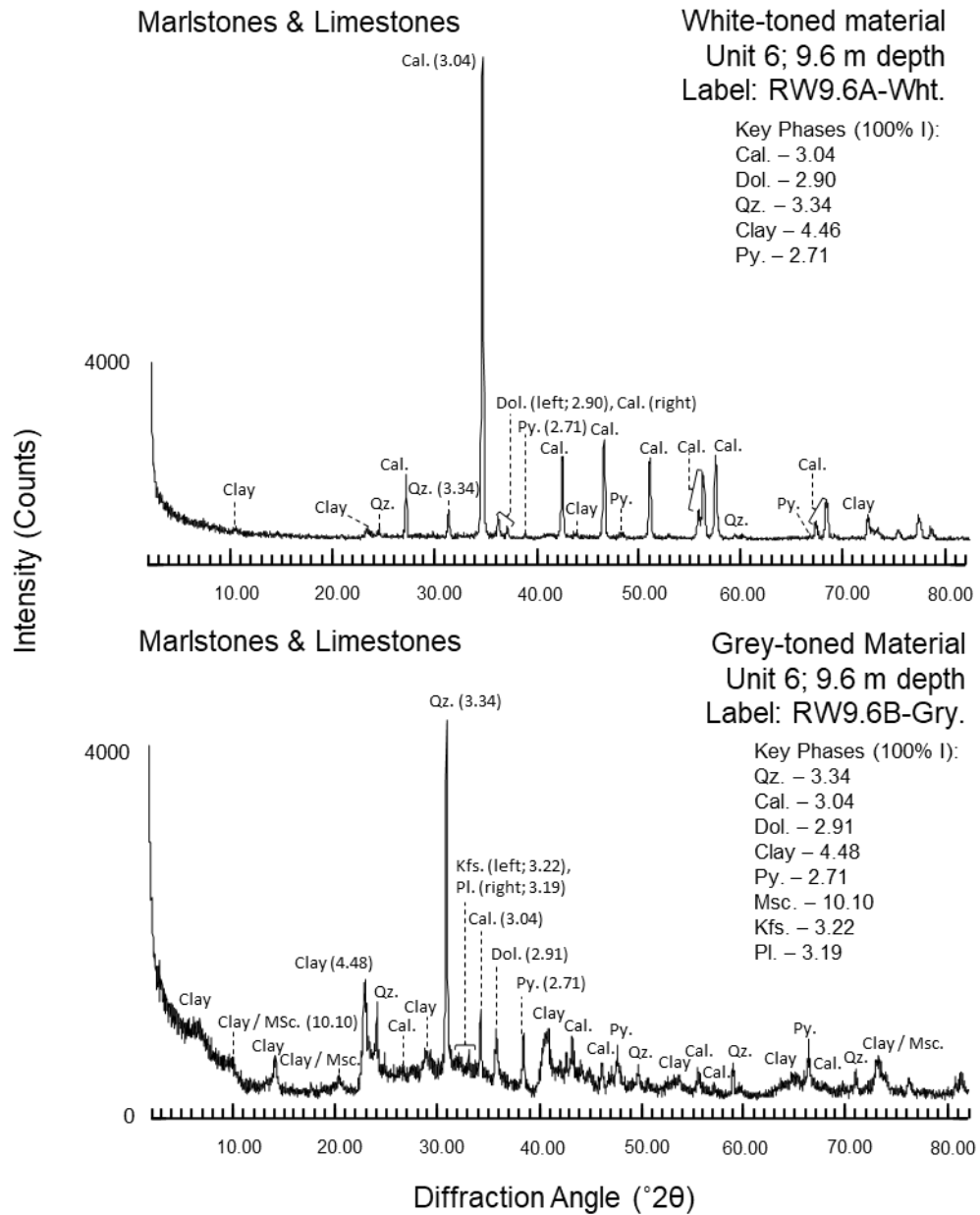


**Figure A.5. 2:** Bulk *p*XRD diffraction patterns of the white toned and grey toned material described for the marlstones of unit 6. The most intense (100 % I), diagnostic peak of each mineral is indicated next to each pattern.

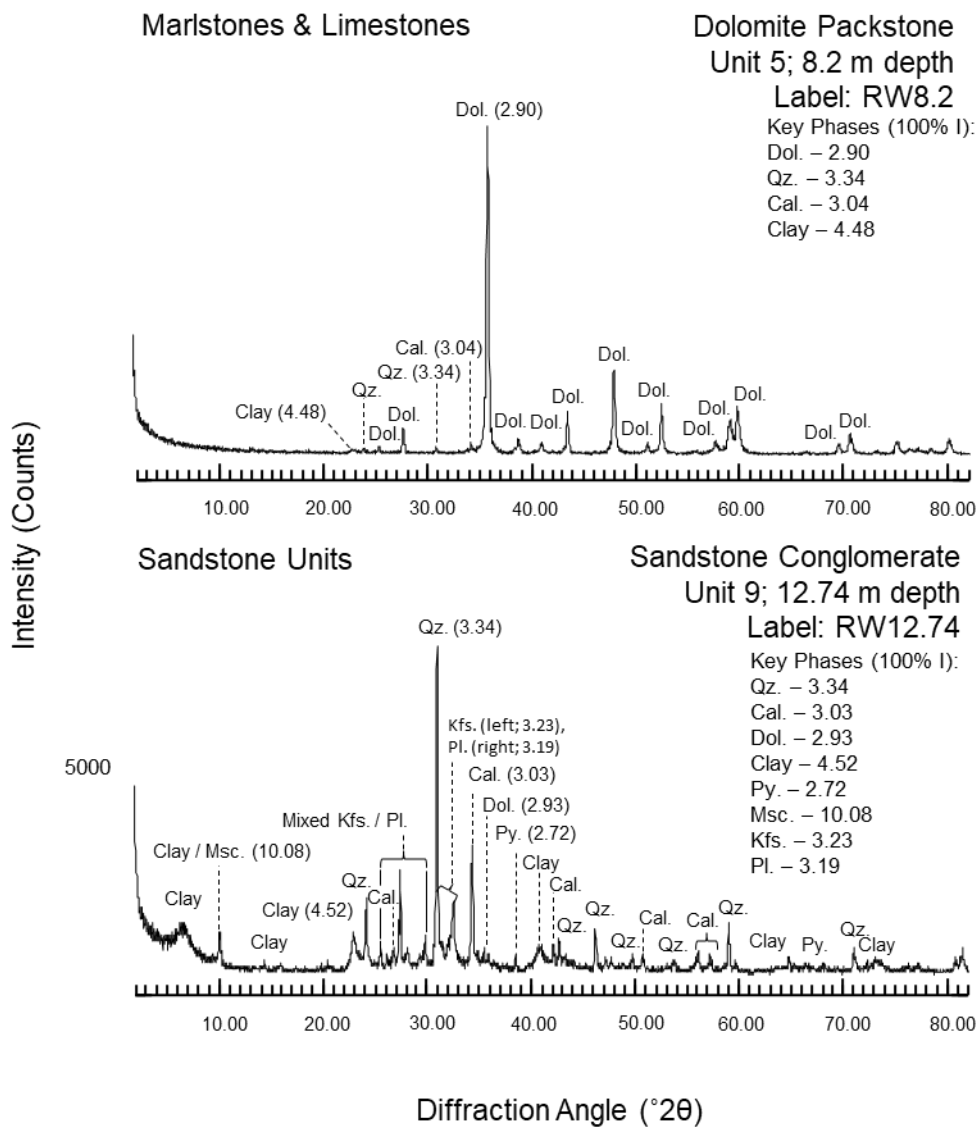


**Figure A.5. 3:** Bulk *p*XRD diffraction patterns of the matrix material from the dolomite packstone and the sandstone conglomerate. The most intense (100 % I), diagnostic peak of each mineral is indicated next to each pattern.

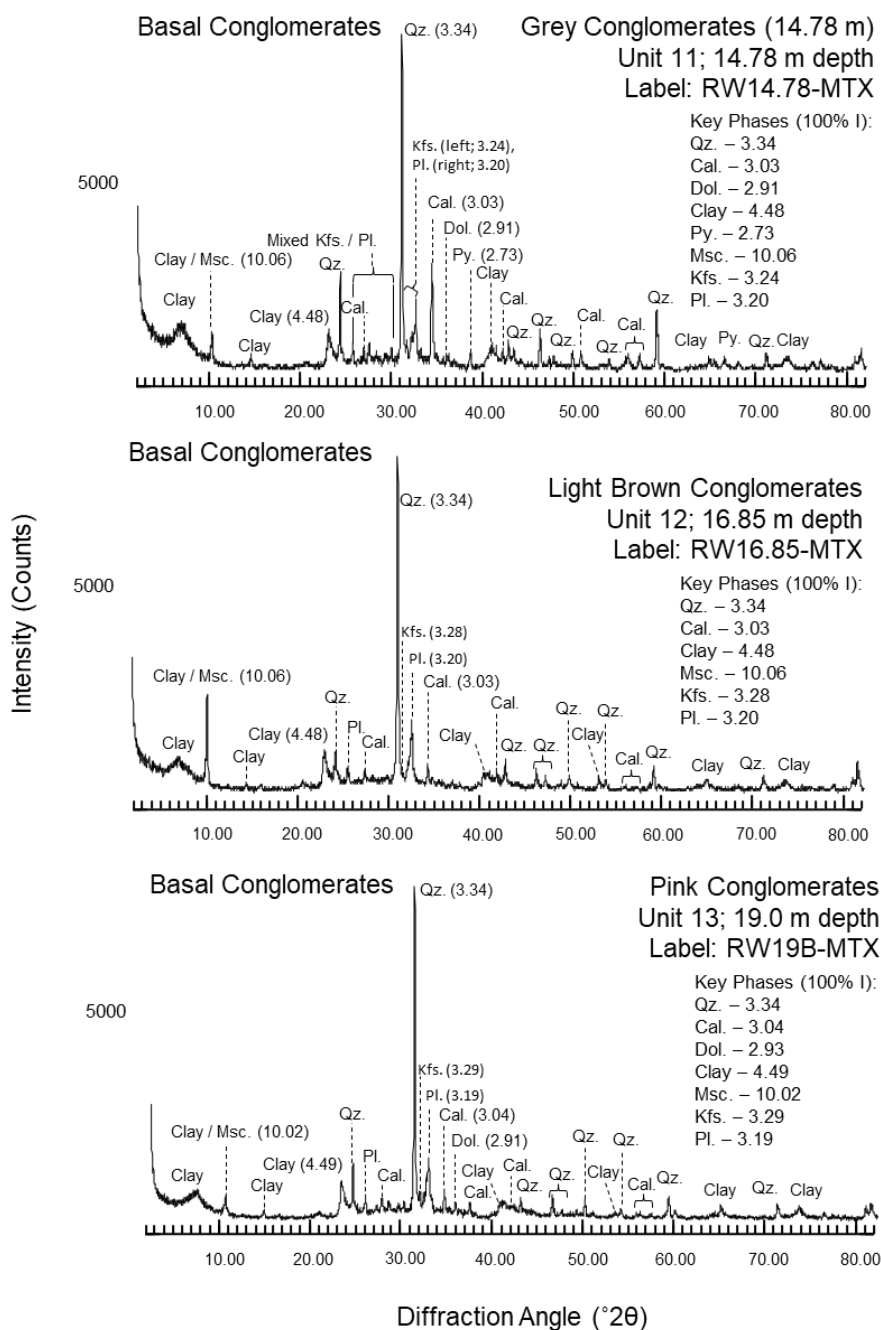


**Figure A.5. 4:** Bulk *p*XRD diffraction patterns of the matrix material from the grey, light brown and pink conglomerate. The most intense (100 % I), diagnostic peak of each mineral is indicated next to each pattern.

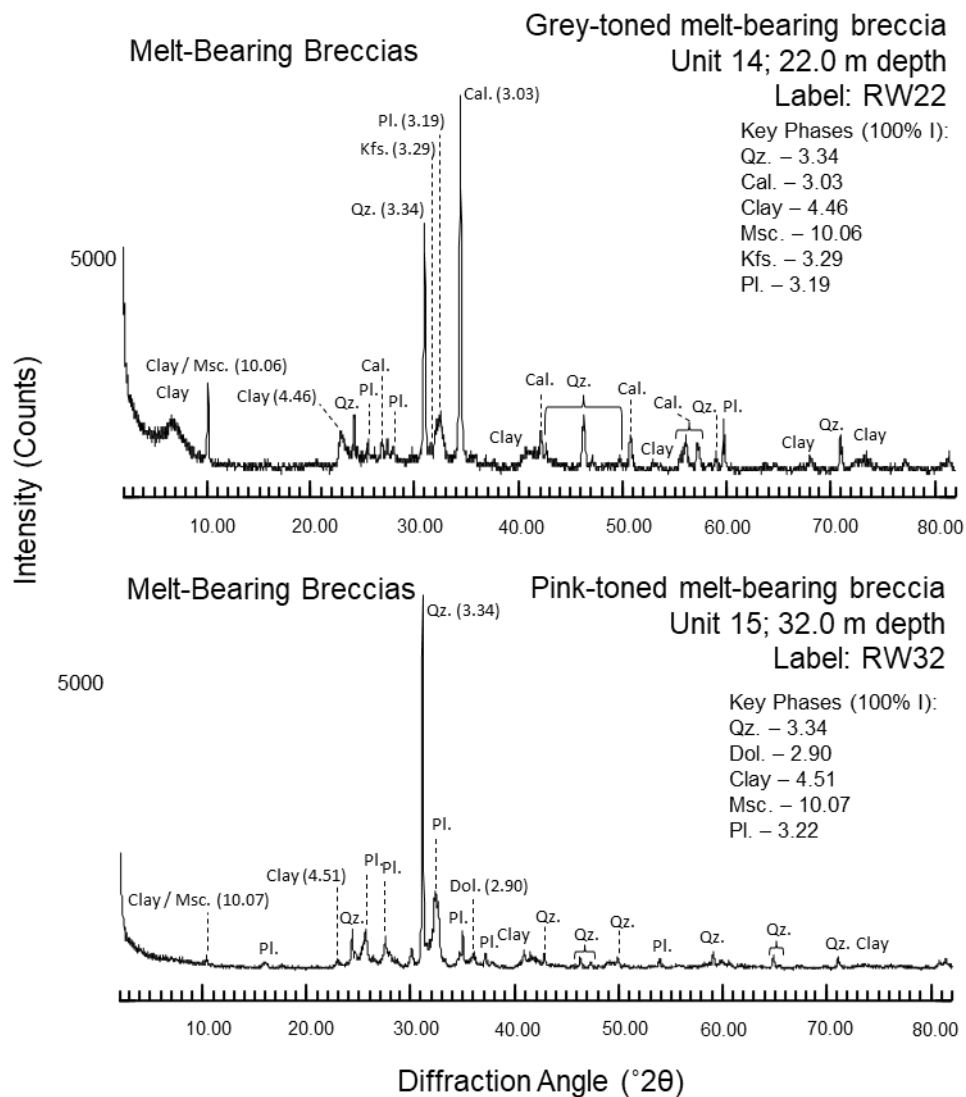


**Figure A.5. 5:** Bulk *p*XRD diffraction patterns of the groundmass from the grey-toned and pink-toned melt-bearing breccias. The most intense (100 % I), diagnostic peak of each mineral is indicated next to each pattern.

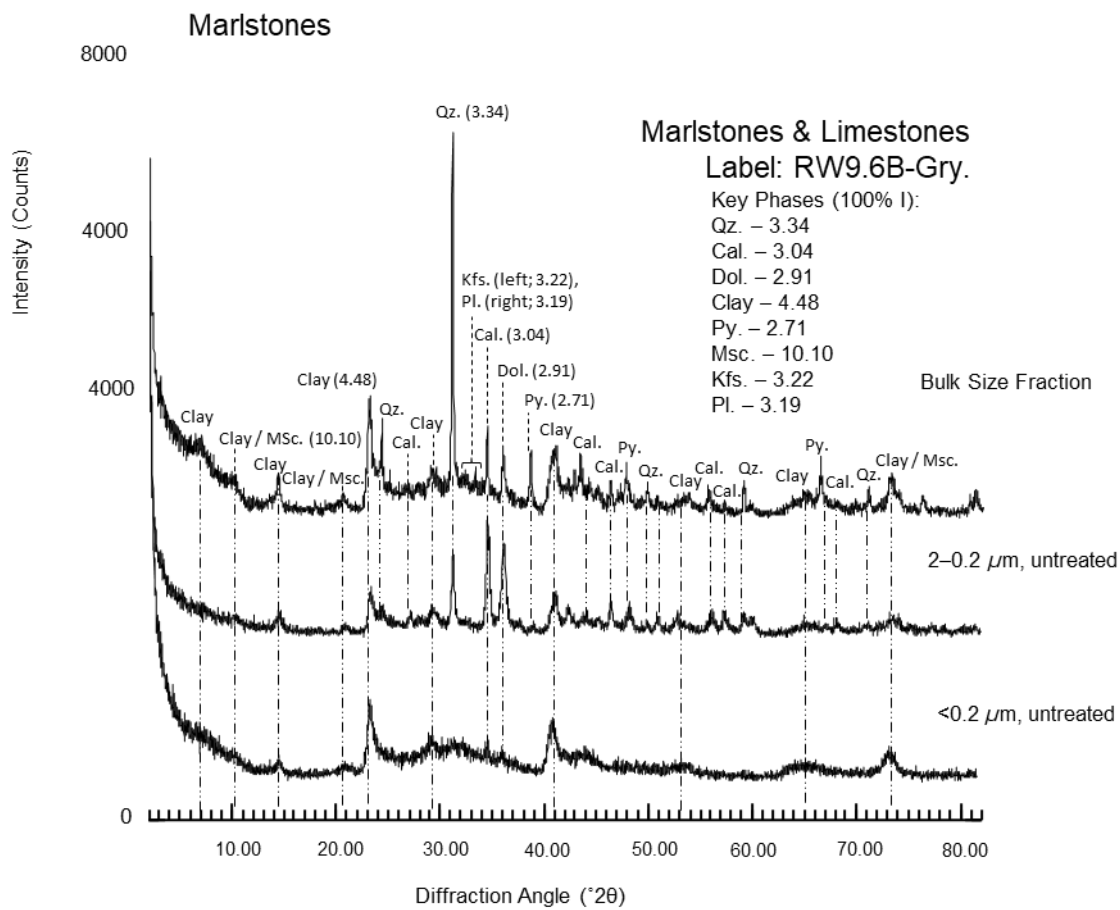


**Figure A.5. 6:** *p*XRD diffraction patterns of the grey toned material described for the marlstones of unit 6 showing differences between the bulk size-fraction, <0.2  $\mu\text{m}$  size-fraction and the 2–0.2  $\mu\text{m}$  size-fraction. Vertical dashed lines indicate the continuity of peaks and mineralogy between size fractions.

Pink Conglomerate d(060)  
(Unit 13; Matrix; 20.10–17.10 m)

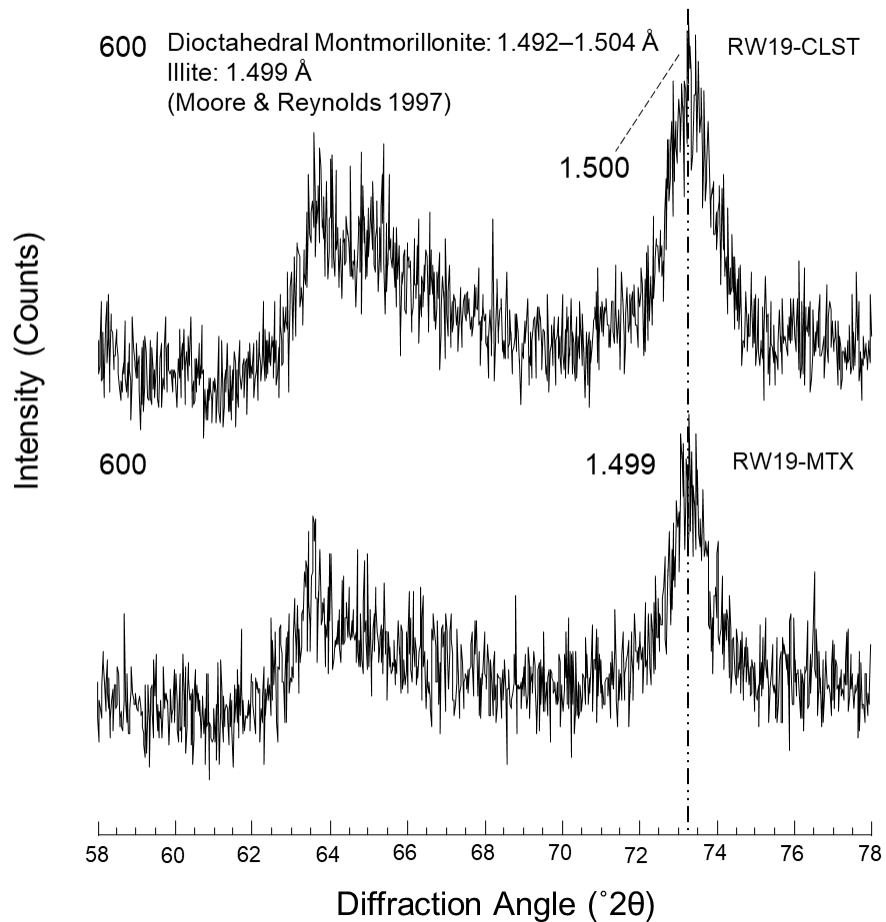


**Figure A.5. 7:** *p*XRD diffraction patterns of the clast (CLST) and matrix (MTX) highlighting the 58–78  $2\theta$  region where d(060) peaks are located. The peaks are labelled with their associated d-spacing (1.500 Å and 1.499 Å), which is consistent with dioctahedral clay minerals such as montmorillonite and illite (Moore & Reynolds 1997). The sample labels associated with each pattern and indicated next to the labelled peak.

## Appendix B: Nördlingen Drill Core Log

This log contains original unrefined notes during field excursions to the Ries impact structure and visits to the Nördlingen Impact Crater Museum, Nördlingen, Germany. Recurring lithologies are named with the use of different “types” to delineate their recurrence.

Depth Extent (m)	Lithology	Unit Description
192-254.6	Siltstone	Highly friable parallel laminated clay-rich siltstone with disconnected laminae and abundant white flecks - could be redox spots?
254.6-255	Siltstone breccia	Dark brown, dramatically undulating parallel laminated silt in a sharp contact with a light grey unit of highly brecciated lithic clasts. The clasts all have weakly undulating parallel lamination. Could be some alteration at the base of the unit. Appears to represent an earthquake or landslide at this section of the basin. Abundance of mm scale calcite (?) vugs relatively aligned.
255-255.8	Siltstone	Parallel laminated clay-siltstone alternating with chaotically laminated clay-siltstone.
255.8-256	Fossil-bearing polymict breccia	Brecciated unit with hydrothermally overprinted clasts and massive coarse matrix in contact with dramatically undulating clay-siltstone. The hydrothermal overprint is concordant with laminae orientation. Snail shells embedded in matrix.

256-260	Siltstone	Parallel laminated clay-siltstone alternating with chaotically laminated clay-siltstone.
260.0-261.0*	Siltstone	Light-grey toned, parallel laminated clay-siltstone with horizontal bedding. Different conformable zones can be distinguished based on the faint mm scale undulations associated with a darker tone. The grain size is too small to distinguish any individual mineralogy.
261.0-261.35*	Interbedded siltstone rhythmite	Only one 4cm thick small chunk of the depth extent is preserved. At the base of the sample is a light grey-white toned section (~0.5cm thick) comprised of similarly gently undulating, parallel laminated clay-siltstone described in the dark toned unit above (260-261). The white undulating siltstone alternates with ~0.5cm thick sections of massive light bluish-grey clay. This alternating unit is approximately 1.75cm thick. The upper 2.25cm thick section of core is entirely comprised of massive clay.
261.35-261.80*	Siltstone	Weakly parallel laminated to massive, grey-white claystone. The nature of transition from the previous unit is unknown. Parallel lamination is faint and difficult to distinguish - it also does not appear to be laterally continuous. Parallel laminations are more visible in the hole drilled for geophysics analyses.

261.80-262.05*	Siltstone	Weakly parallel laminated, grey-white clay-siltstone. The nature of transition from the previous unit is unknown. One mm scale dark layer similar to what was observed in 260.0-260.10 - undulations are absent throughout the entire sample - except at the base where there appears to be some undulating purple material.
262.05-262.6*	Siltstone	Weakly parallel laminated, white-grey, silt-claystone. Some chunks of the core in the bag appear to contain discordant, purple toned, wavy layers - although their relationship to the core immediately surrounding it is difficult to determine as they only exist in small cm scale chunks. There are some very faint, weakly undulating, discontinuous layers of laterally conformable dark material. As observed with some of the chunks of core in the bag - this lateral discontinuity may be related to the purple toned material (possibly to the emplacement mechanism?)
262.6-263.4*	Fine sandstone	Silt-sandstone - massive (?). It is difficult to tell the overall grainsize and structures present in this core as most of it is tightly covered by a plastic, rubber casing, however it does appear to be generally massive and comprised of clay.
263.4-264.2*	Sandstone	Massive, light grey toned coarse silt-sand. The sand contains polymict clasts comprise of 70% 0.5-2mm scale

Fe-oxides and 30% white, amorphous specs (<1mm) - % by total coverage of the surface area.

---

264.2-266.0*	Laminated sandstone	Massive, coarse muddy siltstone with a small clast composition. Potentially cross laminated. Most of the clasts are mm to sub mm scale and are comprised of dark black-grey ameboid spots. There are three prominent cm scale clasts: one sub-rounded glass clast with an Fe-oxide rim, one subrounded, rimless white clast of amorphous material with sub-mm scale black spots and one angular, green possibly lithic clast with an Fe-oxide rim.
266-266.3*	Medium Sandstone	The core is clast rich with a massive, light grey clay-siltstone matrix. The clasts are polymict and are comprised of mm to cm scale white, ameboid blobs that appear to be derived from the dark black, glass clasts most of the "fresher" black clasts are rimmed with a reddish -orange Fe-oxide-like material. There is one ~1cm wide dark green clast with a similar Fe-oxide rim to the black clasts.
266.3-266.6*	Type 1 gravelstone / fine conglomerate	The core contains mostly mm scale clasts with light grey, siltstone comprising the matrix. 35% angular to ameboid mm scale, black glass clasts; 35% white amorphous, powdery, ameboid clasts. The rest of the clasts are cm scale and have varying compositions. There are three white, ameboid shaped ~1.5cm sized clasts with black specs, One ~3cm wide green-grey clast with a prominent black-red

ring possibly made of Fe-oxides and one ~1cm wide likely originally green clast, but heavily overprinted with Fe-oxides so it's difficult to tell.

---

266.6-267.2\*      Conglomerate      Prominent change in composition.... The only preserved sample at 267.2m has a small amount of the light grey siltstone comprising the matrix preserved. In this light grey siltstone matrix, the black clasts are notably absent (or just too fine grained to make out with the naked eye), but the white, powdery amorphous clasts previously described were abundant in mm to sub-mm scale.

The base of the sample appears to have fractured along a contact with a ~7cm wide white-black clast that is reminiscent of the basement gneissic material.

There is a prominent grey-green, angular, lithic clast that appears to be surrounded by one light grey-brown alteration halo and then a second dark brown alteration halo

A fine, clast supported **conglomerate** comprises the upper half of the sample. The conglomerate has very little matrix but most of what it does have appears to be heavily altered. There is a wide range of clast compositions that appear to mostly consist of mm scale, angular to sub-angular clasts with a brown-green overprint. The clast composition has a small component of rounded to sub-angular, white pebbly, lithic clasts and white amorphous, powdery material. The matrix and overprint both have a light brown-green color.

267.2-267.5*	Fine siltstone / claystone	Fine grained, parallel laminated silt-claystone with dark, sub-mm scale, gently undulating bands
267.5-268.5*	Massive claystone	Massive, light grey-white claystone
268.5-268.75*	Conglomerate	Prominent alteration feature with approximately the same composition as what was observed in the 266.6-267.2 range, but without the conglomerate unit. There is a weakly overprinted gneissic clast and little preserved matrix.
267.75-269.0*	Massive claystone	Massive, light grey-white claystone
269.0-269.5*	Conglomerate	Coarse, blue-grey siltstone-clay matrix with abundant polymict clasts 50% comprised of altered / overprinted grey-green clasts and 45% white, amorphous, ameboid shaped, powdery clasts - similar to what was observed in Wör. 13.15-13.20. There is one prominent 3.5cm wide basement-like clast with a dark brown-green alteration halo.

---

269.5-270*	Coarse sandstone / conglomerate	The clast composition and morphology of 269.5-270 is approximately the same as 267.2-269.5 with a notable increase in clasts overprinted with brown-orange Fe-oxides. The matrix is significantly sandier and more friable.
270-270.8*	Type 1 conglomerate	Coarse, blue-grey silty-clay matrix with abundant polymict crystalline and sedimentary sub angular to angular clasts. Coarsest clasts are heavily oxidized. Some white, amorphous, ameboid shaped, powdery clasts. The lithic clasts appear to be primarily felsic but have become very powdery and friable due to weathering. Some lithic clasts have a dark green overprint. Poorly sorted. Standard type 1 breccia.
270.8-271.5*	Massive siltstone	Massive, coarse muddy siltstone with a small clasts composition. Most of the clasts are mm to sub mm scale and are comprised of dark black-grey flecks. There is one prominent cm scale clasts: one sub-rounded glass clast with an Fe-oxide rim. Similar to 264.2-266.
271.5-271.8*	Pervasively altered gravelstone	Coarse, green-grey silty-clay matrix with 65% mm scale rounded to sub-angular black and 35% white clasts with the same clast morphology reminiscent of a pervasively altered crater-fill suevite. There is a prominent black-brown alteration feature although it is not preserved in contact with the surrounding core. The green tone is likely due to alteration.

---

---

271.8-272.7*	Red / dark- brown gravelly chunks of silt and clay	The core is highly friable and crumbled in a bag where only a few cm scale pieces remain relatively intact. Most of the core is comprised of an amorphous, <b>dark-brown</b> silty-clay material which makes up the matrix. Light green and white irregularly shaped clasts make up roughly 30% of the total volume of the material although it is possible that the white clasts may have been more prominent as they would crumble out and be lost first. The green clasts appear to be lithic, but overprinted with the green coloration and may have been derived from basement material. One cm scale black glass clast with white, powdery patches is preserved.
<hr/>		
272.7-273.3*	Light-brown gravelly chunks of silt and clay	The core is highly friable and crumbled in a bag where several cm scale fragments of clumped matrix and some clasts remain relatively intact. Most of the core is comprised of an amorphous, <b>light-brown</b> silty-clay material which makes up the matrix. There are three main clast compositions observed. The first is a white powdery amorphous material with ranging sizes from mm to cm scale and ranging shapes from rounded to sub-angular. There are less abundant black, glassy clasts that follow the same morphology as the white clasts and some mm to cm scale, rounded to sub-rounded lithic clasts with a green-brown overprint, possibly derived from basement material.
<hr/>		
273.3-273.8*	Type 1 conglomerate	Coarse, blue-grey silty-clay matrix with abundant polymict crystalline and sedimentary sub angular to angular clasts.

Coarsest clasts are heavily oxidized. Some white, amorphous, ameboid shaped, powdery clasts. The lithic clasts appear to be primarily felsic but have become very powdery and friable due to weathering. Some lithic clasts have a dark green overprint. Poorly sorted. Standard type 1 breccia.

---

273.8-274.8*	Sandy siltstone	Massive, sandy siltstone, with ~5% surface coverage sub-mm scale sub-rounded clasts comprised of 50% black flecks, 45% white powders and 5% (one mm scale grain) of subhedral calcite. There are some pockets on the surface of the core where it fractured where it appears as though some grains have been plucked out; these were possibly calcite grains suggesting there was once a greater abundance of them in this section of the core. There are some minor brown weathering / Fe-oxide overprints
--------------	-----------------	---

---

274.8-275.0*	Weathered sandstone	Massive, light grey-white sandy-silt matrix with cm scale, ameboid shaped, interconnected, white powdery clasts with a pinkish surficial overprint. In addition to the white powdery material are individual dark black, and black and white clasts - often observed with Fe-oxide alteration rims. The clast sizes range from sub-mm to mm scale. There are also a few flecks of the white powdery material in addition to the sample wide, interconnected coverage.
--------------	---------------------	---

---

275.0-275.8*	Coarse conglomerate	Massive, light grey-white, highly friable silty-clay matrix with a single ~ 2.5cm wide, white powdery clast. There is a
--------------	---------------------	---

small dark brown alteration feature in contact with the white clast and Fe-oxidation appears to be more prominent as the crumbled core in the bag appears to have a higher concentration of the orange-brown material. In addition to the white powdery material are individual dark black, and black and white clasts - often observed with Fe-oxide alteration rims. The clast sizes range from sub-mm to mm scale. There are also several flecks of the white powdery material in addition to the sample wide, interconnected coverage.

---

275.8-278.9*	Massive claystone	Massive light grey toned claystone with no visible clasts or bedding - except for very rare metallic flecks - possibly mica. The core has a rubber casing and appears to be moderately friable.
278.9-279.5*	Type 1 conglomerate	Coarse, blue-grey silty-clay matrix with abundant polymict crystalline and sedimentary sub angular to angular clasts. Coarsest clasts are heavily oxidized. Some white, amorphous, ameboid shaped, powdery clasts. The lithic clasts appear to be primarily felsic but have become very powdery and friable due to weathering. Some lithic clasts have a dark green overprint. Poorly sorted. Standard type 1 breccia.
279.5-280.0*	Type 1 conglomerate	Highly friable and crumbled material reminiscent of suevite. The matrix appears to have once been a light blue

---

grey clay, but altered to a white-green powdery material. There are white crystalline clasts with red-brown alteration rims and a greenish overprint.

---

280-280.9	Fine type 1 conglomerate	Coarse, blue-grey silty-clay matrix with abundant polymict crystalline and sedimentary sub angular to angular clasts. Coarsest clasts are heavily oxidized. Some white, amorphous, ameboid shaped, powdery clasts. The lithic clasts appear to be primarily felsic but have become very powdery and friable due to weathering. Some lithic clasts have a dark green overprint. Poorly sorted. Clasts are generally 1 cm diameter or less. Matrix is a more prominent component than other type 1 breccias.
<hr/>		
280.9-281.3	Massive silt- claystone	Massive grey-white silty claystone with two types of mm scale clasts. There are 50% clasts comprised of white irregularly shaped amorphous material, 45% clasts comprised of red, rounded Fe-oxides and 5% metallic mica flecks
<hr/>		
281.3-281.5	Type 2 gravelstone	Coarse, green-grey silty-clay matrix with 65% mm scale rounded to sub-angular white and 35% black clasts with the same clast morphology as pervasively altered crater-fill suevite. The green tone may be due to alteration.
<hr/>		
281.5-282	Type 1 conglomerate in contact	Coarse, blue-grey silty-clay matrix with abundant polymict clasts 10% comprised of altered / overprinted grey-green clasts and 90% white, amorphous, sub-rounded, powdery

---

with massive siltstone	clasts - similar to suevite transition in Wor 13.15-13.20, but with predominantly white clasts. There are a few cm scales basement-like clast with dark brown-green alteration rims. There is a 3cm deep unit of massive clay with a very sharp undulating contact with the overlying blue suevite-like unit. There are some clasts at the base of the clay unit suggesting it may transition back into the blue suevite-like unit before progressing again into the green suevite unit described previously.
---------------------------	---

---

282-282.20	Pervasively altered coarse conglomerate	Coarse, green-toned, suevite like material with a green-grey, silty clay matrix. The 30% surface area coverage of polymict clasts and green-grey / green-yellow tone are the most striking features of this section of core. A prominent deep green-brown, highly altered, irregularly shaped, cm scale section of the core hosts ameboid, white powdery clasts almost exclusively and also has what appears to be dark, black glass clasts behaving like veins. The clasts size ranges from mm to cm scale with 60% of the clasts on a mm scale and 40% on a cm scale. The mm scale clasts are comprised of mostly angular to sub-rounded white powdery clasts that mostly appear to be derived from the larger lithic clasts. Some look completely made up of K-spar in some cases and biotite in others (both with angular habits and occurring infrequently with biotite occurring the least frequently. The cm scale clasts are mainly shocked, lithic clasts derived from basement material and in some cases are completely altered out.
------------	---	---

Most have a dark brown alteration rim. The other cm scale clasts are either comprised of a white amorphous powder or a dark, black powdery material.

---

282.20-282.30	Type 1 gravelstone	Coarse, green-grey silty-clay matrix with 65% mm scale rounded to sub-angular white and 35% black clasts with the same clast morphology reminiscent of a pervasively altered crater-fill suevite. The green tone may be due to alteration.
282.30-283.5	Coarse sandstone / conglomerate	Coarse, blue-grey silty-clay matrix with some polymict clasts 10% comprised of altered / overprinted grey-green clasts and 10% white, amorphous, ameboid shaped, powdery clasts. There are multiple cm scale basement-like clast with dark brown-green alteration rims. The material is highly friable and is covered in a rubber casing.
283.5-283.6	Coase sandstone	The material appears to be mostly comprised of sand with some influences of suevite in the composition of the polymict mm scale clasts that appear often only marginally larger than the matrix material. The matrix is comprised of a light grey-brown fine sand. The sub-mm scale polymict clasts have a roughly 40% surface area coverage and are

---

comprised of 50% white powdery, angular to sub-angular flecks, 30% powder rounded black flecks, 5% mm scale angular biotite, 10% red, weathered (?) Fe-oxide clasts and 5% angular K-spar

---

283.6-284.4	Coarse sandstone / conglomerate	Massive light grey toned claystone with no visible clasts or bedding - except for very rare metallic flecks - possibly mica. The core has a rubber casing and appears to be moderately friable.
284.4-284.75	Massive siltstone	Massive light grey toned siltstone with no bedding or clasts other than rare mm scale ameboid shaped, white amorphous material
284.75-285.60	Type 1 gravelstone	Mostly comprised of sand with some influences of suevite in the composition of the polymict mm scale clasts with rare cm scale basement derived clasts with a green overprint and brown rim. The matrix is comprised of a light grey-brown fine sand. The sub-mm scale polymict clasts have a roughly 40% surface area coverage and are comprised of 50% white powdery, angular to sub-angular flecks, 30% powder rounded black flecks, 5% mm scale angular biotite, 10% red, weathered (?) Fe-oxide clasts and 5% angular K-spar
285.60-285.70	Fine sandstone / conglomerate	Massive light grey toned sandstone with no bedding or grading, but does contain polymict clasts ranging in size with two dominant compositions. Sizes range from sub-

---

mm to cm scale with the two compositions being white amorphous material and reddish-brown oxidized material.

---

285.70-286.40	Type 1 gravelstone	Mostly comprised of sand with some influences of suevite in the composition of the polymict mm scale clasts with rare cm scale basement derived clasts with a green overprint and brown rim. The matrix is comprised of a light grey-brown fine sand. The sub-mm scale polymict clasts have a roughly 40% surface area coverage and are comprised of 50% white powdery, angular to sub-angular flecks, 30% powder rounded black flecks, 5% mm scale angular biotite, 10% red, weathered (?) Fe-oxide clasts and 5% angular K-spar
<hr/>		
286.4-287	Massive sandstone	Massive light grey toned sandstone with no bedding or clasts other than rare mm scale ameboid shaped, white amorphous material
<hr/>		
287-287.30	Type 1 gravelstone / conglomerate	Suevite-like material with a blue-grey toned, clay matrix with a 50% clast coverage comprised of polymict clasts with a range of compositions and sizes. 25% cm scale, subrounded basement clast with light green overprint and no brown rim, 35% ameboid shaped white, cm and mm scale, powdery clasts, 15% cm scale, angular basement clasts with no overprint or rim, 10% dark black biotite flecks, 5% angular mm scale K-spar, 10% angular Fe-oxides

287.30-288.4	Massive siltstone	Massive light grey toned siltstone with no bedding or clasts other than rare mm scale ameboid shaped, white amorphous material
288.4-288.55	Massive siltstone	Massive grey toned siltstone with no bedding or clasts other than rare mm scale ameboid shaped, white amorphous material *** It may have some bedding that is exaggerated by the coating on the core, which may imply it has some undulating laminations or possible ripples (?)*** difficult to say.
288.55-289.9	Type 1 gravelstone / conglomerate	The material appears to be mostly comprised of sand with some influences of suevite in the composition of the polymict mm scale clasts with rare cm scale basement derived clasts with a green overprint and brown rim. The matrix is comprised of a light grey-brown fine sand. The sub-mm scale polymict clasts have a roughly 40% surface area coverage and are comprised of 50% white powdery, angular to sub-angular flecks, 30% powder rounded black flecks, 5% mm scale angular biotite, 10% red, weathered (?) Fe-oxide clasts and 5% angular K-spar
289.9-290	Type 2 conglomerate	Coarse, green-grey silty-clay matrix with 65% mm scale rounded to sub-angular white and 35% black clasts with

the same clast morphology like a pervasively altered crater-fill suevite. The green tone may be due to alteration.

---

290-290.2	Sandy siltstone	Moderately friable, light grey, sandy siltstone with abundant sub-mm scale black and white (45%/45%) rounded to sub-angular clasts and 10% sub-mm scale Fe-oxides
290.2-293.2	Type 1 gravelstone / type 2 conglomerate	Coarse, green-grey silty-clay matrix with 65% mm scale rounded to sub-angular white and 35% black clasts with the same clast similar morphology to that of a pervasively altered crater-fill suevite. The green tone may be due to alteration.
293.2-296.0	Massive siltstone with mm pyrite	Massive, light-grey clay-siltstone with abundant white, sub-mm, angular to rounded powdery spots - same material also observed filling a sub-mm wide fracture extending for ~4cm across the width of the core. Abundant (and only occurrence) black, ameboid clasts (pyrite) with a sharp boundary between the clast and the matrix.
296.0-298.3	Weathered type 1 conglomerate	Friable and crumbly material reminiscent of suevite. The matrix is a light blue-grey clay. There are white clasts with red-brown alteration rims and a greenish overprint suggesting that they were once the lithic basement derived clasts documented previously but have since been broken down and have become crumbly.

---

---

298.3-298.5	Type 1 gravelstone	Light grey, sandy silt matrix with 40% clast coverage of the surface area. Clasts are mm scale with some reaching low cm scale. Compositions include: 50% white amorphous material, 20% black angular to sub-rounded clasts rarely occurring with green-brown overprints, 25% angular, lithic clasts, 5% angular K-spar
-------------	-----------------------	---

---

298.5-300	Type 2 conglomerate	Darkish grey clay-silt matrix with 30% clast coverage of the surface area on mm to low cm scales. Compositions include: 30% white amorphous material, 25% black angular to sub-rounded clasts commonly occurring with green-brown overprints, 30% angular, lithic clasts, 15% ameboid, black, glassy clasts
-----------	------------------------	---

---

300-300.4	Coarse type 1 conglomerate	Light grey toned, clay matrix suevite with 30% clast coverage - mostly due to the few large 2-5cm wide clasts as there are a relatively small amount of mm to sub-mm scale clasts. The cm scale clasts consist of 50% unaltered gneissic clasts and 30% 2cm sized, heavily altered gneissic clasts with a green overprint and a brown-orange alteration rim - some are completely overprinted with Fe-oxides, whereas others (20%) consist of a white amorphous powdery material. The sub-mm scale clasts consist of 50% white angular to sub-rounded, amorphous, white powdery
-----------	-------------------------------	---

clasts, 25% black, powdery sub-rounded clasts, and 25% lithic clasts containing some K-spar and possibly gneiss

---

300.4-310      Pervasively altered type 2 conglomerate      Darkish green-grey clay-silt matrix with 30% clast coverage of the surface area on mm to low cm scales. Compositions include: 30% white amorphous ameboid clasts, 15% black angular to sub-rounded clasts, 40% angular, lithic clasts commonly occurring with green-brown overprints and sometimes almost completely weathered out, 15% angular, harder than nail, black clasts with sub-mm scale subhedral K-spar and calcite - these were probably present in other similar rocks but were not noticed in hand sample - picture: 20170630\_030534\_1

---

310-311      Massive sandstone      Massive sandstone with a light grey clay sand matrix. The clasts exclusively consist of angular to subrounded, sometimes ameboid shaped, powdery white clasts of amorphous material. There are abundant sub-mm scale tiny black specs that could be micas and faint, wavy, reddish-brown oxidation features visible on the side of the core that appear to be associated with a concentration of the white clasts with coarser material.

---

311-311.5      Pervasively altered type 2 conglomerate      Grey clay-silt matrix with 30% clast coverage of the surface area on mm to low cm scales. Compositions include: 15% white amorphous angular to sub-rounded clasts, 15% black angular to sub-rounded clasts, 55%

angular, lithic clasts usually occurring with green-brown overprints and sometimes almost completely weathered out, 15% angular, harder than nail, black clasts with sub-mm scale subhedral K-spar and calcite.

---

311.5-316 Top of the graded unit (314 -331 m)	Massive siltstone with ameboid (white) sandy clasts (?)	White-brown sandy-silt material with bright micaceous flecks <1mm across. There is a prominent, white sedimentary clasts with irregular shapes and sharp contacts with the matrix material. These clasts appear to have very faint undulating layering conforming lengthwise.
316-316.3	Pervasively altered breccia	Grey clay-silt matrix with 30% clast coverage of the surface area on mm to low cm scales. Compositions include: 15% white amorphous angular to sub-rounded clasts, 15% black angular to sub-rounded clasts, 55% angular, lithic clasts usually occurring with green-brown overprints and sometimes almost completely weathered out, 15% angular, harder than nail, black clasts with sub-mm scale subhedral K-spar and calcite
316.3-318	Massive siltstone with ameboid (red) sandy clasts (?)	Somewhat friable sandstone with a light grey clay sand matrix. There are no visible clasts or layering, but there are abundant sub-mm scale tiny black specs that could be micas and faint, wavy, reddish-brown oxidation features visible on the side of the core and on the cut face
318-318.5	Massive silt-sand matrix	Grey silt-sand matrix with 30% clast coverage of the surface area on mm to low cm scales. Compositions include: 15% white amorphous angular to sub-rounded clasts, 15% black angular to sub-rounded clasts , 55% angular, lithic clasts usually occurring with green-brown

overprints and sometimes almost completely weathered out, 15% angular, harder than nail, black clasts with sub-mm scale subhedral K-spar and calcite

---

318.5-318.9      Cross laminated (?) fine sandstone      Somewhat friable, light grey, medium sandstone with a light grey clay sand matrix. There are no visible clasts or layering, but there are abundant sub-mm scale tiny black specs that could be micas as well as similarly sized and shaped white specs.

---

318.9-319.4      Fine sandstone / shale?      Sharp contact between an unpreserved shale unit and the sandstone\* The shale is blue-grey with only minor parallel laminations with slight undulations visible in hand sample. The sandstone is medium grained, somewhat friable, light grey, sandstone and has a light grey clay sand matrix. There are rare mm scale sub-angular clasts of what amorphous material and faint parallel lamination.

---

319.4-320      Medium sandstone      Somewhat friable, **light grey-green**, medium sandstone with a light grey clay sand matrix. There are no visible clasts or layering, but there are abundant sub-mm scale tiny black specs that could be micas as well as similarly sized and shaped white specs.

---

320-322      Medium sandstone      Coarse, friable, clast-rich sandstone with abundant sub-mm to mm scale clasts and rare cm scale clasts. The sub-mm to mm clasts are by total surface area coverage comprised of

50% white, angular to sub-rounded, powdery material, 35% black, angular to sub-angular, flaky clasts (possibly biotite in some cases), 10% white and black, angular, powdery remnants of the shocked basement and 5% angular K-spar grains. The cm scale clasts are comprised of 70% altered black clasts with prominent green and brown alteration rims, and 30% white, angular powdery casts - possibly remnants of the shocked basement.

---

322-322.1      Conglomerate      Coarse, green-toned, suevite like gravelstone / fine matrix supported conglomerate. Pink-grey, silty clay matrix. The 30% surface area coverage of polymict clasts and pink-grey / yellow-grey color.

The clasts size ranges from mm to cm scale with 60% of the clasts on a mm scale and 40% on a cm scale. The mm scale clasts are comprised of mostly angular to sub-rounded white powdery clasts that mostly appear to be derived from the larger lithic clasts. Some look completely made up of K-spar in some cases and biotite in others (both with angular habits and occurring infrequently with biotite occurring the least frequently. The cm scale clasts are mainly shocked, lithic clasts derived from basement material and in some cases are completely altered out. Most have a dark brown alteration rim. The other cm scale clasts are either comprised of a white amorphous powder or a dark, black powdery material.

---

322.1-323.0	Coarse sandstone	Coarse, friable, <b>light brown</b> , clast-rich sandstone with abundant sub-mm to mm scale clasts and rare cm scale clasts. The sub-mm to mm clasts are by total surface area coverage comprised of 50% white, angular to sub-rounded, powdery material, 35% black, angular to sub-angular, flaky clasts (possibly biotite in some cases), 10% white and black, angular, powdery remnants of the shocked basement and 5% angular K-spar grains. The cm scale clasts are comprised of 70% altered black clasts with prominent green and brown alteration rims, and 30% white, angular powdery casts - possibly remnants of the shocked basement or linked to de-gassing pipes
-------------	------------------	---

---

323.0-324	Coarse sandstone	Coarse, friable, <b>green-light brown</b> , clast-rich sandstone with abundant sub-mm to mm scale clasts and rare cm scale clasts. The sub-mm to mm clasts are by total surface area coverage comprised of 50% white, angular to sub-rounded, powdery material, 35% black, angular to sub-angular, flaky clasts (possibly biotite in some cases), 10% white and black, angular, powdery remnants of the shocked basement and 5% angular K-spar grains. No significant clasts with alteration rims.
-----------	------------------	--

---

324-325.2	Coarse gravelstone	Coarse, green-blue clay matrix with 65% mm scale rounded to sub-angular white and 30% black clasts with
-----------	--------------------	---

the same clast morphology and 5% angular, K-spar clasts, like a pervasively altered crater-fill suevite. The green tone in previous samples was attributed mainly to the matrix, but in this case the matrix appears to be more blue, suggesting the green tone maybe a result of the high overall clast content - each with varying degrees of alteration.

---

325.2-326	Pervasively altered conglomerate / coarse gravelstone	Light, brown-grey toned suevite with common cm scale dark-brown altered clasts and some angular green-black clasts. Some K-spar appears to be present in the lithic - basement like clasts - most of the brown, altered clasts are completely weathered out.
<hr/>		
326-328.2	Pervasively altered conglomerate	Dark-brown-green weathered suevite. The matrix is amorphous - clay-like and has a fluid appearance. There is an approximate clast coverage of 60% with a range of 20% sub-mm scale to 40% cm scale clasts. Sub-mm clast composition: 45% lithic clasts with varying % compositions of K-spar, pyroxenes and Hbl, 30% powdery, irregularly shaped - sometimes squiggly, white amorphous material. 25% black clasts - difficult to tell whether glassy or mica at this scale  The cm scale clasts have varying degrees of alterations with a brown-green overprint - most appear to be gneissic-granitic in composition with varying amounts of K-spar, pyroxenes and Hbl

---

328.2-329.4	Pervasively altered conglomerate	Dark-brown-green weathered suevite - same overall composition, but this section has a significantly higher %cm scale clasts (70%)
329.4-330	Pervasively altered conglomerate	Clay-rich grey-brown matrix with several heavily altered and overprinted clasts - the clasts and matrix are a roughly uniform colour. Rare well rounded clasts in contact without surrounding fines - may be related to the degassing pipe documented previously.
330-332	Coarse conglomerate	Dark-brown-green weathered suevite - same overall composition, but this section has a significantly higher %cm scale clasts (70%)
332-334	Melt-bearing breccia (crater-fill suevite)	Light, brown-grey toned suevite with common cm scale dark-brown altered clasts and some angular green-black clasts. Some K-spar appears to be present in the lithic - basement like clasts - most of the brown, altered clasts are completely weathered out.
334-334.6	Melt-bearing breccia (crater-fill suevite)	Dark-brown-green weathered suevite. The matrix is amorphous - clay-like and has a fluid appearance. There is an approximate clast coverage of 60% with a range of 20% sub-mm scale to 40% cm scale clasts. Sub-mm clast composition: 45% lithic clasts with varying %compositions of K-spar, pyroxenes and Hbl, 30% powdery, irregularly shaped - sometimes squiggly, white amorphous material. 25% black clasts - difficult to tell whether glassy or mica at this scale

---

The cm scale clasts have varying degrees of alterations with a brown-green overprint - most appear to be gneissic-granitic in composition with varying amounts of K-spar, pyroxenes and Hbl

---

## Appendix C: Preliminary $\mu$ XRD results and In-Situ X-Ray Diffraction (ISXRD) Research Contributions.

Appendix C contains the sample descriptions submitted in contribution to the “In-situ X-ray diffraction (ISXRD) for exploring mineralogy and geology of Mars” research project (Flemming et al., 2020). Current contributions comprise samples obtained from the Wörnitzostheim drill core sampled from just beyond the edge of the Ries central basin. The samples contributed for this study and preliminary results, where possible, are summarized below.

### *Appendix C.1: Pink-toned melt-bearing breccia (Unit 15)*

Sample Name: RW32

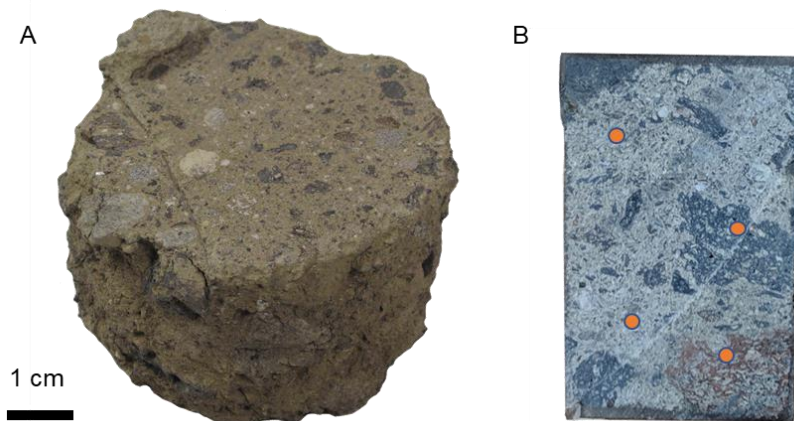


**Figure. C.1.1:** (A) Core sample of impact melt-bearing breccia from a depth of approximately 32 m in the Wörnitzostheim drill core. (B) Spots are selected from a thin section offcut of RW32 for clay-rich matrix, and different types of glass.

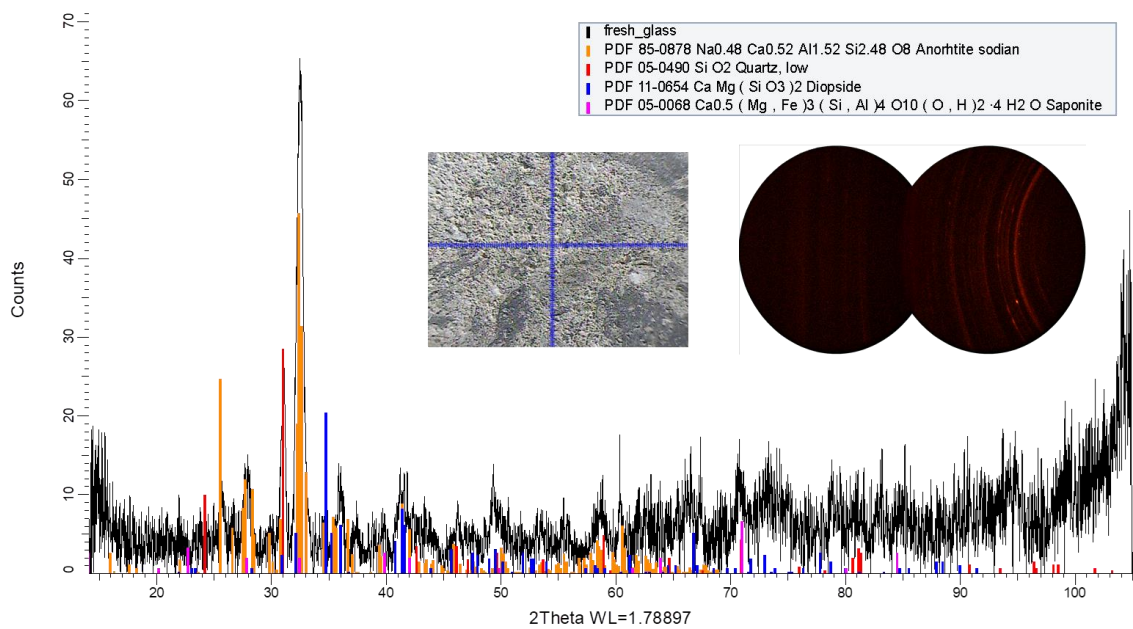


**Figure. C.1.2:**  $\mu$ XRD diffraction pattern with shown with a context image of the “Matrix 1” target material from RW32 and the accompanying GADDS image. Phase identification as shown was conducted using the peak-match function in the *DIFFRAC.EVA* software package using the International Center for Diffraction Data (ICDD) mineral database. Estimation of clay mineral phases here were used as a guide and not were intended for full clay mineral identification.

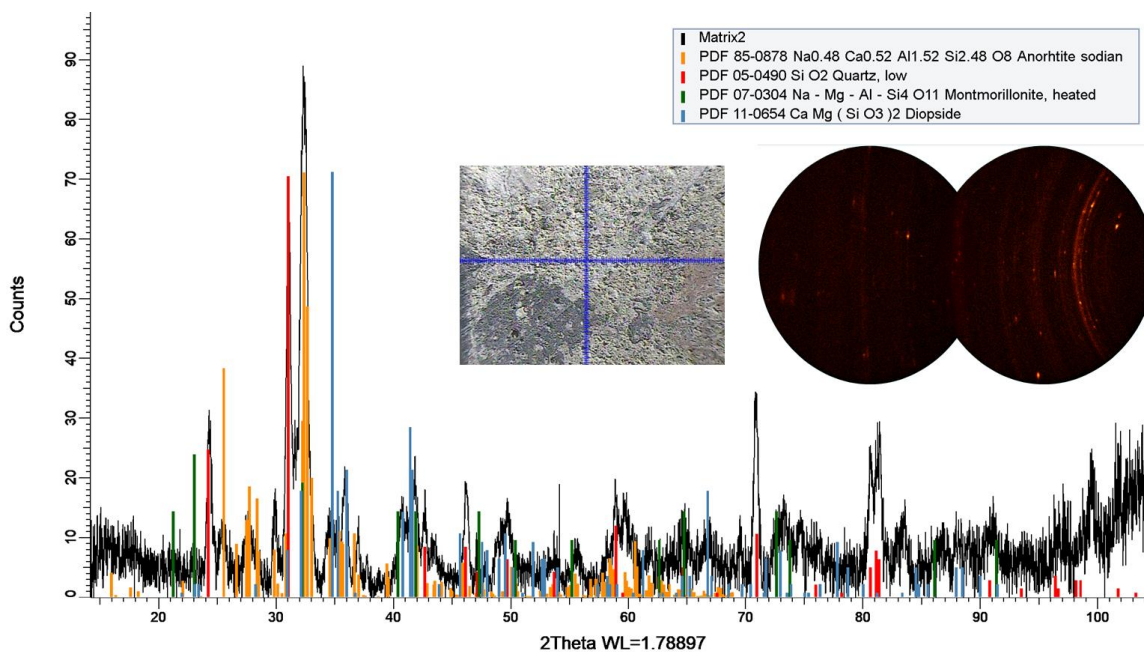


**Figure. C.1.3:**  $\mu$ XRD diffraction pattern with shown with a context image of the “Matrix 2” target material from RW32 and the accompanying GADDS image. Phase identification as shown was conducted using the peak-match function in the *DIFFRAC.EVA* software package using the International Center for Diffraction Data (ICDD) mineral database. Estimation of clay mineral phases here were used as a guide and not were intended for full clay mineral identification.

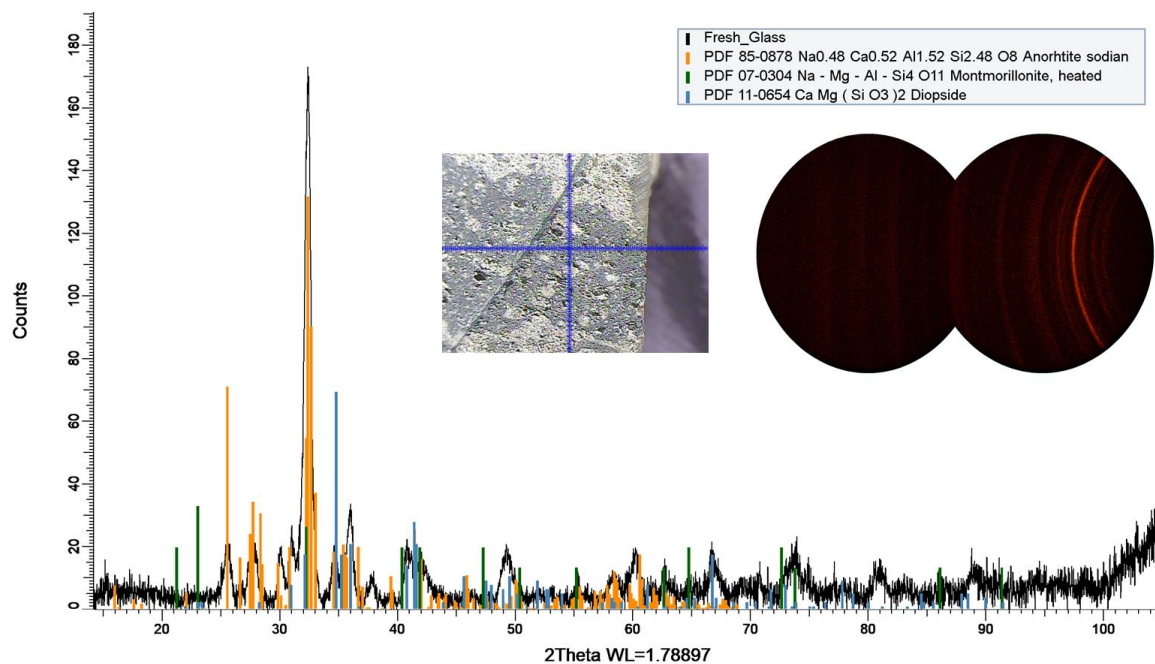


**Figure. C.1.4:**  $\mu$ XRD diffraction pattern with shown with a context image of the “Black Glass” target material from RW 32 and the accompanying GADDS image. Phase identification as shown was conducted using the peak-match function in the *DIFFRAC.EVA* software package using the International Center for Diffraction Data (ICDD) mineral database. Estimation of clay mineral phases here were used as a guide and not were intended for full clay mineral identification.

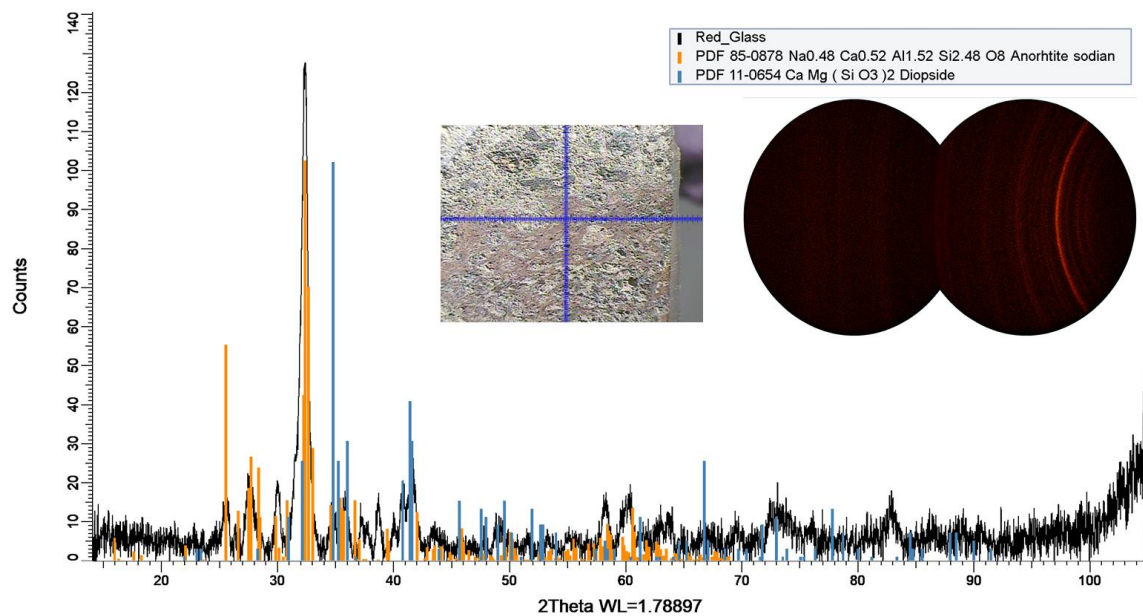


**Figure. C.1.5:**  $\mu$ XRD diffraction pattern with shown with a context image of the “Red Glass” target material from RW32 and the accompanying GADDS image. Phase identification as shown was conducted using the peak-match function in the *DIFFRAC.EVA* software package using the International Center for Diffraction Data (ICDD) mineral database. Estimation of clay mineral phases here were used as a guide and not were intended for full clay mineral identification.

*Appendix C.2: Grey-toned melt-bearing breccia (Unit 14)*

Sample Name: RW22



**Figure. C.2.1:** (A) Core sample of impact melt-bearing breccia from a depth of approximately 22 m in the Wörnitzostheim drill core. (B) Spots are selected from a thin section offcut of RW22 for clay-rich matrix, and impact glass. Phase identification as shown was conducted using the peak-match function in the *DIFFRAC.EVA* software package using the International Center for Diffraction Data (ICDD) mineral database. Estimation of clay mineral phases here were used as a guide and not were intended for full clay mineral identification.

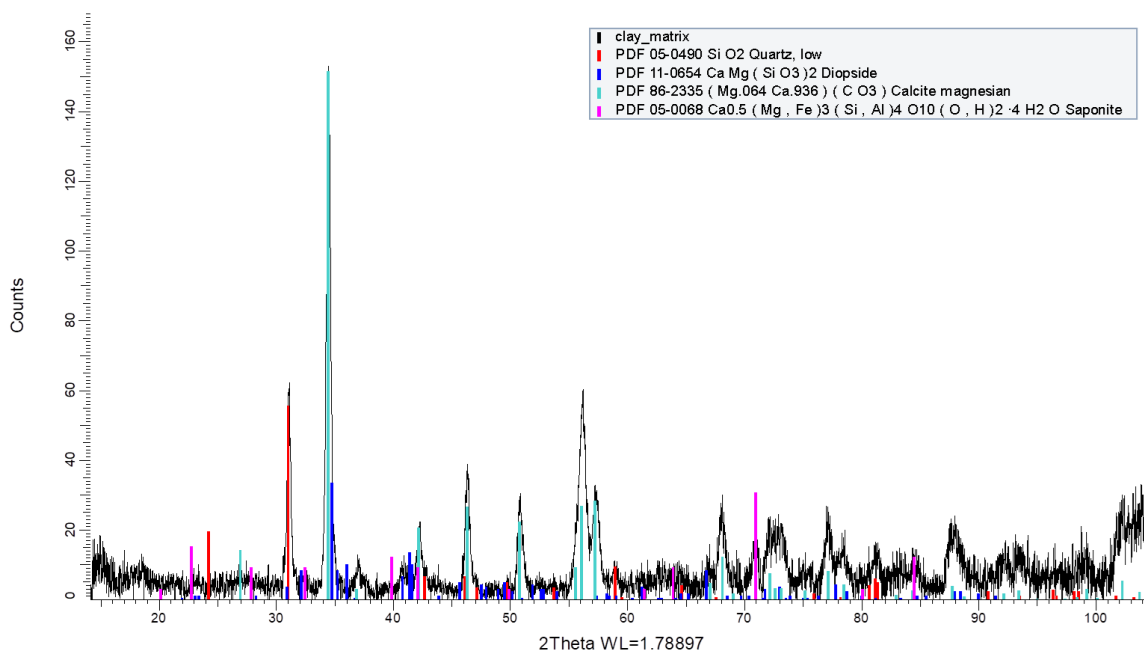


**Figure. C.2.2:**  $\mu$ XRD diffraction pattern with shown with a context image of the “Matrix” target material from RW22 and the accompanying GADDS image Phase identification as shown was conducted using the peak-match function in the *DIFFRAC.EVA* software package using the International Center for Diffraction Data (ICDD) mineral database. Estimation of clay mineral phases here were used as a guide and not were intended for full clay mineral identification.

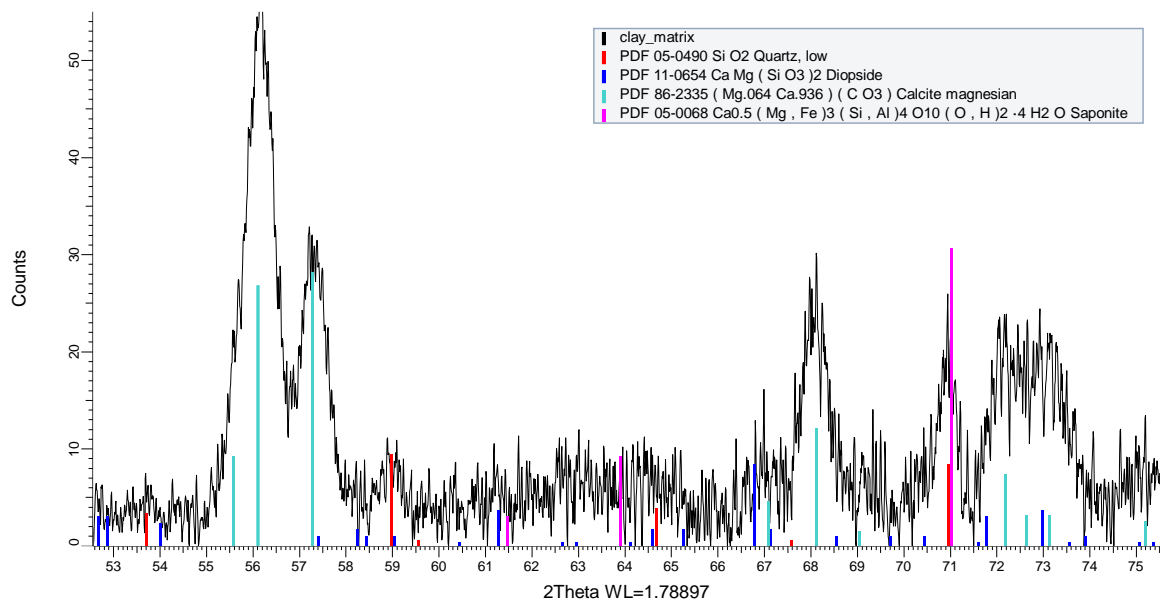


**Figure. C.2.3:**  $\mu$ XRD diffraction pattern shown in Fig. C.2,2 with a focus on the 52–76  $^{\circ}2\theta$  range to highlight possible d(060) reflections from clay minerals in the target (RW22). Results are consistent with dioctahedral smectitic clay minerals. Phase identification as shown was conducted using the peak-match function in the *DIFFRAC.EVA* software package using the International Center for Diffraction Data (ICDD) mineral database. Estimation of clay mineral phases here were used as a guide and not were intended for full clay mineral identification.

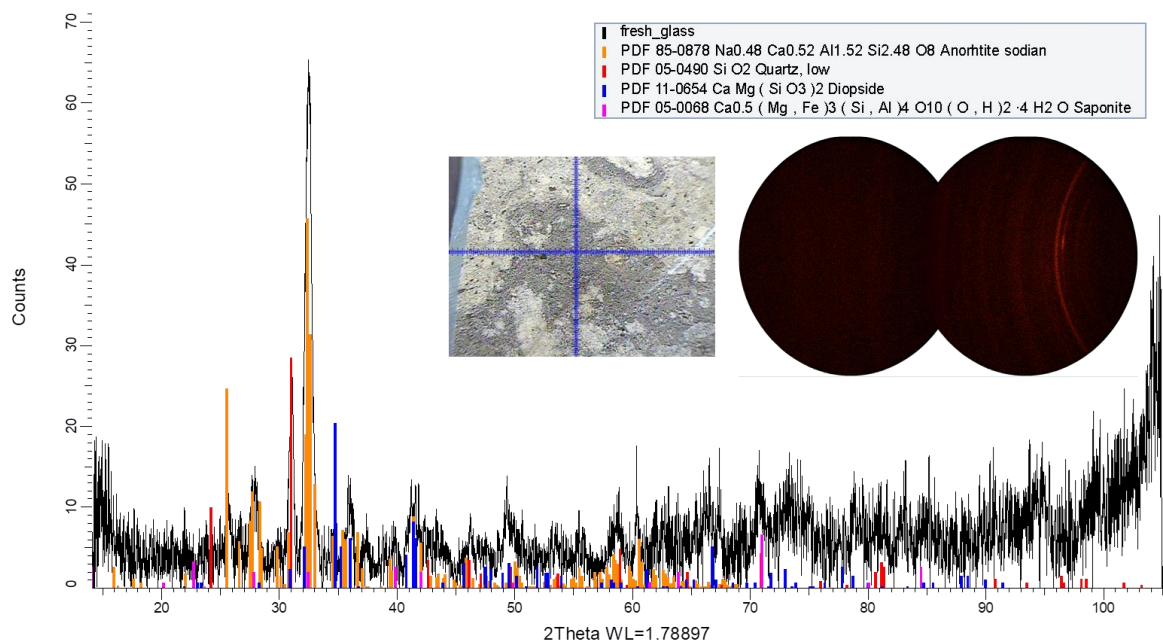


**Figure. C.2.4:**  $\mu$ XRD diffraction pattern with shown with a context image of the “Glass 1” target material from RW 32 and the accompanying GADDS image. Phase identification as shown was conducted using the peak-match function in the *DIFFRAC.EVA* software package using the International Center for Diffraction Data (ICDD) mineral database. Estimation of clay mineral phases here were used as a guide and not were intended for full clay mineral identification.

*Appendix C.3: Weathered breccia (Unit 13)*

Sample Name: RW19

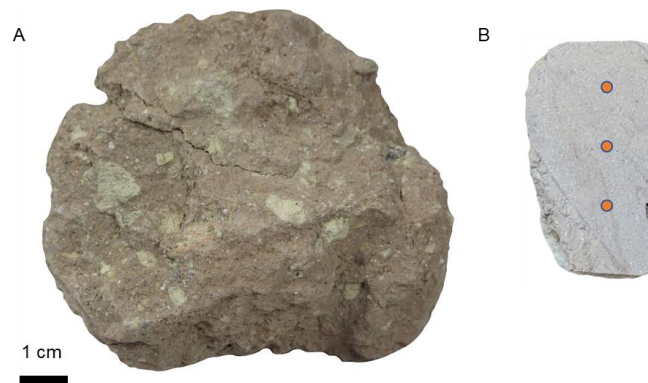


**Fig. C.3.1:** (A) Core sample of weathered breccia from a depth of approximately 19 m in the Wörnitzostheim drill core. (B) Spots are selected from a thin section offcut of RW19 for clay-rich matrix.

*Appendix C.4: Conglomerate (Unit 11)*

Sample Name: RW16.16

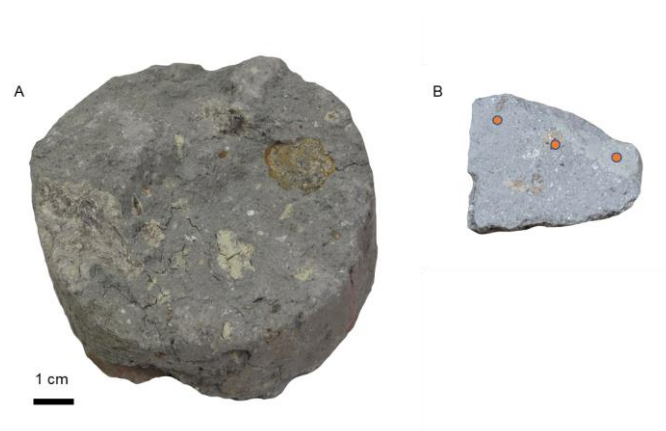


**Fig. C.4.1:** (A) Core sample of weathered breccia from a depth of approximately 16.2 m in the Wörnitzostheim drill core. (B) Spots are selected from a thin section offcut of RW16.16 for clay-rich matrix.

*Appendix C.5: Conglomerate (Unit 11, Fig. C,1)*

Sample Name: RW14.33

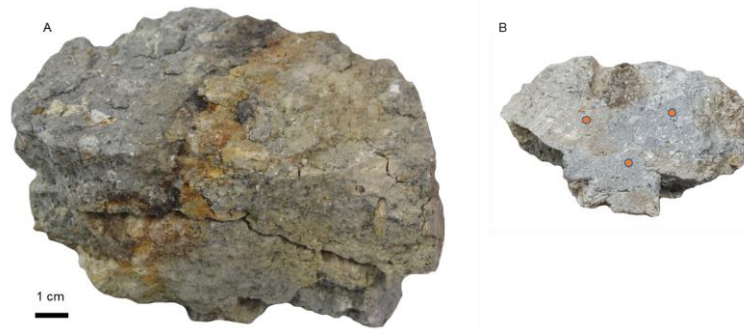


**Fig. C.5.1:** (A) Core sample of weathered breccia from a depth of approximately 14.3 m in the Wörnitzostheim drill core. (B) Spots are selected from a thin section offcut of RW14.33 for clay-rich matrix.

# Curriculum Vitae

**Name:** Matthew Svensson

**Discipline:** Earth Sciences

## Academics & Education

---

**Ph.D. Geology with Planetary Science** (2022) | The University of Western Ontario

Ph.D. Thesis (Dr. G. R. Osinski & Dr. F. J. Longstaffe): Process and Products of Impact Crater Lakes: A Case Study of the Ries Impact Structure, Germany.

**H.B.Sc. Geology** (2016) | Lakehead University

H.B.Sc. Thesis (Dr. S. A. Kissin): Source of Native Iron in Canadian Arctic Artifacts

## Work Experience

---

**The University of Western Ontario (Department of Earth Sciences) | 2016/09 - Present**

Graduate Research Assistant | Dept. of Earth Sciences / The Institute for Earth and Space Exploration

Teaching Assistant | Remote Sensing and Image Analysis; Geology for Engineers; Exploring the Planets; Catastrophic Events in Earth's History

Building Safety Ambassador | Health and Safety (2021/09 – 2022/05)

Conference Tech Support | Science - Office of the Dean (2020/08)

**PSAC Student Union**

Financial Advisory Committee | Financial support application assessment 2018/09 – 2019/05)

**Lakehead University (Geology Department)**

Undergraduate Research Assistant (Dr. P. Fralick): The Badwater Gabbro as an Analogue for the Weathering of Martian Basalts (2015/05 – 2016/05)

Peer Tutor | Geochemistry (2015/01 – 2015/04)

## Mission Experience

---

**STRATOS: CSA's Stratospheric Balloon Program** | *Western U. HAB Project Manager* (2019/09)

The STRATOS program is a collaboration between France's space agency (CNES) and the Canadian Space Agency (CSA). Academic and commercial experiments were launched from the CSA's stratospheric balloon base in Timmins, Ontario via weather balloon up to altitudes of 30+ km to conduct scientific experiments and test instrument and balloon-based drone functionality.

- *Duties:* Lead the flight-critical members of Western's High-Altitude Balloon (HAB) team in their mission to sample microbial aerosols along a transect through the troposphere and stratosphere. Arrange for transportation, facility access, and laboratory / equipment access. Resolve budgeting and timeline conflicts as necessary. Serve as the main point of contact between the Western HAB team and the CSA.

**CanMoon Lunar Analogue Mission** | *Field Team Instrument Operator / LIBS Specialist* (2019/08)

The CanMoon Lunar Analogue Mission is a collaboration between Western University, The University of Winnipeg and the CSA, which simulates a rover-based, sample-return mission to the Moon. The field team, stationed in Lanzarote, Spain, acted as the rover, executing commands issued from Western University.

- *Duties:* Construct a makeshift rover-body and utilize field portable Raman, VNIR, LIBS and cameras to carry out commands within the "rover's" pre-defined operating limits. Mitigate potential simulation interruptions and assure data quality.

**In-Situ XRD Concept Study for the Exploration of Mars** | *Student Collaborator* (2019/01 – Present)

The In-Situ XRD (ISXRD) Concept Study is focused on the use of XRD for analyzing rocks with minimum sample preparation. The ISXRD project aims to demonstrate the utility of XRD for rover-based exploration of the Martian surface.

- *Duties:* Advise on the selection of appropriate Mars analogue material pertaining to meteorite-impact-generated rocks and clay minerals. Assist with sample analyses and interpretation.

**CanMars Mars Sample Return (MSR) Analogue Mission | LIBS Science Team Lead (2016/07)**

The CanMars MSR Analogue Mission is a multi-university and space agency collaboration involving CSA, NASA, UKSA, Western University and other universities designed to simulate a rover-based sample return mission to Mars. An approximate replica of the Curiosity Rover was deployed to an undisclosed Mars analogue site in Utah, USA. The rover, tended by a field team, received commands from mission control at Western University and returned data to be interpreted by specialized teams.

- *Duties:* Present geochemical findings from the LIBS spectrometer and resolve calibration conflicts through cooperation with the field team and device manufacturer.

## Leadership & Project Management

---

**Projects Liaison | Western Space Graduate Student Council (2020/09 – 2021/08)**

Facilitate communication between the Western Space Graduate Student Council and collaborative research initiatives such as the Western Cube-Sat Team and High-Altitude Balloon Initiatives.

**Project Adviser | Western Undergraduate Balloon Team (2020/01 – 2021/08)**

Advise the team leaders (project manager, and science, engineering and outreach leads). Provide guidance and assistance as necessary to ensure the success of the next generation of interdisciplinary student projects.

**Earth Science Rep. | Western Space Graduate Student Council (2019/09 – 2020/08)**

Represent the interests of Earth Science students involved in the activities of the Institute for Earth and Space Exploration to the institute's graduate student council.

**President | Western Space Graduate Student Council (2018/09 – 2019/08; 2021/01 – 2021/08)**

Lead the graduate student council and represent the interests and concerns of all graduate students involved with the Institute for Earth and Space Exploration to the faculty members of the Research Advisory Council.

**Project Manager / Co-Founder | Western University HAB Initiative (2017/12 – 2021/08)**

Lead the senior executive team (science, engineering and outreach team leads) of the Western University High Altitude Balloon (HAB) Initiative. Develop the mission objectives and direction with respect to science, engineering and outreach. Write proposals to generate capital. Allocate capital to project priorities. Oversee project execution while adhering to a strict budget and timeline.

**Vice President | Institute for Earth and Space Exploration Graduate Council (2017/09 – 2018/08)**

Support and advise the president of the graduate student council. Substitute for the president as needed; representing the interests of current graduate students at meetings of the faculty executive council.

## Awards and Distinctions

---

Invited Student Trainee | Canadian Institute for Advanced Research, CIFAR (2022/11)  
Western News, Newsmakers of the Year | Western University (2019)  
Postgraduate Scholarships Doctoral Program (PGS-D) - \$63,000 (CAD) | Natural Sciences and Engineering Research Council of Canada (NSERC) (2019/09 – 2021/09)  
CAN-SBX Travel Grant - \$2,500 | Canadian Space Agency (2019/08)  
Queen Elizabeth II / Ontario Graduate Scholarship (OGS) - \$15,000 (CAD) | Province of Ontario / Western University (2017/09 – 2018/08; 2018/09 – 2019/08)  
Institute for Earth and Space Exploration Volunteer Award (2017/05)  
Global Opportunities Award - \$1,000 (CAD) | Western University (2017/05)  
Eisenbrey Student Travel Award - \$100 (CAD) | Institute of Lake Superior Geology (2016/05)  
Astromaterials Training and Research Opportunity Undergraduate Research Award (ASTRO) - \$5,000 (CAD) | Canadian Space Agency (2015/05 – 2015/08)  
Dean's List | Lakehead University (2014/09 – 2016/05)

## Articles in Peer-Reviewed Journals

---

- [4] **Svensson M. J. O.**, Kissin S. A., et al. 2019. A method for determination of the source of iron in Thule Inuit and Dorset culture artifacts from the Canadian Arctic. *Journal of Archaeological Science*. (Published; Accepted 15/01/2020; 22 pages).
- [3] Caudill C. M., Pontefract A. J., Osinski G. R., Tornabene L. L., Pilles E. A., Battler M., Francis R., Godin E., Galofore A. G., Hlatigin T., Hipkin V. J., Mittelholz A., Poitras J., Simpson S. L., **Svensson M. J. O.**, Xie T., Morse Z. R. 2019. CanMars mission Science Team operational results: Implications for operations and the sample selection process for Mars Sample Return (MSR). *Planetary and Space Science*. 172: 43–56. (Published; Accepted 04/13/2019; 13 pages).
- [2] Osinski G. R., Battler M., Caudill C. M., Francis R., Hlatigin T., Hipkin V. J., Kerrigan M., Pilles E. A., Pontefract A., Tornabene L. L., ... **Svensson M. J. O.** et al. 2018. The CanMars Mars Sample Return Analogue Mission. *Planetary and Space Science*. (Published; Accepted 24/07/2018; 21 pages).
- [1] Caudill C. M., Pontefract A., Osinski G. R., Tornabene L. L., Pilles E., Battler M., Francis R., Godin E., Grau. A., Hlatigin T., Hipkin V., Mittelholz A., Poitras J., Simpson S. L., **Svensson M. J. O.**, Xie T. 2018 CanMars Science Results and Review of Optimization for Sample Selection for Mars Sample Return (MSR) based on Science Operations and Procedures. *Planetary and Space Science*. (Published; Accepted 05/30/2019; 51 pages).

## Conference Publications

---

- [27] **Svensson M. J. O.\***, Osinski G. R., Caudill C. M., Goudge. T. A., Longstaffe F. J., Sapers H. M., Tornabene. L. L. 2022. Insights into clay mineral formation on Mars from the Ries impact structure, Germany, and implications for the exploration of Jezero Crater and Oxia Planum. COSPAR 2022, 44<sup>th</sup> Scientific Assembly. Abstract # 31516. (International Conference; Research Group; Oral).
- [26] Flemming R. L.\*, Sabarinathan J., Pilles E. A., Veinberg L., McCausland P. J. A., McIssac K. A., Osinski G. R., Tornabene L. L., Schmidt M. E., Gellert R., McCraig M. A. ... **Svensson M. J. O.** et al. 2021. In-situ X-ray diffraction (ISXRD) for exploring mineralogy and geology of Mars. *Canadian Space Exploration Workshop – 2022*. (National Conference; Research Group; Poster).
- [25] **Svensson M. J. O.\***, Osinski G. R., Goudge. T. A., Longstaffe F. J., Tornabene. L. L. 2022. The Ries impact structure as an analogue for Jezero Crater's marginal carbonates. *Canadian Space Exploration Workshop*. (National Conference; Ph.D. Thesis; Poster).

- [24] **Svensson M. J. O.\***, Osinski G. R., Longstaffe F. J., Sapers H. M., 2022. Determining the Origin of Framboidal Pyrite in Early Post-Impact Sedimentary Deposits at the Ries Impact Structure, Germany. *AbSciCon. – AGU – 2022. Abstract # 1031810* (International Conference; Ph.D. Thesis; Poster).
- [23] Flemming R. L.\*, Sabarinathan J., Pilles E. A., Veinberg L., McCausland P. J. A., McIssac K. A., Osinski G. R., Tornabene L. L., Schmidt M. E., Gellert R., McCraig M. A. ... **Svensson M. J. O.** et al. 2021. In-situ X-ray diffraction (ISXRD) for exploring mineralogy and geology of Mars. *Geological Association of Canada / Mineralogical Association of Canada (GAC/MAC) – 2021.* (National Conference; Research Group; Oral).
- [22] **Svensson M. J. O.\***, Osinski G. R., Caudill C. M., Goudge. T. A., Longstaffe F. J., Sapers H. M., Tornabene. L. L. 2021. The Ries impact structure, Germany: Insight into the role of impact cratering in forming clay minerals on Mars. *Workshop on Terrestrial Analogues for Planetary Exploration.* (International Conference; Ph.D. Thesis; Oral).
- [21] **Svensson M. J. O.\***, Osinski G. R., Goudge. T. A., Longstaffe F. J., Tornabene. L. L. 2021. The Ries impact structure as an analogue for Jezero Crater’s marginal carbonates. *Workshop on Terrestrial Analogues for Planetary Exploration.* (International Conference; Ph.D. Thesis; Poster).
- [20] **Svensson M. J. O.\***, Osinski G. R., Longstaffe F. J., 2021. Revisiting the origin of the Ries graded suevite: implications for plume fallback preservation. *Lunar and Planetary Science Conference LIII*, Abstract #2478. (International Conference; Ph.D. Thesis; Poster).
- [19] **Svensson M. J. O.\***, Osinski G. R., Longstaffe F. J., 2020. Secondary mineralization along the impactite – lake deposit transition in the Nördlingen 1973 drill core, Ries impact structure, Germany. *Lunar and Planetary Science Conference LI*, Abstract #3072. (International Conference; Ph.D. Thesis; Poster).
- [18] Flemming R. L.\*, Rupert A. N., Field J., Pilles E. A., Sabrinathan J., Veinberg S. L., Leftwich K., Shaw A., Dickinson C., ... **Svensson M. J. O.**, et al. 2020. In Situ X-ray diffraction (ISXRD) for exploring Mars mineralogy and geology. *Lunar and Planetary Science Conference LI*, Abstract #2965. (International Conference; Research Group; Oral).
- [17] **Svensson M. J. O.\***, Osinski G. R., Longstaffe F. J., 2019. Hydrothermal alteration of the basal lake sediments at the Ries impact structure, Germany. *Impacts and their Role in the Evolution of Life – 2019.* (International Conference; Ph.D. Thesis; Poster).
- [16] **Svensson M. J. O.\***, Osinski G. R., Longstaffe F. J., 2019. Hydrothermally altered impact crater lakes and the secondary clay minerals they left behind. *Geological Association of Canada / Mineralogical Association of Canada (GAC/MAC) – 2019.* (National Conference; Ph.D. Thesis; Oral).
- [15] **Svensson M. J. O.\***, Osinski G. R., Longstaffe F. J., 2019. Formation of secondary clay minerals in post-impact lacustrine rocks at the Ries impact structure, Germany. *Space Day at Western.* (Institutional Conference; Ph.D. Thesis; Poster).
- [14] **Svensson M.J.O.\***, Chamma M. A.\*, Pascual A. D. P.\*, Azad B.\*, Andres C. N.\*, Tolometti G. D.\*, et al. 2019. The 2019 Western University High Altitude Balloon Initiative. *Space Day at Western.* (Institutional Conference; Student Research Group; Oral).
- [13] **Svensson M. J. O.\***, Osinski G. R., Longstaffe F. J., 2019. Formation of secondary clay minerals in post-impact lacustrine rocks at the Ries impact structure, Germany. *Lunar and Planetary Science Conference L*, Abstract #2494. (International Conference; Ph.D. Thesis; Poster).
- [12] **Svensson M. J. O.\***, Longstaffe F. J., Osinski G. R., Simpson S. L., 2018. Hydrothermal alteration of the crater lake sediments at the Ries impact structure, Germany. *55<sup>th</sup> Annual Meeting of the Clay Minerals Society*, Page 228. (International Conference; Ph.D. Thesis; Oral).

- [11] **Svensson M. J. O.\***, Osinski G. R., Longstaffe F. J., Simpson S. L. 2018 Hydrothermal alteration of the crater lake sediments at the Ries impact structure, Germany. *Lunar and Planetary Science Conference XLIX*, Abstract #1370. (International Conference; Ph.D. Thesis; Poster).
- [10] **Svensson M. J. O.\***, Fralick P. W. 2018. The Badwater Gabbro as an analogue for the weathering of Martian basalts. *Lunar and Planetary Science Conference XLIX*, Abstract #1372. (International Conference; Undergraduate Research Assistantship; Poster Presentation).
- [9] Simpson S. L.\*, Osinski G. R., Longstaffe F. J., Kring D. A., Schmieder M., **Svensson M. J. O.**, Gulick S. P. S. 2018. Characterization of impact glass alteration and associated secondary clay mineralogy through the upper Chicxulub peak ring. *Lunar and Planetary Science Conference XLIX*, Abstract #2518. (International Conference; Research Group; Poster).
- [8] **Svensson M. J. O.\***, Flemming R. L., Osinski G. R. 2017. Hydrothermal alteration in the crater lake sediments of the Ries impact structure, Germany. *Geological Association of Canada / Mineralogical Association of Canada (GAC/MAC) – 2017*. Abstract #368. (National Conference; M.Sc. Thesis; Poster).
- [7] **Svensson M. J. O.\***, Malloney M., Duff S., Osinski G. R. 2017. Laser induced breakdown spectroscopy (LIBS) as a simulated stand-off instrument in the CanMars 2016 analogue mission. *Space Day at Western*. (Institutional Conference; Analogue Mission; Poster).
- [6] Innis L.\*, **Svensson M. J. O.\***, 2017. The potential for a high-altitude balloon (HAB) mission through the Centre for Planetary Science and Exploration (CPSX). *Space Day at Western*. (Institutional Conference; Western Space Outreach; Oral Presentation).
- [5] Osinski G. R.\*, Caudill C. M., Cockell C. S., Pontefract A. J., Sapers. H. M., Simpson S. L., Svensson M. J. O., Tornabene L. L. 2017. The role of meteorite impacts in creating a habitable early Mars. *Lunar and Planetary Science Conference XLVIII*, Abstract #3071. (International Conference; Research Group; Poster).
- [4] Osinski G. R.\*, Battler M., Caudill C. M., Pilles E., Allard P., Balachandran K., ... **Svensson M. J. O.** et al. 2017. Overview of the 2016 #CanMars Mars sample return analogue mission. *Lunar and Planetary Science Conference XLVIII*, Abstract #2417. (International Conference; Analogue Mission; Poster).
- [3] **Svensson M. J. O.**, Malloney M., Duff S., Osinski G. R.\* 2017. Laser induced breakdown spectroscopy (LIBS) as a simulated stand-off instrument in the CanMars 2016 analogue mission. *Lunar and Planetary Science Conference XLVIII*, Abstract #1511. (International Conference; Analogue Mission; Poster).
- [2] **Svensson M. J. O.\***, Kissin S. A. 2016. Source of Native Iron in Canadian Arctic Artifacts. *61<sup>st</sup> Meeting of the Institute of Lake Superior Geology*. (International Conference; Honours Thesis; Poster).
- [1] **Svensson M. J. O.\***, Fralick P. W. 2016. The Badwater Gabbro as an analogue for the weathering of Martian basalts. *61<sup>st</sup> Meeting of the Institute of Lake Superior Geology*. (International Conference; Undergraduate Research Assistantship; Oral).